Polish Academy of Sciences

Institute of Fundamental Technological Research

Department of Theory of Continuous
Media and Nanostructures

Low Energy Field Electron Emission from Nanostructures: Theoretical Framework

Submitted for
PhD Thesis

Naira Grigoryan

Supervisor: Dr hab. eng. Piotr Chudziński

Warsaw, 2024

Acknowledgements

Completing this PhD thesis has been a profoundly challenging journey, and it would not have been possible without the support and encouragement of those around me.

First and foremost, I would like to express my deepest gratitude to my supervisor, Dr hab. eng. Piotr Chudziński. His invaluable guidance, insightful feedback, and unwavering support have been essential in the completion of this work. His patience and encouragement along with the commitment to my academic and personal development, have inspired me throughout this journey. I am profoundly thankful for the numerous opportunities he has provided me to grow as a researcher and for believing in my potential even during the toughest times.

I would also like to extend my gratitude to the head of our department, Prof. Giersig, for fostering a friendly and supportive atmosphere that has greatly contributed to my academic journey. I am also deeply grateful to the late Prof. Pęcherski, who played an essential role in my academic journey and introduced me to my current supervisor. I would also like to acknowledge Prof. Nasalski whose guidance helped shape my early academic path.

I would like to express my profound gratitude to the Institute of Fundamental Technological Research of the Polish Academy of Sciences (IPPT PAN) and its dedicated staff for providing a friendly and highly conducive research environment and the essential resources needed for my work. I want to thank my colleagues, who have been a constant source of support. The collaboration and friendship have made this journey more enjoyable and stimulating.

I want to express my profound gratitude to my parents for their unconditional love and belief in me which gave me the strength to persevere. I thank my grandfather, whose constant cheering and belief in my abilities have been a source of immense motivation for me.

My heartfelt thanks go to my family and friends, whose thoughtfulness and encouragement have kept me motivated and focused.

Special thanks to my husband for his understanding, patience, and support. His love and belief in me are my strength and foundation.

Finally, I would like to thank everyone else who has supported me in any way during this journey.

Thank you all!

Abstract

Field electron emission (FEE) is a crucial tool of nanotechnology, a source of electron beams valued for its stability, luminescence, and nowadays, safety and low energy consumption. Carbon Nanotubes (CNTs) have been identified as excellent sources for field emission. However, a theoretical framework to describe low-energy field emission is currently unknown, primarily due to unavoidable, correlated behaviour of one-dimensional (1D) materials. This work aims to develop such a theoretical formalism.

It is known, that for over four decades, that 1D systems have been described by the Tomonaga-Luttinger liquid (TLL) theory, which is based on collective modes such as plasmon-type modes, thereby automatically accounting for interactions. Our hypothesis is that the TLL can be used here to provide a description of field emission from these systems. The collective effects have been included in both the density of states (DOS) and the tunneling amplitude, as these are the primary factors to calculate. Therefore, the TLL effects have been incorporated into both of these calculations.

Along with the calculations of the transmission for the general case of barrier described by a fractional power law, the canonical Fowler-Nordheim (FN) theory has been expanded. An exact analytical formula, expressed in terms of Gauss hypergeometric functions, has been derived. It fully captures the emission for this generalized problem, including the screened interaction with the image potential. Initially, the accuracy of the approximation has been compared to the most advanced FN formulation where transmission is expressed in terms of elliptic integrals. Subsequently, the dependence of the current on the exponent of the power law has been thoroughly analyzed. To align with experiments, several examples of rough metallic surfaces and dielectric-covered surfaces have been observed demonstrating their compatibility with formalism.

In the following, parameters were identified that allow for exact analytical expressions for the finite temperature local density of states (LDOS) of TLL. Merging the results for LDOS $N(r, \omega; T)$ and the transmission probability $T(\omega, F)$, the current $J(\omega, F)$ was obtained, thus establishing a formalism that simultaneously captures the collective effects due to electron-electron interactions and thermionic emission. The results reveal that different types of nanotubes, along with their minigap and compressibility parameters, can be easily distinguished, based on field emission measurements of these materials.

Overall, this thesis presents an investigation of the quantum mechanical phenomena of FEE from CNTs, emphasizing the application of many-body physics to explain the effects of electron-electron interactions in these nanostructures.

Streszczenie

Emisja polowa (ang. Field Electron Emission, FEE) jest podstawową metodą produkcji wiązek electronów swobodnych. Takie wiązki elektronów wykorzystuje się w mikroskopii elektronowej, która umożliwiając nam obserwację struktur o rozmiarach nanometrów jest krytyczna dla rozwóju nanotechnologii. Kluczowymi parametrami źródeł emisji są stabilność, wysoka luminescencja, a od niedawna również bezpieczeństwo i niskie zużycie energii. Nanorurki węglowe (CNT), a w szczególności matryce nanorurek wielościennych (ang. arrays of MWCNT), są obecnie uznawane za najbardziej obiecujące źródła emisji polowej w najbliższej przyszłości. Jednakże teoretyczne ramy opisu emisji polowej nanorurek, szczególnie w kluczowym reżimie niskiej energii, były jak dotąd niezane. Istotną przeszkodą było podanie opisu uwzględniającego skorelowane zachowanie elektronów, a takie zachowanie jest nieuniknione w materiałach jednowymiarowych (1D), których sztandarowym przykładem są CNT. Niniejsza praca ma na celu rozwinięcie takiego teoretycznego formalizmu.

Wiadomo, już od lat 80-tych dwudziestego wieku, że systemy 1D opisuje teoria cieczy Tomonagi-Luttingera (TLL), która opiera się na modach kolektywnych, takich jak mody typu plazmonowego, automatycznie uwzględniające korelacje. Nasza hipoteza zakłada, że teorię TLL można zastosować także do opisu emisji polowej z nanorurek węglowych. Efekty korelacji należy uwzględnić zarówno przy obliczeniach gęstości stanów (DOS), jak i w amplitudzie tunelowania. Oba te problemy rozwiązano w przedstawionej pracy.

Dla obliczenia amplitudy tunelowania, $T(\omega, F)$, rozważano transmisje przez barierę dla ogólnego przypadku bariery opisanej prawem potęgowym ułamkowym. W tem sposób rozszerzono kanoniczną teorię Fowlera-Nordheima. Wyprowadzono dokładny wzór analityczny, wyrażony w postaci funkcji hipergeometrycznych Gaussa, który w pełni opisuje emisję w tym uogólnionym problemie, uwzględniając zarówno ekranowanie pola jak i oddziaływanie z potencjałem ładunku pozostawionego w nanorurce. Dokładność tego rozwiązania potwierdzono poprzez porównanie z dotychczas najbardziej zaawansowanym sformułowaniem teorii Fowlera-Nordheima, gdzie transmisja wyrażana jest w postaci całek eliptycznych. Następnie dokładnie przeanalizowano zależność prądu od wykładnika prawa potęgowego bariery. W celu rozważenia rzeczywistych sytuacji w eksperymentach, przedyskutowano kilka przykładów szorstkich powierzchni metalicznych i powierzchni pokrytych dielektrykiem.

W kolejnej części pracy zidentyfikowano parametry, które pozwalają na podanie dokładnych wyrażeń analitycznych dla lokalnej gęstości stanów (LDOS) TLL w skończonej temperaturze, $N(r, \omega; T)$. Łącząc wyniki dla LDOS $N(r, \omega; T)$ i prawdopodobieństwa transmisji $T(\omega, F)$, otrzymano prąd emisji polowej $J(\omega, F)$. W ten sposób otrzymano formalizm, który jednocześnie ujmuje efekty kolektywne, spowodowane oddziaływaniami elektron-elektron, oraz emisje termiczną. Wyniki pokazują, że na podstawie pomiarów emisji polowej rozważanego materiału – matryc MWCNT – można rozróżnić różne typy nanorurek, wraz z wielkością ich miniprzerwy i parametrami ich cieczy elektronowej. Podsumowując, niniejsza praca przedstawia zastosowanie mechaniki kwantowej i fizyki wielu ciał do opisu FEE w nanostrukturach typu CNT.

List of Publications

The following peer-reviewed publications present the main results and methods discussed in this work:

I. Grigoryan, N., Roszkiewicz, A., and Chudzinski, P., Generalizing Fowler – Nordheim Tunneling Theory for an Arbitrary Power Law Barrier. Physica Status Solidi (b), 260(6), 2200599, (2023).

II. Grigoryan, N. and Chudzinski, P., Role of electron-electron interactions in electron emission from nanotube materials. Physical Review Materials, 8(1), 016003, (2024).

Oral Presentations at Conferences related to the work:

1. Grigoryan, N., Chudzinski P., The role of electron-electron interactions in electron emission from arrays of nanotubes, DPG Spring Meeting of the Condensed Matter Section (SKM2023), 2023-03-26/03-31, Dresden, Germany.

2. Grigoryan, N., Chudzinski P., The role of electron-electron interactions in electron emission from nanotube materials, VII Conference of Doctoral Students of the PAS (KonDokPAN2023), 2023-10-13/10-15, Wrocław, Poland.

3. Grigoryan, N., Chudzinski P., Generalizing field emission theory for surfaces with strong electron-electron interactions, 2nd International Virtual Conference on Materials Science and Engineering (Materials Science Meeting 2023), 2023-11-11/11-12.

Abbreviations

1D	One Dimensional
2D	Two Dimensional
3D	Three Dimensional
AFM	Antiferromagnet
ARPES	Angle-Resolved Photoemission Spectroscopy
BKT	Berezinskii–Kosterlitz–Thouless
BZ	Brillouin zone
CNT	Carbon Nanotube
CVD	Chemical vapor deposition
CCVD	Catalytic chemical vapor deposition
CFT	Conformal field theory
DOS	Density of states
FEE	Field Electron Emission
FE	Field Emission
FN	Fowler-Nordheim
FT	Fourier transform
gFN	generalized Fowler-Nordheim
HRTEM	High-Resolution Transmission Electron Microscopy
JWKB	Jeffreys-Wentzel-Kramers-Brillouin
LDOS	Local density of states
LEED	Low-Energy Electron Diffraction
MWCNT	Multi-walled carbon nanotube
MWNT	Multi-walled nanotube
NMR	Nuclear magnetic resonance
ODE	Ordinary differential equation
PE	Plasma enhanced
PVD	Physical Vapor Deposition
RG	Renormalization Group
RPA	Random-phase approximation
SEM	Scanning Electron Microscope
STM	Scanning Tunneling Microscope
SWCNT	Single-walled carbon nanotube
SWNT	Single-walled nanotube
TEM	Transmission Electron Microscopy
TLL	Tomonaga–Luttinger liquid
UV	Ultraviolet
WKB	Wentzel-Kramers-Brillouin
ZBA	Zero-bias anomaly

Symbols

$\mathcal{T}$	Transmission Probability
ω_0	Work function of the metal
F	Local electric field
e	Elementary charge
m_e	Electron mass
J	Electron emission-current density
$\hbar_P$	Planck's constant
y_N	Nordheim parameter
ϵ_0	Electric constant
K_ρ	Charge Compressibility
K_σ	Spin Compressibility
μ	Chemical Potential
T	Temperature
β	Inverse Temperature

Contents

CONTENTS

List of Figures

iv

LIST OF FIGURES

List of Tables

Part I

Background

Chapter 1

Introduction

> Somewhere, something incredible is waiting to be known.
>
> *Carl Sagan*

In this chapter, we give an introduction to three main research areas of this thesis: electron emission, carbon nanotubes and the Tomonaga-Luttinger liquid.

1.1 Electron Emission

Many critical tools of nano- and atomic-scale engineering rely on our capability to create and steer free electron beams. Obviously, the first step in this direction is to create the free electron source. This requires finding a reliable way to extract electrons from the material - a process called electron emission - which has become a major field of research at the intersection of solid state physics, materials science, and vacuum technology over the decades.

Electron emission, an important concept in physics and materials science, is the process where an electron escapes from the surface of a material, usually a metal. At the atomic level, every atom has a positively charged nucleus surrounded by negatively charged electrons. In some cases, these electrons are loosely bound to the nucleus, making them susceptible to external influences. A small amount of energy, like a little push or a tap, may cause these electrons to fly out of their orbits.

There are free electrons inside a metal surface. These electrons, although not bound to any particular nucleus, do not easily escape from the surface of the metal. This is due to the overall neutral charge of the metal. When an electron leaves the surface, it gives a positive charge to that area, creating an attractive force to pull the electron back. Therefore, a surface barrier is formed at the metal interface, effectively containing the free electrons inside the metal. To take these electrons out from the metal surface, sufficient force must be applied to overcome this surface barrier.

Various physical mechanisms can cooperate to cause electron emission. To define them, each mechanism should be considered separately, which may perhaps seem artificial but it promotes a better explanation. This is a paraphrase of the list originally proposed in Ref. [1]:

- **Field emission** (indicated by the blue arrow in Fig. 1.1) occurs when high electric fields facilitate electron emission through quantum mechanical tunneling, a process described by the Fowler–Nordheim equation [2].

- **Photoemission** (indicated by the green arrow in Fig. 1.1) is the process where the emission of electrons occurs due to the absorption of photons, allowing the electrons to gain sufficient energy to overcome the potential barrier. This phenomenon is described by the Fowler-DuBridge equation [3].

- **Thermal emission** or thermionic emission (indicated by the red arrow in Fig. 1.1) refers to the process where electrons are emitted as a result of heating the cathode, enabling the electrons in the thermal tail of the distribution function to gain enough energy to pass the surface barrier. This phenomenon is quantitatively explained by the Richardson-Laue-Dushman equation [4].

We see that each of these mechanisms is distinguished by the original source that caused the emission. There are also phenomena where electron-electron interactions dominate:

i. **secondary emission** (indicated by the green arrow in Fig. 1.1) involves the release of electrons due to the hitting of a surface by high-energy primary electrons. These primary electrons transfer sufficient energy to secondary electrons allowing them to overcome the surface barrier. This process is mathematically described by the Baroody equation [5].

ii. **space-charge limited emission** refers to the phenomenon where the current is limited due to the accumulation of charge in the anode–cathode (AK) gap, which acts to hinder the electric field at the surface of the cathode or to limit the amount of charge crossing the gap [6].
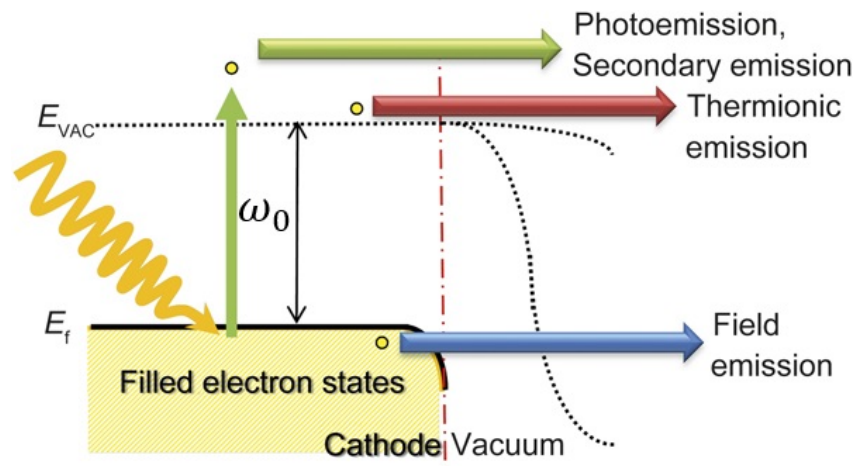
Figure 1.1: Energy-band illustration of the electron-emission mechanisms for a material describing the initial energy state of electrons. The solid/vacuum interface is represented by the red dashed-dotted line, while the dotted lines represent the vacuum level for the different electron-emission mechanisms: field electron emission – blue arrow, thermal emission – red arrow, secondary emission and photoemission – green arrow. Here, E_{VAC} is the vacuum level, E_f is the Fermi level, and ω_0 is the cathode work function (Figure adapted from [7]).

The last two are in essence many-body phenomena, separated artificially from others, as in fact they are present during each emission event no matter what the original driving force had been. Describing these is an active field of research. An ongoing research is also in a mutual collaboration of various mechanisms, e.g. how light (i.e., photon assistance) or finite temperature does affect the field emission.

Electron emission is widely used in numerous scientific and technological sectors, including electronics, communication, imaging, energy transformation, and detection[1]. Devices employing electron emission include vacuum tubes [8], cathode ray tubes (CRT) [9], [10], vacuum diodes [11], [12], triodes [13], [14], magnetrons [15], field emission displays [16], [17], [18], electron microscopes [19], [20], [21], nanoelectronic devices [10], [22], solar cells [23], photodetectors [24], photomultipliers [25], cameras [26], [27], and scintillators [28]. In our formalism, the primary focus is on field emission (explained in detail in later sections of this chapter), although when the energy of an electron is varied, discussions about photon-assisted field emission can be held, which is closely related to photoemission. While our model does not primarily focus on thermionic emission, temperature variations are accounted for. This enables the study of the transition between field emission, dominant at lower temperatures, and thermionic emission, which becomes significant at higher temperatures.

1.1.1 Historical Review of Field Electron Emission

In order to explain the impact of field emission on contemporary engineering sciences, we will provide here a very short review of the historical development of relevant technologies, particularly emphasizing open research questions. A more extensive version of these developments can be found either in Ref. [29] or in Ref. [30] and the *"2nd gate to microcosm"*, an autobiography of Ernst Ruska, the scientist who was a founding father of electron microscopy, for which he obtained Nobel Prize in Physics 1986, on which this subsection is based on.

The earliest recorded observations of field electron emission can be traced back to Winkler in 1744 [31], who reported electrical discharges from wire electrodes. An interesting phenomenon that further clarifies the nature of electron emission was observed by Thomas Edison, often referred to as the "Edison effect" [6]. During Edison's experiments with the incandescent lamp, unexpected electrical discharges were discovered. This phenomenon, initially a mystery to the scientists of the time, was eventually understood, the observed current being recognized as cathode rays. This discovery formed a fundamental basis for understanding electron emission. Debates over the nature of these rays, whether ethereal or material, ultimately concluded with the confirmation of their particle nature. This early research laid the foundation for later, more structured studies of electron behavior, significantly advancing the field.

However, a proper understanding of the phenomenon did not emerge until after J.J. Thomson's discovery of electrons in 1897 [32]. At Cambridge University, Thomson's seminal work involved demonstrating the deflection of cathode rays in a capacitor plate setup. This research established the particle nature of cathode rays and also earned him the Nobel Prize in Physics in 1906. It laid the groundwork for more structured studies of electron behavior, significantly advancing the field.

Before a comprehensive understanding of field electron emission, related phenomena like thermal emission (Richardson effect) observed in 1916 [33] and photoemission (Einstein's

---

[1]It is necessary for each application requiring the free electron beam.

photoelectric effect) observed in 1905 [34] were documented. These phenomena involved the emission of electrons due to thermal energy or photons, respectively.

After 1922, various experimental efforts were undertaken to investigate field electron emission. Groups led by Millikan [35] at Caltech, Gossling [36] at General Electric in London, and Lauritsen [37] and Oppenheimer [38] independently, sought to characterize the current-voltage relationship in field electron emission.

A significant theoretical breakthrough occurred after the development of quantum mechanics. In 1928, Fowler and Nordheim proposed a theory[2] of field emission based on the quantum tunneling of electrons. They introduced the Fowler-Nordheim (FN) equation that predicted a specific current-field dependence, which matched experimental results. The success of this theory provided evidence for quantum tunneling and Fermi-Dirac statistics for electrons. The most direct application of field emission is field electron microscope (FEM). Erwin Mueller's development of FEM in 1937 marked a major advancement [39]. FEM allows to image the surface of the tip. It became a powerful tool for studying material characteristics and structures, leading to developments in the field of surface science. It was the first one that enabled us to see single atoms in 1951. This innovation opened up new possibilities for investigating surface properties and behaviours. The concept of the field electron microscope was extended to various other instruments in surface science, contributing to advancements in understanding the properties and behaviors of materials at the atomic and subatomic levels.

FEM allows imaging of the tip only, so it is not very versatile but the stable beam of electrons allowed for development of other tools. The mid-20th century witnessed a transformative leap in the ability to probe the nanoscale world through the development of transmission electron microscopy (TEM). TEM used electron beams to overcome the limits of classical optical microscopy, building on the foundations of field electron emission. This progress was made possible by the need for a stable source of electron beams, an important requirement met by developments in field electron emission technology. Field emission provides the consistent, high-intensity electron beam essential for the high-resolution imaging capabilities of TEM and SEM.

Since the discovery of the wave nature of electron in the late twenties of the 20th century, researchers have been aware that these electron waves can overcome the optical diffraction limit. Finally, the electron microscope's version of Ruska, built in 1933, could achieve magnifications ten times greater than existing light microscopes, for example, a magnification of more than 12,000 times. The reason for this significant improvement is the shorter wavelength of electrons compared to light. Electrons, having much shorter wavelengths, allow TEM to bypass the diffraction limit that restricts the resolution of traditional optical microscopy, allowing much finer detail to be resolved.

In the 1960s, Albert Crewe and his team made significant advancements in electron optics and imaging techniques, which led to the development of the first commercial high-resolution electron microscope. However, the development of aberration–corrected electron microscopes in the 1990s further improved TEM's resolution and imaging capabilities leading to phase sensitive technique with Å, single atom resolution. Scientists Harald Rose, Maximilian Haider, and Knut Urban played a crucial role in developing aberration correction technologies that effectively addressed defects in electron lenses, leading to enhanced resolution. Nowadays, all these aberration controlled High-Resolution Transmission Electron Microscopy (HRTEM) relies, on the top of interference, on high-performance-computation methods where the knowledge about energy distribution of original, emitted electron beam plays a central role. Thus, the engineering of HRTEM devices meets here developments in materials science of electron sources.

A different path of electron microscopy development was that of low-energy-electron microscopy; it first became operational thanks to works by Ernst Bauer and Wolfgang Telieps in 1985. Here, the aim is to study real-time dynamics that takes place on larger areas of the surface, answering research questions on phase transitions, mesoscopic orderings, and self-organization. This class of methods is actively pursued – further derivatives of the LEEM are: bright and dark field micro-imaging, spin-resolved imaging, mirror and reflectivity contrast imaging and even electron holography. In all those cases, particularly in holography, detailed knowledge about the incoming electron beam is again crucial. The electron diffraction methods described below were also derived from the LEEM.

In 1981, German physicists Gerd Binnig and Heinrich Rohrer refined both FEM and SEM approaches by developing a technique similar to field emission, but on an extremely small scale. They used a concept similar to having a cathode, which is like a plate, on top of the material and gradually shrinking it down. This gradual size reduction enabled the probing of objects from macroscopic down to nanoscopic scale. Further miniaturization of the cathode to an extremely small size comparable to a single atom led to the development of the Scanning Tunneling Microscope (STM). This innovative microscope duplicates the principle of field emission, where the material is probed with an increasingly small cathode, performing the remarkable achievement of atomic resolution. The STM complements rather than competes with Ruska's transmission microscope. Therefore, in 1986, Ruska, Binning, and Rohrer shared the Nobel Prize in Physics.

Another application of stable electronic beams is in electron wave diffraction experiments. Here, the control of beam's monochromaticity is crucial. In 1927, the de Broglie hypothesis, claiming that the mass of an electron was small enough to exhibit the properties of both particles and waves, was experimentally confirmed at Bell Labs by Clinton Davisson and Lester Germer [40]. They conducted an experiment where they fired low-energy electrons at a crystalline nickel target, observing diffraction patterns in the angular dependence of the intensity of backscattered electrons [40], [41]. Shortly after, Thomson and Reid published their own electron-diffraction work, using much higher kinetic energy [42], thousands of times greater than that employed by Davisson and Germer. These investigations provided strong evidence for the wave properties of electrons and marked the inception of electron-diffraction research. The significance of low-energy electron diffraction (LEED) grew in the 1960s. This surface-sensitive approach was critical in determining the atomic arrangement of crystalline surfaces and in gaining a better knowledge of nanoscale material characteristics. Along with TEM, LEED transformed the comprehension of the nanoscale world, revealing detailed surface structures and interactions and laying the foundation for contemporary materials research. In addition to the remarkable historical events outlined earlier, the area of electron emission has experienced ongoing growth with a multitude of contemporary achievements that have advanced the comprehension of materials, nanoscale phenomena, and time–resolved imaging methods. These achievements have transformed multiple disciplines and cleared the path for the latest research and applications.

1.1.2   Tunneling Phenomena and Field Electron Emission: Basic Explanation

Field electron emission, also known as electron field emission or just field emission, is a quantum mechanical phenomenon that occurs when electrons tunnel from a metallic solid into free space, typically a vacuum, under the influence of a strong electric field. Unlike

other electron emission methods, such as surface photoemission or thermionic emission, the field electron emission does not require electrons to exceed an energy threshold. Instead, it depends on their ability to tunnel through a potential barrier. This phenomenon can be explained only by quantum mechanics. In classical mechanics, potential barriers are impenetrable. However, quantum mechanics allows particles to tunnel through these barriers, appearing on the other side. This fundamental mechanism underlies field electron emission.

The field electron emission process is determined by the work function of the material, which is the energy required for an electron to escape the surface of the metal. Metals have a substantial barrier, characterized by the work function that is several electronvolts above their Fermi energy. The detailed discussion is in Chapter 6, Sec. 6.7.

From the view of fundamental physics, field electron emission is a quantum tunneling phenomenon from solids to a vacuum. More precisely, field emission is a method for electron emission applying an electric field to modify the shape of the barrier (see Fig. 4.1). When a highly positively charged metal plate is placed next to a metal surface, the positive charges inside that anode pull out free electrons from the metal surface (Fig. 1.2). If the positive potential on the anode is strong enough, it will overcome the work function and release free electrons from the metal's surface.
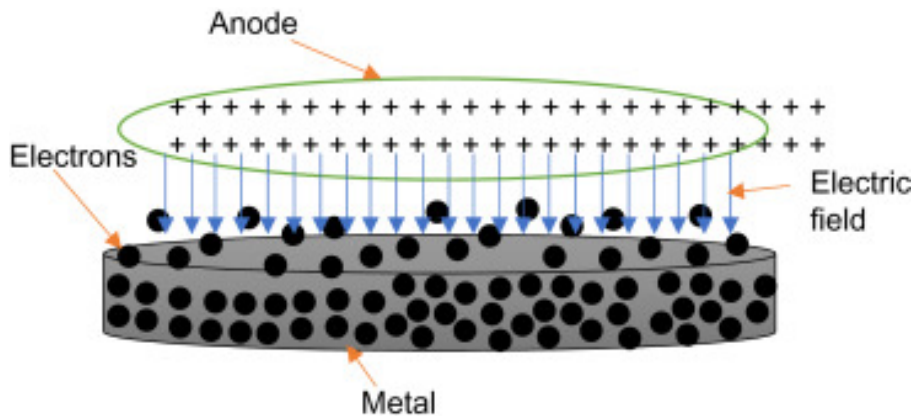
Figure 1.2: Illustration of field electron emission: electrons are emitted from a metal surface due to the influence of a strong electric field by a positively charged plate (anode) (Figure from [43]).

To produce field emission, a strong field between the anode and the metal is necessary. The field emission can then occur at low temperatures, that's why it is often called cold-cathode emission [2].

Electrons are negatively charged, and when they start moving due to the electric field, they can influence the *locally* distribution of other electrons around them. This interaction can cause a "screening" effect, which can make the process quite challenging to describe theoretically. Actually, the process is quite complex: when an electron is emitted, it leaves a "hole" in the electron distribution at the metal surface. This hole can also affect the behavior of the emitted electron and interact with other electrons, leading to "many-body effects." These interactions can impact the energy and trajectory of the emitted electron, thus modifying the measured current. One question addressed in this thesis is whether such modification is substantial or not.

1.1.3 Fowler-Nordheim theory

Field emission is a profoundly quantum mechanical phenomenon; hence, its theoretical description has been possible only after the development of quantum mechanics. The first successful model for the emission from bulk metals was proposed by Fowler and Nordheim in 1928 [2]. The Fowler-Nordheim (FN) theory is an elementary field electron emission theory. It has an essential role in the theory of field electron emissions. Fowler and Nordheim presented an analytic formula for the emission current density as a function of the external electric field. The FN formula (shown later as Eq. 3.14) describes the fundamental behaviour of field electron emission from metals and is transformed into a basic field emission equation. The essential idea behind the FN approach is to use a supply function (later it will be called density of states(DOS)) to represent the emission current density as the product of the supply function and the transmission coefficient.

FN is a theory of a single electron escaping from the material. It is well established by the seminal works of Landau [44], the single particle description works well for three-dimensional (3D) materials. Ultimately, this is the reason why FN has worked so well, being the foundation of FE for several decades: all the materials considered were large bulk 3D electrodes. The necessity to improve it arose only in the last few years, with the development of nanotechnology.

FN is a single-particle description and does not take these many-body processes into account. These later ones are considered here by the methods derived in Sec. 3.1.3.

1.2 Carbon Nanotubes

Up to the late 20th century only two carbon allotropes were known: graphite and diamond. Then, with an advent of nanotechnology, researchers were able to discover that carbon atoms make distinct structures also on this scale. Carbon nanotubes (CNTs) are a fascinating class of nanomaterials with a wide range of applications. CNTs were first observed by Sumio Iijima in 1991 and are characterized by their nanosized hollow tube-shaped structures [45]. Iijima described the production and characterization of carbon nanotubes, emphasizing their characteristic helical and tubular form consisting of carbon atoms. This finding was a significant turning point in the study of nanomaterials, and since then it has prompted intensive research into the characteristics and possible uses of CNTs in a variety of sectors, ranging from electronics [46] and materials science [47] to medicine [48], [49], [50] and energy storage [51], [52].

1.2.1 Classification of Carbon Nanotubes

Carbon Nanotubes (CNTs) are categorised into two main types based on their diameters and structures: single-walled carbon nanotubes (SWCNTs) and multi-walled carbon nanotubes (MWCNTs).

SWCNTs are seamless cylinders composed of a single layer of graphene rolled up into a tube. They have relatively small diameters, typically ranging from 0.7 to $10nm$, with most falling below $2nm$. Despite their small size, SWCNTs can achieve significant lengths, often reaching up to several μms. One of the distinguishing features of SWCNTs is their electronic properties, which can be either metallic or semiconducting, depending on their

(a)   (b)
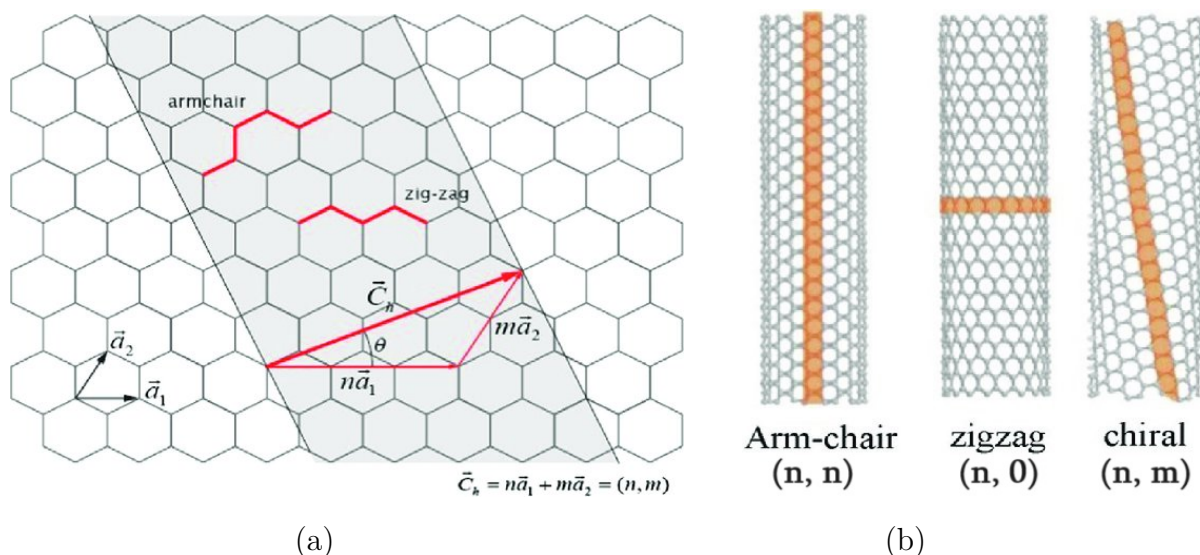
Figure 1.3: (a) A Schematic diagram of a graphene sheet, representing a single layer of carbon atoms arranged in a hexagonal lattice pattern. $\vec{a}_1$ and $\vec{a}_2$ are the basis vectors of the graphene lattice, defining the unit cell of the graphene structure. The red lines on the graphene sheet indicate the section that will be rolled to form a carbon nanotube. This pattern determines the tube's twist and resulting electrical properties. The chiral vector $\vec{C}_h$ is defined in Eq. 1.1, and the chiral angle θ is the angle between the chiral vector $\vec{C}_h$ and the vector $\vec{a}_1$. (b) The rolled-up lattice structures form armchair, zigzag, and chiral carbon nanotubes, each labelled with their respective chiral indices n and m. (The segments highlighted in red in part (a) correspond to the orange-highlighted regions here, indicating the formation of the carbon nanotubes from the graphene lattice.) The figures are reproduced from [53].

helical arrangement. However, it's important to note that while SWCNTs are easier to describe theoretically, they can be challenging to obtain and characterise experimentally.

MWCNTs consist of several SWCNTs encapsulated one inside another, sharing one main axis, perpendicular to their chiral vectors $\vec{C}_h$ (as defined in Eq. 1.1). Each SWCNT is thus a shell, a parallel building block, of the MWCNT. MWCNT can have a diameter reaching more than $100nms$. MWCNTs are easier to synthesize and can be considerably longer, with lengths that can range from several μms to even mms. An experimental finding is that, unlike SWCNTs, MWCNTs are always metallic, regardless of their chirality. This means that they conduct electricity well and have a characteristic band structure that results in metallic behavior independent of their specific structural configuration.

The theory that describes MWCNTs is built upon theories developed for SWCNTs, but it has to incorporate additional complexities arising from the interaction between the multiple walls or shells. These interactions can involve van der Waals forces, as well as more complicated effects caused by electrical or thermal connections between the layers. Although theories for SWCNTs give a basic foundation, characterising the behaviour and properties of MWCNTs requires a more extensive theoretical approach. In the simplest approximation, one takes the following picture: since the number of shells N_s is usually large, certainly $N_s \gg 3$, then at least one of these shells fulfils the conditions (see below) to be metallic. This explains experimental facts. In a more refined picture, even if the metallic shell is perturbed (either by distortion or electric potential of other shells), so that carriers should be localized therein, the carriers can always jump onto a neighbouring

SWCNT			MWCNT
Semiconducting	*Metallic*		*Metallic*
$(n - m) \, mod \, 3 \; \neq \; 0$	*Protected*	*Narrow Gap (Chiral)*	*Provided any of the shells is metallic*
	Achiral		

Table 1.1: Classification of SWCNTs and MWCNTs based on electronic properties and chirality

shell and find a parallel way ahead. However, a necessity of these jumps implies that a characteristic velocity of carriers should always be smaller than Fermi velocity in SWCNT. This is also in agreement with experimental observations. The MWCNT can then be imagined as a rolled Moire pattern, with a flat band at the lowest energies. Now, the velocity and the size of the effective unit cell become free parameters of the theory.

In contrast to the above-given complexities of MWCNT, the SWCNT are fully understood, so their full theoretical description can be presented here. In terms of the chiral vector and the chiral angle, SWCNTs are also classified into three varieties: **armchair, zigzag** and **chiral**. These classifications are specifically determined by how the graphene sheet is "rolled up" during the creation process.

Chiral vector can be expressed regarding the base vectors (Fig. 1.3)

$$\vec{C_h} = (n, m) = n\vec{a_1} + m\vec{a_2} \tag{1.1}$$

The relationship between the integers (m, n) and the diameter d of SWCNTs [54] is given by

$$d = \frac{|\vec{C_h}|}{\pi} = \frac{a_0}{\pi}\sqrt{(n^2 + nm + m^2)} \tag{1.2}$$

where a_0 is the unit vector length and $a_0 = 0.246nm$. Hence, the radius of the nanotube will be

$$R = \frac{|\vec{C_h}|}{2\pi} \tag{1.3}$$

And the chiral angle, the angle between the $\vec{C_h} = (n, m)$ and the basis vector $\vec{a_1}$, shown in Fig. 1.3 (a), is given by [54], [55]:

$$\tan\theta = \frac{\sqrt{3}m}{2n + m} \tag{1.4}$$

In **armchair** (n, n) CNTs, both indices (n, n) are the same; they are highly symmetrical and have unique electronic properties, making them particularly interesting for certain electronic applications.

Zigzag $(n, 0)$ CNTs are formed when one of the indices is zero (0), and the other index (n) determines the size of the nanotube. Zigzag CNTs also have distinctive electronic

properties and are studied for their potential applications in nanoelectronics and other fields.

Chiral (n, m) CNTs have different values for both indices (n and m), meaning that they are formed with a combination of rolling angles relative to the hexagonal lattice. They exhibit a wide range of electronic and optical properties, depending on the specific values of n and m. These nanotubes are adaptable and may be used for various applications.

CNTs are utilized in nanotechnology, materials science, and electronics. They improve the electrical and mechanical properties of materials, have applications in nanoelectronics, sensors, energy storage, and medicine, and are integral to the development of innovative nanoscale devices and systems. Their remarkable versatility remains a driving force behind ongoing research and innovation across a wide range of disciplines.

1.2.2 Semiconducting, narrow-gap and metallic nanotubes

Carbon Nanotubes (CNTs) are distinguished by their unique electrical properties, which can be classified as *semiconducting*, *narrow-gap semiconducting* or *metallic*.

This diversity is due to their distinctive structural configurations, particularly their chirality and diameter. The electronic properties of CNTs are determined by their band structure, which is derived from the band structure of graphene, a single layer of carbon atoms arranged in a hexagonal lattice.

In graphene, the conduction and valence bands meet at specific points, known as the K and K' valleys. These valleys (Fig. 1.4) play a crucial role in determining the electronic properties of CNTs. Electrons in graphene behave as massless Dirac fermions on account of the linear energy dispersion near the K and K' Dirac points of the Brillouin zone. This results in a cone-like energy dispersion, often referred to as the Dirac cone (Fig. 1.4), see Eq. 6.3 for mathematical formula describing it.
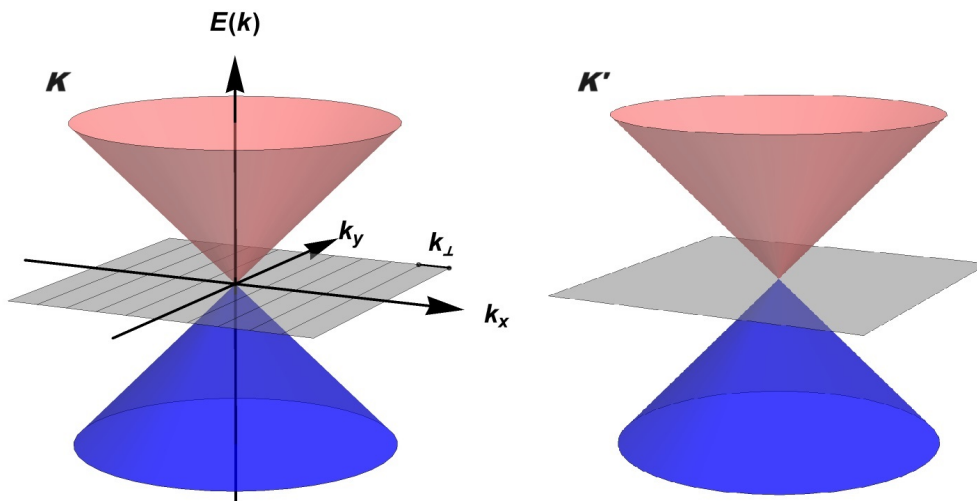
Figure 1.4: Illustration of the band structure of 2D graphene (or, more generally, any hexagonal bi-partite 2D material): Dirac cones showing energy dispersion at the K and K' valleys in semimetal graphene. Characteristics of a semimetal is that there is only one point where conduction (red cone) and valence (blue cone) bands touch (as shown in the K point). An intersection of perpendicular quantization with the Dirac point correlates with metallic properties in carbon nanotubes, while deviations indicate semiconducting characteristics.
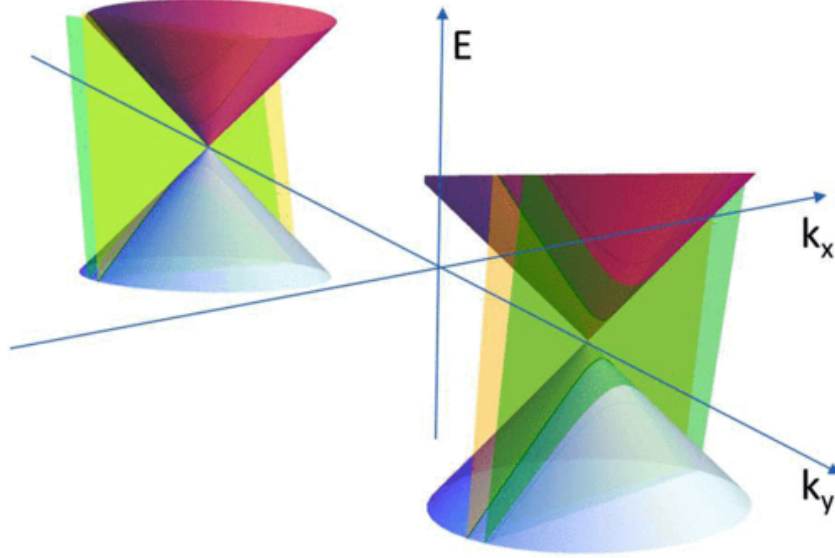
Figure 1.5: Visualization of the low-energy electronic band structure for a CNT belonging to the zigzag(like) class. Anisotropy of $t_{\vec{r},\vec{d}}^{\bar{\sigma}}$ leads to the cones shifting away from K and K' points of a reciprocal unit cell. The plane cross-sections are caused by circumferential quantization conditions; the values of quantized k_y, closest to Dirac points, are demonstrated. Each cone has two dispersions $E(k_x)$ (Figure from [56]).

When graphene is rolled into a nanotube, its electronic properties depend on perpendicular quantization. The chiral angle, which is the angle of the graphene lattice relative to the axis of the nanotube, determines whether the nanotube is metallic or semiconducting. This is because the chiral angle affects how the hexagonal lattice of graphene aligns along the circumference of the nanotube. In a carbon nanotube, quantization occurs as a result of the confinement of electrons around its circumference. The allowed
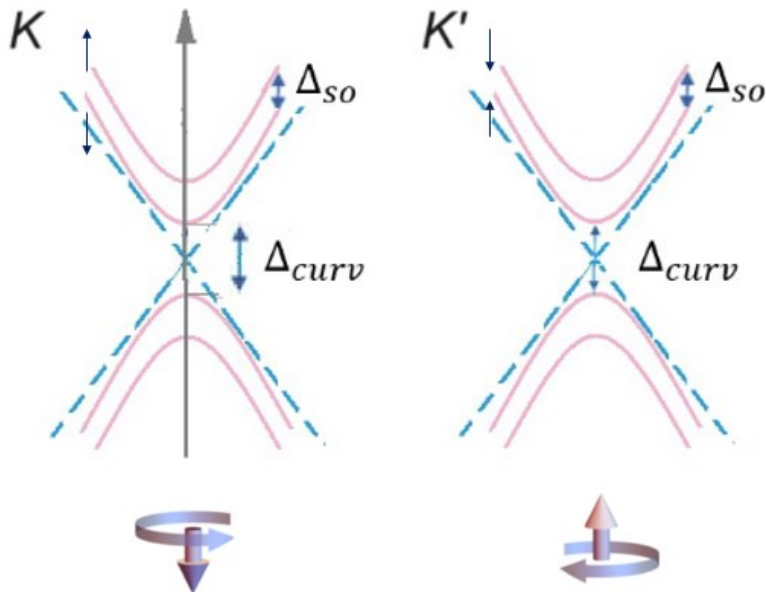
Figure 1.6: Energy band diagrams showing spin-orbit coupling effects at K and K' points in the Brillouin Zone: blue dash lines show the metallic behaviour of nanotube (without curvature effects).
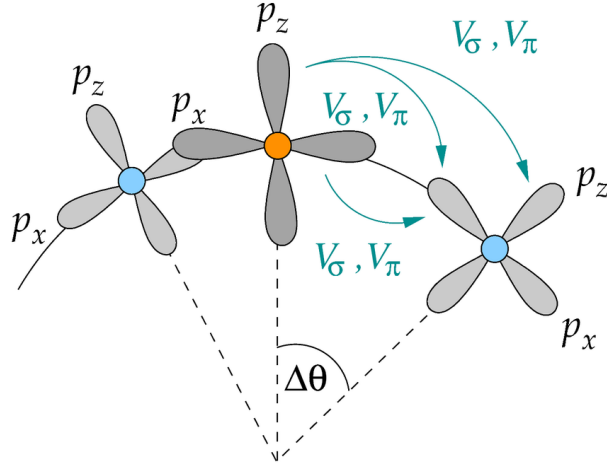
Figure 1.7: Illustration of the curvature effect of the nanotube on the transfer integrals between the orbitals of the closest neighbor atoms. The p_z orbitals on different sites are no longer parallel, therefore there is mixing with the $p_{x,y}$ orbitals forming the σ bonds (Figure from [57]).

energy states (standing waves) depend on the diameter of the nanotube. Larger diameters allow for more standing waves, leading to denser quantization bands. These bands represent different quantized values of the wave vector perpendicular to the nanotube axis ($k_\perp = i\frac{\pi}{|C_h|}$). The key question is whether any of these quantization bands intersect with the Dirac point in the energy dispersion relation. If a quantization band crosses the Dirac point, the nanotube exhibits metallic behaviour: at the Dirac point, the energy gap between the valence and conduction bands vanishes, allowing the free movement of electrons (metallic behaviour), in other respects, it is semiconducting.

Depending on the energy dispersion and the positioning of the quantization bands relative to the Dirac point, one can determine the electronic nature of the nanotube. The proximity of these bands to the Dirac point determines whether the nanotube behaves as a metal or a semiconductor. In general, when chirality is such that $n - m$ is divisible by
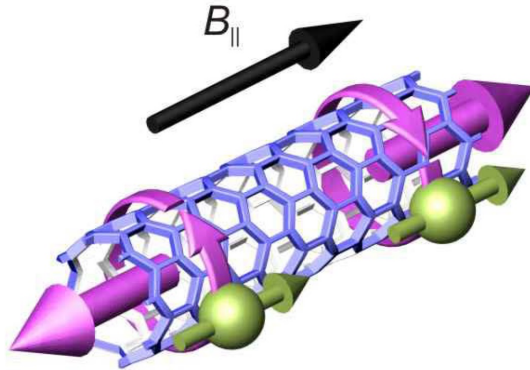
Figure 1.8: Electrons that are held in a nanotube segment have quantized energy levels, each of which is four-fold degenerate in the absence of spin-orbit coupling and defect scattering. The purple arrow on the left indicates the current and magnetic moment arising clockwise, while the one on the right – from anticlockwise orbital motion around the nanotube. The green arrows indicate positive moments due to spin (Figure from [58]).

three, one of the quantized bands crosses the Dirac point and the nanotube is metallic. Otherwise, the nanotube will be a large gap semiconductor, with the size of the gap inversely proportional to its diameter.

Up to this point, the rolling of the graphene sheet has been discussed with an assumption that graphene bands will stay unaltered during the rolling, i.e., that atomic overlaps t will stay the same (see Eq. 3.44 for the Hamiltonian). This is of course an approximation. There are further, small perturbations that will turn the metallic tube into a narrow gap semiconductor. Fig. 1.5 illustrates the low-energy band structure of a zigzag CNT. The vertical axis indicates the electron energy E, while the horizontal axes represent the momentum space k_x and k_y. The conical structures describe the electron dispersion relations near the Dirac points, which are typical of the hexagonal lattice of graphene. The planes encode the quantization condition. The anisotropy of the hopping parameter $t_{\vec{r},\vec{d}}^{\bar{\sigma}}$ shifts these cones slightly away from the K and K' points. This shift is caused by the CNT's curvature and spin-dependent interactions. The resulting 1D low-energy band structure is illustrated in Fig. 1.6, where narrow gaps Δ_{curv} and Δ_{so} are shown. As illustrated in Fig. 1.7, the systems of coordinates on different sites are no longer parallel; thus, the overlaps between previously (in flat graphene) orthogonal p orbitals are now possible, as shown in Fig. 1.7. This produces a finite Δ_{curv}. The origin of the Δ_{so} shift is due to the spin-orbit coupling effect, the physical origin of which, the emergent magnetic field from a screwdriver motion of carriers along the CNT, is illustrated in Fig. 1.8.

The cross-sectional points of the cones with the horizontal planes resulting from circumferential quantization show the quantized energy levels available to the electrons, with particular focus on the levels close to the Dirac points. This quantization is a direct consequence of the cylindrical geometry of CNTs. An energy gap, denoted as Δ_{curv}, appears due to the shift from the Dirac points. Conversely, the splitting of the energy dispersions on the cones, indicated by Δ_{so}, is a manifestation of spin-orbit coupling effects. These effects also cause a slight tilt in the horizontal planes correlated with Δ_{so}' and measuring them will provide a deeper understanding of the spin-orbit interactions. This indicates the complex interaction between the topological features and electronic properties of CNT, offering insight into the conductive behaviour of materials and the potential for innovative applications in nanotechnology.

1.2.3 Arrays of Carbon Nanotubes

An array of CNTs is an organised formation of many nanotubes where individual carbon nanotubes are aligned in parallel along their axis and possibly in an organized manner within the perpendicular plane. They are often referred to as "forests" of CNTs since many nanotubes are grown as trees from the same substrate, akin to forests, simply happening on a nanoscale. These are specialized nanostructures consisting of vertically CNTs on various substrates, including silicon [61], [62], [63], quartz [64], [65], [66], sapphire [67], [68], stainless steel [69], [70] and copper [71], [72]. The array configuration maximises the collective mechanical, electrical, and thermal properties of the CNTs, making it highly desirable for various advanced applications in nanotechnology, electronics, and materials engineering.

In Fig. 1.9 (a), high magnification SEM micrograph of MWCNT at a higher plasma intensity is shown [59], and in Fig. 1.9 (b), the idealized structure is presented which will be used for our theoretical model [60].

<div align="center">(a)   (b)</div>
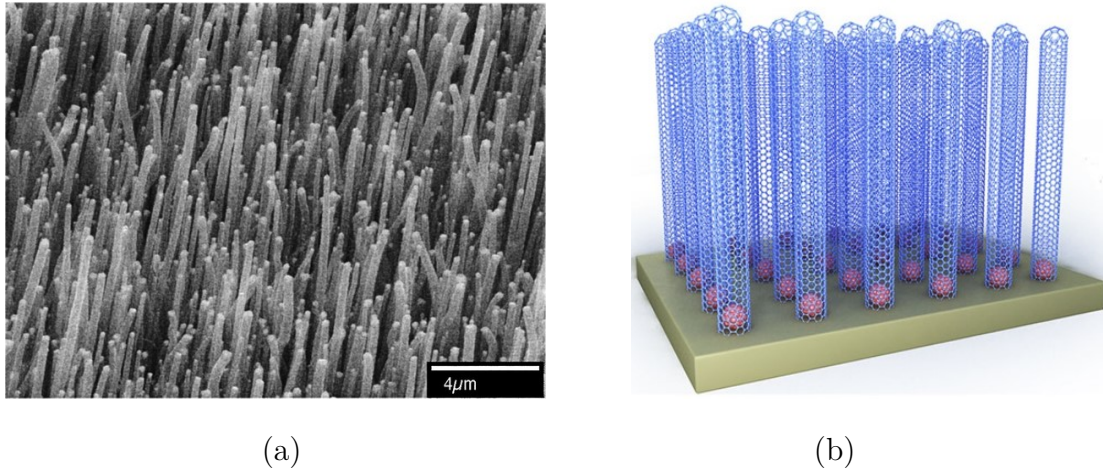
Figure 1.9: VACNT array grown on a substrate (a) High magnification SEM micrograph of MWCNT at a higher plasma intensity under the conditions $0.2A, 640V, 140W$ (Figure from [59]), (b) The idealized structure is to be captured with our theoretical model (Figure from [60]).

1.2.4 Synthesis Techniques of Carbon Nanotubes

The synthesis of CNTs typically involves three main methods: **electric arc discharge**, **laser ablation**, and **chemical vapor deposition (CVD)**. Each of these methods has its complexities and subtleties. In Fig. 1.10, schematic experimental setups for nanotube growth methods are presented.

Electric arc discharge method

The electric arc discharge method for synthesizing CNTs operates at high temperatures (above $1700°C$) and involves an arc discharge between high-purity graphite electrodes in a helium-filled chamber at subatmospheric pressure [74]. This process produces less structural defects in CNTs compared to other methods.

The chamber contains a graphite cathode and anode, along with evaporated carbon molecules and metal catalyst particles such as cobalt, nickel, and iron. The direct current heats the chamber to approximately $4000K$, leading to the formation of a cylindrical hard deposit on the cathode and hard gray shell, chamber soot, and cathode soot.

In general, the synthesis of MWCNTs doesn't typically require catalyst precursors, whereas the synthesis of SWCNTs often involves the use of their different types. For the expansion of SWCNTs during arc discharge, a complex anode is used, which is a composition of graphite and metal [75].

The main advantage of this method is its ability to produce large quantities of nanotubes. However, its downside includes limited control over the alignment of nanotubes and the need for purification due to the use of metallic catalysts.

Laser ablation

The laser ablation method for synthesizing CNTs is a specialized Physical Vapor Deposition (PVD) process [76]. In this method, a graphite target is placed in the center
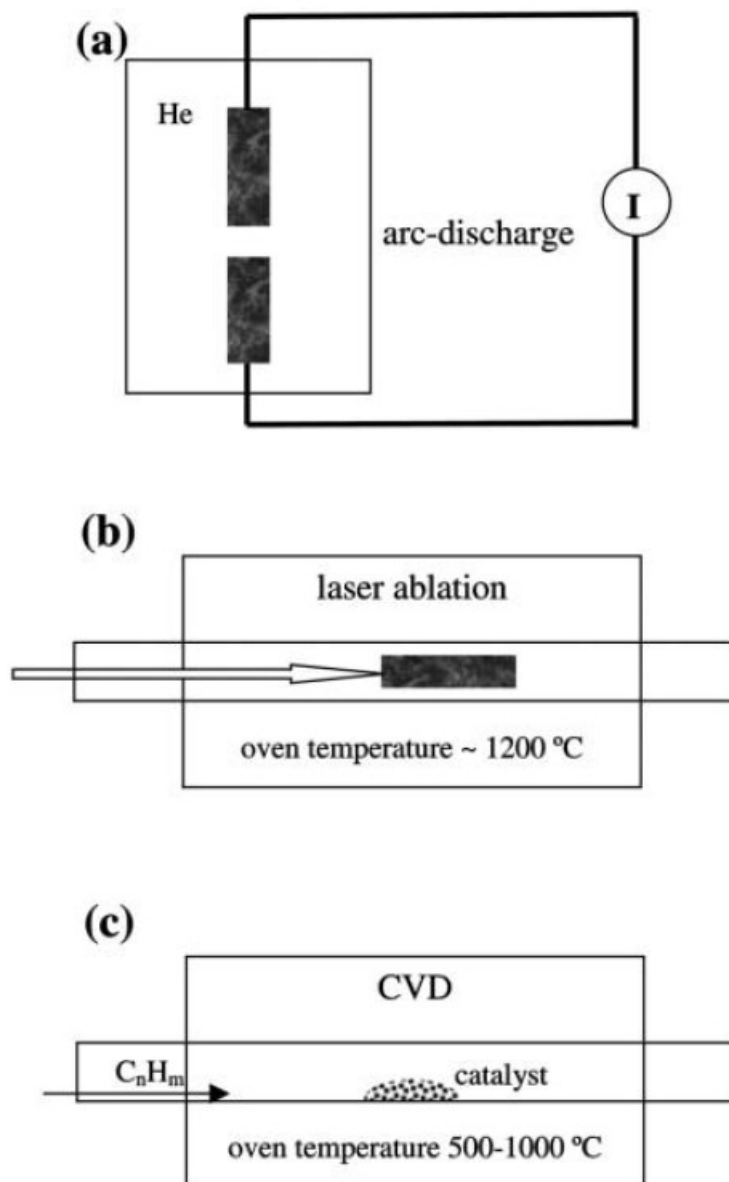
Figure 1.10: Schematic experimental setups for nanotube growth methods: (a) arc-discharge method using helium gas, (b) laser ablation process with an oven temperature of approximately 1200°C, and (c) CVD technique with a hydrocarbon feedstock and a catalyst, within an oven temperature range of 500-1000°C (Figure from [73]).

of a quartz chamber, filled with argon gas, and maintained at a temperature of around $1200°C$. The graphite target is then vaporized using a laser, which can be either continuous or pulsed. In a continuous laser setup, the graphite is vaporized constantly, while a pulsed laser allows more controlled vaporization, correlating each laser pulse with a specific amount of vaporized carbon atoms.

The main strengths of this method are its good yield and low levels of metal impurities because metal atoms usually evaporate when the tube closes. However, a disadvantage is that the produced nanotubes are often not completely straight and may branch out. From an economic point of view, this method does not meet expectations because it requires high-quality graphite rods and high laser power, sometimes two lasers are required, and it does not make as many nanotubes each day as the arc-discharge method does.

Chemical vapor deposition (CVD)

Chemical Vapor Deposition (CVD) is a process used for depositing solid material films on a substrate surface through a controlled chemical reaction in the vapor phase [77]. This technique, also known as thin-film deposition, is widely applied in sectors such as electronics, optoelectronics, catalysis, and energy, particularly in manufacturing semi-conductors, preparing silicon wafers and creating printable solar cells.

CVD is the most used technique to grow CNTs. There are many different types of CVD such as catalytic chemical vapor deposition (CCVD), thermal, or plasma-enhanced (PE) oxygen-assisted CVD, and water-assisted CVD. However, CCVD is the standard technique for the synthesis of carbon nanotubes.

The development of CNTs using CVD can be categorized into two main types based on the position of the catalyst: *gas phase growth* and *substrate growth*. (Fig. 1.11 provides a visual representation of these growth mechanisms, distinguishing between the tip-growth model (often associated with gas-phase growth) and the base-growth model (common in substrate growth)). Each of these growth mechanisms can be further divided into two subtypes: bulk carbon diffusion and surface carbon diffusion models. In the gas phase growth process, catalyst formation and nanotube synthesis occur in mid-air. Substrate growth involves depositing catalyst nanoparticles or metal precursors on a base material like SiO_2 or on a high-surface-area powder before initiating growth. The fundamental chemical processes that lead to nanotube formation from nanoparticles are similar in both methods, typically falling into the categories of surface carbon diffusion and bulk carbon diffusion.
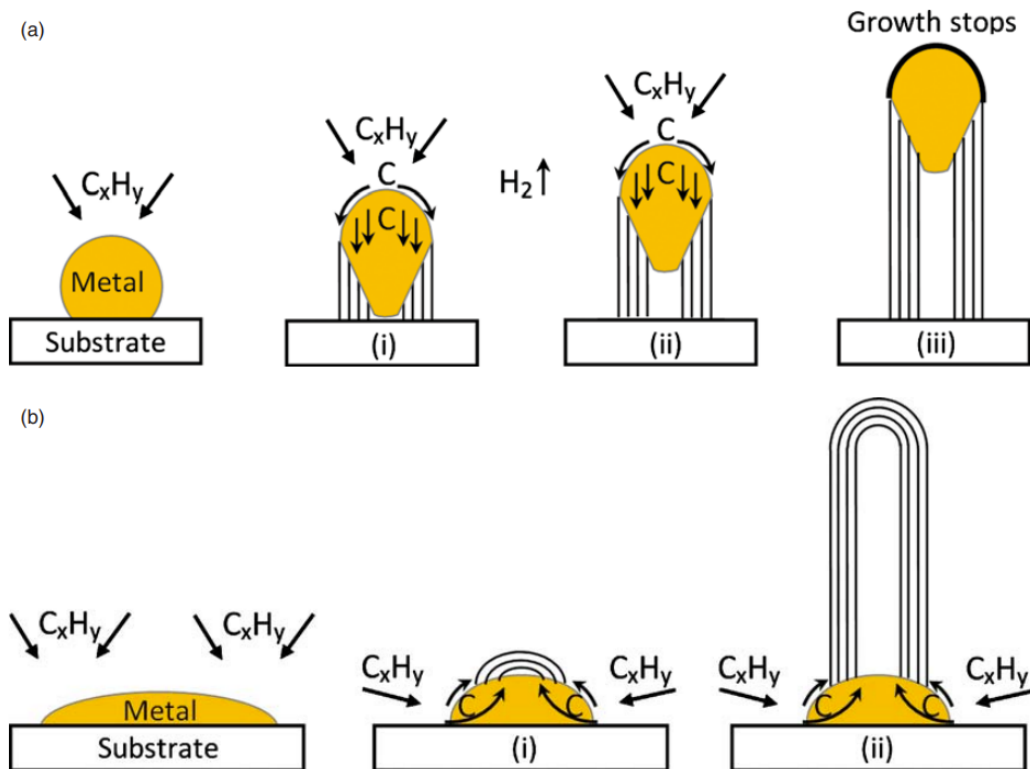
Figure 1.11: Widely accepted growth mechanisms for CNTs: (a) illustrates the tip-growth model, corresponding to surface carbon diffusion, and (b) shows the base-growth model, related to bulk carbon diffusion (Figure from [78]).

1. **Surface Carbon Diffusion**: In this process, the metal particle remains in a solid state while the decomposed carbon migrates across the surface of the particle. Here, the CNT starts forming at the side of the metal particle. As carbon consistently decomposes on the particle, the nanotube keeps growing. This mechanism is frequently employed to describe growth at lower temperatures, especially when using Ni (nickel) catalyst nanoparticles [79]. Fig. 1.11 (a) illustrates this surface carbon diffusion process, as seen in the tip-growth model.

2. **Bulk Carbon Diffusion**: Here, similar to surface carbon diffusion, the carbon feedstock breaks down on the metal particle's surface. The metal nanoparticle absorbs the carbon until it reaches a saturation point, after which a CNT with one or several walls begins to grow from the outer surface of the nanoparticles. Here, the metal may either stay solid or transform into a liquid nanodroplet. When it turns liquid, the process can be visualised as the droplet absorbing carbon until saturation. Subsequently, a nanotube emerges, and the ongoing absorption of carbon supports the growth process following the hydrocarbon vapour-metal-carbon-liquid-crystalline carbon solid pathway, known as the vapor-liquid-solid model. This model, originally proposed for explaining the formation of silicon and germanium whiskers in the 1960s [80], [81], was later adapted to elucidate nanotube formation [82]. Fig. 1.11 (b) corresponds to this bulk carbon diffusion, depicted through the base-growth model.

For constant-size catalyst particles, the growth of CNTs generally continues until hydrocarbon supplies cease. This cessation may occur either by withdrawing the feedstock from the reaction zone, or when the particle gets completely covered with amorphous or graphical carbon, obstructing the gas. Furthermore, base growth might decelerate or stop due to the slow diffusion of hydrocarbons to the nanoparticle at the base of the CNT. Continuous growth depends on an uninterrupted carbon supply and nanotube extrusion. However, competing reactions, like forming graphitic layers or amorphous carbon deposits, may occur. Under suboptimal conditions, amorphous carbon may cover the nanoparticle, stopping the growth by cutting off the carbon source. Also, if the emerging nanotube encounters too much external force, a graphitic carbon shell might form around the nanoparticle, disconnecting it from the feedstock.

This thesis focuses on CVD-created MWCNTs, as this is the method used by the experimental team at IPPT PAN. Since there is always some contribution from Surface Carbon Diffusion during growth, the top of the MWCNT is never pure carbon but has characteristics of a quantum dot with Coulomb blockade and potentially some plasmonic features prone to aging. Therefore, we focus on the theoretically easier-to-describe stationary emission from the nanotube's side.

1.2.5   Carbon Nanotubes Properties and Applications

CNTs, especially MWCNTs, are very strong as they are a single chain of unbroken covalent carbon-carbon bonds. Moreover, they have many carbon-carbon bonds at each step, so breaking a CNT requires breaking many strong covalent bonds. CNTs are made of a two-dimensional (2D) matrix of carbon-carbon bonds formed into cylinders. This implies they can bend and twist without breaking bonds but can't extend too far before bonds break. This means they are highly resistant to extension beyond a certain point. That is what we mean by "strong."

CNTs have extraordinary electrical conductivity, heat conductivity and mechanical properties.

- **High Electrical Conductivity**: The thermal conductivity of CNTs enables their use in heat dissipation applications. They can be used in thermal interface materials for electronic cooling or integrated into materials requiring efficient heat transfer. The low thermal expansion coefficient of CNTs also means they don't deform easily under thermal stress, making them suitable for applications that require thermal stability.

- **High Thermal Conductivity And Heat Expansion**: The thermal conductivity of CNTs enables their use in heat dissipation applications. They can be used in thermal interface materials for electronic cooling or integrated into materials requiring efficient heat transfer. The low thermal expansion coefficient of CNTs also means they don't deform easily under thermal stress, making them suitable for applications that require thermal stability. For SWCNTs, the thermal conductivity at room temperature typically ranges from 1750 to 5800 W/mk. This range reflects variations based on factors like nanotube structure, defects, and the specific measurement method. For MWCNTs, it can exceed 3000 W/mk. MWCNTs often exhibit even higher thermal conductivity than SWCNTs due to the multiple concentric layers. The fact that CNTs can achieve thermal conductivities about three times better than diamonds, highlights their potential as highly efficient thermal conductors.

- **Strength and Elasticity:** Carbon atoms in graphite form a planar honeycomb lattice in which each atom is connected to three neighbouring atoms by strong chemical bonds. Owing to these strong bonds, the basal plane elastic modulus of graphite is one of the largest known materials.

- **Aspect Ratio:** CNTs are tiny, high aspect ratio conductive additives used in plastics. Their unique shape allows for lower concentrations to achieve the same electrical conductivity as other additives, like carbon black or stainless steel fiber. This efficient use of CNTs preserves the toughness and other key properties of the polymer resins, especially at low temperatures, making CNTs an effective choice for enhancing electrical conductivity in plastics.

- **Chemically stable**: CNTs are chemically stable, making them suitable for use in harsh environments. This stability is beneficial to chemical sensors and filtration systems, where they can withstand exposure to corrosive substances or high temperatures. In addition, their chemical inertness makes them useful in biomedical applications, such as drug delivery systems or tissue engineering scaffolds.

Due to their excellent physical and chemical properties, CNTs are used in a wide range of applications:

- CNTs are highly conductive, both electrically and thermally, making them ideal for use in electronic devices.

- Due to the strong UV/Vis-NIR absorption characteristics of SWNTs, their use in solar cells is a very promising application.

- Due to their large surface area, CNTs have been successfully used in medicine and pharmaceuticals to adsorb or conjugate a wide variety of medicinal and diagnostic agents.

- CNTs have several unique chemical, dimensional, optical, electrical, and structural properties that make them attractive as drug delivery and biosensing platforms for the treatment of various diseases and noninvasive monitoring of blood levels and other chemical properties of the human body accordingly.

- One of the most important applications of arrays of CNTs is the field electron emission. Because each carbon atom is strongly covalently bonded to three other carbon atoms, carbon nanotubes have an extremely high melting point. This also means that each carbon atom has an extra electron, which forms a sea of localized electrons inside the tube that allows the nanotubes to conduct electricity.

1.2.6 Field emission from Carbon Nanotubes

CNTs are famous for their extensive array of applications, and their versatility and unique properties make them valuable in numerous fields. Among the numerous applications, *field emission* stands out as critical, underscoring the importance of CNTs in advancing technology. The exceptional properties of field emission from CNTs, including their low turn-on field and high emission current density, make them particularly valuable in various technologies and industries. They can be efficient electron emitters in flat panel displays [83], [84]. They offer advantages such as faster response times [85], higher contrast [86], and potentially lower power consumption [87], [88] compared to traditional display technologies.

The higher contrast in CNT-based display technologies is primarily due to the increased electron emission per cm^2 from CNTs [86]. This increase in electron emission per unit area increases the brightness and the overall quality of displayed images. Therefore, the number of electrons emitted per cm^2 is significantly greater, contributing to a brighter and higher-contrast visual experience.

Although the exact reasons for the faster response time in CNT-based applications are still under investigation, it is believed to be due to the collective behavior of the Tomonaga-Luttinger liquid (TLL) inside the carbon nanotubes. This unique internal state may facilitate rapid electron transport, contributing to the observed fast response. CNTs are perfect for electron field emission due to their unique geometry and extraordinary physical characteristics. This efficiency is partly due to their ability to emit a significant number of electrons even at low voltages, resulting in lower power consumption. The low power requirement, characterized by lower voltages, enhances safety, making it safer to work with devices that incorporate CNTs, as they operate at much lower voltages (like 5 V) compared to traditional technologies that might require kilovolts (e.g., 5 KV). Electron field emission from CNTs was first discovered by De Heer, Andre Chatelain, and Daniel Urgate in 1995 [89]. Their work sparked many further studies, aiming to understand and optimize this phenomenon for real-world applications, focusing especially on individual CNTs. The majority of these studies primarily involved electron emission occurring at the tip of the CNTs [90], [91], [92].

The special shape and physical qualities of CNTs make them perfect for use in electron field emission applications. Their high aspect ratio, coupled with remarkable mechanical strength and electrical conductivity, facilitates efficient electron emission, even under the
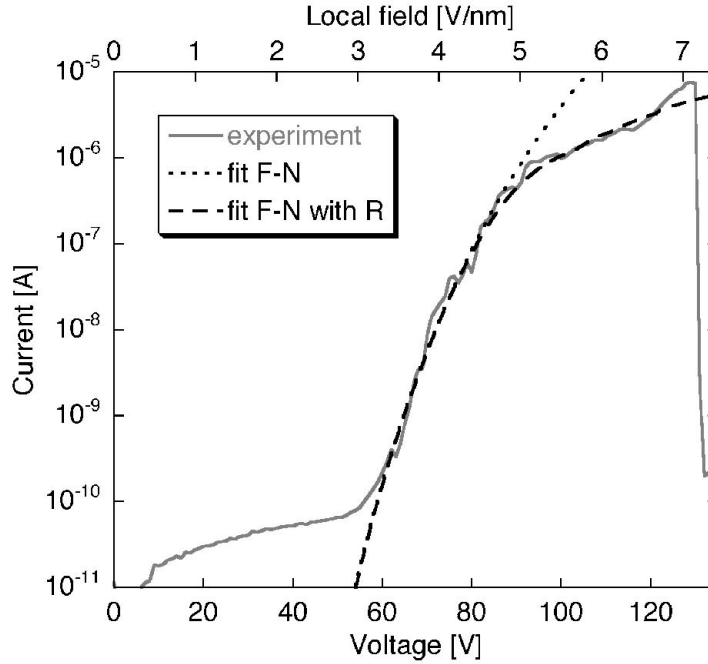
Figure 1.12: Comparison between experimental results and theoretical FN model with and without resistance. At low energy regimes, FE cannot be captured in single-particle theory (Figure from [93]).

influence of low electric fields. These features make it possible to create high-quality field emitters and result in many new technologies and innovative uses.

Furthermore, the use of CNTs in field emission applications also presents environmental and economic advantages. Their lower energy requirements result in lower energy consumption, which is both cost-effective and more environmentally sustainable. In addition, the durability and longevity of CNT-based components contribute to less frequent replacement and reduced material waste.

The detailed research in this field efforts to understand the emission mechanisms and potential optimizations.

The current understanding of emission from carbon nanotubes is insufficient, as highlighted in experimental evidence [93], [94], [95] emphasizing the need for additional research. The standard seminal FN emission theory for single particle emitters does not apply to carbon nanotubes, especially at low voltages.

In Fig. 1.12, the current-voltage characteristics of field emission from a nanotube are compared to the FN model, describing field emission in vacuum electronic devices. At higher voltages, the experimental data closely coincide with the FN fit with resistance, indicating that the FN model with resistance accurately describes the field emission observed in the experiment at these voltages [93]. At lower voltages, the experimental data exhibit a noticeable deviation from both the FN model and the FN fit with resistance.

1.3   Tomonaga–Luttinger liquid

Low energy physics of one-dimensional (1D) electron metals can be described in terms of the Tomonaga–Luttinger liquid (TLL). TLL is a theoretical model describing interacting electrons in a 1D conductor.

1.3.1 The idea of TLL

All theoretical descriptions of electronic liquid in materials are based on a standard assumption: single electron states can be distinguished and the dynamics of the system as a mention of these carriers can be described. Then, it is studied how they effectively scatter to obtain all transport properties from that. This approach is so commonly used that most materials engineers take it for granted.

The key idea behind TLL is that electrons cannot avoid each other when moving along 1D systems [96]. Once the interaction between them is present, even very small, it is impossible to think about single electron particles moving along the system. Instead, when we excite 1D metal, a collective motion begins. A key quantity is now local electronic density. The situation is very similar to sound propagation inside a tube: a motion of a single molecule cannot be followed as it scatters with other molecules (for electrons, it would actually be impossible, as they are indistinguishable). The theory of sound is written as a theory of denser and more diluted volumes of air. The final outcome is a harmony of music that we can hear. The quantities used to extract measurable observables are correlation functions and we can say that for the sound, all macroscopic correlation functions are expressed using this collective variable.

In the same spirit, in 1D we need to write all the correlation functions using collective modes basis. As will be seen in the following chapter, a plane wave with a characteristic Fermi wavelength (ground state just like in any other noninteracting metal) is defined, and then local distortions of the wave due to interactions are observed. A great thing is that the resulting model is that of a 2D membrane, which is exactly solvable. The role of density-density interactions turns out to change the compressibility of the membrane, thus all of them can be taken into account exactly. As we will show in the latter chapters the presence of TLL can be revealed by characteristic power-law behaviour of correlation functions, the exponent of which does depend on interactions and in principle can vary as external fields are applied. Our problem of field emission from nanotube, involving electron-electron interactions, thus, revolves around understanding what wavy collective fluctuations will be caused by a single escaping electron. If the "membrane" of a many-body quantum liquid is pulled, how will it bounce back? In our sound analogy, that would correspond to an issue of how a melody would change if a mass density of the "membrane" has been locally and instantaneously changed.

The subject of electronic liquids is in fact more general and remains an active field of research[97], thus potential applications of formalism developed here can be also broad. Here however we shall focus only on Multi-Wall Carbon Nanotubes (MWCNTs) as the best established example of non-Fermi liquid, which already nowadays is used in many devices and platforms for engineering applications.

1.3.2 History of Luttinger Liquid Theory

The theoretical framework of the TLL, essential for understanding 1D systems, has evolved through significant contributions of various physicists over the decades. It is presently a well-developed field of research in solid state physics. It was first proposed by Sin-Itiro Tomonaga in 1950 [98]. He suggested that excitations in 1D systems could be represented by a quantized field of sound waves, known as phonons. However, subsequent research, particularly by Bohm and Pines in 1953 [99], refined this concept, suggesting that these excitations were more accurately described as plasmons. John M. Luttinger

further developed this theory into a model in 1963 [100]. However, Luttinger's solution contained a significant error. He failed to explain the infinite dimensionality of Hilbert space, which changed the behaviour of the field operator commutators. This resulted in the inaccurate conclusion that the excitations were the same in both interacting and noninteracting electron systems. The model's accurate solution came with the work of Daniel C. Mattis and Elliot H. Lieb in 1965 [101]. They addressed the issue regarding the infinite-dimensional Hilbert space and correctly formulated the field operators, thereby correcting the errors in Luttinger's model.

A significant advancement was made by F.D.M. Haldane in 1981 [102]. The contribution he made to 1D metals is similar to the contribution of Lev Landau in the field of 3D Fermi liquids [44], [103]. Landau showed that despite the presence of many-body interactions in standard metals, one must have well-defined fermions, only with a renormalized mass. Similarly, in 1D Haldane showed that despite capturing only the density-density Hartree-type interaction (which will be defined in Eq. 3.36), there is a regime where TLL will exist because the exchange Fock-type interaction (see Eq. 3.37) renormalizes down to zero. The Fock-terms can then only renormalize the compressibility of the liquid. Thus the TLL is not just an abstract theoretical concept, but it advances into the realm of physical reality. He coined the term 'Luttinger liquid', sometimes called 'Tomonaga–Luttinger liquid' and also provided a profound physical interpretation of the bosonization of 1D fermion excitations. His interpretation brought a deeper understanding of the collective behaviour of electrons in 1D conductors. He was awarded a Nobel Prize in 2016.

Further development of the theory moved in the direction of finite systems and the role of boundary conditions. Seminal advances in this field were done in the 90' by Affleck and Ludwig. In this thesis, we will use a later extension of these works done by Sebastian Eggert [104], principally obtained when he was a student of Ian Affleck. Eggert's contributions, building on Haldane's bosonization approach, added to the comprehensive understanding of the Tomonaga–Luttinger liquid concept in the case when the 1D metal has a boundary and is set at a finite temperature.

TLL remains an active field of research, with the current effort being dedicated mostly to 1D systems away from equilibrium and 1D systems in close vicinity of Berezinskii–Kosterlitz–Thouless (BKT) transition driven by a sine-Gordon perturbation. These recent achievements will not be used in this thesis. Instead, the focus will be on applying known field theory methods to a realistic technological problem.

1.4   Outline of Thesis

This thesis comprises eight chapters and a bibliography, systematically addressing the generalization of Fowler-Nordheim tunneling theory and its applications to nanotube materials. The thesis is divided into two parts: the first part serves as a literature review, providing a comprehensive overview of existing research and theoretical background; the second part presents our own results and contributions to the field.

Chapter 1, titled "Introduction", serves as an overview of the thesis providing essential background information on field electron emission. It reviews key theories in the field, with a special focus on the FN theory, thus setting the stage for the more specialized topics explored in the following chapters.

Chapter 2, called "Motivation", articulates the pressing need and current relevance of the research focus. By delineating the specific research objectives and contributions, this chapter serves as a justification for the scope and direction of the study.

Chapter 3, titled "Methodology", provides the scientific methods that are used in this study. It starts with talking about Schrödinger equation and wave functions, followed by a discussion of a simpler method called the WKB approximation. Subsequently, it moves to a more advanced way of looking at the problem, called "second quantization", offering a detailed explanation of the Hamiltonian formulation within this advanced framework. Additionally, collective modes and field theories are introduced, particularly emphasizing their importance in 1D materials like nanotubes. Finally, the chapter culminates in an in-depth exploration of 1D metals, focusing on the Tomonaga-Luttinger liquid (TLL) theory and its applications in tunneling processes. This chapter establishes the theoretical and methodological ground rules for the specialized analyses presented in the following chapters.

Chapter 4, titled "Generalizing Fowler–Nordheim Tunneling Theory for an Arbitrary Power Law Barrier," is based on a published paper [105], and starts with defining the new model for a tunneling barrier shaped by an arbitrary power law. Then, a generalized formula is derived for tunneling expressed by the Hypergeometric function. The chapter proceeds to validate this formula using Kemble's improved JWKB expression, comparing it against established results for triangular barriers and exploring its performance for different exponents in the power law. The discussion extends to tunneling currents in composite surfaces with varying work functions, and the chapter further compares these analytical findings with numerical methods. Finally, it closes by discussing potential experimental applications of the generalized theory and its relationship with existing quantum mechanical solutions.

The electrons do interact with each other which will affect field emission. Firstly, the spectral distribution of interacting electrons will have a so-called pseudo-gap or zero-bias anomaly (ZBA), which is explored in **Chapter 5**, titled "TLL Density of States". We derive the exact analytic Fourier transform for two cases, which we called Coulomb metal, relevant for CNTs, and Hund metal, relevant for heavier p-elements' nanotubes.

Secondly, the transmission function itself will be modified as the potential felt by electron depends on interactions. When an electron is emitted, it leaves a "hole" in the electron distribution at the metal surface, affecting the behavior of the emitted electron. Moreover, the hole can also interact with other electrons, leading to "many-body effects." These interactions can impact the energy and trajectory of the emitted electron. This is considered in **Chapter 6** which is titled "Field emission from Carbon Nanotubes". This chapter, published as Ref. [106], subsequently explores the Fourier transforms of

TLL local density of states (LDOS) and combines these two components to arrive at a formula for the tunneling current. Next, the discussion switches to the application of these findings to nanotubes, dealing with both gapless nanotubes and those with mini-gaps. The chapter concludes by summarizing the study's implications and its relevance to the broader scientific community. As a result, this chapter expands on the significance of electron-electron interactions in field emission, providing new insights that can be gleaned through field electron emission measurements on 1D nanomaterials.

Chapter 7, titled "Electron Emission Theory for Nanotube Materials: an influence of geometry", explores the vital role of geometrical arrangement in electron emission from nanotube materials. First, it presents the overview of the formalism, laying the foundation for the subsequent exploration. Next, it demonstrates the capability of our modelling to capture the essential features of electrostatic potential, obtaining the current and accurately describing its dependence on various geometrical parameters of an array.

Chapter 8, titled "Conclusion," concludes this thorough thesis. This chapter summarises the important findings, insights, and contributions presented throughout the preceding chapters. It offers a comprehensive overview of the primary research aims, techniques, and results, while also acknowledging the limitations and challenges encountered during the research. In essence, this final chapter summarises the journey undertaken in this thesis, to provide a clear and insightful conclusion to the topic.

Chapter 2

Motivation

The area of field electron emission (FEE) has gained significant attention over the years due to its wide range of applications in advanced electronics, vacuum microelectronics, and materials science. As with any evolving scientific area, people are always looking for the perfect material that can emit electrons well. Many different materials have been tried over the years. But carbon nanotubes are currently leading in this area. They have special shapes and features that make them good for this kind of work. Due to higher brightness and a more monochromatic output, they are setting new standards for what can be done.

While carbon nanotubes are good field emitters, most studies have concentrated on electron emission from the top of the tubes. Surprisingly, there have been few studies about emissions from the sides of the carbon nanotubes. This is where this research comes in. Looking into side emissions might reveal a new layer of possible uses and applications for carbon nanotubes in field emission technologies. This represents an unexplored aspect of carbon nanotube research that has largely gone overlooked, despite its potential importance.

Looking at this relatively unexplored dimension, this research aims to explore new layers of functionality and CNTs in field emission technologies. Side emitters can exhibit various properties compared to tip emitters, such as variations in emission currents, stability under different operating conditions, or even unique electron distribution patterns. These differences can be extremely important in applications where precise control of electron emission is required.

Furthermore, the study on side emissions is not just about discovering a new phenomenon; it's about challenging and potentially expanding the current theoretical frameworks that determine our understanding of electron emissions in nanomaterials. The physics of side emissions involves complex interactions influenced by the unique cylindrical geometry of the nanotubes, the electronic structure of the sidewalls, and the interplay between the nanotube and its substrate. The curvature of these cylinders can concentrate electric fields at certain points, influencing electron emission. Additionally, the chirality of the nanotubes affects whether they are metallic or semiconducting, impacting electron transport along the sidewall. The substrate material can also induce stress or strain in the nanotubes, altering their electronic band structure and affecting the overall field enhancement factor. This complexity presents both a challenge and an opportunity to refine our theoretical models and computational methods.

Investigating side emissions could lead to the development of new CNT-based devices with enhanced or specialized emission characteristics. For example, the ability to use side emissions effectively could lead to the design of more efficient electron sources for

imaging technologies or new types of emitters for electronic displays.

One reason for this oversight is the complication of the study: unlike the relatively straightforward single-particle theory that adequately describes tip emission, emission from the side is influenced by a range of phenomena, including electron-electron interactions. These interactions complicate the investigation of the emission process, making it a challenging but potentially rewarding area. However, these challenges also make it a potentially rewarding field, promising new insights and applications.

One of the most significant advantages of using CNTs is the ability to achieve electron emission at substantially lower voltages, around 1 V. Lower operating voltages make CNT-based devices great candidates for integrated circuits, portable devices, and various other applications. Thus, a better understanding of field emission mechanism in CNT is an important research objective.

ARPES recently moved from high energy probe (hard X-ray) to UV-laser ARPES in order to study the lowest energy and most delicate orderings without destroying them. Taking into account recent interest in nano- to meso- sepic phases, this is also the texture or LEED, so such low-energy beams are highly desired.

The Aim of the Study

The aim of this study is to establish a new theoretical framework for field emission analysis, with a specific focus on tackling this phenomenon at the many-body level. In particular, we wish to focus on novel materials, such as carbon nanotubes, which host electrons with reduced dimensionality. We are interested in low energy field emission, that involves electronic band crossing the chemical potential. We want to know how such factors as temperature and geometry interactions conspire together at such a low energy regime and we wish to understand their joint effect. By incorporating the electron-electron interactions, and thus studying collective behavior in CNTs, this research aims to give deeper insights into mechanisms of field emission. The formalism should answer the following questions: how the electronic liquid is rearranged upon emitting the electron and how the emitted electron experiences and is affected by this rearrangement. It is known that in a low-energy regime, there exists a formalism that captures the effects of interactions non-perturbatively, the Tomonaga-Luttinger liquid (TLL). Therefore, we shall base our investigation on this method.

The Hypothesis

The central hypothesis of this thesis is: *It is possible to derive the closed-form analytical formalism that captures both the effects of strong interactions and temperature and thus will fully describe low energy field emission from arrays of MWCNTs.* With such formalism, researchers will be able to show that interaction at the many-body level plays a significant role in the field emission process, particularly in the context of electron emissions from the sides of CNTs. Since interactions can substantially change the density of states in a 1D system, this modification manifests in all transport coefficients, including resistivity. This hypothesis is based on the fact that an analytic description was possible for all these bulk phenomena. Thus, it can be deduced that the formalism for field emission should also be derivable, illuminating how this quantity is influenced by

electron-electron interactions. In comparison with the standard transport coefficients, in field emission, incorporating a strong external field is necessary. Adding an external field is similar to subjecting carriers to a strong force, thus adding extra energy. Therefore, low energy electrons now affect the motion of finite energy electrons, but since researchers have been able to describe both families of carriers, we hope to merge both descriptions in this work.

Since the emitted current dependence on the applied field can be different from that in conventional materials, this carries relevant implications for potential applications of any arrangement of nanotubes as a field emitter. This hypothesis challenges the traditional understanding of field emission, which so far has predominantly been focused on single-particle processes. It also implies, on a more fundamental level, that field emission current will carry information about the nature of electron-electron interactions in CNT.

Chapter 3

Methodology

The aim of this chapter is to present principal theoretical tools that are used in the thesis. As stated in Chapter 2, the idea of the thesis is to move beyond a traditional single-particle description towards methods that can capture correlated behaviour of many electrons. Actually, this closely resembles the development of quantum mechanics, with more and more complicated systems being solved, thus in a way this chapter explores the evolution of quantum mechanics. First, traditional quantum mechanics is examined as it was developed a century ago, focusing on the fundamental principles that have developed in this area since then (Sec. 3.1.1). In this formalism, Wentzel-Kramers-Brillouin (WKB) approximation is presented. It is a quasi-classical method characterized by simplifying assumptions of the plane and evanescent waves, and is serving as our starting point for understanding tunneling in quantum mechanical systems (Sec. 3.1.2).

Then the emphasis shifts from the analysis of single particles to the many-body theory (Sec. 3.2). This transition is essential for addressing the limitations of early quantum mechanical models, especially in the context of interacting electrons. Our discussion includes the FN theory of field emission, originally developed within classical quantum mechanics. However, we recognize that this theory fails when electron-electron interactions become significant.

To address these challenges, the chapter systematically describes various advanced methods dealing with the multi-body effects of quantum mechanics. This gradual approach of advancing theoretical methods culminates with the formulation of field emission in field theory (Sec. 3.3).

3.1 Field emission theory within wavefunctions framework

3.1.1 Schrödinger equation and wavefunctions

In 1925, Austrian physicist Erwin Schrödinger introduced an equation and published it in 1926 [107], which contributed greatly to the development of quantum mechanics. This equation, known as the Schrödinger equation, describes the behavior of electrons under a wide range of circumstances.

In order to understand field electron emission within the framework of the Schrödinger equation, the wave-like properties of electrons and the concept of tunneling through a potential barrier must be considered.
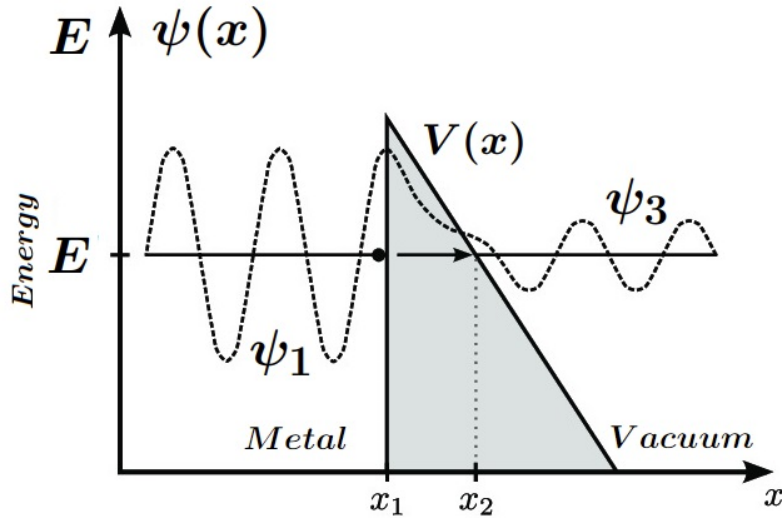
Figure 3.1: Visualization of electron tunneling from metal to vacuum across a potential barrier. In the metal, the wave function is depicted as a plane wave, indicating stable electron presence. Within the barrier, the wave function transitions to the evanescent wave that decays exponentially. In the vacuum, the wave function resumes as a plane wave with diminished amplitude. Figure adopted from Ref. [108].

The Schrödinger equation describes the behaviour of quantum particles, including electrons, in terms of their wavefunctions. In the case of field electron emission, we have a metal-vacuum interface where electrons can tunnel from the metal into the vacuum.

The wave function, denoted as $\psi(x)$, represents a particle, as well as its module $|\psi(x)|$ gives the density of the probability of finding an electron at a particular position x within the quantum system.

Unlike classical mechanics where an object without sufficient energy cannot overcome a barrier, quantum mechanics allows particles, such as electrons, to tunnel through barriers even without the necessary energy. This reflects their wave-like characteristics at the quantum level (Fig. 3.1).

In general, within quantum mechanics, there is an equation $\hat{H}\psi(x) = E\psi(x)$, where the Hamiltonian ($\hat{H}$) is an operator that extracts the energy from a given wave function ($\psi(x)$). We will drop the operator $\hat{\cdot}$ symbol from now on.

For illustrative purposes, a simplified one-dimensional case will be considered. The Hamiltonian operator now takes the form $H = \left(-\dfrac{\hbar^2}{2m}\dfrac{\mathrm{d}^2}{\mathrm{d}x^2} + V(x)\right)$. The Schrödinger equation, a second order differential equation, in one dimension is:

$$-\frac{\hbar^2}{2m}\frac{\mathrm{d}^2\psi(x)}{\mathrm{d}x^2} + V(x)\psi(x) = E\psi(x) \tag{3.1}$$

where $\hbar$ is the reduced Planck's constant, m is the electron mass, $\psi(x)$ is a one-dimensional wave function, $V(x)$ is the electron potential energy, E is the total energy of the electron. In the metal region ($x < x_1$) and the vacuum region ($x > x_2$), the potential energy can be approximated as zero since the electron is free to move. $x_2 - x_1$ represents the thickness of the potential barrier. Therefore, in these regions, the Schrödinger equation simplifies to:

$$-\frac{\hbar^2}{2m}\frac{\mathrm{d}^2\psi(x)}{\mathrm{d}x^2} = E\psi(x) \tag{3.2}$$

The solution in these regions is then a plane wave:

$$\psi(x) = \mathcal{A}\exp\left(ikx\right) + \mathcal{B}\exp\left(-ikx\right) \tag{3.3}$$

where $\mathcal{A}$ and $\mathcal{B}$ are coefficients, k is the wave vector given by $k = \sqrt{\frac{2mE}{\hbar^2}}$.
In the barrier region $(x_1 < x < x_2)$, the potential energy is non-zero and acts as a barrier to the electron's motion. In the simplest case, we can represent this potential energy by a step function:

$$V(x) = \begin{cases} V_0, & \text{for } x_1 < x < x_2 \\ 0, & \text{otherwise} \end{cases} \tag{3.4}$$

In this region, the Schrödinger equation becomes:

$$-\frac{\hbar^2}{2m}\frac{\mathrm{d}^2\psi(x)}{\mathrm{d}x^2} + V_0\psi(x) = E\psi(x) \tag{3.5}$$

The solution to this equation is an evanescent wave, which decays exponentially within the barrier.

$$\psi(x) = \mathcal{C}\exp\left(-\kappa x\right) \tag{3.6}$$

where $\mathcal{C}$ is a complex number and κ is the imaginary wave vector given by $\kappa = \sqrt{\frac{2m(V_0-E)}{\hbar^2}}$. The decay of the wave function is due to the difference between the electron's energy and the potential energy of the barrier that is negative. The evanescent wave indicates the presence of the electron within a limited region inside the barrier, but its probability decreases rapidly with distance from the interface. The study of tunneling through potential barriers has important applications, including the development of nanoelectronics, quantum computing technologies, and advanced materials with specific electronic properties.
In this way, it has been demonstrated how quantum mechanics works in the simplest possible case: a landscape with a *constant* potential. The phenomenon of tunneling, based on the Schrödinger equation and the wave-like properties of electrons, is further analysed using more advanced methods starting from the WKB (Wentzel-Kramers-Brillouin) approximation, which is discussed in the next section.

3.1.2 WKB approximation

The WKB approximation, named after Wentzel [109], Kramers [110], and Brillouin [111], (sometimes it is referred to as the JWKB approximation, where the "J" stands for Jeffreys [112]), is a commonly used method to solve the Schrödinger equation in situations where the potential energy *varies slowly depending on the position.*
Developed in the early days of quantum mechanics, the WKB method linked classical and quantum understanding, offering solutions to problems that are not achievable with just classical methods. In the 1920s, these researchers explored the Schrödinger equation with varying potentials. Their collective efforts highlighted the importance of the WKB

method in connecting classical and quantum mechanics. The WKB approximation provides an approximate solution to the Schrödinger equation by treating the wave function as a semiclassical quantity: a probability density without any further interference effects. Fig. 3.2 illustrates a potential barrier, a fundamental concept in understanding quantum tunneling.
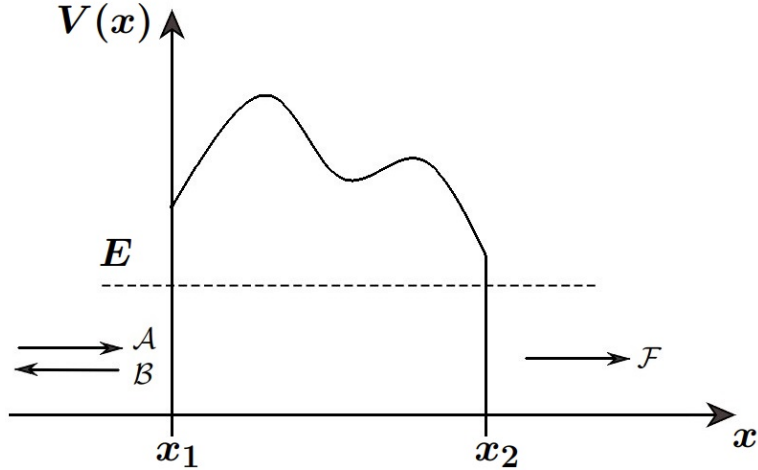
Figure 3.2: Illustration of a quantum mechanical potential $V(x)$ with barrier energy level E, where $\mathcal{A}$ is incident, $\mathcal{B}$ is the reflected and $\mathcal{F}$ is the transmitted wave amplitudes.

The Schrödinger equation can be rewritten as

$$\frac{\mathrm{d}^2\psi(x)}{\mathrm{d}x^2} + k(x)\psi = 0 \tag{3.7}$$

with the abbreviations

$$k(x) = \sqrt{\frac{2m}{\hbar^2}\left(E - V(x)\right)}, \qquad\qquad \text{if } E > V(x)$$

$$k(x) = -i\sqrt{\frac{2m}{\hbar^2}\left(V(x) - E\right)} = -i\kappa(x), \qquad\qquad \text{if } E < V(x)$$

When $k(x) = const$, the solution of the function has the form of $\psi(x) = \exp\left(\pm ikx\right)$, and when k is not a constant but varies at a slow rate, the proposed assumption for the solution takes the form of

$$\psi(x) = \exp\left(\pm i \int k(x)dx\right) \tag{3.8}$$

Substituting with the wave function into Schrödinger equation (Eq. 3.7), we get

$$\frac{d^2\psi}{dx^2} + k(x)^2\psi = \left(\frac{d^2}{dx^2} + k^2\right)\exp\left(\pm i \int k(\varkappa)d\varkappa\right) \tag{3.9}$$

and its one-order approximation solution is

$$\psi_1(x) = -\frac{1}{4}\ln[k(x)] + const \tag{3.10}$$

The wave function of Eq. 3.7 can be written as

$$\psi(x) \approx \begin{cases} \frac{c_1}{k^{1/4}(x)} \exp\left(\pm i \int_{x_0}^{x} \sqrt{k(\varkappa)} d\varkappa\right), & \text{for } E > V(x) \text{ classical region}, \\ \frac{c_1}{k^{1/4}(x)} \exp\left(\pm \int_{x_0}^{x} \sqrt{k(\varkappa)} d\varkappa\right), & \text{for } E < V(x) \text{ non-classical region}. \end{cases} \tag{3.11}$$

where c_1 is a normalization constant.

When applying the WKB approximation, it is crucial to analyze the different regions around a potential barrier. The electron is supposed to move from the left side $(x < x_1)$, to pass through the potential barrier $(x_1 < x < x_2,)$, and enter the right region $(x > x_2)$. Any potential barrier can similarly be divided into three regions. In terms of the WKB approximation, the wave function in the three different regions can be written as:

$$\psi_1 = \mathcal{A} \exp(ikx) + \mathcal{B} \exp(-ikx), \qquad\qquad\qquad x < x_1$$

$$\psi_2 = \frac{\mathcal{C}}{\sqrt{\kappa(x)}} \exp\left(\int_0^x \kappa(\varkappa) d\varkappa\right) + \frac{\mathcal{D}}{\sqrt{\kappa(x)}} \exp\left(-\int_0^x \kappa(\varkappa) d\varkappa\right), \qquad x_1 \le x \le x_2$$

$$\psi_3 = \mathcal{F} \exp(ikx), \qquad\qquad\qquad\qquad x > x_2$$

The amplitudes $\mathcal{A}$, $\mathcal{B}$, $\mathcal{C}$, $\mathcal{D}$ and $\mathcal{F}$ are real numbers that fully describe the behaviour of the wave function in the entire system. These amplitudes describe the amount of each component of the wave function (incoming, outgoing, and transmitted) present in the different regions.

The transmission coefficient D represents the ratio of the squared amplitude of the portion that tunnels through the barrier $|\mathcal{F}|^2$ to the squared amplitude of the incident wave $|\mathcal{A}|^2$, indicating the probability of quantum particle transmission through the barrier:

$$D = \frac{|\mathcal{F}|^2}{|\mathcal{A}|^2} \approx \exp\left(-\frac{2}{\hbar} \int_{x_1}^{x_2} \kappa(x) dx\right) = \exp\left(-\frac{2}{\hbar} \int_{x_1}^{x_2} \sqrt{2m(E - V(x))} dx\right) \tag{3.12}$$

and the reflection coefficient:

$$R = 1 - \exp\left[-\frac{2}{\hbar} \int_{x_1}^{x_2} \sqrt{2m(E - V(x))} dx\right] \tag{3.13}$$

Despite being an approximation, the WKB method is a valuable tool for understanding quantum tunneling phenomena to analyse the behavior of particles in the presence of potential barriers. It provides approximate solutions that are particularly useful when the potential energy varies slowly.

3.1.3 Fowler-Nordheim theory

The Fowler-Nordheim (FN) theory, developed in 1928 by Fowler and Nordheim, provided a fundamental understanding of the electron emission from metals into a vacuum under the influence of strong electric fields. This phenomenon has critical implications in various technological applications such as field emission displays, electron microscopy, and vacuum nanoelectronics.

Mainly, assuming that the emission current moves along the x direction and the emitter surface is on the $y - z$ plane, the emission density [2], [113] can be written as

$$J = \int_0^\infty N(E_x)D(E_x)dE_x \tag{3.14}$$

where $N(E_x)$ is the number of electrons crossing to the $y - z$ plane in the x direction along the current between E_x and $E_x + dE_x$. $N(E_x)$ is the density of states, which is sometimes called the supply function in field emission theories. $D(E_x)$ is the transmission probability of the vacuum potential barrier.

Based on the Sommerfeld model [114], the electron energy in a metal can be expressed as

$$E = E_x + \frac{\hbar k_p^2}{2m}$$

where $k_p^2 = k_y^2 + k_z^2$, the electron group velocity is $v_x = \frac{\hbar k_x}{m}$, and $d^3k = d^2k_p dk_x$. For a given E_x, $d^2k_p = 2\pi k_p dk_p = 2\pi \frac{m}{\hbar^2}dE$ and the constant density of states can be derived

$$N(E_x) = \frac{em_e}{2\pi\hbar^3}\int_{E_x}^\infty \frac{dE}{1+\exp\left(\frac{E-E_F}{k_BT}\right)} = \frac{em_ek_BT}{2\pi\hbar^3}\ln\left[1+\exp\left(-\frac{E_x-E_F}{k_BT}\right)\right] \tag{3.15}$$

where E_F is the Fermi energy of emitter, e is the elementary charge, m_e is an electron mass, k_B is Boltzmann constant and T is the temperature. The transmission coefficient $D(E_x)$ describes the probability of an electron tunneling through the triangular vacuum potential barrier. In the FN theory, this coefficient is often calculated using the WKB method described in the previous section (Sec. 3.1.2).

The tunneling probability through the barrier is related to the transmission coefficient $D(E_x)$, which quantifies the fraction of incident particles (electrons) that penetrate the barrier. It is given by:

$$D(E_x) = \exp\left(\int \sqrt{2m(V(x)-E_x)}dx\right) \tag{3.16}$$

This equation expresses the probability that an electron with energy E_x will tunnel through the potential barrier as a result of the interference between classical and quantum mechanical effects, and $V(x)$ represents the potential energy as a function of position x. The Emission current density is expressed as

$$J_{FN} = \frac{em_ek_BT}{2\pi\hbar^3}D_F\int_0^\infty \exp\left(\frac{E_x-E_F}{d_F}\right)\ln\left[1+\exp\left(-\frac{E_x-E_F}{k_BT}\right)\right]dE \tag{3.17}$$

where d_F is a characteristic energy scale related to the electric field strength and the work function of the metal, which affects the rate of electron field emission;

$$D_F = \exp\left(-\frac{2g_e}{3e}\frac{\omega_0^{\frac{3}{2}}}{F}\right),$$

$$\frac{1}{d_F} = g_e\frac{\sqrt{\omega_0}}{eF},$$

where $g_e = 2\sqrt{\frac{2m_e}{\hbar^2}}$ is a constant that includes physical factors, ω_0 is the work function of the metal, and F is the local electric field.

3.1.4 JWKB improved

The quasiclassical Jeffreys-Wentzel-Kramers-Brillouin (JWKB) approximation [29], [115] assumes that the particle can tunnel through an otherwise inaccessible region, and its wave function in it is determined by an evanescent wave - an exponential function. The key question is how to set up conditions linking outside and inside the barrier, the *connection formula*, as they are located at the barrier edge where the condition of slowly changing potential $V(x)$ is probably not fulfilled. The standard textbook form of JWKB approximation [29], [115] is usually used with linking conditions set by Airy functions (representing the reflection points in triangular barrier approximation). Then the tunneling probability reads:

$$\mathcal{T}(E,F) = \frac{1}{\left(Exp\left(2A_\alpha I(E,F)\right) + Exp\left(-2A_\alpha I(E,F)\right)\right)^2} \approx Exp\left(-2A_\alpha I(E,F)\right)$$
(3.18)

Here, A_α is a numerical factor that will be obtained in the following section, and a shorthand notation for the integral has been used:

$$I(E,F) = \int_{x_1(E,F)}^{x_2(E,F)} \kappa(x,E,F)dx\Big|_{k_1}$$
(3.19)

where E is electron energy at which the tunneling process takes place, F is the strength of an external electric field,

$$\kappa(x,E,F) = \sqrt{\frac{2m}{\hbar^2}(V(x,F) - E)}$$

and $x_{1,2}$ are the inner and outer ends of the barrier. The $x_{1,2}$ are found by solving the equation $V(F,x) = E$. It is assumed that an integral is performed for a given *eigen-state* with a momentum k_1, known from the energy conservation condition. The commonly used approximation that takes us from the top to bottom line in Eq. 3.18 is valid only deep inside the quantum well, away from the top of the tunneling barrier.

Unfortunately, neither form of Eq. 3.18 gives the correct quantum mechanical result right on the top of the barrier, where the exact quantum mechanical solution states that $\mathcal{T} = 1/2$. In Eq. 3.18 when $x_1 = x_2$ and $\kappa = 0$ the bottom formula gives $\mathcal{T} = 1$ which grossly overestimates the transmission coefficient, while the top expression in Eq. 3.18 gives $\mathcal{T} = 0.669$, a value that is still away from $1/2$. Clearly, when one works at the smallest energies, a better expression is needed to obtain the correct $\mathcal{T}(E,F)$ values.

Recent work [116] has studied this problem in detail and found that quite good results can be obtained using Kemble [117] version of WKB, the WKB approximation improved by using a hydrodynamic connection formula. Then the expression is the following:

$$\mathcal{T}(E,F) = \frac{1}{1 + Exp\left(2A_\alpha I(E,F)\right)}$$
(3.20)

an expression that clearly produces the desired quantum mechanical correct result $\mathcal{T} = 1/2$ at the barrier top: when $x_1 = x_2 \Rightarrow I = 0$. Moreover, Ref. [116] showed how, by extending the potential $V(x)$ onto a full complex plane, the Eq. 3.1.4 can be extended to

above-barrier energies. In that work, the optimal complex plane contour has been found that solves $V(x) = E$ equality and minimizes the imaginary part of the potential $V(x)$. In this way, it has been proved [116] that the necessary extension boils down to the same integral as in Eq. 3.1.4, but is performed over a purely imaginary variable. This result is going to be used in the present work.

3.1.5 Further improvements of FN theory

The classic FN theory [29], [118], [119] of field emission from metals describes and reveals the differences in field emission between bulk metallic emitters and low-dimensional emitters. FN tunneling is the wave-mechanical tunneling of electrons through a triangular-type barrier produced at the surface of an electron conductor by applying a very high electric field [120].
The calculations implicate the FN equations [113]. The magnitude J of the electron emission-current density is given by

$$J = \bar{\bar{\lambda}} A \omega_0^{-1} F^2 \exp\left(-\frac{\bar{\bar{\mu}} B \omega_0^{3/2}}{F}\right) \tag{3.21}$$

where ω_0 is the local work function and F is the local field at the surface, $\bar{\bar{\lambda}}$ and $\bar{\bar{\mu}}$ are generalized numerical correction factors, their form depending on the assumptions and approximation made, A and B are respectively the first and second FN constants [118], [119], given by

$$A \equiv e^3/8\pi\hbar_P = 1.541434 \times 10^{-6} A eV V^{-2} \tag{3.22}$$

$$B \equiv \frac{4}{3}(2m_e)^{1/2}/e\hbar = 6.830888 \times 10^9 eV^{-3/2}V m^{-1} \tag{3.23}$$

where e is the elementary charge, m_e is the elecron mass, $\hbar_P$ is Planck's constant and $\hbar = \hbar_P/2\pi$. And the bare scale reads:

$$k_0 = \frac{(2m)^{1/2}}{\hbar} \cong 5.123168 eV^{-1/2}nm^{-1} \tag{3.24}$$

The Nordheim parameter is given by

$$y_N \equiv \frac{CF^{1/2}}{\omega_0} \tag{3.25}$$

where

$$C \equiv (e^3/4\pi\varepsilon_0)^{1/2} = 1.541434 \times 10^{-6} eV V^{-1/2} V m^{1/2} \tag{3.26}$$

and ε_0 is the electric constant.
In the absence of image potential, the tunneling barrier is modelled as a sharp triangular barrier. In elementary FN theory, the transmission probability is

$$D^{el}(F,h) = \exp\left[-\{(8m_e)^{1/2}/\hbar_P\}\int_{\bar{\bar{x}}_{in}}^{\bar{\bar{x}}_{out}}(h - eF\bar{\bar{x}})^{1/2}d\bar{\bar{x}}\right] = \exp[-Bh^{3/2}/F] \tag{3.27}$$

where B is the second FN constant, $\bar{\bar{x}}$ is a spatial coordinate along the tunneling direction, which has a dimension of a $[m]$.

In the presence of an image potential, the potential energy $V(x)$ is

$$V(x) = h - eF\bar{\bar{x}} - \frac{e^2}{16\pi\epsilon_0\bar{\bar{x}}} \tag{3.28}$$

where h is the height of the surface potential barrier, F is the electric field normal to the surface and the last term describes the Coulomb interaction with an image charge left behind in the electrode. The barrier maximum height is

$$V_{max} = h - \left(\frac{e^3 F}{4\pi\varepsilon_0}\right)^{1/2} \equiv h - yh \tag{3.29}$$

where $y = (e^3 F/4\pi\varepsilon_0)^{1/2}/h$ is a non-dimensional parameter and (yh) is the amount of energy that has decreased the top of the image-potential-reduced barrier. The ends of the barrier, as experienced by an electron of a given energy ω_0, correspond to the zeros of $V(x)$. These are given by:

$$\bar{\bar{x}}_{\text{in}}, \bar{\bar{x}}_{\text{out}} = \frac{h}{2eF}(a \pm 1) \tag{3.30}$$

where a is the auxiliary parameter and it has been defined by

$$a = \sqrt{1 - y^2} \tag{3.31}$$

The transmission probability for this barrier, in WKB approximation, is

$$D(F, h) = \exp\left[-\frac{(8m_e)^{\frac{1}{2}}}{\hbar_P}\int_{\frac{h}{2eF}(1-a)}^{\frac{h}{2eF}(1+a)}\left(h - eF\bar{\bar{x}} - \frac{e^2}{16\pi\epsilon_0\bar{\bar{x}}}\right)^{\frac{1}{2}}d\bar{\bar{x}}\right] \tag{3.32}$$

The analytic WKB solution has been obtained [118] as a formula in terms of elliptic integrals:

$$D_{past}(F, h) = \exp\left[-\left(\frac{m_e^{\frac{1}{2}}}{e\hbar_P}\right)\left(\frac{h^{\frac{3}{2}}}{F}\right)I_3(F, h)\right] \tag{3.33}$$

with

$$I_3 = -\frac{2}{3}(1 + a)^{\frac{1}{2}}[E(m) - (1 - a)K(m)] \tag{3.34}$$

$K(m)$ and $E(m)$ are the elliptic integrals of the first and second kind, and $m = \frac{2a}{1+a}$ is the elliptic parameter. This has been the most advanced version of the single-particle theory.

3.2 Many-body formalism

This section explores the many-body problem in quantum mechanics. In the previous sections, the focus was on the wave functions of single, noninteracting electrons. This approach, which exemplifies Fowler–Nordheim theory, effectively captures the behavior of isolated electrons moving through quantum mechanical systems in the absence of electron-electron interactions.

Now, the focus shifts to addressing the complexities of electron-electron interactions which is a fundamental aspect that is neglected in the single-electron approach. In this section, the main questions are addressed: what happens when electrons interact, and how to construct a theory to accurately describe these interactions. This is an important point in the understanding of quantum mechanics, as a transition is made from the relatively simple analysis of individual electrons to the collective modes. This includes exploring new theoretical tools and concepts, such as second quantization. Richer and often unexpected phenomena that arise from electron interactions can be discovered, providing a deeper and more complete understanding of quantum mechanical systems.

3.2.1 Limitations of first quantization

A wave function solution is obtained within a framework also called first quantization. The method, although powerful, has certain limitations and drawbacks. One of the main limitations of the first quantization framework is that it becomes mathematically and conceptually challenging when dealing with systems involving a large number of interacting particles. This is particularly true in cases where the interactions between particles are strong and cannot be treated perturbatively.

We use bra-ket notation, that works irrespective of a chosen basis, to give the many-body electronic wavefunction as some combination of single-electron wavefunction:

$$|\Psi\rangle = |\psi_1 \cdots \psi_N\rangle \tag{3.35}$$

Consider the interaction between two electrons as an illustrative example. The Coulomb interaction involves coordinates of both electrons and (in 1D) its Hartree component can be represented as follows:

$$V_{ij}^{II}(x, x') = \langle \psi_i \psi_j | \frac{1}{|x - x'|} | \psi_i \psi_j \rangle \equiv \int \psi_i^*(x) \psi_j^*(x') \frac{1}{|x - x'|} \psi_i(x) \psi_j(x') dx dx' \tag{3.36}$$

while the Fock, exchange component is:

$$J_{ij}^{II}(x, x') = \langle \psi_j \psi_i | \frac{1}{|x - x'|} | \psi_i \psi_j \rangle \equiv \int \psi_j^*(x) \psi_i^*(x') \frac{1}{|x - x'|} \psi_i(x) \psi_j(x') dx dx' \tag{3.37}$$

Here, x and x' denote the positions of the interacting electrons, and $|\Psi\rangle$ encompasses the wave function of the entire system and contains single electron wave functions of all electrons. Thus the overall interaction $\langle \Psi | V | \Psi \rangle$ will be a sum of contributions from all occupied states i, j.

For example, the wave function representing the case of two interacting electrons is given by:

$$\Psi(x_1, x_2) = \psi_1(x_1)\psi_2(x_2) - \psi_1(x_2)\psi_2(x_1) \tag{3.38}$$

The term $\psi_1(x_1)\psi_2(x_2)$ represents the case where electron 1 is in state ψ_1 and the electron 2 is in state ψ_2. The term $\psi_1(x_2)\psi_2(x_1)$ represents the opposite configuration, where the electron 1 is in state ψ_2 and the electron 2 is in state ψ_1. The two are indistinguishable. To extend the system to include N particles, the wave function must be generalized

through antisymmetrization. This is necessary because particles, such as electrons, comply with the Pauli exclusion principle. This principle requires the wave function to be antisymmetric (e.g. "$-$" sign in Eq. 3.38) when particles are exchanged. Accurately capturing this interaction within the confines of the first quantization framework becomes increasingly formidable as more particles are injected into the system.

Generalizing Eq. 3.38 to N particles requires to work with Slater determinants. They are expressed as:

$$\Psi(\{x_i\}) = \frac{1}{\sqrt{N!}} \begin{vmatrix} \psi_1(\mathbf{x}_1) & \psi_1(\mathbf{x}_2) & \cdots & \psi_1(\mathbf{x}_N) \\ \psi_2(\mathbf{x}_1) & \psi_2(\mathbf{x}_2) & \cdots & \psi_2(\mathbf{x}_N) \\ . & . & & . \\ . & . & & . \\ . & . & & . \\ \psi_N(\mathbf{x}_1) & \psi_N(\mathbf{x}_2) & \cdots & \psi_N(\mathbf{x}_N) \end{vmatrix} \tag{3.39}$$

which is a many-body analogue of the wave function as defined in Eq. 3.11. Varying any of the amplitudes means that one is changing entire column in the determinant. Consequently, the optimization problem (especially if two columns are to be changed simultaneously because of interaction) becomes intractable.

3.2.2 Second quantization

The aim of the first quantization was to construct the wave of probability that describes the system. For many particles, waves start to interfere in a way that is very hard to follow. Thus, it is sensible to fix the basis, so-called Hilbert space basis: to define static waves and shift the interest to the problems of how particles jump from one state to another. Unlike the first quantization, where the focus was on ever-evolving waves, the second quantization will concentrate on how particles are jumping from one state to another.

Unlike the first quantization approach, which focuses on wave functions for individual particles, the second quantization framework treats particles as excitations of underlying quantum fields that extend throughout spacetime. This shift in perspective offers several advantages. First, it provides a more elegant and unified way to incorporate both particles and their interactions, making it particularly suitable for describing systems with numerous interacting particles.

For more complex, interacting systems a method for transparent bookkeeping of the changing occupancy of various quantum states is necessary. To this end, researchers have proposed introducing new operators - creation $c_i{}^\dagger$ and annihilation c_i operators - adding or removing particles from the system. Here, the index i is used here to represent all the relevant degrees of freedom, including the spin of the particles. Second quantization thus gives a fundamental and efficient language for expressing the physics of many-particle systems. *It will be used in this thesis to write down the Hamiltonian of the system.*

The many-body state of a system of electrons, containing the single-particle states $|\psi_i\rangle, i = 1, ..., N$, before given as the Slater-determinant (Eq. 3.39), now can be expressed in a very compact form:

$$|\Psi_i\rangle = \frac{1}{\sqrt{N!}} \sum_P \text{sgn}(P) P(|\psi_1\rangle \cdots |\psi_i\rangle \cdots |\psi_N\rangle) = c_1{}^\dagger \cdots c_i{}^\dagger \cdots c_N{}^\dagger |0\rangle \tag{3.40}$$

where $P(\cdot)$ refers to a permutation of the objects in parentheses and $\mathrm{sgn}(P)$ is the sign of this permutation. $|0\rangle$ notation means the vacuum, defined as a state with no particles. The advantage of this expression is that all the symmetry properties of the Slater-determinant are now embodied in the product of creation operators. For this to be true, the creation operators have to satisfy certain rules.

For the same single-particle state, its creation should not be allowed twice at all, therefore,

$$c_i^\dagger c_i^\dagger = 0 \tag{3.41}$$

and destruction operators must satisfy similar relations

$$c_i c_j = -c_j c_i, \quad \text{for} \quad i \neq j, \quad \text{and} \quad c_i c_i = 0. \tag{3.42}$$

The products of creation and destruction operators corresponding to different states must involve a minus sign when their order is switched and the destructions are taken

$$c_i^\dagger c_j = -c_j^\dagger c_i, \quad \text{for} \quad i \neq j. \tag{3.43}$$

These operators move an electron from an occupied state i to an empty state j or the other way around, and since the order of application in the two products is reversed, corresponding to a permutation, they must come with opposite signs.

The peculiarity of this formulation is that it compactly represents the many-body space of excitations by embedding the properties of ladder operators into simplified commutation relations, eliminating the need for an exact Hilbert space representation. It is considered the foundation on which the extensive structure of quantum field theory is built.

This section will practically introduce the basic elements of second quantization and justify its application, setting the stage for discussions about the operations of quantum mechanics expressed in second quantization terms, such as taking matrix elements, changing bases, and representing operators.

3.2.3 Hamiltonian in second quantization

The formalism of second quantization provides a comprehensive solution for representing the Hamiltonian of complex systems, particularly one-dimensional materials that are of interest in this thesis. This formalism is essential, presenting creation and annihilation operators that signify the addition and removal of particles in various quantum states, providing a detailed insight into the dynamic properties of the system. The algebra of creation and annihilation operators automatically takes into account Pauli exclusion principle.

The energy and further behaviour, as well as transport coefficients of any material, are determined by its Hamiltonian. In general, the Hamiltonian depends on the specific chemical properties of the material or, more generally, the physical system under consideration. Nevertheless, it is commonly used to describe the Hamiltonian using a few model parameters, like in a tight-binding approximation. It gives an immediate understanding of the forces acting on carriers in the material and we shall use it in the thesis for illustrative purposes. The methodology derived here relies on tight-binding approximation, although it is possible to derive collective modes without this assumption. Those derivations would use less transparent methods; the study of these generalizations is in the field of theoretical physics, beyond the scope of this manuscript.

The tight-binding model simplifies the description of electron movement in a solid by discretizing space and parameterizing hopping amplitudes between these sites. In a solid, electrons occupy the locations on atoms and have a negligible probability of being measured in between as they are in there only when hopping to a neighbouring site due to quantum tunneling. Then as our Hilbert basis, we take atomic orbitals ψ_i, one located at each, e.g., i-th, site.

In the tight-binding model, a lattice of sites is considered, and each site can accommodate one or more electrons. The Hamiltonian describes electrons hopping between neighbouring sites and their on-site energies ϵ_i. In its simplest form, the Hamiltonian for a one-dimensional lattice can be written as:

$$H = \sum_i \epsilon_i c_i^\dagger c_i + t \sum_i (c_i^\dagger c_{i+1} + c_{i+1}^\dagger c_i) \tag{3.44}$$

Here, ϵ_i represents the on-site energy or the energy level associated with an electron occupying the i-th lattice site. It is often referred to as the diagonal term of the Hamiltonian. It can be calculated as the following integral:

$$\epsilon_i = \int d\vec{r}\, \psi_i^*(\vec{r}) V_{ion}(\vec{r}) \psi_i(\vec{r})$$

where we are integrating the ionic potential over the single-particle wave functions. The $c_i^\dagger$ and c_i are the creation and annihilation operators, respectively, creating or annihilating an electron at the i-th lattice site. The parameter t represents the hopping integral or the coupling strength between adjacent lattice sites.

It characterizes the probability amplitude for an electron to hop from one site to the next. The terms $c_i^\dagger c_{i+1}$ and $c_{i+1}^\dagger c_i$ describe the hopping of an electron from the i-th site to the $(i+1)$-th site and vice versa. The hopping parameter can also be expressed as an integral:

$$t_{ji} = \int d\vec{r}\, \psi_j^*(\vec{r}) \frac{\nabla^2}{2m} \psi_i(\vec{r})$$

where again we take single-particle wave functions, the base of the Hilbert space, to evaluate it. The entire complexity of the many-body problem is taken into account by the anti-commutation rules of the creation/annihilation operators. The many-body problem is now solved by diagonalizing the tri-diagonal matrix (for nearest neighbour hopping) which can be done by going to reciprocal (momentum) space and that leads to electrons band-structure $E(k)$, in our simplest case $E(k) = \cos(k)$. The advantage is however that one can immediately grasp the physical content of the problem (also for inhomogeneous case) and add interactions which now take nicely compact form:

$$H_{int} = \sum_{ijml} V(i,j,l,m) c_i^\dagger c_j^\dagger c_l c_m \tag{3.45}$$

Where the matrix element:

$$V(i,j,l,m) = \int \int \psi_i^*(\vec{r}) \psi_j^*(\vec{r'}) \frac{e^2}{|\vec{r} - \vec{r'}|} \psi_k(\vec{r}) \psi_l(\vec{r'})\, d\vec{r}\, d\vec{r'}$$

is again defined as integral over single electron states. The matrix is now in general four-dimensional. A problem that is still difficult to solve, but at least one can immediately understand its physical content and look for sensible approximations.

Using the Hamiltonian in the Schrödinger equation, it is possible to derive the energy levels and wave functions of electrons within the lattice. Overall, the tight-binding model

provides a valuable approximation for understanding the electronic properties of various materials, including conductors, insulators, and semiconductors. It serves as a foundational framework for more advanced models in condensed matter physics. Most importantly, the microscopic behaviour of electrons propagating within the system is very transparent in this formalism.

3.3   Collective modes: field theory

Second quantization is a valuable tool for perturbative methods, particularly when the description of the system closely aligns with a known basis, such as Bloch states. It involves the use of creation ($c_i^\dagger$) and annihilation (c_j) operators, which are effective for manipulating particles within a predetermined Hilbert space i, j-indexed basis, making it well-suited for constructing perturbative series and considering small corrections to the single-electron basis. Second quantization is then used to make perturbative expansions, e.g., in interaction term $V(k, k')$, namely we construct diagrams with more and more $V(k, k')$ nodes assuming that higher order gradually dies out – the state mixing is small. But in many cases, there is a need to create infinitely many electrons at various positions to capture the strongly collective nature of the system.

In such a case, in strongly correlated systems, where it is essential to describe an entire ensemble of particles collectively, field theory methods employing field operators become more appropriate. To this end, we first define a boson that describes density fluctuation, sometimes known as plasmon. It reads:

$$b_q^\dagger = \sum_i c_i^\dagger c_{i-q} \tag{3.46}$$

where we see that this new entity at one creates an infinite number of fermions: $c_i^\dagger$ creates an electron in state i, and c_{i-q} annihilates an electron in a state that is momentum q away from state i. These bosons are used whenever one suspects that collective modes determine the physics of the system and constitute the correct basis to begin with. Following Richard Feynman, instead of studying dynamics of a single electron one introduces a notion of fields as objects over which path integrals are performed. This reformulation of quantum mechanics is very similar to the Lagrange reformulation of Newtonian classical dynamics, where the focus was shifted from the particle's motion towards its optimal trajectory.

Now, based on the b-boson we define a field:

$$\phi(x) = \sum_p A_p(x)(b_p^\dagger + b_{-p}) \tag{3.47}$$

where the amplitudes are $A_p(x) = \sqrt{\frac{L|p|}{2\pi}} \frac{1}{p} \exp(-\alpha|p| - \imath p x)$, i.e., it determines how much of each collective mode should be taken at different positions to create an optimal density. These field operators create the entire ensemble of particles simultaneously, capturing the system's collective behavior. They are not single-particle wave functions – inside them, the second quantization operators are incorporated, and these keep track of all anti-commutation rules of many-body state. The field operator $\phi(r)$, where $r = (x, t)$ represents the spatial and temporal coordinates of a quantum 1D system, is a fundamental tool that we shall use in this thesis.

The connection between fermionic and bosonic fields can be described by equations, such as Eq. 3.46, that relate the creation and annihilation operators for fermions to those for bosons. Such equations are essential for understanding the transformation between different representations of the same physical system. We choose the *right* basis that is the closest to capturing the *full* solution of the system. In quantum many-body theory, the choice of formalism is crucial, especially when considering correlations – choosing the right one means that the perturbing term will be very small and we are very close to the final answer. Collective modes in the context of field theory are essential for describing 1D interacting particle systems, because then fermions cannot avoid each other as they move along the nanotube.

3.3.1   Special case of 1D

In the case of a 1D system, any interaction between fermions immediately leads to a breakdown of the single-electron picture. Here, it is strikingly clear that we need to resort to the description in terms of collective modes. Fortunately, expressing the system in terms of fields allows for an immediate solution to the problem.

Upon expressing a system of many fermions (electrons) in terms of field operators defined above the Hamiltonian describing the low-energy properties of a massless one-dimensional system is (for derivation see Appendix A)

$$H = \frac{\hbar}{2\pi} \int dx \left[\frac{uK}{\hbar^2} \left(\pi \nabla \theta(x) \right)^2 + \frac{u}{K} (\nabla \phi(x))^2 \right] \tag{3.48}$$

where we used the collective, many body field $\phi(x)$ defined just above in Eq. 3.47. The $\theta(x)$ is a canonically conjugated momentum field. This is the Hamiltonian of a Tomonaga-Luttinger liquid (TLL) – a new paradigmatic state for 1D fermions that substitutes the well-known Landau Fermi liquid describing conventional 3D metals.

Here, u is the velocity associated with the collective excitations in the system, K is the Luttinger parameter and the bosonic fields ϕ and θ represent the density and phase fluctuations. The gradient terms of these fields, $(\nabla \phi)^2$ and $(\nabla \theta)^2$, give kinetic and density-density interactions. Remarkably derivatives of the bosonic fields correspond to fermionic density fields:

$$\rho_c(x) = \frac{1}{\sqrt{2\pi}} \nabla \phi(x), \quad \pi_c(x) = \frac{1}{\sqrt{2\pi}} \nabla \theta(x) \tag{3.49}$$

Here, $\rho_c(x)$ and $\pi_c(x)$ are the spatial fluctuations of fermion density and fermion momentum density. Mathematically, these are the dual fields to the phase fluctuations, the bosonic fields $\phi(x)$ and $\theta(x)$, respectively. All the observable quantities should now be expressed in terms of these bosonic fields, and then their expectation values can be relatively straightforwardly calculable, taking into account the solvability of the theory given by Eq. 3.48.

Later in Chapter 5, the presence of a simple relation will be demonstrated between the $\phi(x), \theta(x)$ fields and the *all*-fermion field $\Psi(x)$ (an analogue of Eq. 3.39, in the sense that it contains motion of all electrons), approximately:

$$\Psi(x) \propto \exp(\pm k_F x) \exp(\phi(x) \pm \theta(x))$$

It should be emphasized that although the bosonic field appears as simple phase shifts defined on the top of Bloch wave, in fact, they *contain the collective motion of all electrons*

in the system. The fact that such collective motion can be described by a remarkably simple equation of motion Eq. 3.48 is one of the greatest achievements of the theory of correlated systems for which F.D.Haldane received Nobel prize in physics in 2016.

Eq. 3.48 is a Hamiltonian of an elastic membrane, therefore, all our knowledge on that can be significantly useful here. It is one of the rare and remarkable, cases when insights from mechanics inspire the development of fundamental physics.

3.4 TLL and tuneling

3.4.1 Re-defining the problem

We are now ready to tackle the problem of tunneling out of interacting nanotube. In essence, our approach is as follows: since the escaping electron is distinct, we separate quantum (TLL) and (semi-) classical degrees of freedom that describe the motion of that electron. We will proceed by averaging out the TLL to determine its influence on the (semi-) classical motion to get the transmission.

We start by defining the problem, namely: the TLL before and after emission, plus the emitted electron. The problem focuses on studying a model for one-dimensional interacting fermions. Initially, the TLL is characterized by a quantum state with N electrons, represented by the wavefunction $\langle \Psi_{\text{TLL}}^N |$. Due to the emission of an electron, the initial state is transformed into the final state, where the TLL contains $N-1$ electrons (in any q-state, Eq. 3.46) and there is an additional the emitted electron (in some momentum state): $\langle \Psi_{\text{TLL}}^{N-1} | \otimes \langle \Psi_{\text{emit}} |$.

The transmission has been defined at the beginning of this chapter as an overlap of incoming and outgoing wavefunctions. In all-electron language, it can be written as:

$$\mathcal{T}(E) = \int_{x_{in}}^{x_{out}} \langle \Psi_{\text{final}}(E) | x_1, x_2, ..., x_N \rangle \mathcal{G}(x, x') \langle x'_1, x'_2, ..., x'_N | \Psi_{\text{initial}}(E) \rangle dx dx' dx_{1...N} dx'_{1...N}$$

(3.50)

Here, $\mathcal{G}$ is a propagator of the tunneling fermion from point x to x', and we integrate it over the entire barrier area. The variable x can be equal to any of coordinates x_i and variable x' to any of coordinates x'_i, but it is usually assumed that all (indistinguishable) electrons sit on orbitals of the same shape. Thus, $\mathcal{T}$ will be proportional to $N(N-1)$ times, the case when $x = x_1$ and $x' = x'_1$ is chosen (so $\mathcal{G} \propto \delta(x - x_1)\delta(x' - x'_1)$) with all other electrons, playing a role of an effective medium.

The Eq. 3.50 generalizes the previous WKB description in terms of plane waves. The outgoing wave, i.e., the quantum state after the emission process, is a tensor product of emitted electron's states and the states of remaining correlated electronic liquid:

$$\langle \Psi_{\text{final}} | = \langle \Psi_{\text{TLL}}^{N-1} | \otimes \langle \Psi_{\text{emit}} | \tag{3.51}$$

while the initial state is a correlated electronic liquid that contains all electrons:

$$\langle \Psi_{\text{initial}} | = \langle \Psi_{\text{TLL}}^N | \tag{3.52}$$

When, as in our case, the system is a correlated 1D metal, the correlated electronic liquid is the TLL described in the previous sections. Our problem is thus to provide the time

evolution $\Psi_{\text{initial}}(t)$ and extract the part that (after a long time) will give a finite overlap with $\langle\Psi_{\text{final}}|$ as defined above.

Since the emitted electron is geometrically separated and distinct as it moves along the 1D system on its way out, we can simplify the problem and assume that the outgoing electron can be factorized out

$$\langle\Psi_{\text{final}}|= \langle\Psi^{N-1}_{\text{TLL}}|\cdot\langle\Psi_{\text{emit}}| \tag{3.53}$$

where we used simple "·" product instead of tensor "⊗" product because we removed any entanglement between these states. To benefit from this factorization and, at the same time, employ an accurate and complete analysis of the 1D system ≡TLL, the Hamiltonian ought to be split in quantum (TLL) and classical parts.

$$H_{tot} = H_{TLL}[\Phi_{quant}] + H_{tun}[\Phi_{cl}] \tag{3.54}$$

where Φ_{cl} refers to the large displacement of carriers due to emission events, and Φ_{quant} are small fluctuations around this trajectory (solved previously as TLL). To split the Hamiltonian, we follow the method of Fukuyama and Suzumura ([121], [122], [123]), who simply proposed $\phi = \phi_{cl} + \phi_q$. Then the Hamiltonian becomes:

$$\begin{aligned}
H = \int dx &\left(uK(\nabla\theta(x))^2 + \frac{u}{K}(\nabla\phi(x))^2 + V\cos(\theta(x = x_{tun})) \right) \\
= \int dx &\left(uK\left[(\nabla\theta_q)^2 + (\nabla\theta_{cl})^2 \right] + \frac{u}{K}\left[(\nabla\phi_q)^2 + \left(\nabla\phi^2_{cl}\right) \right] \right. \\
&\left. + \frac{u}{K}M^2 + uKP^2 + V\cos\theta_{cl}(x = x_{tun})\left(1 - \frac{\theta_q^2 - \langle\theta_q\rangle^2}{2}\right) \right) \quad (3.55)
\end{aligned}$$

which indeed can be divided into a quantum part

$$H_{TLL}[\Phi_{quant}] = \int dr \left(uK\,(\nabla\theta_q)^2 + \frac{u}{K}(\nabla\phi_q)^2 \right) \tag{3.56}$$

and classical part:

$$H_{tunel}[\Phi_{cl}] = \int dr \left(\frac{u}{K}\,(\nabla\phi_{cl})^2 + uK(\nabla\theta_{cl})^2 + \frac{u}{K}M^2 + uKP^2 + V\cos\theta_{cl}(r)\left(1 - \frac{\theta^2 - \langle\theta\rangle^2}{2}\right) \right) \tag{3.57}$$

where M is a correction to the tunneling electron mass due to quantum fluctuations

$$M^2 \propto \nabla\phi_{cl}(\phi^2 - \langle\phi\rangle^2),$$

and analogous for P^2, the correction to mutual momentum. The last term is a tunneling term, with its amplitude $V \propto F_{ext}$ – proportional to the external electric field F_{ext}.

The quantum part is identical to TLL and from now on, the q index will be neglected. It should be noted that the difficult-to-solve nonlinear term, the cosine corresponding to emission operator, acts only on the classical field ϕ_{cl}. When the cosine is large and dominates the behaviour, a classical description of this term can be continued with $\hbar \to 0$. Then the time evolution can be factorized:

$$U_{total}(t_1 - t_0) = U_{TLL}(t_1 - t_0) \cdot U_{tun}(t_1 - t_0) \tag{3.58}$$

where we could use simple product "·" instead of full quantum tensor product "⊗". Here, U is a time evolution operator which is defined as $U \sim \exp(iH)$, and since the Hamiltonian is split, it is explicitly represented as:

$$\langle \Psi_{final} | \Psi_{initial} \rangle = \langle \Psi_{TLL} | \exp(iH_{TLL}) | \Psi_{TLL} \rangle \langle \Psi_{out} | \exp(iH_{tun}) | \Psi_0 \rangle \qquad (3.59)$$

where $U_{TLL} = \exp(iH_{TLL})$ is simply a response function of the TLL. Since $|\Psi_{TLL}^{N-1}\rangle = c_k |\Psi_{TLL}^N\rangle$, we are interested in the retarded response function of $c_k^\dagger c_k$, "susceptibility", i.e., the imaginary part of the propagator, electron Green's function. It can be written in the mathematical form:

$$\langle \Psi_{TLL} | c^\dagger(t,x) c(0,0) | \Psi_{TLL} \rangle_R = Im[G_{TLL}(t,x)] \qquad (3.60)$$

which is nothing else than the LDOS of TLL, as discussed in the previous section. The other part contains the large-amplitude motion along the classical trajectory. Then, the element that needs to be evaluated is a classical propagator [121], [122], [123]:

$$G_{cl}(t_1 - t_0) = \exp[S_{cl}(t_1 - t_0)] \qquad (3.61)$$

with

$$S_{cl} = \int dr \left(V_F (\nabla \theta_{cl})^2 + (\nabla \phi_{cl})^2 + \left(\frac{u}{K} - 1 \right) \nabla \phi_{cl}^2 + V \cos \theta_{cl} + corrections \right) \qquad (3.62)$$

The first two terms can be refermionized (see Sec. 10C in Ref. [124]), so that they manifestly represent the motion of a single fermion, while the third term regularizes action at the smallest distances. The cosine is the largest term with the characteristic feature of localizing the system at its minimum. The problem is reduced to evaluating tunneling probability between such minima, a problem that has been solved by Coleman [125].

The corrections indicated in Eq. 3.62 are terms $\propto (\theta - \langle \theta \rangle) \equiv P$ and $\propto M^2$. These corrections will capture how quantum fluctuations modify the tunneling trajectory. In all papers that have addressed the problems of tunneling so far, these terms were simply neglected, to make the factorization of quantum and classical parts exact. Physically, this is supposed to be justified by the fact that the emitted electron moves independently from the carriers in the 1D metal. This assumption works well if the trajectory of the electron $q_{cl}(t)$ is such that it immediately loses contact with the cathode.

However, as will be observed, this assumption does not work when the electron moves along the 1D metal. In particular, it entirely misses the interaction with the image-hole left behind in a metal, a feature taken into account in the most advanced version of 3D FN theory. This is accounted for by the M, P terms. Moreover, it is observed that the quantum corrections effectively renormalize the potential experienced by the emitted electron, because $V \to V \left(1 - \frac{\theta^2 - \langle \theta \rangle^2}{2} \right)$. These terms will also be accounted for through the dielectric function of the TLL cathode. Thus, the terms that will be neglected in our reasoning, are only a mutual correlation between the image-hole and the local variations of dielectric functions. These should be smoothed out at the finite temperatures we are interested in.

3.4.2 Back to WKB: Instanton idea of Coleman

We now move to the next stage of our derivation: we identify ϕ_{cl} with the trajectory $q(\tau)$ along which the electron tunnels out. Crucially, for us, the problem of moving from one minimum to another along $q(\tau)$ within the field theory has been solved by Coleman [125] who showed that the semi-classical (WKB-type) approximation works well. We outline this derivation here, below.

What remains to be solved now is the classical part of the problem, the second term in Eq. 3.59 or in other words Eq. 3.61. The breakthrough was achieved through the work of Coleman [125], who demonstrated for potential shown in Fig. 3.3 the existence of an additional solution to the Euler-Lagrange equation that he called an instanton. Just as a soliton in real space, an instanton lives in a temporal domain and describes a sudden jump from one state to another.

Sidney Coleman's innovative integration of the WKB approximation with instanton concepts has been a fundamental element in enhancing the understanding of quantum mechanics and quantum field theory. This section highlights Coleman's seminal contribution to the field, illustrating the interconnections between the WKB approximation and his revolutionary instanton concepts [125].
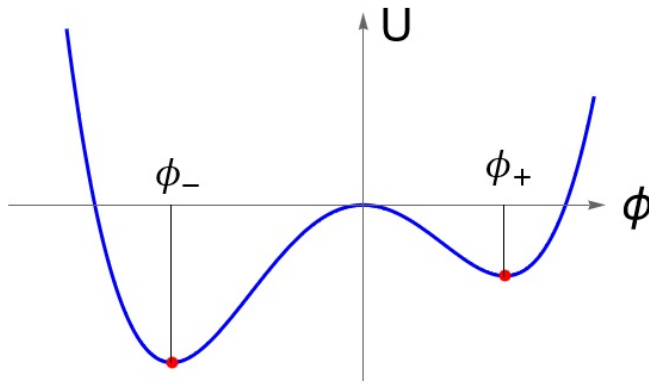
Figure 3.3: Potential energy U as a function of the field ϕ (nonderivative part of the Lagrangian), showing the false vacuum (ϕ_-) and the true vacuum (ϕ_+). The figure is inspired by Ref. [125].

Coleman's contributions have been instrumental in extending these concepts to quantum field theory, providing a more generalized and coherent framework. The quantum field theory of a single scalar field in four-dimensional space-time with nonderivative interactions should be taken into account.

$$\mathcal{L}[\phi] = \frac{1}{2}\partial_\mu\phi\partial^\mu\phi - U[\phi] \tag{3.63}$$

This Lagrangian represents a foundational mathematical structure in the theoretical developments under consideration, describing the dynamics of a scalar field $\phi(r)$ in the presence of a potential $U[\phi]$. $U[\phi]$ is assumed to include two relative minima, $\phi_\pm(r)$, with $\phi_-(r)$ being the absolute minimum (Fig. 3.3). The classical field theory state where $\phi(r) = \phi_-(r)$ represents the unique state of lowest energy, correlating to the unique vacuum state of the quantum theory, at least in perturbative regimes. The classical equilibrium state where $\phi(r) = \phi_+(r)$, called "false vacuum", is stable within the classical framework but is destabilized by quantum effects, notably by barrier penetration. Coleman's theory depends on the idea that quantum fluctuations can include the formation of

a bubble of the $\phi_-(r)$ region. The expansion of this bubble is contingent upon surpassing a certain critical size, beyond which it can grow and convert the available false vacuum $\phi_+(r)$ into a true $\phi_-(r)$. The decay probability of the false vacuum (per unit time per unit volume, Γ/V) is expressed as

$$\Gamma/V = Ae^{-B/\hbar}[1 + O(\hbar)] \tag{3.64}$$

where A and B are theory-dependent coefficients.

Through his instanton concepts, Coleman introduces an approach to understanding and calculating the crucial B coefficient, which determines the probability of decay for the false vacuum. Accurately estimating B is essential as it reveals the complex dynamics and properties of the true vacuum state, thereby illuminating the overall behavior of the quantum field.

Based on a solution for a single particle $q(r)$ trajectory problem, defined by Lagrangian

$$L[q(r)] = \frac{1}{2}\dot{q}^2 - V[q(r)] \tag{3.65}$$

where $V[q]$ denotes the potential, Coleman showed that the field $\phi(x)$ will have three solutions: two well-known Gaussian oscillations around the minima and the jump, a solution in time known as instanton. The jump fulfils the equation

$$\frac{d^2\phi}{dx^2} = V_{saddle}[\phi] \tag{3.66}$$

which can be solved as

$$x = \int_0^{\phi_1} \frac{d\phi}{(2V_{saddle}(\phi))^{\frac{1}{2}}} \tag{3.67}$$

leading to the action

$$S_1 = \int dx \left[\frac{1}{2}\left(\frac{d\phi_1}{dx}\right)^2 + U_+ \right] = \int_{-a}^{a} d\phi \, \{2U[\phi]\}^{1/2} \tag{3.68}$$

To evaluate the coefficient B, the Euclidean action S_E of the bounce solution can be computed:

$$B = S_E = \int d\tau d^d x \left[\frac{1}{2}\left(\frac{\partial\phi}{\partial\tau}\right)^2 + \frac{1}{2}(\vec{\nabla}\phi)^2 + U(x) \right] \tag{3.69}$$

The seminal result by Coleman [125] is that the Euler-Lagrange equation for the field instanton gives classical equation of motion $\ddot{q}(r) = V_{saddle}(q(\tau))$ which admits a tunneling type solution, upon inserting it into the tunneling action one finds:

$$S_{tun} = \int d\tau \sqrt{V_{saddle}(q(\tau))} \tag{3.70}$$

which shows that WKB can serve as a good approximation for Eq. 3.62. Based on the discussion after Eq. 3.62, it is observed that including quantum corrections will lead to a modified potential:

$$V(x) = h - eF\mathbf{d}_0 x^\alpha - \frac{e^2}{16\pi\epsilon_0\mathbf{d}_0 x^\alpha} \tag{3.71}$$

where we split the $\bar{\bar{x}}$ spatial coordinate into x dimensionless variable, and the dimension-carrying parameter $\mathbf{d}_0$. This is because the correlation functions in TLL are given by power-laws with non-universal exponents, which leads to an arbitrary α. A full explanation of a physical meaning of the parameter $\mathbf{d}_0$ will be provided in Chapter 4. It is thus expected that V_{saddle} (Eq. 3.70) will have the form of Eq. 3.71. Remarkably, for the simplest case of straightforward motion perpendicular to the barrier, this becomes equivalent to the quasi-classical WKB result. However, in more complicated cases, such as ours, the trajectory of a particle will follow a path similar in spirit to the path-integral formulation. Now the $q(\tau)$ is the saddle point trajectory, and it is assumed that due to the geometry of the problem (the quantum well in between nanotubes), a significant portion of the trajectory is such that $q(\tau)||x$. For a considerable time, the emitted electron keeps interacting with the surrounding TLLs. Our task is then to average out the quantum fluctuations, which can be achieved for TLL, in order to obtain effective parameters inside $V_{saddle}(x)$.

To complete the connection with the most advanced form of single-particle formalism, Eq. 3.1.4, we turn to density matrix formalism. Since $\rho_{tun} = \exp(-S_{tun})$ and anticipating the result in Eq. 3.70, we obtain that $\mathcal{T}$ is expressed by Kemble's improved Jeffreys–Wentzel–Kramers–Brillouin (JWKB) formula:

$$\mathcal{T}(F, \omega) = \frac{1}{1 + D(F, h = \omega - \omega_0)} \tag{3.72}$$

where D is the transmission probability (as defined in past studies, in Eq. 3.33). The probability that the selected carrier is emitted is generally proportional to the element of the *single-particle* density matrix: $p_{emit} = \rho_{tun}/Z$ where Z is a partition function of the system. For Z, we take $Z = \rho_0 + \rho_{tun} \approx 1 + \rho_{tun}$, assuming that the tunneling process is so negligible that it does not affect the density matrix of the rest of the system. We thus arrive at normalized emission probability:

$$p_{emit} = \frac{1}{1 + \exp(+S_{tun})} \tag{3.73}$$

and the remaining problem is to solve $\exp(+S_{tun})$. For this task, the idea introduced by Coleman is employed, which has been described in this section.

Part II

Results

Chapter 4

Generalizing Fowler-Nordheim tunneling theory for an arbitrary power-law barrier

4.1 Introduction

In this chapter, the canonical Fowler-Nordheim theory has been extended as the transmission for the general case of a barrier described by a fractional power law has been computed. An exact analytical formula has been derived, which is written in terms of Gauss hypergeometric functions, and fully captures the emission for this generalized problem, including the screened interaction with the image potential. Firstly, the quality of the approximation has been benchmarked against the most advanced formulation of Fowler-Nordheim where the transmission is given in terms of elliptic integrals. After that, as the barrier is given by a power law, the dependence of the current on the exponent of the power law is analyzed in detail. To be relevant to the experiments, several examples of rough metallic surfaces and surfaces covered with a dielectric have been considered, showing that these can be described by the formalism. Finally, it is discussed how this solution may be related in some specific cases to an exact quantum mechanical solution of the quantum well problem.

The chapter is organized as follows: the model is defined in Sec. 4.2, then in Sec. 4.3 the generalized formula for tunneling in the case of a barrier described by a power law with an arbitrary exponent is derived. In Sec. 4.4, using Kemble's improved JWKB expression for tunneling, the validity of this expression compared to previous results for bare Coulomb triangular barrier [118] and present results obtained for arbitrary exponents is assessed. The dependence on the exponent of the power law is studied. The transmission probability for composite surfaces with locally varying work functions is also shown in Sec. 4.4.3. Besides, a comparison of our analytical results with a numerical scattering matrix method is made. Finally, in Sec. 4.5, the possible experimental implementations in which our theory could be applied are discussed, and a connection with exact quantum mechanical solutions of the problem is built. The conclusion is in Sec. 4.6.

4.2   The model

We start with the one-dimensional Schrödinger equation for the tunneling electron:

$$-\frac{d^2\Psi(x)}{dx^2} - k_0^2(E - V(x))\Psi(x) = 0 \tag{4.1}$$

where $\Psi(x)$ is a one-dimensional wave function, $V(x)$ is the electron potential energy, E is the electron's total forward energy and $k_0 \cong 5.123168 eV^{-1/2} nm^{-1}$ is a universal constant (see Sec. 3.1.5 for its explicit expression). In our case, $V(x)$ will have a specific form of a sum of two opposite power laws.
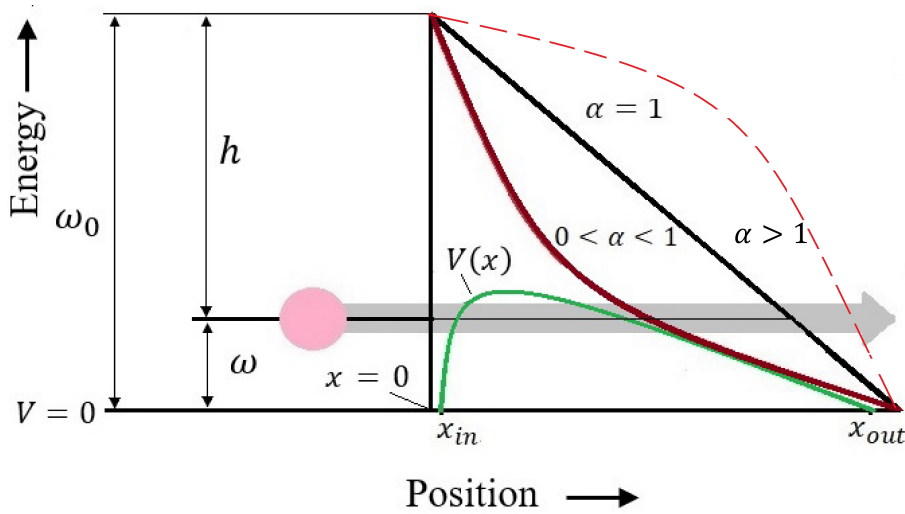
Figure 4.1: Illustration of the image-force-reduced barrier $V(x)$ encountered by a tunneling electron. $\alpha = 1$ corresponds to the exact triangular barrier at a perfectly smooth planar interface, while $0 < \alpha < 1$ corresponds to a reduced dimensionality seen by tunneling electrons at a rough surface above the concave part, while $\alpha > 1$, above the convex part.

4.2.1   Effective potential

It is observed that the entire information about the physics of the problem is inside the effective potential energy experienced by an electron, $V(x)$. The electron image-potential-reduced barrier is shown in Fig. 4.1, where $V(x)$ is the electron potential energy, h is the zero-field (tunneling) barrier height (h_0 is a work-function of a given material) and $x_{in} = x_1$ and $x_{out} = x_2$ are the inner and outer ends of the barrier (when possible notation from Ref. [118] will be used in this subsection to facilitate comparisons). When power-law exponent $\alpha = 1$, it coincides with the exact triangular barrier at a perfectly smooth planar interface, while arbitrary α corresponds to the rough surface.
The expression for a potential is generalized to the following form:

$$V(x) = h - eF\mathbf{d}_0 x^\alpha - \frac{e^2}{16\pi\epsilon_0\mathbf{d}_0 x^\alpha} \tag{4.2}$$

where x is a dimensionless variable because the dimension of $[m]$ is accounted for by the extra parameter $\mathbf{d}_0$, which serves as a characteristic length scale that influences the

effective electric field in our model. In the context of tunneling through the barrier, $\mathbf{d}_0$ essentially rescales the applied voltage, determining the threshold field. $\mathbf{d}_0$ is a free parameter in this Chapter, providing flexibility in modeling various tunneling barriers without committing to a specific material-dependent value. A smaller $\mathbf{d}_0$ results in a larger effective electric field. Now which can be constructed either by formal mathematical construct of a surface fractal [126] or by boundary condition set by experiment $h = \omega_0 - \omega$ is the height of the effective barrier encountered by the tunneling electron. In the absence of any additional exciting force, it is reduced to the material-characteristic work function ω_0. The theory can be straightforwardly generalized to take into account e.g. photon-assisted field emission when the electron gains an additional energy ω before the tunneling. The choice of potential, although not presuming to describe any specific realization at present, may be justified on physical grounds. This is discussed in detail in Sec. 4.5.1.

4.3   Hypergeometric function solution

Finding an analytical form for an overlap integral is one of the most significant outcomes of this work, as detailed in this section.

The expression of the generalized potential has the form of Eq. 4.2. The decay of the evanescent wave function is now described by the following integral, known as an overlap integral:

$$D(F,h) = \exp\left[-\frac{(8m_e)^{\frac{1}{2}}}{\hbar} \int_{\frac{h}{2eF\mathbf{d}_0}(1-a)^{\frac{1}{\alpha}}}^{\frac{h}{2eF\mathbf{d}_0}(1+a)^{\frac{1}{\alpha}}} \left(h - eF\mathbf{d}_0 x^\alpha - \frac{e^2}{16\pi\epsilon_0 \mathbf{d}_0 x^\alpha} \right)^{\frac{1}{2}} \mathbf{d}_0 dx \right] \qquad (4.3)$$

The integration boundaries are defined by the points where the electron enters and exits the potential barrier:

$$x_{in,out} = \left(\frac{h}{2eF\mathbf{d}_0} \right) (1 \mp a)^{1/\alpha}$$

where

$$a = \sqrt{1 - \frac{F}{(\omega_0 - \omega)^2}} \qquad (4.4)$$

is an auxiliary parameter.

In Eq. 4.3, substituting $\eta = x^\alpha \Rightarrow x = \eta^{\frac{1}{\alpha}} \Rightarrow dx = d\left(\eta^{\frac{1}{\alpha}}\right) = \frac{1}{\alpha}\eta^{\frac{1}{\alpha}-1}d\eta$, we obtain

$$D(F,h) = \exp\left[-\frac{(8m_e)^{\frac{1}{2}}\mathbf{d}_0}{\hbar} \int_{\left(\frac{h}{2eF\mathbf{d}_0}\right)^\alpha (1-a)}^{\left(\frac{h}{2eF\mathbf{d}_0}\right)^\alpha (1+a)} \left(h - eF\mathbf{d}_0\eta - \frac{e^2}{16\pi\epsilon_0 \mathbf{d}_0 \eta} \right)^{\frac{1}{2}} \frac{1}{\alpha}\eta^{\frac{1}{\alpha}-1}d\eta \right] \quad (4.5)$$

Then, substituting with a new variable of integration $\xi = \frac{2eF\mathbf{d}_0}{h}\eta \Rightarrow \eta = \frac{h\xi}{2eF\mathbf{d}_0}$, we have $\eta^{\frac{1-\alpha}{\alpha}} = \left(\frac{h\xi}{2eF\mathbf{d}_0}\right)^{\frac{1-\alpha}{\alpha}}$ and $d\eta = d\left(\frac{h\xi}{2eF\mathbf{d}_0}\right) = \frac{h}{2eF\mathbf{d}_0}d\xi$. Therefore,

$$D(F,h) = \exp\left[-\frac{(8m_e)^{\frac{1}{2}}\mathbf{d}_0}{\hbar} \int_{\left(\frac{h}{2eF\mathbf{d}_0}\right)^{\alpha-1}(1-a)}^{\left(\frac{h}{2eF\mathbf{d}_0}\right)^{\alpha-1}(1+a)} \left(h - eF\mathbf{d}_0\frac{h\xi}{2eF\mathbf{d}_0} - \frac{e^2}{16\pi\epsilon_0 \mathbf{d}_0}\frac{2eF\mathbf{d}_0}{h\xi} \right)^{\frac{1}{2}} \frac{1}{\alpha}\left(\frac{h\xi}{2eF\mathbf{d}_0}\right)^{\frac{1-\alpha}{\alpha}}\frac{h}{2eF\mathbf{d}_0}d\xi \right]$$

$$(4.6)$$

where the borders of integral are $\xi_{in,out} = \left(\frac{h}{2eF\mathbf{d_0}}\right)^{\alpha-1}(1 \mp a)$.

$$D(F,h) = \exp\left[-\frac{(8m_e)^{\frac{1}{2}}\mathbf{d_0}}{\hbar}\int_{\xi_{in}}^{\xi_{out}}\left(h - eF\frac{h\xi}{2eF} - \frac{e^2 \cdot 2eF}{16\pi\epsilon_0 h\xi}\right)^{\frac{1}{2}}\frac{1}{\alpha}\left(\frac{h\xi}{2eF\mathbf{d_0}}\right)^{\frac{1-\alpha}{\alpha}}\frac{h}{2eF\mathbf{d_0}}d\xi\right]$$

$$= \exp\left[-\frac{(8m_e)^{\frac{1}{2}}\mathbf{d_0}}{\hbar}\frac{1}{\alpha}\frac{h}{2eF\mathbf{d_0}}\left(\frac{h}{2eF\mathbf{d_0}}\right)^{\frac{1-\alpha}{\alpha}}\int_{\xi_{in}}^{\xi_{out}}\left(h - eF\frac{h\xi}{2eF} - \frac{e^3 F}{8\pi\epsilon_0 h\xi}\right)^{\frac{1}{2}}\xi^{\frac{1-\alpha}{\alpha}}d\xi\right]$$

$$= \exp\left[-\frac{(8m_e)^{\frac{1}{2}}}{\hbar}\frac{1}{\alpha}\frac{h}{2eF}\left(\frac{h}{2eF\mathbf{d_0}}\right)^{\frac{1-\alpha}{\alpha}}\int_{\xi_{in}}^{\xi_{out}}\left(h - eF\frac{h\xi}{2eF} - \frac{e^3 F}{8\pi\epsilon_0 h\xi}\right)^{\frac{1}{2}}\left(\frac{2\xi}{h}\right)^{\frac{1}{2}}\left(\frac{h}{2\xi}\right)^{\frac{1}{2}}\xi^{\frac{1-\alpha}{\alpha}}d\xi\right]$$

$$= \exp\left[-\frac{(8m_e)^{\frac{1}{2}}}{\hbar}\frac{1}{\alpha}\frac{h}{2eF}\left(\frac{h}{2eF\mathbf{d_0}}\right)^{\frac{1-\alpha}{\alpha}}\int_{\xi_{in}}^{\xi_{out}}\left(h\frac{2\xi}{h} - \frac{h\xi}{2}\frac{2\xi}{h} - \frac{e^3 \cdot F}{8\pi\epsilon_0 h\xi}\frac{2\xi}{h}\right)^{\frac{1}{2}}\xi^{-\frac{1}{2}}\xi^{\frac{1-\alpha}{\alpha}}d\xi\right]$$

$$= \exp\left[-\frac{m_e^{\frac{1}{2}}h^{\frac{3}{2}}}{e\hbar}\left(\frac{h}{2eF\mathbf{d_0}}\right)^{\frac{1-\alpha}{\alpha}}\frac{1}{\alpha}\int_{\xi_{in}}^{\xi_{out}}\left(2\xi - \xi^2 - \frac{e^3 \cdot F}{4\pi\epsilon_0 h^2}\right)^{\frac{1}{2}}\xi^{-\frac{1}{2}}\xi^{\frac{1-\alpha}{\alpha}}d\xi\right]\quad(4.7)$$

using $\frac{e^3 \cdot F}{4\pi\epsilon_0 h^2} = y^2$, we get

$$D(F,h) = \exp\left[-\frac{m_e^{\frac{1}{2}}h^{\frac{3}{2}}}{e\hbar F}\left(\frac{h}{2eF\mathbf{d_0}}\right)^{\frac{1-\alpha}{\alpha}}\frac{1}{\alpha}\int_{\xi_{in}}^{\xi_{out}}\left(2\xi - \xi^2 - y^2\right)^{\frac{1}{2}}\xi^{-\frac{1}{2}}\xi^{\frac{1-\alpha}{\alpha}}d\xi\right]\quad(4.8)$$

As mentioned in Ref. [118], simple polynomials can always be expanded in terms of factors involving their zeros, and it is characteristic of JWKB integral that c and d are the zeros of the quadratic expression in Eq. 4.8. It can be easily confirmed that Eq. 4.8 may be written in the form:

$$D(F,h) = exp\left[-\frac{m_e^{1/2}h^{3/2}}{e\hbar F}\frac{1}{\alpha}\left(\frac{h}{2eF\mathbf{d_0}}\right)^{\frac{1-\alpha}{\alpha}}\int_d^c\xi^{\frac{1-\alpha}{\alpha}}\xi^{-\frac{1}{2}}(c-\xi)^{\frac{1}{2}}(\xi-d)^{\frac{1}{2}}d\xi\right]\quad(4.9)$$

where the last term is an integral sometimes called (up to a pre-factor) the Gamow factor, or [127], [128] principal Schottky–Nordheim barrier function. It reads:

$$I(\xi) = \int_d^c\xi^{\frac{1-\alpha}{\alpha}}\xi^{-\frac{1}{2}}(c-\xi)^{\frac{1}{2}}(\xi-d)^{\frac{1}{2}}d\xi\quad(4.10)$$

The analytic solution of the integral $I(E, F)$ has been found, which is given by a Gauss hypergeometric function:

$$I(F,h) = \frac{\pi\alpha d^{\frac{1}{\alpha}-\frac{3}{2}}\left(2c((\alpha-1)c+d)\,_2F_1\left(\frac{1}{2},\frac{3}{2}-\frac{1}{\alpha};1;1-\frac{c}{d}\right) - \alpha d(c+d)\,_2F_1\left(-\frac{1}{2},\frac{3}{2}-\frac{1}{\alpha};1;1-\frac{c}{d}\right)\right)}{\alpha^2 - 4}\quad(4.11)$$

Here, $I(F, E \equiv h)$ is an *implicit* function of F and h, since $c = \left(\frac{h}{2eF\mathbf{d_0}}\right)^{\alpha-1}(1+a)$ and $d = \left(\frac{h}{2eF\mathbf{d_0}}\right)^{\alpha-1}(1-a)$.

It is not accidentally that the Gamow factor found by us (Eq. 4.11) can be expressed by the function that belongs to the $_2F_1$ family. As it has been previously identified [128], for the case when $\alpha = 1$, the defining equation for Fowler-Nordheim tunneling is indeed the Gauss Hypergeometric ODE. This can be shown manifestly if we rewrite Eq. 4.11 as follows:

$$I(F,h) = \frac{\pi\alpha d^{\frac{1}{\alpha}+\frac{1}{2}}}{\alpha^2 - 4}\left(2((\alpha-1)\frac{c}{d}+1)\frac{c}{d}\,_2F_1\left(\frac{1}{2},\frac{3}{2}-\frac{1}{\alpha};1;1-\frac{c}{d}\right) - \alpha(\frac{c}{d}+1)\,_2F_1\left(-\frac{1}{2},\frac{3}{2}-\frac{1}{\alpha};1;1-\frac{c}{d}\right)\right)$$
$$(4.12)$$

It can now be easily observed that by taking[1] a variable $z \equiv \frac{c}{d}$, the two terms in Eq. 4.12 are in fact two solutions of the hypergeometric ODE:

$$(1-z)zw''(z) + w'(z)(\bar{c} - z(\bar{a} + \bar{b} + 1)) - \bar{a}\bar{b}w(z) = 0 \qquad (4.13)$$

precisely, they are solutions of the second type in the Kummer list of twenty-four solutions [129], namely those of the form:

$$w_{2,1}(z) =_2 F_1\left(\bar{a}, \bar{b}; \bar{a} + \bar{b} - \bar{c} + 1; 1 - z\right)$$

and

$$w_{2,2}(z) = z_2 F_1\left(\bar{c} - \bar{b} + 1, \bar{c} + \bar{a} + 1; \bar{a} + \bar{b} - \bar{c} + 1; 1 - z\right).$$

with the following ODE's parameters

$$\bar{a} = -1/2, \ \bar{b} = -1/\alpha + 3/2, \ \bar{c} = -1/\alpha + 1.$$

Obviously, in our solution $w(z)$ there are distinct terms, e.g., the term $((\alpha - 1)\frac{c}{d} + 1)$ appearing in front of the second solution. This implies that Eq. 4.13 needs to be modified, for instance by changing the expression in front of the $w''(z)$, as $(1-z)z \to (1-z)z/(z+1)$. However, this does not change the number of singular point and it has been proved [130] that every second-order ordinary differential equation with at most three regular singular points can be transformed into the hypergeometric differential equation. Thus WKB problem in general belongs to this class of ODE's. It should be also noted that previously analyzed case $\alpha = 1$ is indeed special, as then some of the terms $\sim (\alpha - 1)$ drop, and the differential equation is simpler, namely, it does not contain the "damping" term $\sim w'(z)$. We thus see that a simpler ODE identified in Ref. [128] with solution Eq. 3.34 is a special case and for any further quasi-classical analysis of the tunneling mechanism (for instance, with time dependence), one should use ODE identified by us, Eq. 4.13.

4.4 Results: Illustration

Returning to observable quantities, an overlap quantity $D(F, h)$ is defined:

$$D(F, h) = \exp\left[-\left(\frac{m_e^{\frac{1}{2}}}{e\hbar}\right)\left(\frac{h^{\frac{3}{2}}}{F}\right)\left(\frac{h}{2eF\mathbf{d}_0}\right)^{\frac{1-\alpha}{\alpha}}\left(\frac{1}{\alpha}\right)I(F, h)\right] \qquad (4.14)$$

The results of the previous section can now be put together, and the transmission probability can be expressed in the following way:

$$\mathcal{T} = \frac{1}{1 + D^{-1}(F, h)} \qquad (4.15)$$

which will be used in the following to generate the results. This expression, which is a modification of standard WKB [127], [131] that suits better concave barriers with a single turning point, has been derived for the first time in Ref. [117]. In Ref. [132] it was shown

---

[1]Taking $z \equiv \frac{c}{d}$ implicitly assumes that c/d can vary while d can stay constant which is *mathematically* sound but *physically* hard to reconcile with the fact that the external electric field F is the quantity that one can easily change, which affects equally both c, d. However, $c = x_{out}$ is mostly determined by external fields and one can imagine protocols where only x_{out} varies keeping x_{in} intact.

that when the top of the tunneling barrier can be approximated by a parabola, then the $\mathcal{T} = 1/2$ holds for the energy of an electron right on the top of the barrier and the Eq. 4.15 (derived due to improved "hydrodynamic" connection formulae [117]) reproduces this result. The formula, Eq. 4.15, has been recently extensively benchmarked against Hill-Wheeler, Wong and exact quantum mechanical solutions in Ref. [116] showing that Kemble's result can be used for the tunneling process both below and above the barrier top. Details are explained in Chapter 3.

4.4.1 Comparison with the elliptic integrals solution

We are now comparing Eq. 4.14 for the general case obtained by us and Eq. 3.33 for the known special elliptic integrals: by definition, they must coincide when $\alpha = 1$. In this case, the value of the expression $\left(\frac{h}{2eF\mathbf{d}_0} \right)^{\frac{1-\alpha}{\alpha}}$ becomes 1, since $\alpha = 1$. However, in the plots presented later in this chapter (except Fig. 4.5), we set $\mathbf{d}_0 = 1\text{Å}$. If energy h is measured in $[eV]$ then the term $F\mathbf{d}_0$ needs to be in $[V]$ since only then the extra pre-factor $\left(\frac{h}{2eF\mathbf{d}_0} \right)$ with non-universal power $\frac{1-\alpha}{\alpha}$ is dimensionless. Thus, choosing the $\mathbf{d}_0 = 1\text{Å}$ sets the characteristic scale of electric field as $[V/\text{Å}]$. Actually, this choice of $\mathbf{d}_0 = 1\text{Å}$ falls very close to the length scale defined by the second FN constant B in Eq. 3.23.

The comparison is made to assess the quality of our new formula since the exact solution is known and widely used in terms of these elliptic integrals. The result of this comparison is presented in Fig. 4.2. Indeed, the new function works very well as the surfaces perfectly overlap for all regimes of the external field F and applied photon energy.
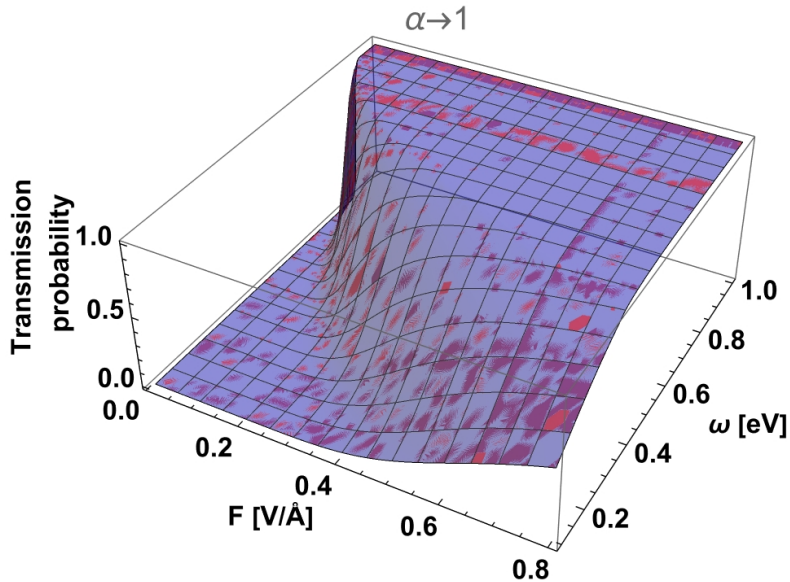
Figure 4.2: Transmission probability as computed by our general formula, Eq. 4.11, (in the case when $\alpha = 1$), in red, and previous result that has been expressed as the elliptic integrals, Eq. 3.34, in blue. Perfect overlap of the two opalescent surfaces results in a single surface with purple color.

4.4.2 Transmission probability dependence on α

Thanks to the fact that we have the generalized formula, now we can explore how the tunneling probability depends on α.

In Fig. 4.3, the transmission probability was obtained by our general formula, when α is below 1 and when it is above 1 ($\alpha = 0.3, 0.5, 0.8, 1.2, 1.5, 1.8$). As can be seen, the overall shape of the tunneling probability changes substantially. For small values of α, the transmission probability changes sharply, for instance, when $\alpha = 0.3$, there is a very big region where transmission probability is 0, and a very big region where it is 1.

For the larger values of $\alpha(> 0.75)$, the transmission probability seems to be changing more gradually: the slope of T varies slowly as a function of both external field F and energy ω. It should be taken into account that the ω is proportional to, e.g., photon energy that is capable of shifting the chemical position and thus the effective barrier h (Fig. 4.1). E.g., when $\alpha = 0.8$, there is a region where transmission probability is equal to 0, then, at a small region of work function or height of the potential, it smoothly elevates from 0 to 1 and there is also a very big region where it is equal to 1. Furthermore, when $\alpha > 1$, an extra edge appears at larger ω. If an experiment studying photon-assisted field emission with light of varied frequency is performed, a response with a singularity is expected for $\alpha < 0.75$, a smooth peak for intermediate values of α, and a smaller singularity as a satellite of a broad peak response for $\alpha > 1.5$.

To investigate this effect further, in Fig. 4.4 the three-dimensional image of the transmission probability dependence on α and F is shown when effective barrier ($\omega_0 - \omega$) is constant and equal to (a) $0.4eV$, (b) $0.55eV$, (c) $0.75eV$, and (d) $0.9eV$ accordingly. In all cases, α ranges from 0.1 to 2.5, and the profiles shown in the bottom panel are for the case when $F = 0.5V/\text{Å}$. A small barrier indicates a broad range of field, with $T = 1$, while a big barrier means a small range of field, with $T = 1$, intending a large area with $T = 0$. The area of small T is always favoured by small α (and small F).

There are clearly two regimes: one where the transmission probability dependence is decreasing and the other where it is increasing as a function of α, and there is a critical line between these two regimes, where the quantity is independent of the values of α.

If we have a method of varying α in a controlled manner, for instance, by applying stress to an array of nanotubes (see the next chapter), then T will also change. But it is not obvious which way. Making potential more shallow (i.e., increasing α), can both increase and decrease T depending on the tunneling barrier. F_{ext} can even be varied to pin the point at which α dependence is not present; in this way, an independent measure of work function can be obtained. The absence of α dependence would mean zero amplitude of some IR peaks, therefore this diagnostic tool is feasible.

Figure 4.5 illustrates the influence of $\mathbf{d}_0$ on the transmission probability when $\alpha = 0.8$ and $F = 0.8V/\text{Å}$. As shown in the figure, the dependence on $\mathbf{d}_0$ is relatively weak and becomes even less significant as $\mathbf{d}_0$ increases. Notably, the frequency dependence remains qualitatively similar across different $\mathbf{d}_0$ values. At high frequencies, where the transmission probability approaches 1, the influence of $\mathbf{d}_0$ becomes negligible. Thus, the $\mathbf{d}_0$ dependence is primarily observed at lower frequencies, where the transmission probability has not yet reached 1.
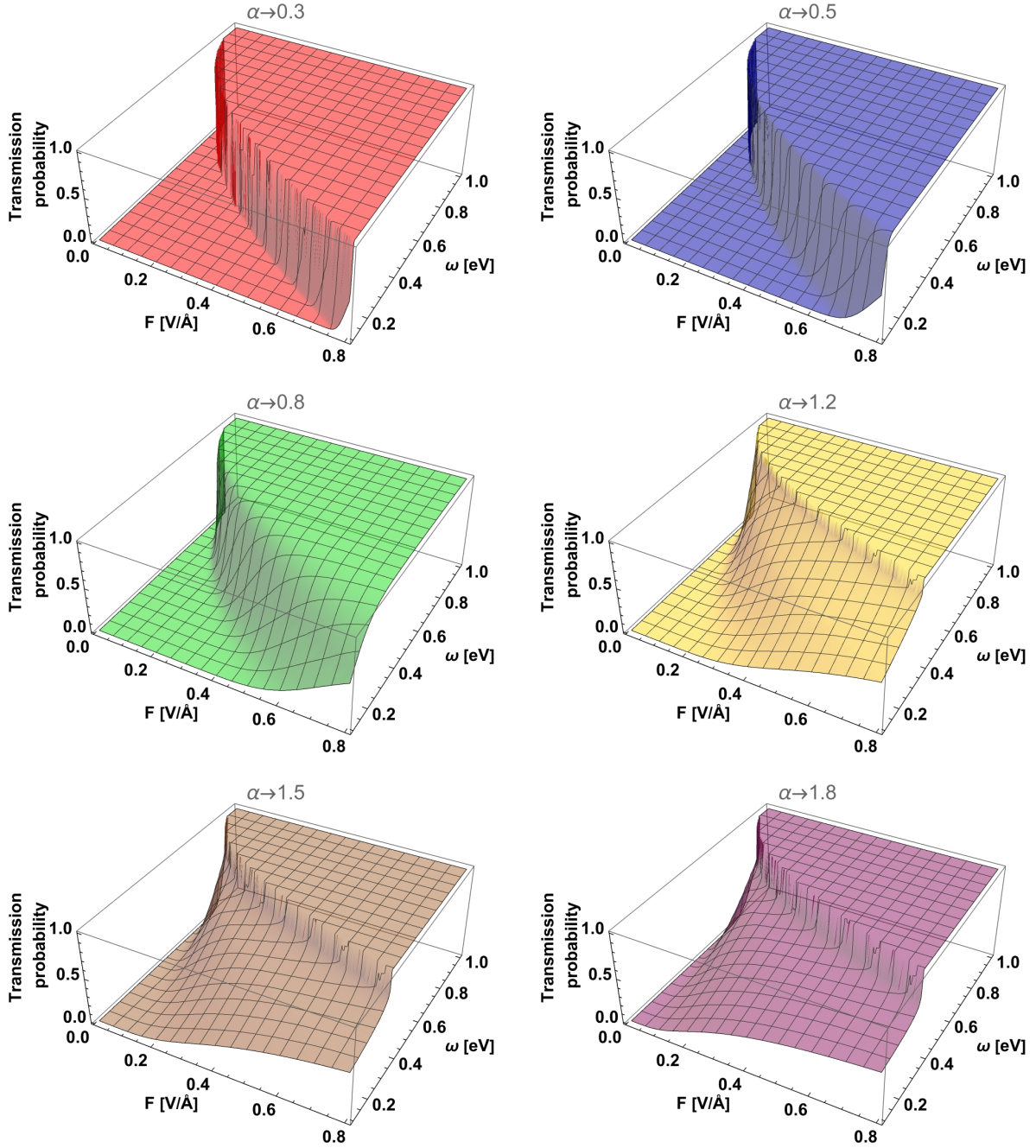
Figure 4.3: Transmission probability calculated by the new general formula expressed by Hypergeometric function for the cases (left to right, top to bottom) when $\alpha = 0.3$ (red), $\alpha = 0.5$ (blue), $\alpha = 0.8$ (green), $\alpha = 1.2$ (yellow), $\alpha = 1.5$ (brown), $\alpha = 1.8$ (purple). Here, and in all the following plots (except Fig. 4.5) in this Chapter, $\mathbf{d}_0 = 1\text{Å}$

.

4.4.3   Contributions from various areas of the surface

We have also been able to simulate a surface with spatially varying emission properties. The most general form of emission for a two-component surface reads:

$$\mathcal{T}_{tot} = s_1 \mathcal{T}(F, E; \alpha_1)\Big|_{E=\omega_{01}-\omega} + s_2 \mathcal{T}(F, E; \alpha_2)\Big|_{E=\omega_{02}-\omega} \tag{4.16}$$
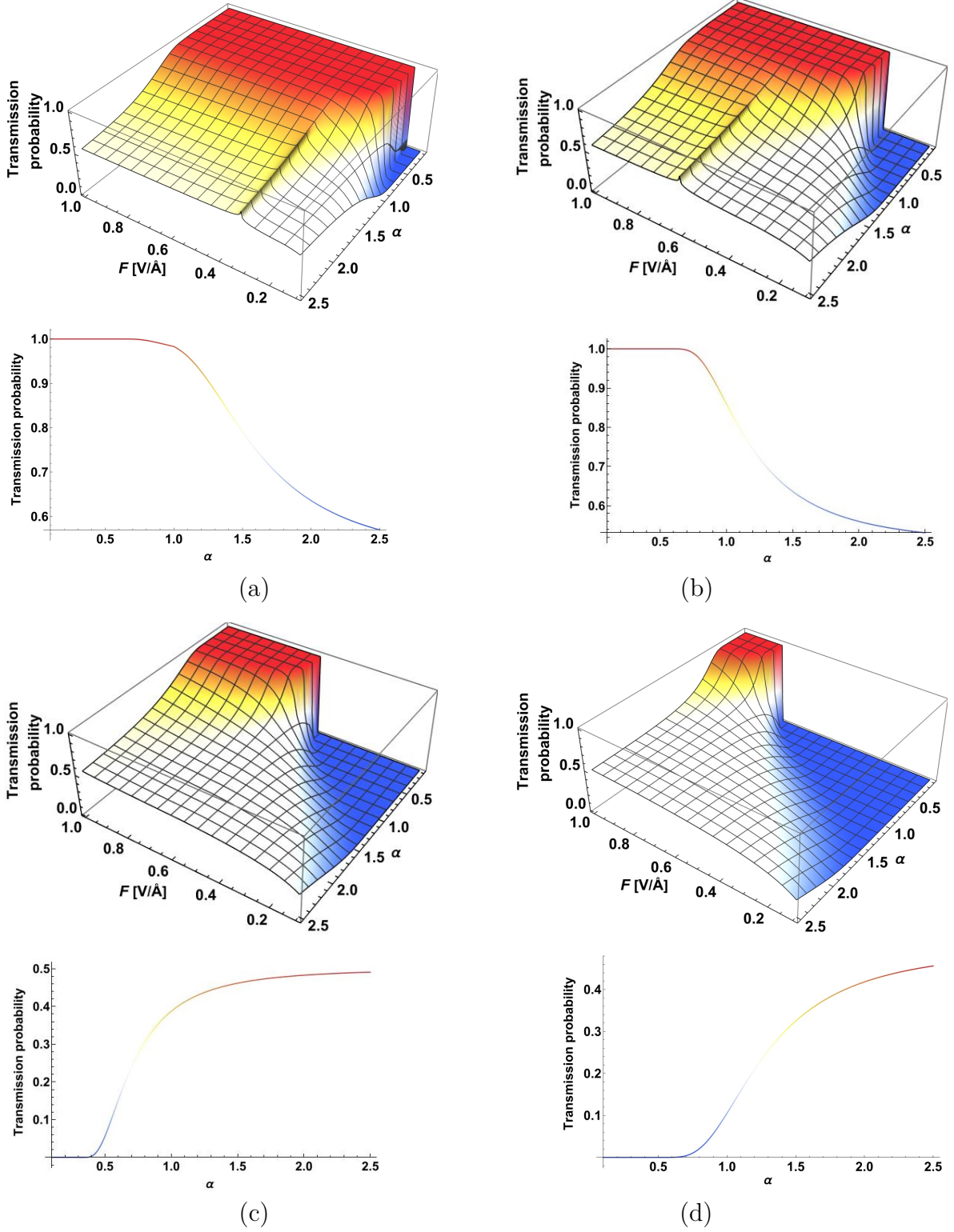
Figure 4.4: The transmission probability dependence on α, when effective barrier is (a) $0.4eV$ (b) $0.55eV$ (c) $0.75eV$ (d) $0.9eV$ and α changes from 0.1 to 2.5. Profiles in the corresponding bottom panels are shown in the case of $F = 0.5V/\text{Å}$.

where $\mathcal{T}(F, E; \alpha_i)$ is given by Eq. 4.15 parameterized by a given α_i. For instance, a corrugated metallic surface (see Sec. 4.5.1) can produce the effect of varying exponent α. From the electrostatics textbook, we know that the electrostatic potential behaves
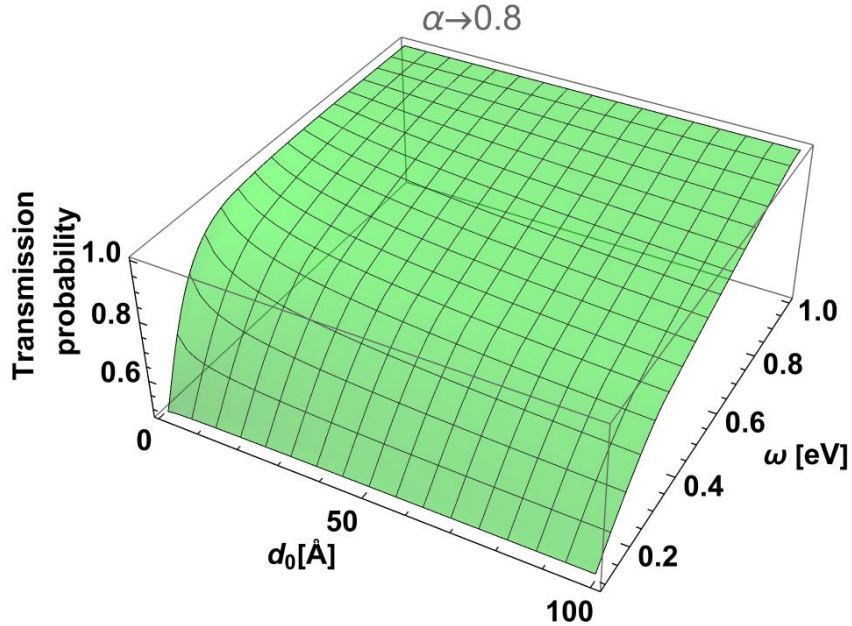
Figure 4.5: Transmission probability dependence on $\mathbf{d}_0$ and ω, calculated by Eq. 4.14, when $\alpha = 0.8$, $F = 0.8 V/\text{Å}$.

like $x^{\pi/\gamma}$, where γ is the outer angle of the surface. Thus for flat surface, one has x^1 (as usual), the convex part with $\gamma < \pi$ will result in $\alpha > 1$, while the concave part $\gamma > \pi$ will have $\alpha < 1$ (and thus singularity of a derivative of the potential i.e., the electric field amplitude). It is straightforward to realize that the wrapped surface will contain both concave and convex regions. Then it is expected that $\gamma_1 \approx \pi - \gamma_0$ and $\gamma_2 \approx \pi + \gamma_0$ (where γ_0 is deviation from flat situation). In order to match the experimental situation, different area proportions of these regions (and possibly their different densities of states) can be assumed, and the change in the total emission current can be observed.

In Fig. 4.6 the transmission probability from the composite surface is presented. Here, for illustrative purposes, the simplest situation will be considered first, where both contribute equally, i.e. $s_1 = s_2 = 1/2$.

$$\mathcal{T}_0 = \frac{1}{2}\mathcal{T}(F, E; \alpha_1)\Big|_{E=\omega_{01}-\omega} + \frac{1}{2}\mathcal{T}(F, E; \alpha_2)\Big|_{E=\omega_{02}-\omega} \tag{4.17}$$

Two distinct situations are considered: the work functions ω_{0i} of the two components are either equal or different from each other. In Fig. 4.6 (a), concave and convex regions have $\alpha_1 = 0.8$ and $\alpha_2 = 1.8$, respectively, and $\omega_{01} = \omega_{02} = 1eV$. Here $\mathcal{T}(E)$ is a monotonically increasing function of F, as expected from the continuously increasing Gamow factor. There are only small, subtle differences in comparison with an average $\bar{\alpha} = 1.4$ case: the intermediate $\mathcal{T}(E)$ range is smaller, and its increase is smoother and more concave. In Fig. 4.6 (b) ($\alpha_1 = \alpha_2 = 0.8$ and $\omega_{01} = 0.9eV$, $\omega_{02} = 1eV$) and (c) ($\alpha_1 = \alpha_2 = 1.8$ and $\omega_{01} = 0.9eV$, $\omega_{02} = 1eV$), there is situation where the two regions have the same values of α and different values of work function. As shown in the figures, when $\alpha < 1$ (Fig. 4.6 (b)), the edge of transmission probability is still sufficiently sharp because of the smaller value of α; while in the case when $\alpha > 1$ (Fig. 4.6 (c)), the transmission probability is spread more. In both cases, double-edge structures occur due to two different work functions. As regards Fig. 4.6 (d), where $\alpha_1 = 0.8$, $\omega_{01} = 1eV$ and $\alpha_2 = 1.8, \omega_{02} = 0.9eV$, we have both different α and ω_0 and the figure demonstrates an initial sharp transmission due to the lower α followed by a broader spread to the higher value of α, highlighting

the interactions between these surface characteristics. A double-edge structure is indeed obtained due to the two different work functions of the surface.

A situation when local work functions are different on different areas on the surface may be induced by different crystallographic orientations on the surface (hence differences in surface electric dipole moment), but can also be induced by many-body effects (e.g. CDW formation). It is observed that the double edge is particularly well visible in the regime of small ω (deep inside the well) and large enough external field. In our calculations, it was also discovered that the double edge is well pronounced when $\alpha_1 < \alpha_2$ and $\omega_{01} > \omega_{02}$, but much less pronounced in the opposite case when $\alpha_1 < \alpha_2$ and $\omega_{01} < \omega_{02}$.

In the context of analyzing transmission probabilities from various surface areas, the situations were also discussed when

$$\mathcal{T}_1 = \frac{1}{4}\mathcal{T}(F, E; \alpha_1)\Big|_{E=\omega_{01}-\omega} + \frac{3}{4}\mathcal{T}(F, E; \alpha_2)\Big|_{E=\omega_{02}-\omega} \tag{4.18}$$

$$\mathcal{T}_2 = \frac{3}{4}\mathcal{T}(F, E; \alpha_1)\Big|_{E=\omega_{01}-\omega} + \frac{1}{4}\mathcal{T}(F, E; \alpha_2)\Big|_{E=\omega_{02}-\omega} \tag{4.19}$$
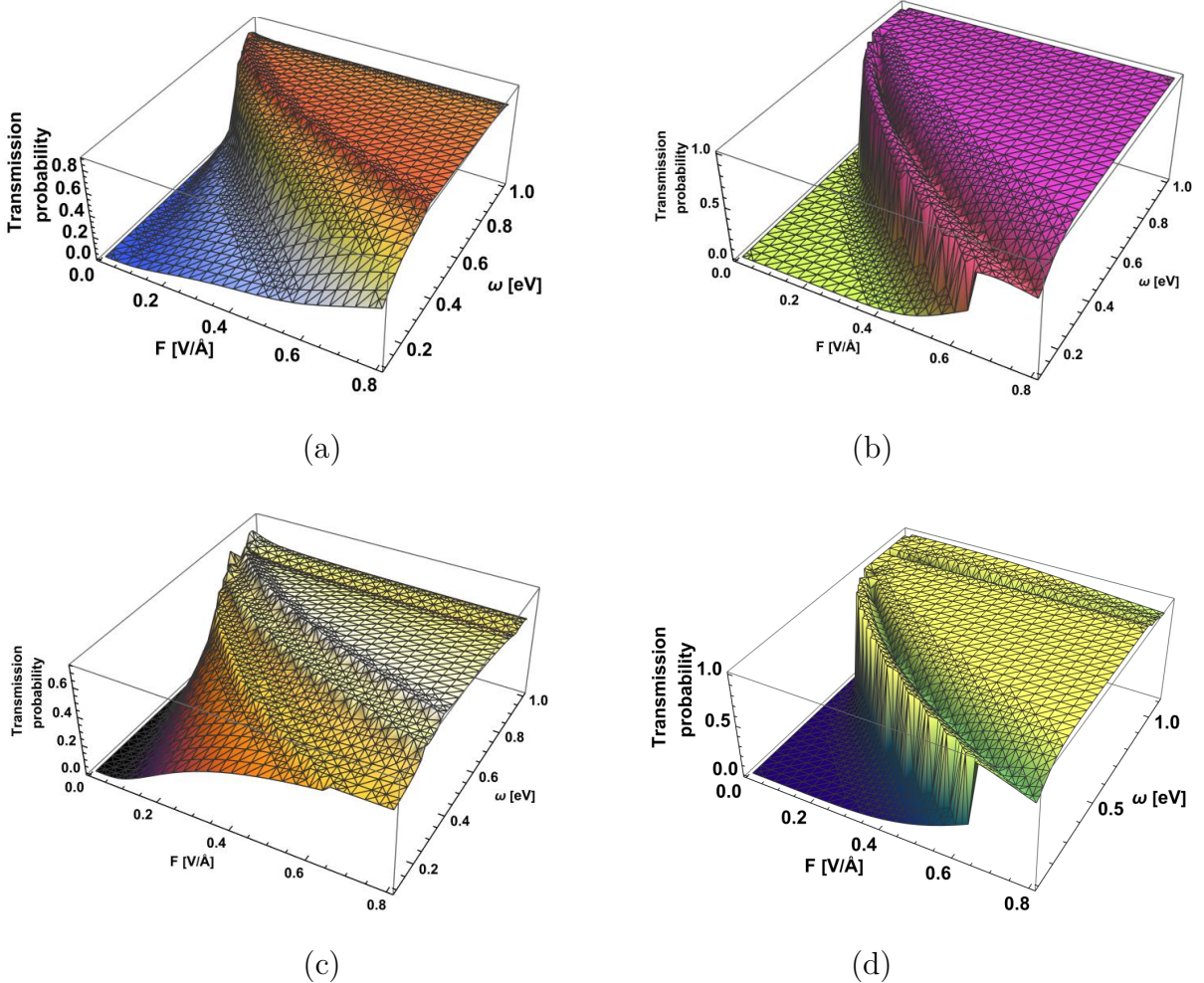
Figure 4.6: The transmission probability with the composite surface computed by Eq. 4.17, when (a) $\alpha_1 = 0.8, \alpha_2 = 1.8$ and $\omega_{01} = \omega_{02} = 1eV$, (b) $\alpha_1 = \alpha_2 = 0.8$ and $\omega_{01} = 0.9eV$, $\omega_{02} = 1eV$, (c) $\alpha_1 = \alpha_2 = 1.8$ and $\omega_{01} = 0.9eV$, $\omega_{02} = 1eV$, (d) $\alpha_1 = 0.8$, $\alpha_2 = 1.8$, and $\omega_{01} = 1eV$, $\omega_{02} = 0.9eV$.
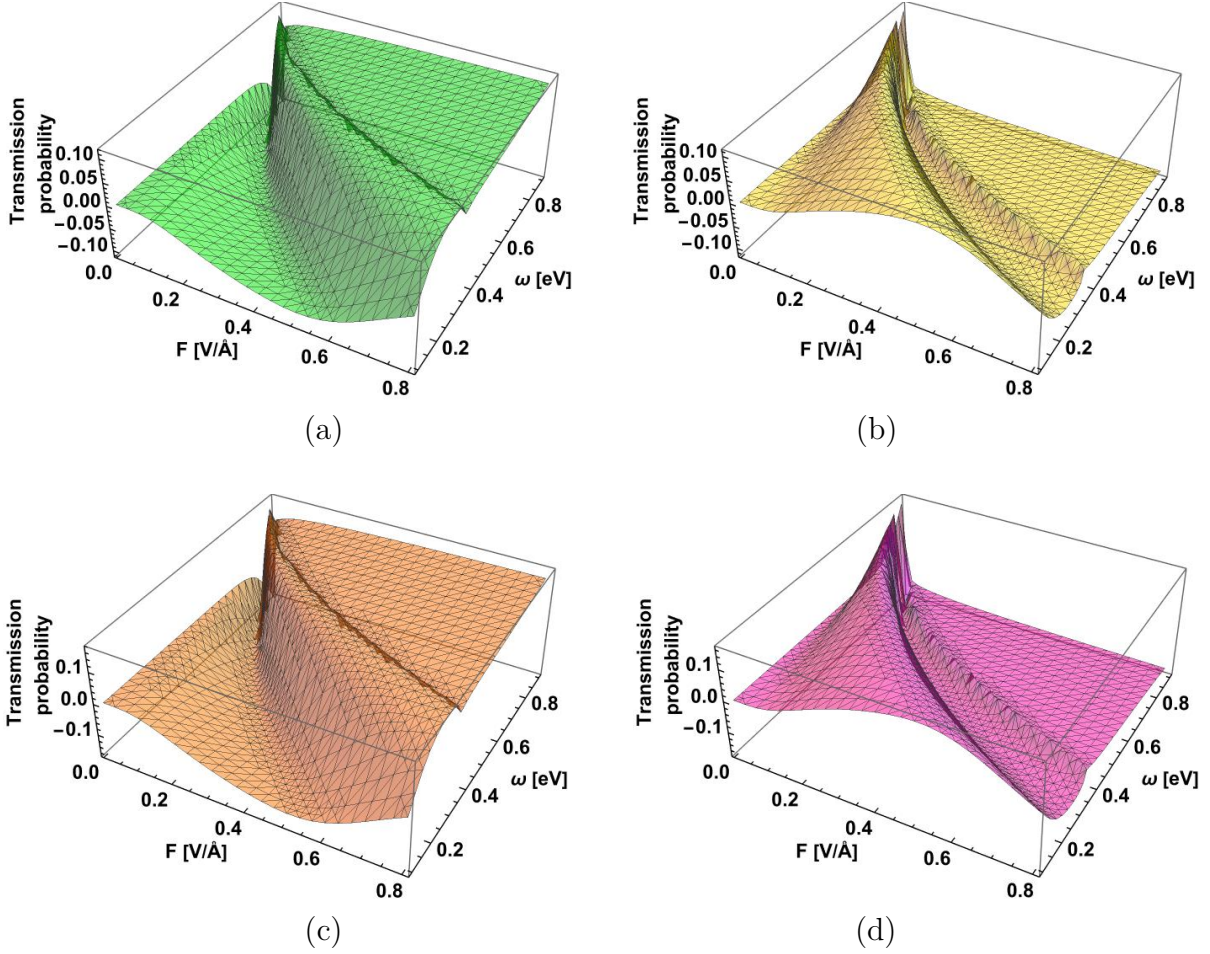
Figure 4.7: The subtraction between (a) T_0 (Eq. 4.17,) and T_1 (Eq. 4.18), (b) T_0 (Eq. 4.17) and T_2 (Eq. 4.19), (c) T_0 (Eq. 4.17,) and T_3 (Eq. 4.20), (d) T_0 (Eq. 4.17,) and T_4 (Eq. 4.21), when $\alpha_1 = 0.8, \alpha_2 = 1.8$ and $\omega_{01} = \omega_{02} = 1eV$.

$$\mathcal{T}_3 = \frac{1}{8}\mathcal{T}(F, E; \alpha_1)\Big|_{E=\omega_{01}-\omega} + \frac{7}{8}\mathcal{T}(F, E; \alpha_2)\Big|_{E=\omega_{02}-\omega} \tag{4.20}$$

$$\mathcal{T}_4 = \frac{7}{8}\mathcal{T}(F, E; \alpha_1)\Big|_{E=\omega_{01}-\omega} + \frac{1}{8}\mathcal{T}(F, E; \alpha_2)\Big|_{E=\omega_{02}-\omega}. \tag{4.21}$$

Fig. 4.7 (a) shows the difference between T_0 (Eq. 4.17,) and T_1 (Eq. 4.18), and Fig. 4.7 (b) shows the difference between T_0 (Eq. 4.17,) and T_2 (Eq. 4.19), (c) shows the difference between T_0 (Eq. 4.17,) and T_3 (Eq. 4.20), (d) shows the difference between T_0 (Eq. 4.17,) and T_4 (Eq. 4.21), as T_0 is taken as the *reference* level. It is essential to note that $\mathcal{T}_0 - \mathcal{T}_1 = -(\mathcal{T}_0 - \mathcal{T}_2)$ and $\mathcal{T}_0 - \mathcal{T}_3 = -(\mathcal{T}_0 - \mathcal{T}_4)$. Studying such a relative change makes sense from experimental point of view: changing orientation of external electric field makes some cross sections on corrugated surface more likely to emit. By measuring the difference we shall obtain a signal similar to the one presented in Fig. 4.7. Please note that, if one crystal facet can be passivated faster than another, then the ω_{0i} and α_i parameters will be gradually modified, a process that only analytical formula can easily capture.

As it is observed from the Fig. 4.7, cases (a) and (c) possess similar behaviour: initially, the *relative change* of transmission probability is close to zero, it is simply because the

$T(\omega, F) = 0$ in this regime. As ω increases slightly, the relative change of transmission probability enters a concave region, indicating minimal or slightly decreasing values. With further growth of ω, the relative change of transmission probability increases, forming a convex shape. The relative change of transmission probability reaches its maximum at a specific range of ω and F. Identifying this line and extracting it from experimental data can serve as an important tool to diagnose the emitting surface. Beyond this peak, further increases in F cause the relative change of transmission probability to decline down to zero – the unitary transmission regime is reached for all values of parameters. Just like before we had a double ridge structure due to two types of the surface, now we see that changing the proportion indeed reduces one of the ridges with respect to another, thus confirming our conjecture.

Remarkably, in all cases, we observe a peak of the relative change of $T(\omega, F)$ in the regime when the transition from small to large $T(\omega, F)$ takes place for the smallest external electric field F (this is for large ω, i.e., when chemical potential is close to the barrier top). We see that in this regime the measured signal is very fragile, susceptible to the details of the surface, which can be prohibitive for some applications (that require stable electron beams over a long time), but beneficial for applications when a small external field is supposed to affect the signal (for example vacuum electronics).

Similarly, in both figures (b) and (d), the *relative change* of transmission probability starts at zero. As the ω and F increase, the relative change of transmission probability rises, creating a bulging effect. This is followed by a recessing phase where the relative change of transmission probability decreases. Subsequently, there is another phase of increase, forming a second bulge. Finally, the relative change of transmission probability subsides to zero at higher values of ω and F.

In the expression provided above (Eq. 4.16), the constant featureless density of states (DOS) is assumed for the entire 2D surface. In fact, this needs to be substituted by independently computed material-specific data, e.g. calculated using *ab initio* methods. Examples of material-specific local density of states (LDOS) will be given in the following chapters of this thesis. Nevertheless, our formula plays an important role as any DOS has to be multiplied by our result to obtain a measurable quantity. This allows us to distinguish the proportion of each phase, with different ω_{0i}, on the surface, and possibly even determine the phases that sit on the convex and concave structures.

4.4.4 Comparison with numerical methods

The problem of tunneling through a barrier is frequently solved numerically, using the scattering matrix (or related transfer matrix) technique. Here a small comparison will be made between those methods and our analytic formula using a light-matter equivalence [133]. The numerical analysis is based on the two-dimensional Fourier Modal Method with the implementation of the scattering matrix algorithm and proper factorization rules, extended to multilayer structures [134]. First, it should be noted that any transfer matrix-type method improves with an increasing number of sub-systems and ultimately becomes an ideal approximation in the limit where one divides the potential into an infinite number of slabs, i.e., there is an infinite multiplication of matrices involved. Of course, this is impossible from the numerical viewpoint, but it has been shown [135] that this limit is actually *equivalent* to the WKB solution, *provided* the off-diagonal reflection coefficients are neglected.

From this fact, two conclusions can be drawn. Firstly, the smoother shape of the potential, the smaller internal reflectivity, the better WKB will work. This implies that WKB should not be used for tunneling through a potential barrier hosting resonant level sub-systems, e.g. quantum dot or ad-atom on the surface, or to be more precise, WKB could be used only for each sub-system separately and then their transfer matrices combined. Secondly, in order to make a comparison with the scattering matrix approach, it is necessary to take into account multiple events when the carrier is scattered back (twice) into the barrier and only after that is transmitted. At present all scattering formalism by default includes these corrections, as does the approach introduced in Ref. [136] with which we compare.

Fortunately, the reflection coefficient can also be easily deduced from our result, since $R(F, \omega) = 1 - \mathcal{T}(F, \omega)$. Thus, a series of higher order transmission terms can be constructed:

$$\mathcal{T} = \mathcal{T}_{WKB} + R^2 \Upsilon^2 \mathcal{T}_{WKB} + R^4 \Upsilon^4 \mathcal{T}_{WKB} + ... \qquad (4.22)$$

which can be re-summed as a geometric series. Above, an additional factor Υ was introduced that describes the wavefunction decay as it propagates. For the waves above the barrier, or very close to the barrier top it is expected that $\Upsilon = 1$, but deep inside the barrier, for evanescent wave solution it is expected that $\Upsilon \to 0$ and there indeed pure WKB works well (see Fig. 4.8).

In Fig. 4.9, a comparison of the numerical method with the zeroth order WKB result and such a re-summation with $\Upsilon = 1$ is shown. It is observed that the re-summation of the geometrical series allows us to establish quite good correspondence between the numerical and analytical methods for larger ω. In the range of the highest transmissions, the numerical method reveals the presence of oscillations that are due to the quantum interference effect.

Our method cannot capture these, however, an extension in this direction could be possible in principle. In any case, the effect turned out to be tiny for our power-law barriers. There are also advantages of the exact analytical WKB formula: since the result is given

(a)   (b)
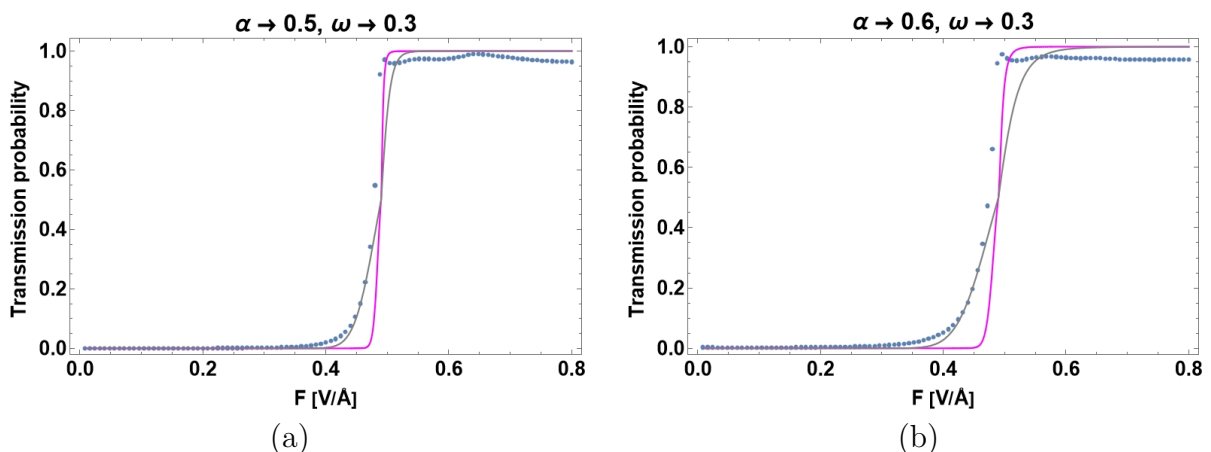
Figure 4.8: The transmission probability comparison between numerical and analytical solutions: the blue points indicate the scattering matrix method calculation with 20 slabs, the pink line indicates the WKB solution considering the internal reflections, and the grey line shows the pure WKB solution. (a) $\alpha = 0.5$, $\omega = 0.3$, and (b) $\alpha = 0.6$, $\omega = 0.3$.
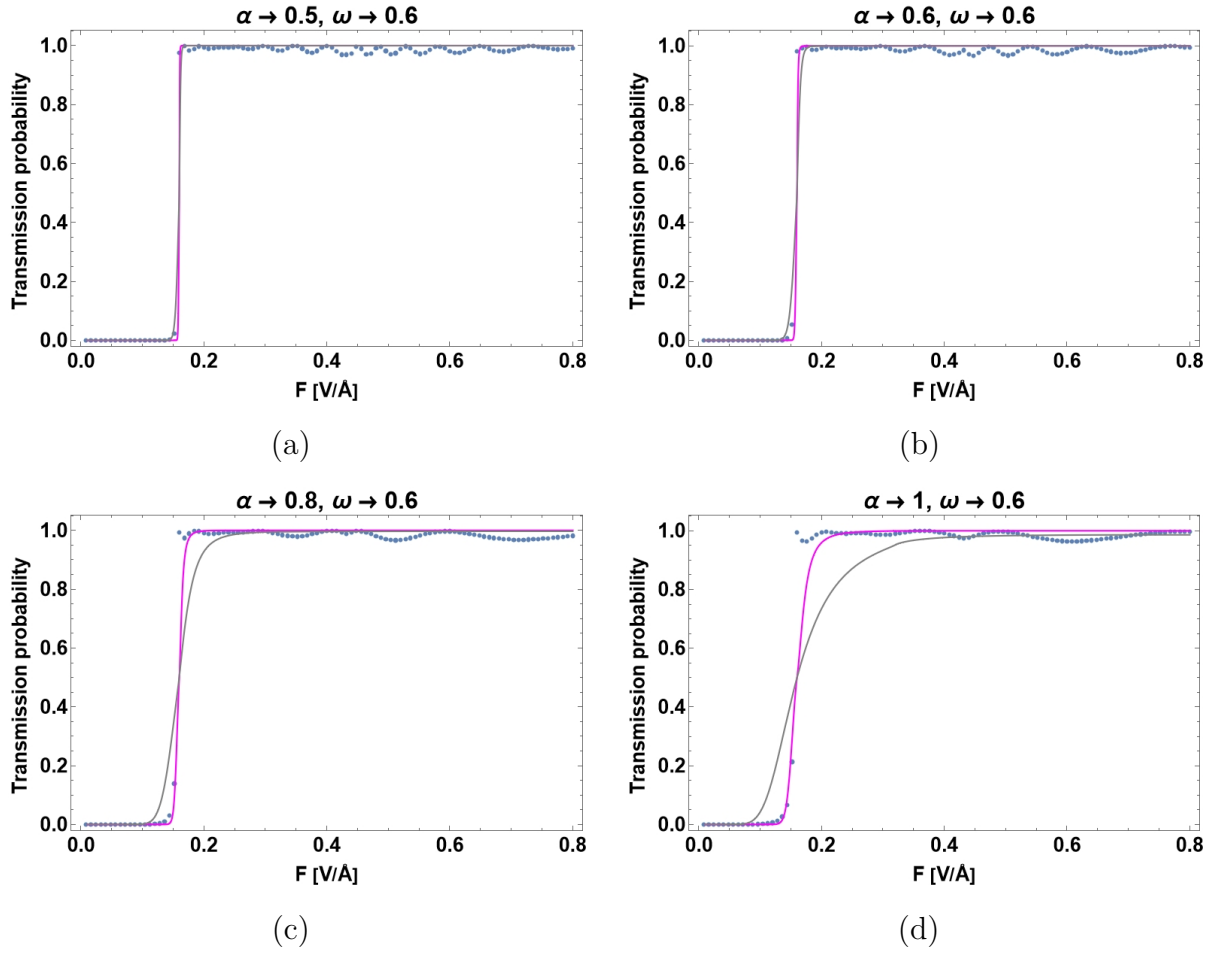
Figure 4.9: The transmission probability comparison between numerical and analytical solutions: the blue points indicate the scattering matrix method calculation with 20 slabs, the pink line indicates the WKB solution considering the internal reflections, and the grey line shows the pure WKB solution. (a) $\alpha = 0.5$, $\omega = 0.6$, (b) $\alpha = 0.6$, $\omega = 0.6$, (c) $\alpha = 0.8$, $\omega = 0.6$, and (d) $\alpha = 1$, $\omega = 0.6$.
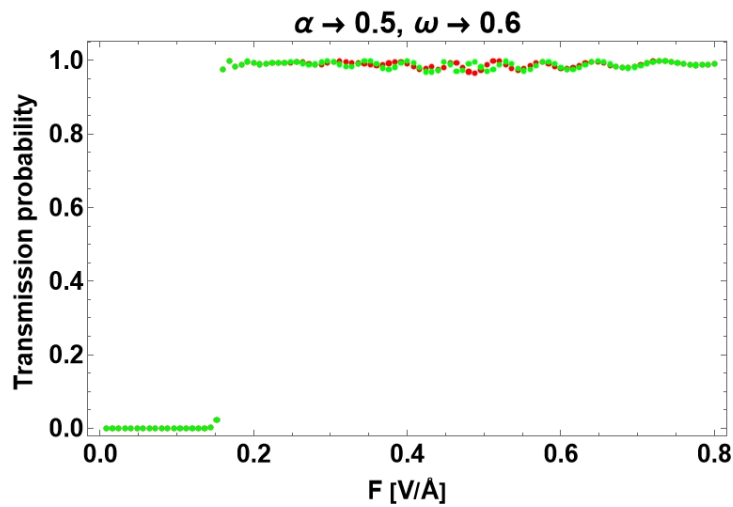
Figure 4.10: The transmission probability calculated by scattering matrix method: red points indicate calculation with 5 slabs and green ones with 20 slabs.

as a single special function (i.e., there is no demand for a final summation of a series or a convolution of special functions) its computational cost is negligible, comparable to a few matrix multiplications. For the numerical method, it is observed that the result becomes stable when ~ 20 slabs are taken (see Fig. 4.10), moreover one needs to be prudent with numerical stability of the matrix multiplication. Finally, it is a challenge to compute numerically data that would generate an analogue of Fig. 4.4, which is particularly relevant for systems where α may change in the course of experiment, such as sputtering phenomena mentioned in the introduction.

4.5 Discussion

4.5.1 Experimental relevance

Due to its technological importance, the research field of field emission applied theory is extremely broad. While the largest amount of work is done purely numerically, we ought to point out works where an analytical approach to external potential has been used, and in fact, there have been many. A literature search solely for the case of the ellipsoidal tip reveals cases, where the potential has been approximated either as an ellipsoid [137] (with logarithmic dependence $V(r)$) or a power series in term of Legendre functions [138]. An extensive list of such analytical potentials has been given in Ref. [139]. The need for these works was due to the fact that the authors wished to have an insight in how parameters of the potential affect the transmission, hence a similar motivation to ours, however, the last WKB integral was always performed numerically. In our work, we *assume* a given shape of the potential to get a closed analytical formula for the final result – the transmission itself. We cannot presume to achieve similar detail description of potential as the above mentioned works, dedicated to this subject. However, we wish to point out a few arguments showing that our assumption is actually plausible, certainly not unrealistic.

Metallic surfaces

If the surface is metallic, the knowledge from basic electrostatics can be used to predict power law behavior in its vicinity. In terms of a wrapped metallic surface, it is stated in electrostatic textbooks [e.g. Jackson, Chap.2.11 [140]] that the power law of external potential depends on the angle of each metallic corner. In general, the following power law of electric field is expected: $x^{\pi/\beta}$. For elevated areas, with corner angles larger than π we then expect a behaviour like r^α with $\alpha < 1$, hence faster decay of external field (but definitely as a power law). In the extreme case of the sharp tip, we have $\beta = 2\pi \Rightarrow \alpha = 1/2$ which is the smallest possible value of α for an entirely metallic 2D surface. On the other hand, for lower (convex) areas the corner angles are smaller than π and so we now expect a behaviour like r^α with $\alpha > 1$ for the external field. The image potential, the other term in Eq. 4.2, will also change depending on surface corrugation: when an electron approaches narrow, fine corners, it is necessary to introduce more (artificial) image charges. This corresponds to dipolar and quadrupolar moments, resulting in the potential diverging faster than $1/r$. Overall, the spatial dependence of

both terms, the external field and image potential change, but in both cases these changes can potentially be captured by our formula Eq. 4.2.

Other, non-metallic surfaces

In the above-given situation, a purely metallic but corrugated surface was considered where the elementary electrostatic solution is readily accessible. In general, two coexisting phases on the surface can be assumed: a dielectric and a metal. The details will depend on the system under consideration, but a few general remarks can be made. For the dielectric, e.g. a layer of an oxide gradually covering all available areas, it is probable that a fractal structure will be encountered, with a partial (Hausdorf) dimension which upon averaging will lead to varying dielectric constant $\epsilon(x)$ that goes down to ≈ 1 as we move towards the outside medium. In the effective medium approximation, the local $\epsilon(x)$ will be proportional to the surface coverage of the dielectric (within a given cross-section) which leads to a power-law dependence $\epsilon(x) \sim x^b$. Naturally, this will affect both ingredients in the interaction part of the Hamiltonian: the image potential will be rescaled by a factor $1/\epsilon(x)$, while the external potential will be rescaled by a factor $\epsilon(x)$. This simply means that in the absence of corrugation, but in the presence of the oxide layer, one should take $\alpha = 1 + b$.

The reasoning can also be extended to the case when the kinetic energy part of the Hamiltonian varies in the direction perpendicular to the surface. As shown in Ref. [126], through a proper substitution of the x-variable we can rewrite the system with varying content of metallic phase (again as a fractal) or a system with a varying mass $m(x)$ into the form Eq. 4.2, hence our formalism should be also applicable.

4.5.2 The case of $\alpha = 2$ and connection with an exact quantum solution

It is observed that the expression we found, Eq. 4.11, suffers from a singularity when $\alpha = 2$. Numerical studies allowed us to check that any small deviation $\pm\epsilon \to 0$ removes instability and produces a sensible result. Hence, only the case $\alpha = 2$ requires a separate insight. Firstly we note that the $1/x^2$ potential well is known [141] to be a pathological case. When the Schrödinger equation for the inverse square potential is written as:

$$\nabla^2 \psi + (1/x^2 - f) = 0 \tag{4.23}$$

The authors of Ref. [141] showed that the presence of the external force f introduces a natural energy scale in the problem, which regularizes it. It is not a pathological problem any longer (in the sense that a unique, self-adjoint ground state can be found) and, actually, it admits an exact analytic solution in terms of Kummer and Triconi functions (see below). Thus the well-defined quantum states can be defined only by imposing a UV cut-off in the problem and adding extra boundary condition for a derivative.

The need to add a derivative boundary condition implies that one must go beyond the WKB to remove the singularity. Quite remarkably, when $\alpha = 2$ the Eq. 4.11 actually *simplifies*, as now the second index of hypergeometric functions equals to one:

$$_2F_1\left(\frac{1}{2}, \frac{3}{2} - \frac{1}{\alpha}; 1; 1 - \frac{c}{d}\right) \xrightarrow[\alpha \to 2]{} {}_2F_1\left(\frac{1}{2}, 1, 1, 1 - \frac{c}{d}\right).$$

This can be also written as $_2F_1\left(\frac{1}{2},1,1,\frac{2a}{a-1}\right)$, where a was defined in Eq. 4.4. The second and third indexes are now equal which means that $_2F_1 \to {}_1F_0$, and the last function gives simply a power law

$$_1F_0(1/2;z) \propto \sqrt{1-z}.$$

This is the same power law as the asymptotic of the modified Bessel function $I_{1/2}(1/z)$, introduced below Eq. 4.27.

However here, for reasons that will become clear shortly, we prefer to use the fact that
i) the derivative

$$_2F_1'(a,b,c,z) = {}_2F_1(a+1,b,c,z),$$

and ii) the exponential function (in Eq. 4.14) can be expressed as hypergeometric function, it is the simplest hypergeometric function $_0F_0$. Therefore, in Eq. 4.15, we actually have a composite function of two hypergeometric functions, which will also lead to power series. The result can be written as:

$$\mathcal{T} = \frac{1}{1 + f(x_{in}/x_{out})f'(x_{in}/x_{out})} \tag{4.24}$$

where, we transformed $\exp(A+B) = \exp A \exp B$, and for our choice of indexes and physically sensible range of x_{in}/x_{out} the

$$_0F_0[{}_1F_0(1/2;2a/(a-1))] \approx {}_1F_1(1/2;2a/(a-1)).$$

In the following we will also use a relation between $_2F_0$ and $_1F_1$ from Ref. [142]:

$$_1F_1(a,b;z) = z^a \, _2F_0(a,a-b+1;-1/z) \tag{4.25}$$

resulting in a simplification to $_1F_1$, otherwise known as Kummer and Triconi confluent hypergeometric functions. Thus, we have re-written our WKB result: we used simpler hypergeometric functions for $\alpha = 2$.

Now we move to an exact quantum mechanical solution of the full problem, which is Eq. 4.23 plus external field $\propto x^2$. The point is that, as mentioned above, the scattering problem for a parabolic potential is analytically solvable, and the solution can be written as a combination of two solutions of ODE, precisely of the Kummer $U(a,b;z)$ and Triconi $M(a,b;z)$ functions. For instance, from Ref. [143], we find that the following Schrodinger equation:

$$(-\nabla^2 + \xi^2 - \beta/\xi^2)\psi(\xi) = 0 \tag{4.26}$$

where ξ is measured in units a and $\beta = aa^*$, has the following solutions:

$$\psi(\xi) = U(1/4(1-\beta),1/2,\xi) \tag{4.27}$$

and

$$\psi(\xi) = M(1/4(1-\beta),1/2,\xi) \tag{4.28}$$

Thus general solution can indeed be written as a combination of Kummer and Triconi confluent hyperbolic functions. Some languages of symbolic calculations return the solution in terms of generalized Laguerre polynomial or in terms of modified Bessel functions, but for our indexes both these are equivalent to the Kummer function. The small values approximation of Bessel function is indeed the index dependent power law $I_{2\nu}(x) \propto x^{-2\nu}$, so indeed we have a full correspondence with $_1F_0$ if we neglect the $\propto \beta$ shift of the first index in Eq. 4.27-4.28.

Thus the solution for wave function at the point x_{out}, for a given a (determined by F, ω_0) reads:

$$\psi(a) = \exp(-\imath k_0 a)(1-a) \, {}_2F_0\Big(\pm 1/2 + \imath \frac{a}{1-a}, 1 + 2\imath\frac{a}{1-a}, \frac{1-a}{2a}\Big), \qquad (4.29)$$

the form that is remarkably similar to our Eq. 4.11 when $\alpha = 2$ (or to the simplified form found in Eq. 4.25).

To elaborate on this comparison, we now move on to measurable quantity, i.e., the transmission probability. Based on matrix expression given in Ref. [143], a full quantum mechanical expression for tunneling can be obtained:

$$\mathcal{T} \approx \frac{1}{\left[2 + \exp\left(\imath k_0 \left(x_{in} - x_{out}\right)\right) \left(\frac{f'\left(\frac{x_{in}}{x_{out}}\right) f\left(\frac{x_{in}}{x_{out}}\right) - g'\left(\frac{x_{in}}{x_{out}}\right) g\left(\frac{x_{in}}{x_{out}}\right)}{f'\left(\frac{x_{in}}{x_{out}}\right) g\left(\frac{x_{in}}{x_{out}}\right) - g'\left(\frac{x_{in}}{x_{out}}\right) f\left(\frac{x_{in}}{x_{out}}\right)} \right)^2 \right]} \qquad (4.30)$$

where energy current conservation was used, and the f, g are the two linearly independent solutions of Schrödinger equation, the $\psi(x)$ in Eq. 4.29 i.e., the Kummer and Triconi functions in our specific case. We see that when functions' derivatives are equal to zero (the case of barrier top) then indeed $\mathcal{T} = 1/2$ which confirms Kemble's version of WKB that we used.

The WKB result for $\alpha = 2$, the Eq. 4.24, can be compared to the above quantum mechanical result. For the $\alpha = 2$, it can be observed that a *full* connection with the quantum mechanical solution can be established by adding an extra phase shift in the first index of ${}_1F_1(1/4 + \imath a, 1/2, a)$ functions, by adding the second solution g and by including the derivatives of f' and g' in the denominator. Upon expanding hypergeometric function we see that the index shift is equivalent to multiplying ${}_2F_1$ times a power series with energy dependent coefficients (the a depends on energy and changes from real to imaginary as we cross the barrier top). This is reminiscent of the geometric series, that we proposed as a conjecture in Eq. 4.22. The derivatives f', g' and the wave interference between the two solutions were, naturally, neglected in WKB. It should be noted that the derivative of Eq. 4.11 will naturally contain the problematic $1/(\alpha^2 - 4)$ factor and therefore in the full solution the singularities in the numerator and denominator will cancel each other. The presence of the two interfering (counter-propagating) solutions will be particularly important on the resonance, thus our generalization should be able to capture these effects. Indeed in the resonant case, if the peak is Lorentzian, then numerator and denominator are equal, but opposite and so $\mathcal{T} = 1$.

In summary, this detailed study of $\alpha = 2$ case allowed us to establish a direct link with the exact quantum mechanical solution of the problem. This not only justifies the Kemble version of JWKB but also demonstrates the usefulness of generalizing the tunneling expression and expressing it in terms of hypergeometric ${}_2F_1$ functions from a fundamental viewpoint.

In passing we note the situation for other special values of α. For $\alpha \to 0$ one can use the following mathematical transformation:

when

$$\bar{\beta} \to \infty$$

then

$$_2F_1(a, \bar{\beta}b, c; \bar{\beta}z) \to {}_1F_1(a, c; z).$$

Thus, we are back with confluent hypergeometric function but since in our problem $\bar{\beta}z$ was finite to begin with, thus now $z \to 0$ and we can look only at the first term of

the polynomial expansion. We then arrive at the exponential function, known to be the solution for quantum rectangular barrier (see Chapter 3). For $\alpha = 1$ the situation is less clear: following our conjecture we shall arrive at bi-confluent hypergeometric function $_2F_2(1/2, 1/2, 1, 1; 2a/(a-1))$. The quantum problem when $\alpha = 1$ is a bi-confluent Heun equation and we were not able to find exact analytic solutions of this equation in the literature. In passing we note that the exact analytic solution, in terms of Airy functions, exists but only for the case without $\propto 1/x$ screening term.

It remains to be shown whether the corrections to JWKB identified here can be applied for any value of α (the general solution of the quantum mechanical problem for an arbitrary α is not available at present), but this mathematical problem is well beyond the scope of this thesis. Nevertheless, our conjecture, can serve as a relevant and valuable benchmark for future experiments and numerical studies. Such a pragmatic, engineering approach to the $\mathcal{T}(E)$ problem can also be used to gain in-depth understanding, through analytic solution, of much more complicated problems where resonances are present on the surface.

4.6 Partial conclusions and perspectives

In conclusion, the main result of this chapter is deriving the exact analytic tunneling formula in the JWKB approximation for the barrier described by a fractional power law. The formalism incorporates the external electric field, as well as interaction with an image charge left behind in the surface. Our potential is quite specific as it involves two power laws of precisely opposite exponents, but the existence of the exact closed analytic solution for the transmission $\mathcal{T}(E)$, expressed in terms of an easy-to-evaluate single special function, is nevertheless a remarkable result. In the next chapters, we will show that this specific case is actually realized in a broad class of important materials.

Based on this, we have demonstrated that quite rich tunneling spectrum is possible for the composite surface, paving the way for future analytical modelling of experimental findings. We have also shown that nanostructuring is an efficient way to modify $\mathcal{T}(E)$. Finally, we have demonstrated that our result is general enough to build a connection with some cases of the exact quantum mechanical result.

One future perspective is to capture the situation where a quantum dot is attached to the surface. Generally speaking, such system can be described as a double tunneling barrier and a set of discrete energy levels in between. Each of these levels will contribute to an overall transmission. One faces the situation where tunneling and scattering processes on each of these levels (and their quantum interference) have to be computed; we shall have tensor quantities with an index corresponding to the energy level number. An example of such calculation has been presented in Ref. [144]. We see that in this case, the overall tunneling $T(E)$ (i.e., a scalar quantity that we have been evaluating so far) will be proportional to a trace of a tensor product of the transfer matrices $T^{QM}_{dot}(E) \otimes T^{QM}_{surface}(E)$ on both barriers (surface-to-dot and dot-to-vacuum). The fact that we have obtained the connection with $T^{QM}_{surface}$ point is a position where such tensor products can be evaluated.

Chapter 5

TLL Density of States

5.1 Introduction

The recognition of the purely collective properties of one-dimensional (1D) electrons, a concept originally proposed in the 1950s by Tomonaga and Luttinger, has profoundly influenced the understanding of low-dimensional systems. This paradigm shift was further advanced in 1981 when Duncan Haldane developed the Tomonaga-Luttinger liquid (TLL) as a new theoretical framework. This model, which provides an alternative to the traditional Landau-Fermi liquid theory, has been instrumental in describing low-dimensional metals. The beautiful thing is that this non-trivial model, dominated by many-body effects admits an exact analytic solution. This works also at finite temperatures and, as shown in seminal works of Affleck and Ludwig [145], [146], [147], [148], close to the edges of low dimensional system. These last features are particularly important for realistic applications in nanostructures where the edges frequently play a crucial role. Haldane's work [102], which later got the Nobel Prize for theoretical discoveries in topological phase transitions and topological phases of matter, underscores the significance of this theoretical advance in condensed matter physics.

Despite this, there have been only a few previous studies of field emission within the TLL framework, focusing on a zero-temperature, infinitely long 1D system, suspended flat on the top of a surface [149], [150]. This is a completely different geometry than in the devices of currently common interest. Two developments of the theory are necessary to achieve the aim of bringing theoretical description closer to the experimental setting. First, for a low energy field emission, the tunneling process cannot be considered as instantaneous, so it is required to abandon the anti-adiabatic approximation and consider the dynamics of the tunneling at least in a saddle point approximation. Second, it is essential to abandon the assumption of translational invariance; in order to explore varying tunneling probabilities along the nanotube, it is required to derive the local density of states (DOS) along the nanotube. Both of these developments are achieved in this work.

In particular, in nanostructures, an unavoidable presence of boundaries breaks the translational invariance and if we are interested in this class of materials it is definitely worth investigating what the electron distribution in their vicinity is. For the noninteracting system, homogeneous distributions are expected from Bloch waves plus Friedel oscillations that always decay like $1/x^1$ in 1D. Including interactions can make this simple picture much more complicated and interesting. Uncovering this phenomenology is the object of this chapter.

Unfortunately, the exact analytic solution is known only for correlation functions in real

(space-time) coordinates, while most experiments, for instance, STM, can measure a signal in frequency (energy) space. Thus, it becomes necessary to perform a (partial) Fourier transform: we need to Fourier transform the time domain while keeping the information about the distance from the edge. It should be noted that in our problem, with translational invariance broken, we shall have a relative real-space coordinate and an absolute distance from the edge. The first variable is considered constant and small (at least in the case of an STM probe) while the second is the variable of our interest here.

There are not that many examples of such $t \rightarrow \omega$ Fourier transforms, which is unfortunate because the correlation functions contain singularities which make numerical integration tricky. *This work aims to provide two examples of such LDOS, one for what we call Coulomb metal and the other for Hund metal, and a comparison of the two.*

The Chapter is organized as follows: Sec. 5.2 presents the TLL and how to compute its correlation functions. In Sec. 5.3, the density of states is examined, emphasizing the importance of the boundary condition and the validity of open boundary conditions. Sec. 5.4 presents the results of the Fourier transformation of LDOS, an analytic expression for the Coulomb metal and Hund metal. In Sec. 5.5, $4k_F$ charge susceptibility is investigated. Finally, Sec. 5.6 concludes the chapter.

5.2 TLL and how to compute its correlation functions: two modes

We will generalize here results from Chapter 3, where single-mode TLL was considered.

5.2.1 Multimode 1D liquid

TLL is a low-energy state of collective excitations that provides a highly nontrivial solution for a strongly correlated 1D system. While the fermionic system is strongly interacting, upon bosonization the solvable theory is reached. The fermionic field operators $\psi(x)$ are rewritten in terms of bosonic density $\phi(x)$ and momentum $\theta(x)$ fields:

$$\psi(x) = \exp \imath k_F x \exp \imath \left(\sum_{\nu}^{N} \phi_{\nu}(x) + \theta_{\nu}(x) \right) / \sqrt{N} \tag{5.1}$$

where N is the number of bosonic fields in the model. In Eq. 5.1, the bosonized representation of the fermionic operator captures the low-energy excitations in terms of collective bosonic fields. This formulation effectively separates the fast oscillations due to the Fermi momentum from the slowly varying bosonic degrees of freedom. The details of these fields and the bosonization procedure can be found in Appendix A, Sec. A.1. The bosonized Hamiltonian of the TLL state, written in terms of fluctuations of these collective bosonic modes, is

$$H^{1D} = \sum_{\nu}^{N} \int \frac{\mathrm{d}x}{2\pi} \left[(v_{\nu} K_{\nu})(\pi \Pi_{\nu})^2 + \left(\frac{v_{\nu}}{K_{\nu}} \right) (\partial_x \phi_{\nu})^2 \right] \tag{5.2}$$

where $\nabla \phi_{\nu}(x)$ gives the local density of fluctuations, while v_{ν} and K_{ν} are respectively the velocity and the TLL parameter ($\sim$ compressibility) of a given bosonic mode ν that depend on electron-electron interactions with small momentum exchange. In the simplest

approximation, Galilean invariance is assumed, which implies $v_\nu K_\nu \approx v_F$, where v_F is a Fermi velocity which in turn is approximated by Λ, an energy scale associated with the UV cut-off of our theory ($\equiv$ bandwidth for a single band material, but more generally Λ spans the energy range where dispersion is linear). When, as is the case for carbon nanotubes (CNTs), the gapless states can be grouped into pairs existing in two valleys at K, K' points of Brillouin zone, there are two bands crossing the Fermi level and a two-leg ladder description applies. Then, $N = 4$, i.e, there are four bosonic modes $\rho\pm$, $\sigma\pm$, corresponding to the spin and charge modes oscillating symmetrically or anti-symmetrically within the two legs of the ladder, referred to as the total and transverse modes, respectively. The total mode is a density fluctuation occurring simultaneously in both legs (the valleys), while the transverse mode is a density fluctuation propagating in the opposite direction in two adjacent legs of the ladder.

The K_ν parameters, proportional to compressibilities of collective modes, incorporate all electron-electron interactions with small momentum exchange $W_{Hart}(q \to 0)$, the so-called Hartree interactions. This is particularly useful for materials such as CNTs with electron-electron Coulomb interactions character, where $W(q) \sim 1/q$ so that $W_{Hart}(q \to 0)$ indeed dominates. Furthermore, if these interactions do not depend on spin and valley degrees of freedom, only the parameters of the total charge mode $\rho+$ will be affected.

In condensed matter physics and solid-state physics, the DOS of a system describes the number of modes per unit frequency range. In particular, we shall distinguish two cases.

   Coulomb metal will be the case when only the charge mode compressibility will be different from one $K_{\rho+} \neq 1$, and it can be different from one by a large margin. The values for all other parameters will stay close to one. This can happen in the case of a material dominated by long-range Coulomb interactions, hence the name. One example is a free (un-bundled) carbon nanotube where interactions are only weakly screened. These are usually modelled by a two-leg ladder Hamiltonian (or multi-leg ladder for MWCNT), but there is always a single, totally symmetric charge mode and it is the one that will be affected.

   Hund metal will be the case when both charge and spin modes are subjected to long-range interactions. This may occur in a multi-orbital system which is in an orbitally selective Mott phase. The Mott insulating bands will provide a magnetically ordered background (usually anti-ferromagnetic) which upon averaging out will provide interaction-mediating bosons for the remaining metallic state. The orbital that remains metallic is usually split by the Hund's coupling, hence the name we have chosen. Since the same bosons are mediating charge and spin interactions, it is expected that K_ρ and K_σ will be approximately equal. Hund splitting becomes important for heavier elements.

5.2.2 Values of TLL parameters

The density-density long-range Coulomb-type interactions between electrons in a nanotube can be expressed as:

$$H_{Coul} = \sum_{k,q,\mu} [c_\mu^\dagger(k)c_\mu(k)]V_{Coul}(k,k')[c_\mu^\dagger(k+q)c_\mu(k+q)] = \int dx dx' \nabla\phi_{\rho+}(x)V_{Coul}(x-x')\nabla\phi_{\rho+}(x')$$

(5.3)

which we have expressed both in the fermionic second quantization language (that makes the physical content of the interaction transparent by summing over all μ valley, spin, and sub-lattice states) and in the bosonic field language. In the bosonic language, it is

clear that only the $\rho+$ mode is affected, which is due to the fact that this mode contains the electric charge.

Ref. [151] provides an extensive derivation of Coulomb interactions in a nanotube. It has been found that upon integrating out (evenly) all degrees of freedom along the SWCNT circumference, the following formula for interaction is obtained:

$$V_{Coul}(q) = \frac{2e^2}{\kappa}(|ln(qR)|+c_0) \tag{5.4}$$

where κ is electric permittivity of the nanotube and $c_0 = \gamma + \pi/2ln2 = 0.51$ is a constant, with γ – Euler's constant. This led the authors to the desired formula for $K_{\rho+}$:

$$K_{\rho+} = 1/\sqrt{1 + 4 \cdot 2.7 \cdot ln(R/L)} \tag{5.5}$$

where the numerical parameter 2.7 was found by the authors through comparison with experimental data. Clearly $K_{\rho+} \ll 1$, so it is in a strongly correlated regime and it does depend on the geometrical parameters of the tube. One expects quite substantial variation in this parameter which is indeed observed in SWCNT.

However, in MWCNT the situation is different. As mentioned in Chapter 1, the MWCNT was introduced as a multi-shell system, with electrons randomly jumping from one SWNT to another within the MWCNT, always choosing the most conducting shell in a given region. This model is in agreement with the previous experimental [152], [153], [154], [155] and theoretical [156], [157], [158], [159], [160] studies. Thus, R is a random variable, and in fact the propagation length L is random as well, and the variance can be as large as R itself $\delta R/R \propto 1$. One expects normal, Gaussian distribution of these radii. Therefore, in Eq. 5.4 one has to take a logarithm of a Gaussian distribution $\mathcal{G}(R)$ with variance δR. The solution to this problem is known from the theory of normal distributions. In the $q \to 0$ limit, the case contributing to $K_{\rho+}$, we have $ln(\mathcal{G}(R)) \to ln(2\pi)$, which, upon substitution to formula for $K_{\rho+}$, gives:

$$K_{\rho+} \to 1/\sqrt{1 + 4 \cdot 2.7 \cdot 1.84} = 0.22 \tag{5.6}$$

A correction to V_{Coul} due to variance reads:

$$\delta V_{Coul}(q) = -ln(\delta R) \tag{5.7}$$

and is momentum *independent.* The next order correction $\sim q^2$ is expected to be smaller (when δR is substantial), and will also be counteracted by Fock exchange corrections proportional to gradients of density (so-called GGA corrections), thus also $\propto q^2$.

To make further progress, we note that the large momentum exchange component of electron-electron interactions (which has been neglected so far) leads to non-linear terms $\sim \cos \phi_\nu$, the most relevant of which are quarter-filling (two-site unit cell) umklapp terms:

$$H_{umkl} = \int dx g_3(x) \cos 2\phi_{\rho+} \tag{5.8}$$

where g_3 is the amplitude of umklapp (LL $\to$ RR) scattering. The umklapp terms emerge from backscattering interactions at specific commensurate fillings. The bosonized form is obtained using standard bosonization techniques (see Appendix A), where the charge mode $\phi_{\rho+}$ captures the collective dynamics of the system. This has been extensively discussed in the literature (e.g., [151]) and even textbooks ([96] Chap.4), but remains an active field of experimental research [161]. These terms are not captured by the TLL, but can be incorporated in low energies by gradually averaging higher energies. This is the
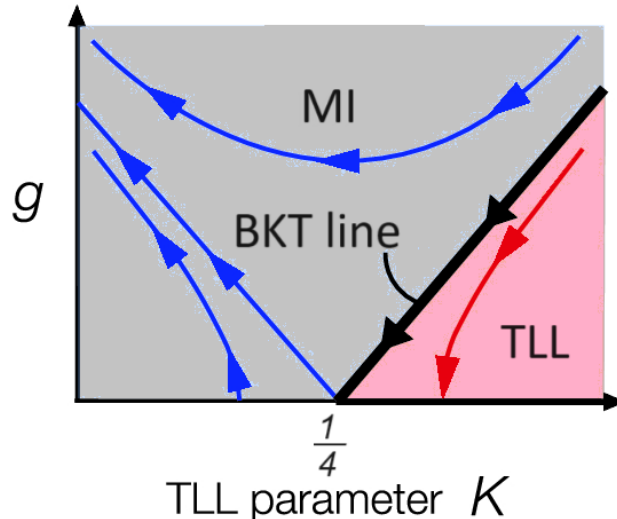
Figure 5.1: Kosterliz-Thouless (KT) Renormalization Group (RG) flow. It shows how the TLL parameter (and the non-linear term g) changes as the characteristic energy in the system is reduced. When g is sufficiently small (and K is sufficiently large), the TLL is stable. When $g \approx K$, the system is close to the straight line that terminates at K^*. Then this will be the parameter of TLL measured at experimental temperatures (Figure is adopted from Fig. 3.2 in Ref. [162]). The BKT flow was discovered in Ref. [163], [164].

so-called Renormalization Group procedure, a very well-developed method. Its canonical result, the Kosterliz-Thouless flow, is shown in the figure below (Fig. 5.1).

Without going into details of the method, which is beyond this work dedicated more towards applications of 1D materials, we note that the $K^* = 0.25$ is a special point of this flow – the system flows towards it in a straight line. To be precise, whenever the deviation of $K_{\rho+}$ from K^* and the value of g_3 are close to each other, then we are in the vicinity of the straight line of the flow, thus indeed flowing towards $K^*_{\rho+} = 0.25$. It should be emphasized here that in our problem, the high energy is the bandwidth of carbon p_z orbitals, which in SWCNT is above $3eV$, while in MWCNT is reduced, for instance by half (it can be more, each situation can be captured by our theory). At the same time, the energies/temperatures at which field emission devices are working are around $30meV$ which is smaller by a factor 50. This order of magnitude will be used below. This is still distinct from temperatures used in theoretical physics works which are usually smaller by a factor $10^{-5} \div 10^{-3}$.

There are, of course, also Coulomb interactions between the nanotubes. The "other-than-the-metallic" shells of MWCNTs will provide screening, which makes the problem immensely complicated. However, two definite statements can be made:

- following the argument given by H. Schulz in Ref. [165], again only the $\phi_{\rho+}$ bosonic mode will be affected, and the entire effect can be captured by minor modification of $K_{\rho+}$,

- due to variations of the metal shell positions (that is, how deep inside MWCNT the metallic shell is), the screening is also random, which brings us back to the central limit theorem argument given above.

Overall, a very non-trivial result has been obtained here: although the $K_{\rho+}$ parameter is the most affected by interactions and naively has the strongest dependence on geometry,
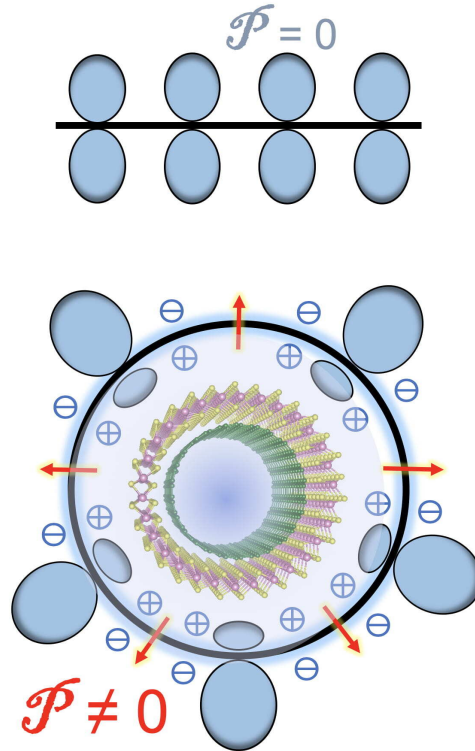
Figure 5.2: The electrical potential (P) of atoms on either side of a graphene sheet (top) are identical, so then the p_z orbitals of carbon are unaffected, but this assumption breaks down when the sheet is curved into a nanotube (bottom). Double-walled nanotubes (bottom) show unique effects as P in inner and outer tubes are staggered. Local electric field will break the perfect symmetry on the nanotube circumference. Yakobson Research Group/Rice University [166].

due to generic disorder present in MWCNT, it is possible to simplify the problem of computing it. Contrary to SWCNT, in MWCT, the measured value of this parameter turns out to be universal.

This dichotomy between SWCNT and MWCNT prevails also in other TLL modes. Any deviation from perfectly symmetric situation – even summation over all μ in Eq. 5.3 – will modify the other three TLL parameters. While SWCNT was generically very symmetric, in MWCNT, the interactions between shells can break the central axis rotational symmetry. The neutral K_ν modes, $\nu = \sigma_\pm, \rho_-$, can be modified by external fields, which are defined as fields external to the metallic shell. They can be either generated outside MWCNT in the laboratory or induced due to the presence of other shells. For instance, to modify the spin channel compressibility $K_{\sigma+}$, a field that couples with total spin density, namely the local magnetic field, is required. To modify the relative charge mode TLL parameter (i.e. compressibility of this mode) $K_{\rho-}$, a force acting differently on two sites of bi-partite lattice is needed, such as a local strain or local dipolar moment. Recent experimental findings, illustrated in Fig. 5.2, show that such forces can indeed be induced in a double wall MWCNT.

In order to predict how the neutral TLL parameters depend on the characteristic features of the material, a deeper understanding of the interactions is required. In Ref. [151] the authors showed that:

$$K_\nu(x_i) \approx 1 - \nu f(x_i) \tag{5.9}$$

where $\nu = \pm 1$ for $\nu = \sigma+, \rho-$ respectively. The x_i are some microscopic parameters
that determine geometry of electron wavefunction. The f is a constant proportional to a
deviation from a perfect circumferential symmetry, the C_∞. It is a ratio: $f = V_{real}(q \rightarrow
0)/V_{C\infty}(q \rightarrow 0)$. We aim to evaluate it now. To this end, we need to carefully examine
how the interaction amplitudes are computed when one moves to the second quantization
description (see Chapter 3, Sec. 3.2). The bare Coulomb potential in a nanotube of radius
R and thickness d_z reads:

$$\bar{V}_{Coul}(\vec{r} - \vec{r'}) = \frac{e^2/\kappa}{\sqrt{(x-x')^2 + 4R^2 \sin^2((y-y')/2R) + d_z^2}} \qquad (5.10)$$

where the d_z is the thickness of the toroid (here we shall consider physical nanotube
as a geometrical, stereometric solid figure – a toroid). The scattering amplitude (i.e.
a quantity that enters into the second quantization Hamiltonian) of the Hartree-type
interaction is given by an integral over the elementary cell:

$$V(\vec{r}, \vec{r'}) = \int d\vec{r} \Psi^*(\vec{r}) \Psi^*(\vec{r'}) \bar{V}_{Coul}(\vec{r} - \vec{r'}) \Psi(\vec{r}) \Psi(\vec{r'}) \qquad (5.11)$$

where $\Psi^*(\vec{r}), \Psi^*(\vec{r'})$ are wave-functions of interacting electrons, Bloch waves along the
x-direction and, in a perpendicular plane, a section of a toroid of a given thickness (the
charge density in MWCNT is in general spread over a section of a distorted toroid). We
add an extra parameter ζ that accounts for inhomogeneity along the circumference of
the toroid where $\zeta = 0$ corresponds to symmetric homogeneous distribution (or constant
radius) like in a SWCNT nanotube. Hence we shall generalize expression given by Egger
and Gogolin in Ref. [151] for the symmetric SWCNT. We integrate over perpendicular
coordinates to get an interaction amplitude along the b-axis $V(x)$:

$$V(x) = \int_{\phi R}^{2\pi R} \int_{\phi R}^{2\pi R} \frac{dy}{2\pi R} \frac{dy'}{2\pi R} \frac{\bar{V}_{Coul}(\vec{r} - \vec{r'})}{1 - \zeta \sin((y-y')/2R)} \qquad (5.12)$$

The integral is known also in this more general case:

$$V(x - x') = \bar{U}_{\gamma\delta\bar{\sigma}\bar{\sigma}'}^{\alpha\beta} \frac{(\phi^2 + 1) \Pi \left(\phi; \zeta \left| \left(\frac{2R}{\sqrt{d^2 + 4R^2 + (x-x')^2}} \right)^2 \right. \right)}{\left(\zeta \sqrt{d^2 + 4R^2 + (x-x')^2} \right)} \qquad (5.13)$$

where $\Pi(\phi; \zeta | 1/\tilde{x})$ is the incomplete elliptic integral of the third kind, $\tilde{x} = (x - x')/R$, the
relative distance in R units. The integral is parameterized by U (chosen appropriately
depending on screening in the MWCNT). The parameters ϕ (angle of the sector of the
toroid) and ζ (distortion of the toroid) are determined by material specific considerations,
namely:

- parameter ζ captures the situation shown in Fig. 5.2, where the density of electrons
  along the circumference, related to $\Psi(y, z)$, is not constant. This may be either a
  static effect induced by Moire-type potential from other shells, or a dynamic effect
  induced by exciting a phonon (or both). In this second case, there is a possibility
  to tune the amplitude of ζ by adjusting the amplitude of IR radiation applied to
  the emitter

- parameter ϕ is related to the fact that electrons can move only within a part of
  nanotube's circumference. One can easily imagine that such a phenomenon will be

induced by impurities evaporated on the surface of MWCNT. Then by adjusting the concentration of impurity atoms, the experimentalists and engineers should be able to decrease the average ϕ, thereby decreasing the sector of the toroid available for mobile electrons $\propto \Psi(y, z)$. Importantly, this effect depends on the chirality of the nanotubes:

- when the metallic nanotube (shell of MWCNT) is armchair (achiral), its wave-function $\Psi(y, z)$ forms a simple standing wave with a node on the circumference, meaning that the equation $\Psi(y_0, z_0) = 0$ can be fulfilled. The position of the node can be adjusted to the position of the impurity, so for small concentrations of impurities, there will be no effect

- when the metallic nanotube (shell) is zig-zag (achiral), it features a uniform wave on the circumference $\Psi(y, z)$ but allows for the degenerate standing wave solution along the nanotube that could admit $\Psi(x \pm a/2) = 0$. Atomistic disorder may thus be avoided (by the same argument as above), but the fermionic velocity v_F can be reduced

- for the chiral tubes, the wavefunction $\Psi(x, y, z)$ is a plane wave running in a screw motion along the nanotube. The impurity cannot be in general avoided (although for armchair-like tubes with two K, K' points located at finite $\pm q_0$, there is some adjustment possible, so the influence of atomistic disorder can be weaker). In general, we expect that the smaller the chiral angle, the plane wave will move closer to the nanotube axis. Thus, the "shadow" of impurity will extend along a longer section of the nanotube.

Of course, as the electron jumps from one least conducting shell to another, then the ϕ will vary. One takes an average value in the above formula.

The equation Eq. 5.4, that was used to estimate $K_{\rho+}$, is in fact a long-wavelength approximation for a Fourier transform of the elliptic integral of the first kind $K(x)$, the result of reasoning in Ref. [151] done for the symmetric case $\zeta = 0$. Thus parameter f
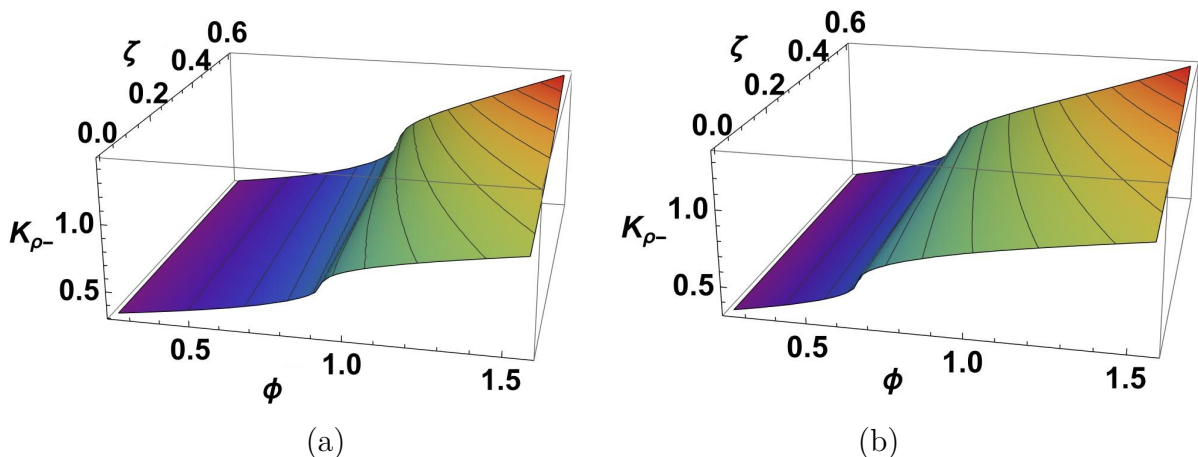
Figure 5.3: The "neutral", charge-less TLL parameter $K_{\rho-}$ from Eq. 5.14 plotted as a function of the angular span ϕ (in radians) of the CNT electronic wavefunction and its inhomogeneity parameter ζ. In panel (a) we use $a_0 = R\left(\left(1 - \frac{1}{\sqrt{5}}\right) + 1\right)$ and in (b) $a_0 = R\left(3\left(1 - \frac{1}{\sqrt{5}}\right) + 1\right)$ where R is an average radius of the MWCNT.
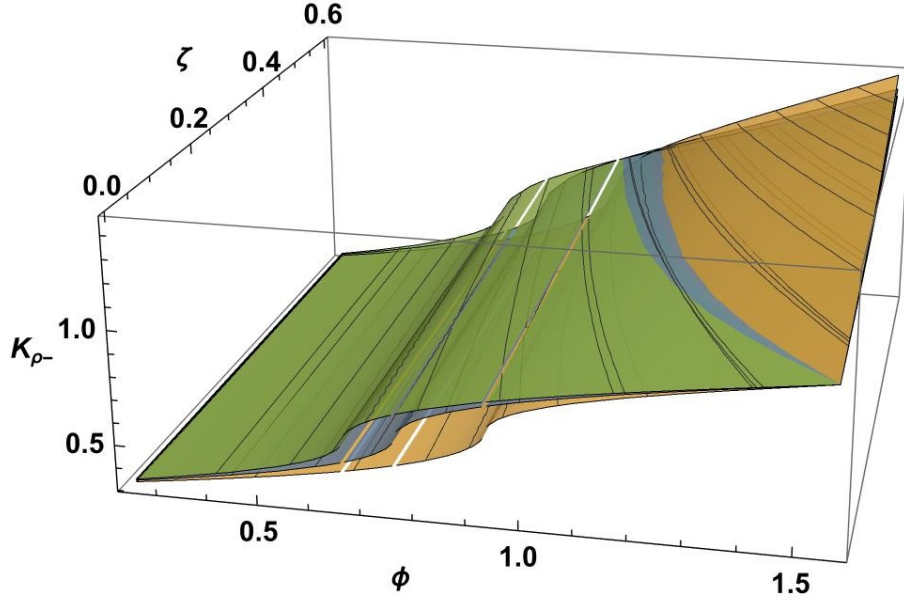
Figure 5.4: The "neutral", charge-less TLL parameter $K_{\rho-}$ from Eq. 5.14 plotted as a function of the angular span ϕ (in radians) of the CNT electronic wavefunction and its inhomogeneity parameter ζ. We show them here together to visualize the role of $a_0 = R\left(j\left(1 - \frac{1}{\sqrt{5}}\right) + 1\right)$ variations; orange: $j = 1$, blue: $j = 2$, green: $j = 3$.

in Eq. 5.9 is thus in fact a ratio of the elliptic function of the third and of the first kind, namely:

$$f(\phi, \zeta) = \left.\frac{\Pi(\phi; \zeta | 1/\tilde{x})}{K(\tilde{x})}\right|_{\tilde{x}=a_0} - 1 \tag{5.14}$$

where a_0 is the size of the unit cell along the nanotube. We multiply it with $1 - K_{\rho+}$, to ensure that all K_ν parameters change proportionally. The results are presented in Fig. 5.3 and Fig. 5.4.

5.2.3 Correlation functions in TLL

Having estimated the TLL parameters based on material specific considerations, we are now in a position to predict measurable quantities. In TLL, the fermionic correlation functions are translated into a bosonic form, which for a single-mode TLL reads (up to a pre-factor):

$$\langle \psi^\dagger(x, t)\psi(0, 0)\rangle \approx \langle \exp(\phi(x, t) + \theta(x, t)) - (\phi(0, 0) + \theta(0, 0))\rangle \tag{5.15}$$

The correlator in Eq. 5.15 can be evaluated as a Gaussian integral:

$$\langle \exp \imath A(\phi_\nu(x, t) - \phi_\nu(0, 0))\rangle = \exp -\frac{1}{2}[A\langle(\phi_\nu(x, t) - \phi_\nu(0, 0))\rangle]^2 =$$

$$\exp -\frac{1}{2}A^2\langle\phi_\nu(x, t)\phi_\nu(0, 0)\rangle = \exp\left(-\frac{1}{2}A^2 K_\nu^2 ln(r)\right) = r^{-\frac{1}{2}A^2 K_\nu^2} \tag{5.16}$$

where A is some numerical constant (peculiar for the chosen observable, e.g. $A = 1/\sqrt{N}$ for Green's function), and $r = \sqrt{x^2 + t^2}$. In the first line, Debye-Waller relation was

used for the average of an exponential. In the second line, a central result of TLL is used: the correlation function of bosonic modes results in a simple logarithmic decay multiplied by the TLL parameter K^2 for ϕ modes; for θ modes, it is an inverse K^{-2}. For correlators of the dual θ field, the procedure is the same; the final result can be recovered by simple substitution $K \to 1/K$. This leads to power laws with non-universal, interaction-dependent exponents $\sim K$.

For a multimode TLL, there is a straightforward generalization. The fundamental bosonization formula now reads:

$$\psi_{R,L}(x,t) = \exp \imath A \left(\sum_{\nu} (\phi_\nu(x,t) \pm \theta_\nu(x,t)) \right) \tag{5.17}$$

i.e., each electron splits into several bosonic modes (in the above formula, a plus sign denotes right-going and a minus sign – left-going fermions).

Following the same steps as before for a single-mode case, now we find that for many modes, the fermionic propagator reads:

$$\langle \psi^\dagger(x,t)\psi(0,0) \rangle = \prod_{\nu} \left\{ \exp\left[-\frac{1}{2}A^2\langle\phi_\nu(x,t)\phi_\nu(0,0)\rangle\right] \exp\left[-\frac{1}{2}A^2\langle\theta_\nu(x,t)\theta_\nu(0,0)\rangle\right] \right\} \tag{5.18}$$

the above formula is factorized in bosonic modes (index ν) because $\langle\phi_\nu^\dagger(x,t)\phi_{\nu'}(0,0)\rangle = 0$ when $\nu \neq \nu'$. This is a manifestation of the famous spin-charge separation, postulated theoretically and then observed experimentally in 1D systems.

A great advantage of working with TLL is that all correlation functions can be computed exactly, in principle, at least in real space (x,t). For instance, the result for the spectral function in an infinite TLL was calculated more than four decades ago [165], [167], [168], [169] and now can be also found in textbooks [96], [170] and reads:

$$A_0(x,t;T=0) = -iY(t)\langle[\psi_{rs}(x,t),\psi_{rs}^\dagger(0,0)]_+\rangle = -i\frac{Y(t)}{2\pi}e^{irk_Fx}\lim_{\epsilon\to0}\left\{\frac{\alpha_{cut-off}+i(v_Ft-rx)}{\epsilon+i(v_Ft-rx)}\right.$$

$$\times \prod_{\nu=\rho,\sigma}\frac{1}{\sqrt{\alpha_{cut-off}+i(u_\nu t - rx)}}\left(\frac{\alpha_{cut-off}^2}{(\alpha_{cut-off}+iu_\nu t)^2+x^2}\right)^{\gamma_\nu} + \left.\begin{pmatrix} x \to -x \\ t \to -t \end{pmatrix}\right\} \tag{5.19}$$

where $\alpha_{cut-off}$ is the high energy cut-off of the theory, for instance, the bandwidth. The exponent γ_ν is

$$\gamma_\nu = \left(K_\nu^2 + K_\nu^{-2} - 2\right)/8 > 0 \tag{5.20}$$

From this, the following Fourier transform can be found:

$$A_{R,s}(q,\omega) \sim (\omega - v_\sigma q)^{\zeta-1/2}|\omega - v_\rho q|^{(\zeta-1)/2}(\omega + v_\rho q)^{\zeta/2} \tag{5.21}$$

where the overall exponent $\zeta = \sum_\nu \gamma_\nu$. However, this is the simplest case $T = 0$, $L \to \infty$. The details of the derivation of Eq. 5.19 can be found in Appendix A, Sec. A.2.

5.3 The density of states

The density of states (DOS) encodes the electronic properties of any material, determining its electrical conductivity, thermal conductivity, and optical properties. This is because it provides crucial information about the behaviour of electrons, including their occupation and propagation characteristics. Here we wish to incorporate the effects of interactions, since it is known that in 1D, propagating electrons cannot avoid each other and therefore become strongly correlated.

Usually, the evaluation of any correlation function in a strongly correlated state is a prohibitively difficult task, especially considering the finite size and the finite temperatures. Calculating spectral function $A(q, \omega)$ for all values of energies in 1D liquid at $T = 0$ can be done by means of Bethe ansatz [171], while for the finite temperatures - only with the most advanced numerical methods such as tDMRG; both results were shown in Ref. [172]. Therein, for the spin chain with characteristic energy J, it was found that a linearized theory works up to energy scales of $\approx 1.5J$. This linearized theory is precisely the TLL framework introduced in Chapter 3 and used here.

Fortunately, as described in Chapter 1, the CNTs can be described through the TLL formalism. Therefore, in the following, we take $n_{tube}(F, \omega, r) = n_{TLL}(F, \omega, r)$. The Green's function and thus also DOS for an infinite TLL are well known [96], actually, the way to obtain them was demonstrated in Sec. 5.2.3. Thanks to the conformal invariance of the underlying field theory, the TLL correlation functions are known for infinite 1D wires at finite temperatures as well. This allows for a direct comparison with the experiments that are unavoidably performed at finite temperatures. Remarkably, in Ref. [173], Mattsson and co-workers obtained finite-temperature LDOS also for a finite-size spin-full 1D system. Their result explicitly demonstrates the LDOS dependence on a distance from the top of the nanotube. Their solution is presented in Eq. 5.22. A product of two $Sinh^{a_i}(r, v_i t)$ functions is observed, each corresponding to a pole of Green's function characterized by a velocity v_i.

The method to evaluate TLL correlations with a boundary was obtained by Affleck and Eggert [174], [175]. Since the correlation function on the boundary remains factorized[1], just like in a bulk, we give here an example of a single-mode procedure. The procedure involves several transformations of the fields as summarized in the box below.

As a result, even for equal-space correlation functions $x = x' = r$, correlators $\langle \phi(r, t)\phi(r, t')\rangle$ as well as $\langle \phi(r, t)\phi(-r, t')\rangle$, are obtained. The latter produce terms $\propto (2r \pm v_\nu t)$, and this r dependence indicates translational symmetry breaking.

---

[1]This assumption is broken only by boundary terms of the form $\cos \vartheta(x = 0)$ where ϑ is a linear combination of at least two modes. Physically, to have a strong mixing, the two modes must have the same velocity (which excludes holon) and some symmetry, such as valley symmetry, has to be broken on the boundary.

The boundary procedure, **BP**, involves several transformations of the bosonic fields, namely the fermionic field undergoes the following series of mappings:

Initially the relation between fermionic field $\psi(x)$ and bosonic fields ϕ, θ reads as usual:

$$\psi_R(x_1, \tau_1) \propto e^{-i[\phi(x_1,\tau_1)-\theta(x_1,\tau_1)]}.$$

Step 1 Rescale ϕ fields by K and θ fields by $1/K$ (this is to move to noninteracting fields $\tilde{\phi}$, to avoid the nonlocal interactions later on)

$$\psi_R(x_1, \tau_1) \propto e^{-i\left[K\tilde{\phi}(x_1,\tau_1)-\frac{1}{K}\tilde{\theta}(x_1,\tau_1)\right]}.$$

Step 2 Move to basis of chiral $\tilde{\phi}_{L,R}$ fields

$$\psi_R(x_1, \tau_1) \propto e^{-i\left[K\left(\frac{\phi_L-\phi_R}{2}\right)-\frac{1}{K}\left(\frac{\phi_L+\phi_R}{2}\right)\right](x_1,\tau_1)}.$$

Step 3 When the boundary condition is set by large $\cos\phi$, thus by pinning $\phi(x=0)=0$, in terms of chiral fields this translates to a nonlocal condition

$$\phi_L(x) = \phi_R(-x)$$

upon which the fermion field is transformed as

$$\psi_R(x_1, \tau_1) \propto e^{-\frac{i}{2}\left[\left(K-\frac{1}{K}\right)\phi_R^e(-x_1,\tau_1)-\left(K-\frac{1}{K}\right)\phi_R^e(x_1,\tau_1)\right]}.$$

Step 4 One can now move back from chiral fields to $\tilde{\phi}, \tilde{\theta}$ fields

$$\psi_R(x_1, \tau_1) \propto e^{-\frac{i}{2}\left[\left(K-\frac{1}{K}\right)[\theta^e-\phi^e](-x_1,\tau_1)-\left(K-\frac{1}{K}\right)[\theta^e-\phi^e](x_1,\tau_1)\right]}.$$

The real-space expressions for correlation functions have been also obtained for a finite temperature TLL with a boundary in Ref. [173]. It reads:

$$N(x=0,t,r;\beta) = \left(\frac{\sinh\frac{\pi}{\beta}t}{\frac{\pi}{\beta}\alpha}\right)^{-a_s-a_c} \left|\frac{\sinh\frac{\pi}{v_c\beta}(2r+v_ct)\sinh\frac{\pi}{v_c\beta}(2r-v_ct)}{\sinh^2\frac{2\pi r}{v_c\beta}}\right|^{-\frac{b_c}{2}}$$

$$\times \left|\frac{\sinh\frac{\pi}{v_s\beta}(2r+v_st)\sinh\frac{\pi}{v_s\beta}(2r-v_st)}{\sinh^2\frac{2\pi r}{v_s\beta}}\right|^{-\frac{b_s}{2}} \quad (5.22)$$

where the exponents $a_{s,c}$ and $b_{s,c}$ depend on K_ν as will be shown in the next subsection (Sec. 5.3.1). Because of $a_{s,c}(K_\nu)$ dependence, electron-electron interactions enter through K_ν in a highly non-trivial, non-perturbative way – they modify the exponents of the power law. This implies that the result is non-perturbative.

The further advantage of TLL is that it obeys conformal invariance, allowing correlation functions to remain accessible even at a finite temperature and a finite size. The finite temperature expressions can be found through CFT mapping [176] of a plane on a cylinder (thus imposing a periodic condition in time) which is equivalent to a substitution $r \to sinh(r/\beta)$ (here β is an inverse temperature). The finite temperature correlations are obtained due to the usual conformal symmetry transformation $z \to \beta/2\pi log(z)$, which leads to the $sinh()$ functions above, in Eq. 5.22.

5.3.1 Importance of the boundary condition

The relation between the exponents a, b and the TLL parameters is determined by the nature of the boundary itself. If the boundary is set by backscattering potential, the fields ϕ_ν are locked at $x = 0$. This is the standard case that has been applied in Ref. [173]. Then we would have $a_{s,c} = \frac{K_{s,c}{}^2 + K_{s,c}^{-2}}{4}$, $b_{s,c} = \frac{K_{s,c}^{-2} - K_{s,c}{}^2}{4}$ and indeed at the boundary the correlation function decays with $1/K$ exponent because the fluctuations of $\phi(x = 0)$ are frozen (while correlation in the bulk still follow Eq. 5.19). However, different situations with different boundary conditions at $x = 0$, are also possible.

In Ref. [173] the authors used standard Dirichlet boundary condition that assumes a hard wall boundary at the end of the nanotube, which, in turn, results in a boundary condition $\phi_\nu(x = 0) = 0$. However, what is more appropriate for a nanotube in a finite electric field, constantly emitting a stream of electrons, are the radiative boundary conditions as derived in [177]. These conditions are also consistent with a physical situation most likely implemented when the residue of metal catalysts rests on each nanotube's top: a small quantum dot in a double tunneling regime is present at the top of the nanotube. Assuming charge flow continuity, without voltage drop, between the nanotube and the quantum dot the boundary condition for the canonically conjugated field $\theta_{\rho\pm}(x = 0) = cste$ is reached. This can be easily accommodated in Mattsson's and co-workers' formalism by making a substitution $K_{\rho\pm} \to 1/K_{\rho\pm}$. This can be proven as follows:

It is possible to consider the situation when there is an intense emission of carriers close to the end of a 1D system. The so-called *radiative* boundary conditions are then applied. These were first identified in Ref. [174] and can be written as

$$(V_F g^{-2} \partial_x + \partial_t)\phi(x_i) = p(x_i)$$

where $p(x_i)$ is a probability of emitting/injecting carrier at a point x_i. This sets the boundary condition for canonically conjugated momentum field $\theta(x = 0)$. As a result, the following modification in the above procedure by Affleck and Eggert is necessary: *in the step 3. of **BP** we now impose the boundary condition for the original θ field thus now for the chiral field the boundary condition reads:*

$$\phi_L(x) = -\phi_R(-x) \tag{5.23}$$

The entire reasoning thus stays the same, but signs need to be changed in front of some coefficients which ultimately results in a change of sign in Eq. 5.25.

For the spin sector, this unusual boundary condition will have a different interpretation: a local DM interaction, that is locally generated spin-flip processes. It could be expected that such a term would naturally arise on the edge of heavy atom chain with nonequivalent (lower symmetry) lattice sites. Usually, DM interaction approaches zero because contributions from various sites cancel out. However, this cancellation will not work on the edge of the wire where only one site is present.

Furthermore, when $K_\rho < 0.5$ (such as in our case), then $g \gg V_F$ (please note that $K_\rho = 0.5$ correspond to $U \to \infty$ in the Hubbard model), thus the first term in the boundary condition can be neglected, leaving only the time derivative, namely the boundary condition for the canonically conjugated field $\theta(x_0) = 1$. Since fluctuations of $\theta(x = 0)$ field at the boundary are now frozen, a different relation between exponents a, b and K_ν, needs to be set, namely:

$$a_{s,c} = \frac{K_{s,c}{}^2 + K_{s,c}^{-2}}{4} \tag{5.24}$$

	Coulomb	Hund
a_s	0.25	1.5
a_c	2.015	2.015
$\boldsymbol{b_s}$	**0**	**−2**
$\boldsymbol{b_c}$	**−2**	**−2**

Table 5.1: The a_ν and b_ν parameters' values that were used for the Coulomb and Hund models. The values of $\boldsymbol{b_\nu}$ are in bold font because they are fixed in our method.

$$b_{s,c} = -\frac{K_{s,c}^{-2} - K_{s,c}^{2}}{4} \tag{5.25}$$

The two-leg ladder description is obviously much more complicated than the spin-full chain that we considered so far, as there are four $\rho\pm, \sigma\pm$ instead of two bosonic modes. However, an extremely useful aspect of nanotubes dominated by the long-range interaction is that only the velocity of the charge-full $\rho+$ mode, the $v_{\rho+}$, is strongly modified, while for the remaining three modes the respective velocities stay close to V_F. Thanks to that our original formulas for space-dependent spectral functions $N(\omega, r)$ can be still applied, however, we need to take into account that now three modes K_ν will contribute to what was before a_s:

$$\tilde{a}_s = \frac{K_{\sigma+}^{2} + K_{\sigma+}^{-2} + K_{\sigma-}^{2} + K_{\sigma-}^{-2} + K_{\rho-}^{2} + K_{\rho-}^{-2}}{8} \tag{5.26}$$

where we took into account that $N = 4$ in the denominator. In Ref. [173] the case of the simplest single-mode TLL was considered, and the impurity term $\cos\phi(x = 0)$ was responsible for setting the boundary where the radiation took place[2]. In the case of a multimode TLL setting boundary is a non-trivial step that also contains some physics within the problem. There are several, to be precise, eight possible two body terms $c_0^\dagger c_0$ [178], [179], and the choice among them is determined by the nature of boundary scattering. If the scattering on the boundary is featureless, $\phi_\nu \to \theta_\nu$ is chosen for all the boundary conditions. However, if there is a spin-flip of valley-flip, like in a quantum dot attached on the top of a nanotube, the scattering will involve $\cos\theta_{\sigma+}$ or $\cos\theta_{\rho-}$, respectively. Therefore, the radiative boundary condition will now be set for $\phi_{\sigma+}$ or $\phi_{\rho-}$. On the boundary, these fields will become frozen; consequently, the boundary exponent will depend on $1/K_{\sigma+}$ or $1/K_{\rho-}$ as usual (contrary to the radiative boundary condition for $\rho+$ which will always have $\theta_{\rho+}$ frozen, resulting the boundary exponent depending on $K_{\rho+}$).

The list of all values of a_ν and b_ν used for the calculations is presented in Table 5.1. The values of b_ν are fixed in our method.

This statement can be further generalized: if the standard TLL is in contact with a highly non-trivial electrode such as a helical TLL where $(\phi \pm \theta)|_{x=0}$ boundary condition is set, or more generally with a spiral TLL where $(\cos(\alpha)\phi \pm \sin(\alpha)\theta)|_{x=0}$ boundary condition (with a K−dependent rotation angle α) is imposed, the boundary condition will be defined through emission of such carriers and strong back-scattering of orthogonal

---

[2]Please note that in Ref. [173] the canonical notation is swapped $\phi \leftrightarrow \theta$.

carriers. Anticipating the results obtained in Sec. 5.4.2 will lead to a prediction of particle accumulation causing fluctuation onto the external electrode.

Validity of open boundary condition

We work in the case where $K \ll 1$ and analyzing the transmission function $\mathcal{T}(\omega; \alpha)$ as obtained in Chapter 4, when $\alpha \ll 1$, it is observed that for sufficiently small ω and a sufficiently coarse-grained lattice, the radiative boundary condition becomes sharp. This implies that there exists $x_0(\Lambda)$ such that any carrier located there will be emitted with probability $p(x_0) \to 1$. Furthermore, as will become clear from our analysis of the $4k_F$ component of charge susceptibility, the dielectric function in the vicinity of the boundary keeps the α power (in the potential) small but constant down to some specific distance. Beyond this distance, α abruptly decreases to zero, making the above-defined condition for $\mathcal{T}(\omega; \alpha \to 0)$ even sharper.

5.4 Results: Fourier Transform of LDOS

5.4.1 Analytic expression

Physically, accessible quantities are usually measured in the frequency domain. Consider, for instance, an STM measurement done along 1D wire. Also, when computing a response of some composite system in a series, the generalized "susceptibilities" entering multiplicatively will be in the frequency domain (in the time domain we shall have convolutions). The expression, as given above, thus requires partial Fourier transformation, namely, the integral transform needs to be performed only along the time-axis into a frequency domain. Although it may seem straightforward, this is a significant technical issue. In the simplest case of single-mode TLL, the Fourier transform of finite temperature expression takes the form of a hypergeometric Beta function [96]. Analytical formulas are known only for the cases of bosonic modes with one common velocity (such as the hypergeometric Beta function) and with two velocities (such as the Appel hypergeometric function [180]). For the boundary problem, the formula is expected to be even more complicated. On the other hand, analytical formulae have a great advantage, since both the $N(x, t)$ and $N(x, \omega)$ have singularities. Therefore, numerical integrals are notoriously hard to control, which is particularly important if $N(x, \omega)$ is intended to be used as an input for some further calculations.

Therefore, it is observed that this task is non-trivial and can be done only for a few special cases, probably only for a few special values of K_ν TLL parameters.

The main part of electronic propagator is the chiral Green's function which is a correlator $G_{RR} = \langle \psi_R^\dagger(x, t) \psi_R(0, 0) \rangle$, where the right-going many-body electronic wave remains right-going when it propagates space-time interval from (x', t') to (x, t) (it should be noted that due to the boundary, the translational invariance is broken). The finite temperature, real-space (and real-time) LDOS in a 1D TLL has been obtained in Ref. [173], where Mattsson, Eggert and Johanesson provided the expression for frequency- (energy-) dependent LDOS as a regularized integral (which they later solved numerically). The expression is a straightforward Fourier transform of Eq. 5.22 and it reads:

$$N(\omega, \beta, r) = \frac{2}{\alpha_{cut-off}\pi^2} v_c^{-a_c} v_s^{-a_s} \int_0^\infty dt \cos\gamma(t) \left[\cos\omega t \left(\frac{\sinh\frac{\pi}{\beta}t}{\frac{\pi}{\beta}\alpha} \right)^{-a_s-a_c} \right.$$

$$\times \left| \frac{\sinh\frac{\pi}{v_c\beta}(2r+v_ct)\sinh\frac{\pi}{v_c\beta}(2r-v_ct)}{\sinh^2\frac{2\pi r}{v_c\beta}} \right|^{-b_c/2} \left| \frac{\sinh\frac{\pi}{v_s\beta}(2r+v_st)\sinh\frac{\pi}{v_s\beta}(2r-v_st)}{\sinh^2\frac{2\pi r}{v_s\beta}} \right|^{-b_s/2}$$

$$\left. - \left(\frac{t}{\alpha_{cut-off}} \right)^{-a_s-a_c} \left| 1 - \left(\frac{v_ct}{2r} \right)^2 \right|^{-b_c/2} \left| 1 - \left(\frac{v_st}{2r} \right)^2 \right|^{-b_s/2} \right] \quad (5.27)$$

where the exponents for space-independent $a_{s,c}$ and space-dependent $b_{s,c}$ parts depend on TLL parameters presented in Eq. 5.24 and Eq. 5.25.

The above given expressions provide the only contribution to the bulk case, without the boundary. In the presence of the boundary, there is also a staggered contribution to the Green's function, which is a correlator

$$G_{LR}(x, x', t', t) = \langle \psi_L^\dagger(x, t)\psi_R(x', t') \rangle.$$

Here, a right-going many-body electronic wave has turned into a left-going one during the space-time interval from (x', t') to (x, t), due to scattering off the boundary at $x = 0$. In the single-particle context, these are known as Friedel oscillations. We derived the integral, an analogue of Eq. 5.27, for this component of Green's function (as before for the case when $x = x' = r$). It reads as follows:

$$N_{LR}(\omega, \beta, r) = \frac{2}{\alpha_{cut-off}\pi^2} v_c^{-a_c} v_s^{-a_s} \int_0^\infty dt \cos\gamma(t) \left[\cos\omega t \left(\sinh\frac{\pi}{\beta v_c}(v_ct+2r) \right)^{-\frac{a_c}{2}} \right.$$

$$\times \left(\sinh\frac{\pi}{\beta v_c}(v_ct-2r) \right)^{-\frac{a_c}{2}} \left(\sinh\frac{\pi}{\beta v_s}(v_st+2r) \right)^{-\frac{a_s}{2}} \left(\sinh\frac{\pi}{\beta v_s}(v_st-2r) \right)^{-\frac{a_s}{2}}$$

$$\times \left(\frac{\sinh\frac{\pi}{\beta v_c}(v_ct-2r)}{\sinh\frac{\pi}{\beta v_c}(v_ct+2r)} \right)^{\frac{1}{4}} \left(\frac{\sinh\frac{\pi}{\beta v_s}(v_st-2r)}{\sinh\frac{\pi}{\beta v_s}(v_st+2r)} \right)^{\frac{1}{4}} \left(\frac{1}{\sinh\left(\frac{\pi t}{\beta}\right)} \right)^{b_c} \left(\frac{1}{\sinh\left(\frac{\pi t}{\beta}\right)} \right)^{b_s} \left(\sinh\frac{2\pi r}{v_ct} \right)^{b_c}$$

$$\left. \times \left(-\sinh\frac{2\pi r}{v_st} \right)^{b_s} - \left(\frac{t}{\alpha_{cut-off}} \right)^{-a_s-a_c} \left| 1 - \left(\frac{v_ct}{2r} \right)^2 \right|^{-b_c/2} \left| 1 - \left(\frac{v_st}{2r} \right)^2 \right|^{-b_s/2} \right] \quad (5.28)$$

Unfortunately, we were not able to find any values of K_ν which would admit exact analytical expression for the above integral Eq. 5.28. Fortunately, the numerical studies of Eggert and collaborators suggest that this is sub-dominant contribution already for the hard-boundary condition and it is expected to be even smaller for our radiative boundary conditions.

The real space result of Eq. 5.27 has been written as a product of powers of sine-hyperbolic functions. The difficulty in integrating rests in the fact that for our purposes frequency dependence of LDOS is required, which is obtained through partial Fourier transform. Obviously, this can be done through a direct numerical evaluation; however, already in Ref. [173] the singularity of LDOS was pointed out, which needs to be regularized. This is a nontrivial task to achieve for the numerical integration, especially since we wish to use it as a basic ingredient for later calculations. We then turned our attention to possible analytic expressions, for specific cases when the Fourier transform can be done exactly.

The integral of LDOS (Eq. 5.27) as obtained by Eggert has been expressed as:
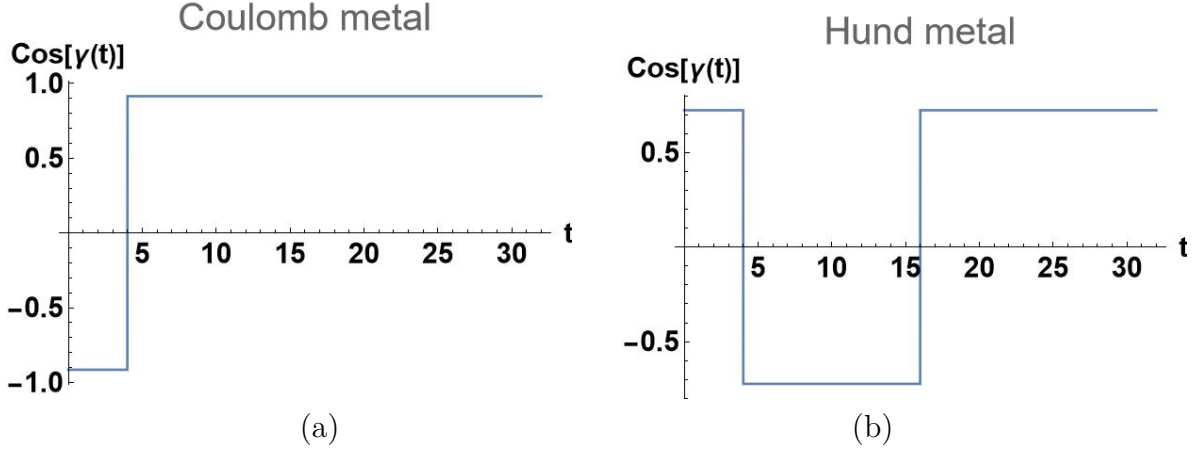
Figure 5.5: Time evolution of the boundary phase shift $\cos(\gamma(t))$ for (a) Coulomb metal and (b) Hund metal. The function illustrates the induced modulations in the LDOS through boundary conditions within a TLL framework.

$$A(x,t) = \cos(\gamma(t))\bar{A}(x,t) \tag{5.29}$$

where $\bar{A}(x,t)$ is the time ordered correlation function of TLL, the complicated function expressed in terms of $Sinh^a(x,t)$. The additional dependence, that enters into retarded correlation function, is introduced by a boundary phase shift, the $\cos(\gamma(t))$ and has a form of a sequence of step-functions:

$$\gamma(t) = \begin{cases} \frac{\pi}{2}(a_s + a_c), & 0 < t < \frac{2r}{v_c} \\ \frac{\pi}{2}(a_s + a_c + b_c), & \frac{2r}{v_c} < t < \frac{2r}{v_s} \\ \frac{\pi}{2}(a_s + a_c + b_c + b_s), & \frac{2r}{v_s} < t < \infty \end{cases} \tag{5.30}$$

The overall time integral (t-domain Fourier transform to ω-domain) can be solved by means of integration by parts, namely taking

$$dv = \bar{A}(x,t)$$

and

$$u = \cos(\gamma(t)) \approx sign(t - t_0).$$

Then we have:

$$\int_0^\infty u\,dv = -\int_0^\infty v\,du + vu\Big|_0^\infty$$

Since du is a sum of Dirac deltas (derivative of the sequence of step functions), the first term simply gives $v = \int \bar{A}(x,t)$. The second term, depending on the position of phase shift, may cancel out the value of v at zero. This fenomenon ocuurs for Coulomb metal but not for Hund metal.

5.4.2 Coulomb metal

A case has been identified where an exact analytic solution can be derived. The choice of $-b_c/2 = 1$ and $-b_s/2 = 0$ is the one, for which the analytic Fourier transformation of Eq. 5.27, is the following:

$$N(\omega, \beta, r) = \frac{2}{\alpha_{cut-off}\pi^2} v_c^{-a_c} v_s^{-a_s} \left[\pi^{a_c+a_s} \operatorname{csch}^2\left(\frac{2\pi r}{v_c\beta}\right) \left[2^{-2+a_c+a_s} e^{-\frac{\pi t(a_c+a_s)}{\beta}} \right. \right.$$

$$\times \left(-e^{-\frac{\pi t}{\beta}} + e^{\frac{\pi t}{\beta}}\right)^{-a_c-a_s} \left(-1+e^{\frac{2\pi t}{\beta}}\right) \cosh\left(\frac{4\pi r}{\beta v_c}\right) \sinh^{a_c+a_s}\left(\frac{\pi t}{\beta}\right) \left(\frac{\beta \sinh\left(\frac{\pi t}{\beta}\right)}{\alpha_{cut-off}}\right)^{-a_c-a_s}$$

$$\times \left(\frac{e^{\frac{t(-i\beta\omega+\pi a_c+\pi a_s)}{\beta}}\beta\, {}_2F_1\left[1, \frac{1}{2}\left(2-\frac{i\beta\omega}{\pi}-a_c-a_s\right), \frac{1}{2}\left(2-\frac{i\beta\omega}{\pi}+a_c+a_s\right), e^{\frac{2\pi t}{\beta}}\right]}{i\beta\omega - \pi a_c - \pi a_s} \right.$$

$$\left. - \frac{e^{\frac{t(i\beta\omega+\pi a_c+\pi a_s)}{\beta}}\beta\, {}_2F_1\left[1, \frac{1}{2}\left(2+\frac{i\beta\omega}{\pi}-a_c-a_s\right), \frac{1}{2}\left(2+\frac{i\beta\omega}{\pi}+a_c+a_s\right), e^{\frac{2\pi t}{\beta}}\right]}{i\beta\omega + \pi a_c + \pi a_s} \right)$$

$$- 2^{-3+a_c+a_s} e^{-\frac{\pi t(a_c+a_s)}{\beta}} \left(-e^{-\frac{\pi t}{\beta}} + e^{\frac{\pi t}{\beta}}\right)^{-a_c-a_s}$$

$$\times \left(-1+e^{\frac{2\pi t}{\beta}}\right) \beta \sinh^{a_c+a_s}\left(\frac{\pi t}{\beta}\right) \left(\frac{\beta \sinh\left(\frac{\pi t}{\beta}\right)}{\alpha_{cut-off}}\right)^{-a_c-a_s}$$

$$\times \left(-\frac{e^{\frac{t(-2\pi-i\beta\omega+\pi a_c+\pi a_s)}{\beta}}\, {}_2F_1\left[1, -\frac{1}{2}\left(\frac{i\beta\omega}{\pi}+a_c+a_s\right), \frac{1}{2}\left(-\frac{i\beta\omega}{\pi}+a_c+a_s\right), e^{\frac{2\pi t}{\beta}}\right]}{-2\pi - i\beta\omega + \pi a_c + \pi a_s} \right.$$

$$- \frac{e^{\frac{t(2\pi-i\beta\omega+\pi a_c+\pi a_s)}{\beta}}\, {}_2F_1\left[1, \frac{1}{2}\left(4-\frac{i\beta\omega}{\pi}-a_c-a_s\right), \frac{1}{2}\left(4-\frac{i\beta\omega}{\pi}+a_c+a_s\right), e^{\frac{2\pi t}{\beta}}\right]}{2\pi - i\beta\omega + \pi a_c + \pi a_s}$$

$$- \frac{e^{\frac{t(-2\pi+i\beta\omega+\pi a_c+\pi a_s)}{\beta}}\, {}_2F_1\left[1, \frac{1}{2}\left(-\frac{i\beta\omega}{\pi}+a_c+a_s\right), \frac{1}{2}\left(\frac{i\beta\omega}{\pi}+a_c+a_s\right), e^{\frac{2\pi t}{\beta}}\right]}{-2\pi + i\beta\omega + \pi a_c + \pi a_s}$$

$$\left. \left. - \frac{e^{\frac{t(2\pi+i\beta\omega+\pi a_c+\pi a_s)}{\beta}}\, {}_2F_1\left[1, \frac{1}{2}\left(4+\frac{i\beta\omega}{\pi}-a_c-a_s\right), \frac{1}{2}\left(4+\frac{i\beta\omega}{\pi}+a_c+a_s\right), e^{\frac{2\pi t}{\beta}}\right]}{2\pi + i\beta\omega + \pi a_c + \pi a_s} \right) \right]$$

$$\left. - \frac{1}{4}t\left(\frac{t}{\alpha_{cut-off}}\right)^{-a_c-a_s}\left(\frac{t^2 v_c^2}{r^2(a_c+a_s-3)} - \frac{4}{a_c+a_s-1}\right) \right] \tag{5.31}$$

It is stated that the case when $-b_c/2 = 1$, $-b_s/2 = 0$, corresponds to $a_c = 2.015$, $a_s = \frac{1}{4}$. This implies $K_{\rho+} = K^* = 0.25$, and we further take $K_{\sigma-} = 1$ which is used in further calculations while $K_{\rho-}$ and $K_{\sigma+}$ are kept as free parameters. There is only one mode with velocity v_c, the holon, and for this pole the value b_c automatically determines $K_{\rho+}$. If a simple spin-full fermionic chain were focused on, $b_s = 0$ would imply a "noninteracting" (i.e. SU(2) invariant) spin degree of freedom with $K_s = 1$. In the case of two-leg ladder (that is examined in this chapter), the other pole has three bosonic modes $\nu = \sigma_+, \sigma_-, \rho_-$ contributing (see Eq. 5.26). Thus, even with setting $b_s = 0$, there is a certain freedom in the choice of these TLL parameters. It should be emphasized that the condition $b_s = 0$ does not mean the complete absence of the spin degree of freedom in the system, as $a_s \neq 0$, but rather that there is no spatial dependence induced by the spin degree of freedom.

$$K_s = K_{\rho-} + K_{\sigma+} + K_{\sigma-} \tag{5.32}$$

$$K_{\rho-} + K_{\sigma+} + K_{\sigma-} = 1 \tag{5.33}$$

While this is a result obtained at a particular point, it should be emphasized that since the $N(r, \omega; \beta)$ is a continuous function of K_ν, our results are expected to provide a good indicator for an overall behaviour of this function in a strongly correlated case. Furthermore,
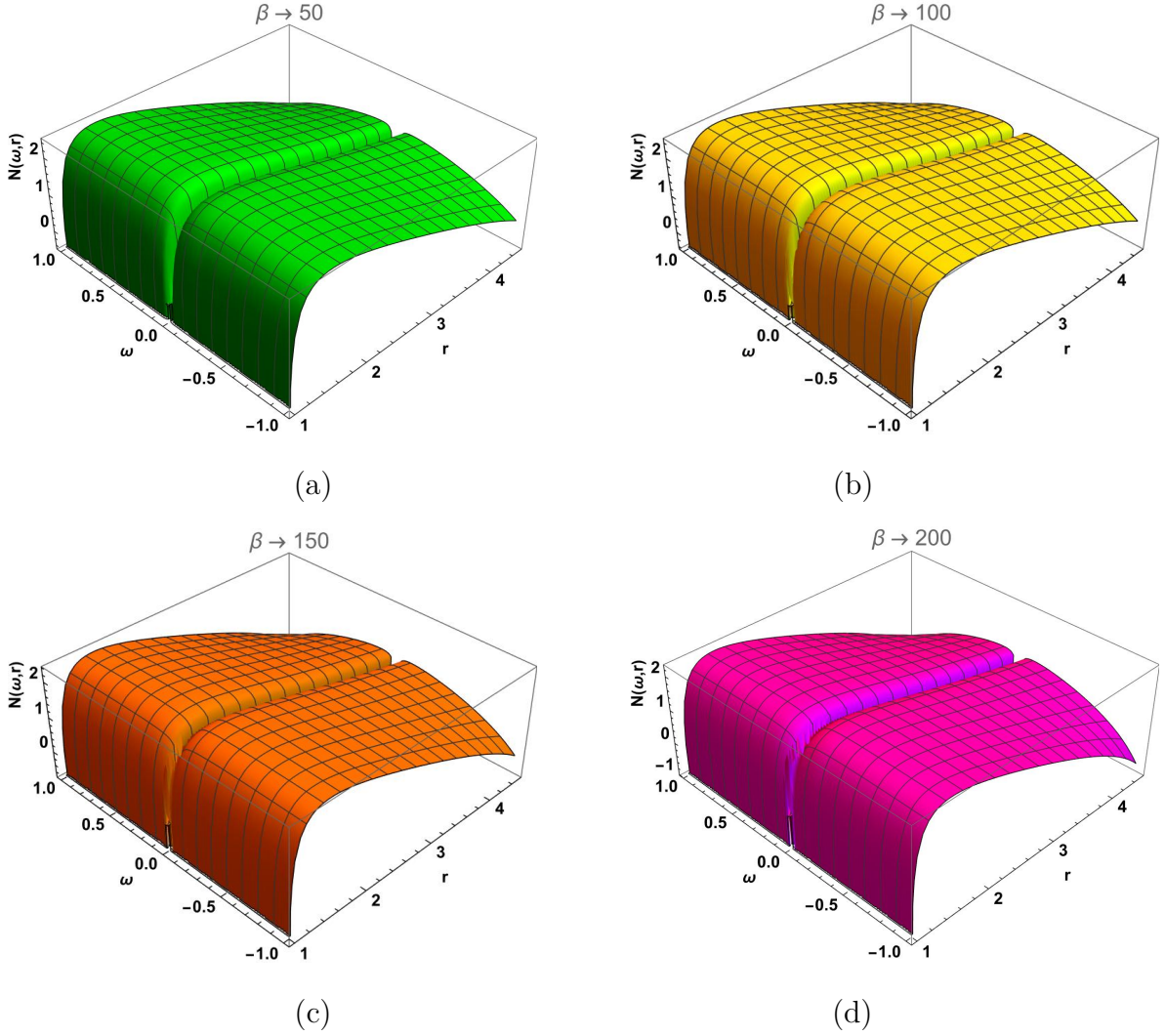
Figure 5.6: TLL DOS for **Coulomb metal** as a function of energy ω and the distance from the boundary r (tip of the carbon nanotube, unit of r is $1/V_F$); when (a) $\beta = 50$, (b) $\beta = 100$, (c) $\beta = 150$, (d) $\beta = 200$. The $\beta = 1/T$ is inverse temperature with a unit set by the fact that the unit of energy was set by $v_F = 1$.

the obtained value lies close to a limiting (separatrix) behaviour of a sine-Gordon model, i.e. a TLL with a cosine perturbation, where the latter term may arise backscattering. Thus, this result is expected to manifest frequently in real-life experiments. Finally, it should be noted that although the problem was solved with two bosonic poles (velocities), this can correspond to the situation with indeed only two modes, and equally well to the situation with more modes provided that there are only two velocities (i.e. some modes are degenerated).

Thus our solution works for the physically relevant case when $K_\rho \approx 1/4$ as measured experimentally [181]. This also corresponds to a close vicinity of marginal RG flow for the case of a half-filled band. The proximity of nanotubes to the Mott-insulating phase has been identified in several earlier works [182]. Here it is assumed that in the charge sector the system can flow towards the Mott phase consistently moving towards the critical value $K^* = 1/2$. However, due to weak incommensurability, such as co-doping between SWNT shells of MWNT, the system is in a Luther-Emery liquid with parameter $K^*/2 = 1/4$. If intra-tube repulsive interactions are too weak to push the system towards these small
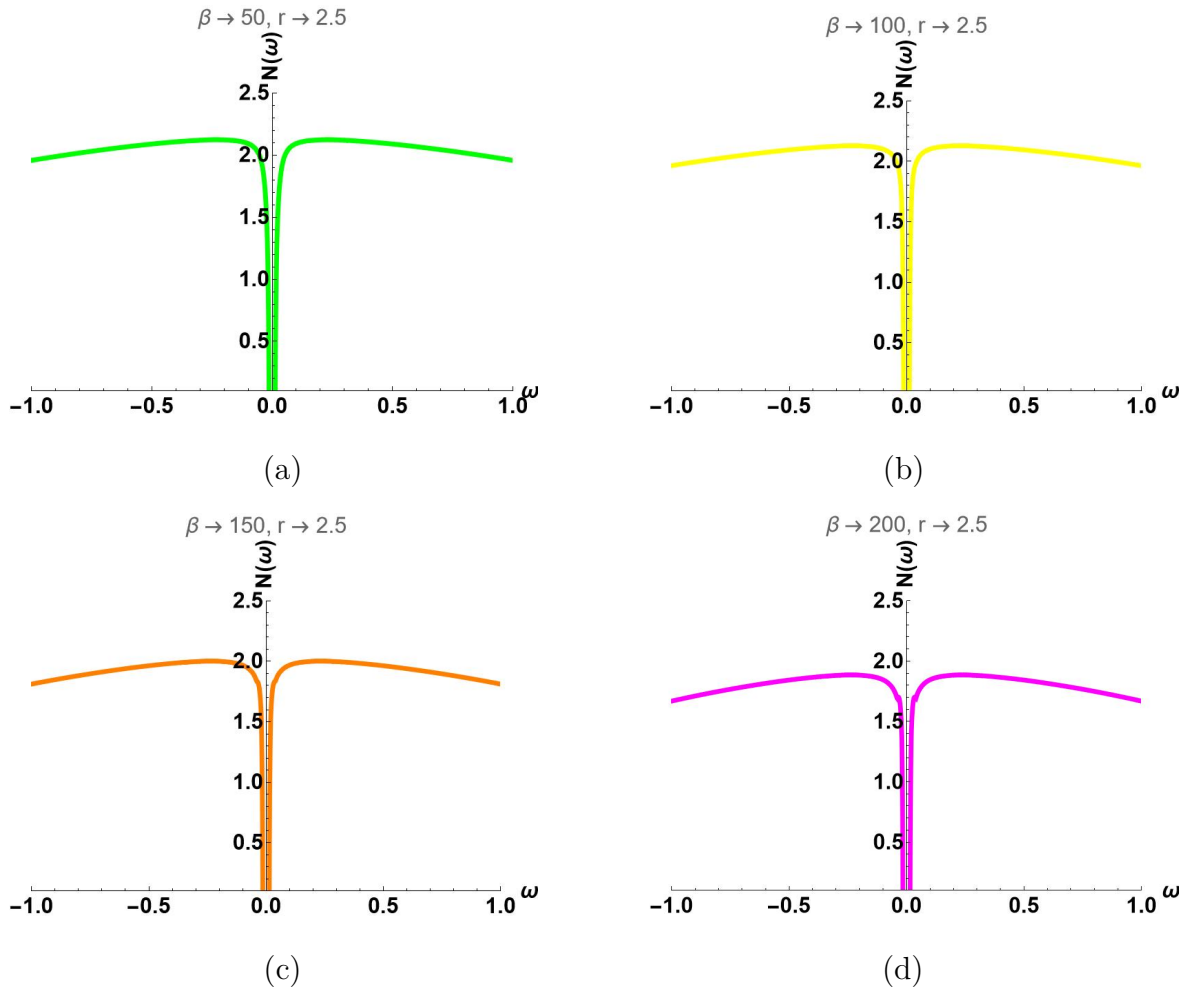
Figure 5.7: TLL DOS for **Coulomb metal** as a function of energy ω. The distance from the boundary r (tip of the carbon nanotube) is a constant and $r = 2.50\frac{1}{V_F}$, (a) $\beta = 50$, (b) $\beta = 100$, (c) $\beta = 150$, (d) $\beta = 200$.
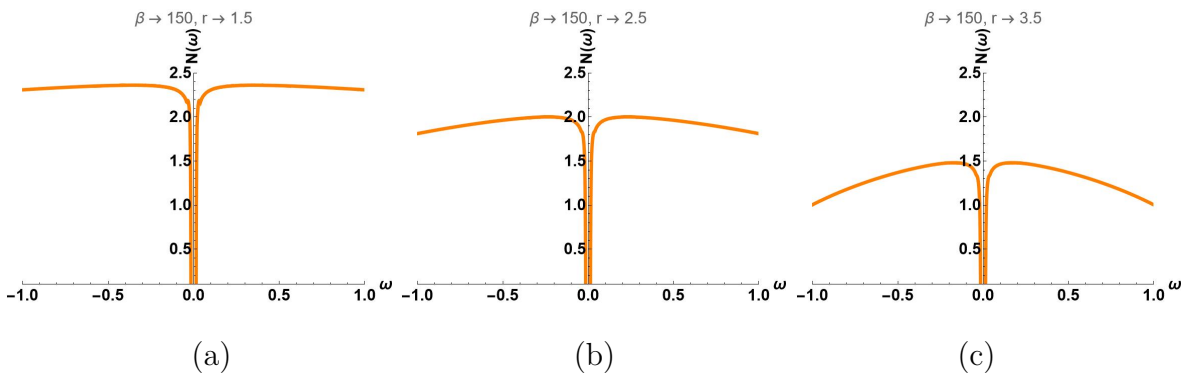
Figure 5.8: TLL DOS for **Coulomb metal** as a function of energy ω. r is the distance from the boundary (tip of the carbon nanotube, a unit of r is $1/V_F$); when $\beta = 150$, (a) $r = 1.5$, (b) $r = 2.5$, (c) $r = 3.5$.

values, there are always inter-tube Coulomb interactions that can be incorporated in our modelling and will further modify downwards the $K_{\rho+}$ parameter [165]. This explains why such a value is frequently observed in experiments done on SWCNT. At absolute zero temperature, it is established that DOS diminishes to zero at the Fermi energy following a power law in ω, known as a zero-bias anomaly (ZBA). Here, the DOS for TLL will be analized under finite temperature conditions.

Fig. 5.6 illustrates the LDOS as a function of ω and r at various temperatures, where ω is measured relative to the Fermi energy and r is the distance from the boundary. At $\omega = 0$, the energy corresponds to the Fermi level, serving as a critical reference point for energy levels. This deep at $\omega = 0$ is a well-documented signature of 1D physics, known as the "zero-bias anomaly" that has been experimentally observed in various systems, for instance, in carbon nanotubes [181] or in semiconductor gated wires [183], [184], and quite recently, even in controlled 2D to 1D crossover [185]. The figure (Fig. 5.6) shows LDOS both below and above the Fermi energy, providing valuable insights into the energy distribution characteristics within the confined TLL of the nanotube.

A profound deep is observed close to $\omega = 0$ and a deep when r is going down to 1. These features are sharper at temperatures lower; in this case, when $\beta = 200$, it is sharper than when $\beta = 50$. Then, it increases to a maximum when r is a few lattice spacing, after which it decreases as we move deeper into the carbon nanotube. It is important to mention that the double peak structure observed for values where $\omega > 0$ may be probably related to the well-established 1D hallmark known as spin-charge separation that was also experimentally measured in several systems [183], [184], [186], [187], [188].

Fig. 5.7 illustrates the LDOS as a function of ω, when the distance from the boundary r is a constant and $r = 2.50 \frac{1}{V_F}$.

Fig. 5.8 illustrates the LDOS as a function of ω at a fixed inverse temperature $\beta = 150$, when the distance from the boundary r is (a) $1.50 \frac{1}{V_F}$, (b) $2.50 \frac{1}{V_F}$, and (c) $3.50 \frac{1}{V_F}$. We observe

- large amplitude for smaller r,

- faster decay (as ω) for larger r,

- ZBA is probably sharper for smaller r.

5.4.3 Hund metal

The case where $b_s = 0$ corresponds to the situation when $K_s = 1$ (all $K_\nu = 1$ for all neutral modes), representing a noninteracting value. This can be realized for purely charge and long-range interactions such as Coulomb interactions. The case of $b_s = b_c$ implies that both spin and charge sectors are equally shifted away from the noninteracting point. This can be implemented for on-site interactions under the condition that only parallel spin electrons interact. Such a situation may arise, for instance, in a Hund metal, where Hund exchange J_H dominates low-energy physics. Hund's rules state that (due to anti-symmetrization of the wavefunction) the states with maximum multiplicity, i.e., states with parallel spins, are energetically favoured. Materials where the Hund's rule dominates are the base of late d-orbital transition metal compounds (e.g. oxides or chalcogenides of iron, cobalt or nickel) but they will play an important role also in neighbouring heavy p-orbital materials based on tin and lead. Importantly, each of these

materials also exists in 2D form, e.g. stanene or plumbene, so in the future, they may also be rolled up into nanotubes, just as graphene into CNTs.

In a special case where $-b_c/2 = 1$ and $-b_s/2 = 1$ the integral can be performed analytically, and the resulting indefinite integral reads:

$$N(\omega, \beta, r) = \frac{2}{\alpha_{cut-off}\pi^2} v_c^{-a_c} v_s^{-a_s} \left[\pi^{a_c+a_s} \operatorname{csch}^2\left(\frac{2\pi r}{v_c\beta}\right) \operatorname{csch}^2\left(\frac{2\pi r}{v_s\beta}\right) \left[2^{-4+a_c+a_s} e^{-\frac{\pi t(a_c+a_s)}{\beta}} \right. \right.$$

$$\times \left(-e^{-\frac{\pi t}{\beta}} + e^{\frac{\pi t}{\beta}}\right)^{-a_c-a_s} \left(-1 + e^{\frac{2\pi t}{\beta}}\right) \sinh^{a_c+a_s}\left(\frac{\pi t}{\beta}\right) \left(\frac{\beta \sinh\left(\frac{\pi t}{\beta}\right)}{\alpha_{cut-off}}\right)^{-a_c-a_s}$$

$$\times \left(\frac{e^{\frac{t(-i\beta\omega+\pi a_c+\pi a_s)}{\beta}} \beta \, _2F_1\left[1, \frac{1}{2}\left(2 - \frac{i\beta\omega}{\pi} - a_c - a_s\right), \frac{1}{2}\left(2 - \frac{i\beta\omega}{\pi} + a_c + a_s\right), e^{\frac{2\pi t}{\beta}}\right]}{i\beta\omega - \pi a_c - \pi a_s}\right.$$

$$\left.- \frac{e^{\frac{t(i\beta\omega+\pi a_c+\pi a_s)}{\beta}} \beta \, _2F_1\left[1, \frac{1}{2}\left(2 + \frac{i\beta\omega}{\pi} - a_c - a_s\right), \frac{1}{2}\left(2 + \frac{i\beta\omega}{\pi} + a_c + a_s\right), e^{\frac{2\pi t}{\beta}}\right]}{i\beta\omega + \pi a_c + \pi a_s}\right)$$

$$+ 2^{-4+a_c+a_s} e^{-\frac{\pi t(a_c+a_s)}{\beta}} \left(-e^{-\frac{\pi t}{\beta}} + e^{\frac{\pi t}{\beta}}\right)^{-a_c-a_s} \left(-1 + e^{\frac{2\pi t}{\beta}}\right)$$

$$\times \cosh\left(\frac{4\pi r\left(\frac{1}{v_c} - \frac{1}{v_s}\right)}{\beta}\right) \sinh^{a_c+a_s}\left(\frac{\pi t}{\beta}\right) \left(\frac{\beta \sinh\left(\frac{\pi t}{\beta}\right)}{\alpha_{cut-off}}\right)^{-a_c-a_s}$$

$$\times \left(\frac{e^{\frac{t(-i\beta\omega+\pi a_c+\pi a_s)}{\beta}} \beta \, _2F_1\left[1, \frac{1}{2}\left(2 - \frac{i\beta\omega}{\pi} - a_c - a_s\right), \frac{1}{2}\left(2 - \frac{i\beta\omega}{\pi} + a_c + a_s\right), e^{\frac{2\pi t}{\beta}}\right]}{i\beta\omega - \pi a_c - \pi a_s}\right.$$

$$\left.- \frac{e^{\frac{t(i\beta\omega+\pi a_c+\pi a_s)}{\beta}} \beta \, _2F_1\left[1, \frac{1}{2}\left(2 + \frac{i\beta\omega}{\pi} - a_c - a_s\right), \frac{1}{2}\left(2 + \frac{i\beta\omega}{\pi} + a_c + a_s\right), e^{\frac{2\pi t}{\beta}}\right]}{i\beta\omega + \pi a_c + \pi a_s}\right)$$

$$+ 2^{-4+a_c+a_s} e^{-\frac{\pi t(a_c+a_s)}{\beta}} \left(-e^{-\frac{\pi t}{\beta}} + e^{\frac{\pi t}{\beta}}\right)^{-a_c-a_s} \left(-1 + e^{\frac{2\pi t}{\beta}}\right)$$

$$\times \cosh\left(\frac{4\pi r(v_c + v_s)}{\beta v_c v_s}\right) \sinh^{a_c+a_s}\left(\frac{\pi t}{\beta}\right) \left(\frac{\beta \sinh\left(\frac{\pi t}{\beta}\right)}{\alpha_{cut-off}}\right)^{-a_c-a_s}$$

$$\times \left(\frac{e^{\frac{t(-i\beta\omega+\pi a_c+\pi a_s)}{\beta}} \beta \, _2F_1\left[1, \frac{1}{2}\left(2 - \frac{i\beta\omega}{\pi} - a_c - a_s\right), \frac{1}{2}\left(2 - \frac{i\beta\omega}{\pi} + a_c + a_s\right), e^{\frac{2\pi t}{\beta}}\right]}{i\beta\omega - \pi a_c - \pi a_s}\right.$$

$$\left.- \frac{e^{\frac{t(i\beta\omega+\pi a_c+\pi a_s)}{\beta}} \beta \, _2F_1\left[1, \frac{1}{2}\left(2 + \frac{i\beta\omega}{\pi} - a_c - a_s\right), \frac{1}{2}\left(2 + \frac{i\beta\omega}{\pi} + a_c + a_s\right), e^{\frac{2\pi t}{\beta}}\right]}{i\beta\omega + \pi a_c + \pi a_s}\right)$$

$$+ 2^{-5+a_c+a_s} e^{-\frac{\pi t(a_c+a_s)}{\beta}} \left(-e^{-\frac{\pi t}{\beta}} + e^{\frac{\pi t}{\beta}}\right)^{-a_c-a_s}$$

$$\times \left(-1 + e^{\frac{2\pi t}{\beta}}\right) \beta \sinh^{a_c+a_s}\left(\frac{\pi t}{\beta}\right) \left(\frac{\beta \sinh\left(\frac{\pi t}{\beta}\right)}{\alpha_{cut-off}}\right)^{-a_c-a_s}$$

$$\times \left(-\frac{e^{\frac{t(-4\pi-i\beta\omega+\pi a_c+\pi a_s)}{\beta}} \, _2F_1\left[1, -\frac{1}{2}\left(2 + \frac{i\beta\omega}{\pi} + a_c + a_s\right), \frac{1}{2}\left(-2 - \frac{i\beta\omega}{\pi} + a_c + a_s\right), e^{\frac{2\pi t}{\beta}}\right]}{-4\pi - i\beta\omega + \pi a_c + \pi a_s}\right.$$

$$- \frac{e^{\frac{t(4\pi-i\beta\omega+\pi a_c+\pi a_s)}{\beta}} \, _2F_1\left[1, \frac{1}{2}\left(6 - \frac{i\beta\omega}{\pi} - a_c - a_s\right), \frac{1}{2}\left(6 - \frac{i\beta\omega}{\pi} + a_c + a_s\right), e^{\frac{2\pi t}{\beta}}\right]}{4\pi - i\beta\omega + \pi a_c + \pi a_s}$$

$$- \frac{e^{\frac{t(-4\pi+i\beta\omega+\pi a_c+\pi a_s)}{\beta}} \, _2F_1\left[1, \frac{1}{2}\left(-2 + \frac{i\beta\omega}{\pi} - a_c - a_s\right), \frac{1}{2}\left(-2 + \frac{i\beta\omega}{\pi} + a_c + a_s\right), e^{\frac{2\pi t}{\beta}}\right]}{-4\pi + i\beta\omega + \pi a_c + \pi a_s}$$

$$- \frac{e^{\frac{t(4\pi + i\beta\omega + \pi a_c + \pi a_s)}{\beta}} \, _2F_1\left[1, \frac{1}{2}\left(6 + \frac{i\beta\omega}{\pi} - a_c - a_s\right), \frac{1}{2}\left(6 + \frac{i\beta\omega}{\pi} + a_c + a_s\right), e^{\frac{2\pi t}{\beta}}\right]}{4\pi + i\beta\omega + \pi a_c + \pi a_s}\Bigg)$$

$$- 2^{-5 + a_c + a_s} e^{-\frac{\pi(4r + t a_c v_c + t a_s v_c)}{\beta v_c}} \left(-e^{-\frac{\pi t}{\beta}} + e^{\frac{\pi t}{\beta}}\right)^{-a_c - a_s}$$

$$\times \left(1 - e^{\frac{2\pi t}{\beta}}\right)^{a_c + a_s} \sinh^{a_c + a_s}\left(\frac{\pi t}{\beta}\right) \left(\frac{\beta \sinh\left(\frac{\pi t}{\beta}\right)}{\alpha_{cut-off}}\right)^{-a_c - a_s}$$

$$\Bigg(\frac{ie^{\frac{t(2\pi - i\beta\omega + \pi a_c + \pi a_s)}{\beta}} \beta \, _2F_1\left[a_c + a_s, \frac{1}{2}\left(2 - \frac{i\beta\omega}{\pi} + a_c + a_s\right), \frac{1}{2}\left(4 - \frac{i\beta\omega}{\pi} + a_c + a_s\right), e^{\frac{2\pi t}{\beta}}\right]}{2i\pi + \beta\omega + i\pi a_c + i\pi a_s}$$

$$+ \beta\Bigg(\frac{e^{\frac{t(-2\pi - i\beta\omega + \pi a_c + \pi a_s) + \frac{8\pi r}{v_c}}{\beta}} \, _2F_1\left[a_c + a_s, \frac{1}{2}\left(-2 - \frac{i\beta\omega}{\pi} + a_c + a_s\right), \frac{1}{2}\left(-\frac{i\beta\omega}{\pi} + a_c + a_s\right), e^{\frac{2\pi t}{\beta}}\right]}{-2\pi - i\beta\omega + \pi a_c + \pi a_s}$$

$$+ \frac{e^{\frac{t(-2\pi + i\beta\omega + \pi a_c + \pi a_s) + \frac{8\pi r}{v_c}}{\beta}} \, _2F_1\left[a_c + a_s, \frac{1}{2}\left(-2 + \frac{i\beta\omega}{\pi} + a_c + a_s\right), \frac{1}{2}\left(\frac{i\beta\omega}{\pi} + a_c + a_s\right), e^{\frac{2\pi t}{\beta}}\right]}{-2\pi + i\beta\omega + \pi a_c + \pi a_s}$$

$$+ \frac{e^{\frac{t(2\pi + i\beta\omega + \pi a_c + \pi a_s)}{\beta}} \, _2F_1\left[a_c + a_s, \frac{1}{2}\left(2 + \frac{i\beta\omega}{\pi} + a_c + a_s\right), \frac{1}{2}\left(4 + \frac{i\beta\omega}{\pi} + a_c + a_s\right), e^{\frac{2\pi t}{\beta}}\right]}{2\pi + i\beta\omega + \pi a_c + \pi a_s}\Bigg)\Bigg)$$

$$- 2^{-5 + a_c + a_s} e^{-\frac{\pi(4r + t a_c v_s + t a_s v_s)}{\beta v_s}} \left(-e^{-\frac{\pi t}{\beta}} + e^{\frac{\pi t}{\beta}}\right)^{-a_c - a_s}$$

$$\times \left(1 - e^{\frac{2\pi t}{\beta}}\right)^{a_c + a_s} \sinh^{a_c + a_s}\left(\frac{\pi t}{\beta}\right) \left(\frac{\beta \sinh\left(\frac{\pi t}{\beta}\right)}{\alpha_{cut-off}}\right)^{-a_c - a_s}$$

$$\Bigg(\frac{ie^{\frac{t(2\pi - i\beta\omega + \pi a_c + \pi a_s)}{\beta}} \beta \, _2F_1\left[a_c + a_s, \frac{1}{2}\left(2 - \frac{i\beta\omega}{\pi} + a_c + a_s\right), \frac{1}{2}\left(4 - \frac{i\beta\omega}{\pi} + a_c + a_s\right), e^{\frac{2\pi t}{\beta}}\right]}{2i\pi + \beta\omega + i\pi a_c + i\pi a_s}$$

$$+ \beta\Bigg(\frac{e^{\frac{t(-2\pi - i\beta\omega + \pi a_c + \pi a_s) + \frac{8\pi r}{v_s}}{\beta}} \, _2F_1\left[a_c + a_s, \frac{1}{2}\left(-2 - \frac{i\beta\omega}{\pi} + a_c + a_s\right), \frac{1}{2}\left(-\frac{i\beta\omega}{\pi} + a_c + a_s\right), e^{\frac{2\pi t}{\beta}}\right]}{-2\pi - i\beta\omega + \pi a_c + \pi a_s}$$

$$+ \frac{e^{\frac{t(-2\pi + i\beta\omega + \pi a_c + \pi a_s) + \frac{8\pi r}{v_s}}{\beta}} \, _2F_1\left[a_c + a_s, \frac{1}{2}\left(-2 + \frac{i\beta\omega}{\pi} + a_c + a_s\right), \frac{1}{2}\left(\frac{i\beta\omega}{\pi} + a_c + a_s\right), e^{\frac{2\pi t}{\beta}}\right]}{-2\pi + i\beta\omega + \pi a_c + \pi a_s}$$

$$+ \frac{e^{\frac{t(2\pi + i\beta\omega + \pi a_c + \pi a_s)}{\beta}} \, _2F_1\left[a_c + a_s, \frac{1}{2}\left(2 + \frac{i\beta\omega}{\pi} + a_c + a_s\right), \frac{1}{2}\left(4 + \frac{i\beta\omega}{\pi} + a_c + a_s\right), e^{\frac{2\pi t}{\beta}}\right]}{2\pi + i\beta\omega + \pi a_c + \pi a_s}\Bigg)\Bigg)$$

$$- 2^{-5 + a_c + a_s} e^{-\frac{\pi(4r + t a_c v_c + t a_s v_c)}{\beta v_c}} \left(-e^{-\frac{\pi t}{\beta}} + e^{\frac{\pi t}{\beta}}\right)^{-a_c - a_s}$$

$$\times \left(1 - e^{\frac{2\pi t}{\beta}}\right)^{a_c + a_s} \sinh^{a_c + a_s}\left(\frac{\pi t}{\beta}\right) \left(\frac{\beta \sinh\left(\frac{\pi t}{\beta}\right)}{\alpha_{cut-off}}\right)^{-a_c - a_s}$$

$$\Bigg(\frac{ie^{\frac{t(2\pi - i\beta\omega + \pi a_c + \pi a_s) + \frac{8\pi r}{v_c}}{\beta}} \beta \, _2F_1\left[a_c + a_s, \frac{1}{2}\left(2 - \frac{i\beta\omega}{\pi} + a_c + a_s\right), \frac{1}{2}\left(4 - \frac{i\beta\omega}{\pi} + a_c + a_s\right), e^{\frac{2\pi t}{\beta}}\right]}{2i\pi + \beta\omega + i\pi a_c + i\pi a_s}$$

$$+ \beta\Bigg(\frac{e^{\frac{t(-2\pi - i\beta\omega + \pi a_c + \pi a_s)}{\beta}} \, _2F_1\left[a_c + a_s, \frac{1}{2}\left(-2 - \frac{i\beta\omega}{\pi} + a_c + a_s\right), \frac{1}{2}\left(-\frac{i\beta\omega}{\pi} + a_c + a_s\right), e^{\frac{2\pi t}{\beta}}\right]}{-2\pi - i\beta\omega + \pi a_c + \pi a_s}$$

$$+ \frac{e^{\frac{t(-2\pi + i\beta\omega + \pi a_c + \pi a_s)}{\beta}} \, _2F_1\left[a_c + a_s, \frac{1}{2}\left(-2 + \frac{i\beta\omega}{\pi} + a_c + a_s\right), \frac{1}{2}\left(\frac{i\beta\omega}{\pi} + a_c + a_s\right), e^{\frac{2\pi t}{\beta}}\right]}{-2\pi + i\beta\omega + \pi a_c + \pi a_s}$$

$$+ \frac{e^{\frac{t(2\pi+i\beta\omega+\pi a_c+\pi a_s)+\frac{8\pi r}{v_c}}{\beta}} \,{}_2F_1\left[a_c+a_s,\frac{1}{2}\left(2+\frac{i\beta\omega}{\pi}+a_c+a_s\right),\frac{1}{2}\left(4+\frac{i\beta\omega}{\pi}+a_c+a_s\right),e^{\frac{2\pi t}{\beta}}\right]}{2\pi+i\beta\omega+\pi a_c+\pi a_s}\Bigg)\Bigg)$$

$$-2^{-5+a_c+a_s}e^{-\frac{\pi(4r+ta_c v_s+ta_s v_s)}{\beta v_s}}\left(-e^{-\frac{\pi t}{\beta}}+e^{\frac{\pi t}{\beta}}\right)^{-a_c-a_s}$$

$$\times\left(1-e^{\frac{2\pi t}{\beta}}\right)^{a_c+a_s}\sinh^{a_c+a_s}\left(\frac{\pi t}{\beta}\right)\left(\frac{\beta\sinh\left(\frac{\pi t}{\beta}\right)}{\alpha_{cut-off}}\right)^{-a_c-a_s}$$

$$\times\Bigg(\frac{ie^{\frac{t(2\pi-i\beta\omega+\pi a_c+\pi a_s)+\frac{8\pi r}{v_s}}{\beta}}\beta\,{}_2F_1\left[a_c+a_s,\frac{1}{2}\left(2-\frac{i\beta\omega}{\pi}+a_c+a_s\right),\frac{1}{2}\left(4-\frac{i\beta\omega}{\pi}+a_c+a_s\right),e^{\frac{2\pi t}{\beta}}\right]}{2i\pi+\beta\omega+i\pi a_c+i\pi a_s}$$

$$+\beta\Bigg(\frac{e^{\frac{t(-2\pi-i\beta\omega+\pi a_c+\pi a_s)}{\beta}}\,{}_2F_1\left[a_c+a_s,\frac{1}{2}\left(-2-\frac{i\beta\omega}{\pi}+a_c+a_s\right),\frac{1}{2}\left(-\frac{i\beta\omega}{\pi}+a_c+a_s\right),e^{\frac{2\pi t}{\beta}}\right]}{-2\pi-i\beta\omega+\pi a_c+\pi a_s}$$

$$+\frac{e^{\frac{t(-2\pi+i\beta\omega+\pi a_c+\pi a_s)}{\beta}}\,{}_2F_1\left[a_c+a_s,\frac{1}{2}\left(-2+\frac{i\beta\omega}{\pi}+a_c+a_s\right),\frac{1}{2}\left(\frac{i\beta\omega}{\pi}+a_c+a_s\right),e^{\frac{2\pi t}{\beta}}\right]}{-2\pi+i\beta\omega+\pi a_c+\pi a_s}$$

$$+\frac{e^{\frac{t(2\pi+i\beta\omega+\pi a_c+\pi a_s)+\frac{8\pi r}{v_s}}{\beta}}\,{}_2F_1\left[a_c+a_s,\frac{1}{2}\left(2+\frac{i\beta\omega}{\pi}+a_c+a_s\right),\frac{1}{2}\left(4+\frac{i\beta\omega}{\pi}+a_c+a_s\right),e^{\frac{2\pi t}{\beta}}\right]}{2\pi+i\beta\omega+\pi a_c+\pi a_s}\Bigg)\Bigg)\Bigg]$$

$$-\frac{1}{16}t\left(\frac{t}{\alpha}\right)^{-a_c-a_s}\left(-\frac{t^4v_c^2v_s^2}{r^4(a_c+a_s-5)}+\frac{4t^2\left(v_c^2+v_s^2\right)}{r^2(a_c+a_s-3)}-\frac{16}{a_c+a_s-1}\right)\Bigg] \quad (5.34)$$

Although the formulas themselves are quite lengthy, some useful remarks can be made from their functional form. Each formula consists of several building blocks with hypergeometric $_2F_1$ function in the numerator. Some of these include an extra π phase shift in the argument and spatially dependent pre-factors $\sim v_\rho r$.

There are two types of spatially dependent pre-factors for the Hund metal case:

$$\sim (v_\rho+v_\sigma)/2r$$

and

$$\sim (v_\rho-v_\sigma)/2r.$$

This is a manifestation of the fact that i) now both spin and charge contribute to spatial dependence; ii) the two waves can interfere. The known relation can be used between the hypergeometric $_2F_1$ function and the incomplete Beta function:

$$B_\varkappa(a,b)=\frac{\varkappa^a(1-\varkappa)^{b-1}}{a}\,{}_2F_1(1,1-b,a+1;\frac{\varkappa}{\varkappa-1}) \quad (5.35)$$

which upon substitutions

$$\varkappa\to\left(1-\exp\left[-\frac{2\pi}{\beta}t\right]\right)^{-1}$$

$$a\to\frac{1}{2}\left(a_c+a_s+\frac{i\beta\omega}{\pi}\right)$$

$$b\to\frac{1}{2}\left(a_c+a_s-\frac{i\beta\omega}{\pi}\right)$$

proves that our formula can be re-expressed in terms of hypergeometric Beta functions. It is well known that the Fourier transform in the bulk TLL is given in terms of the Beta
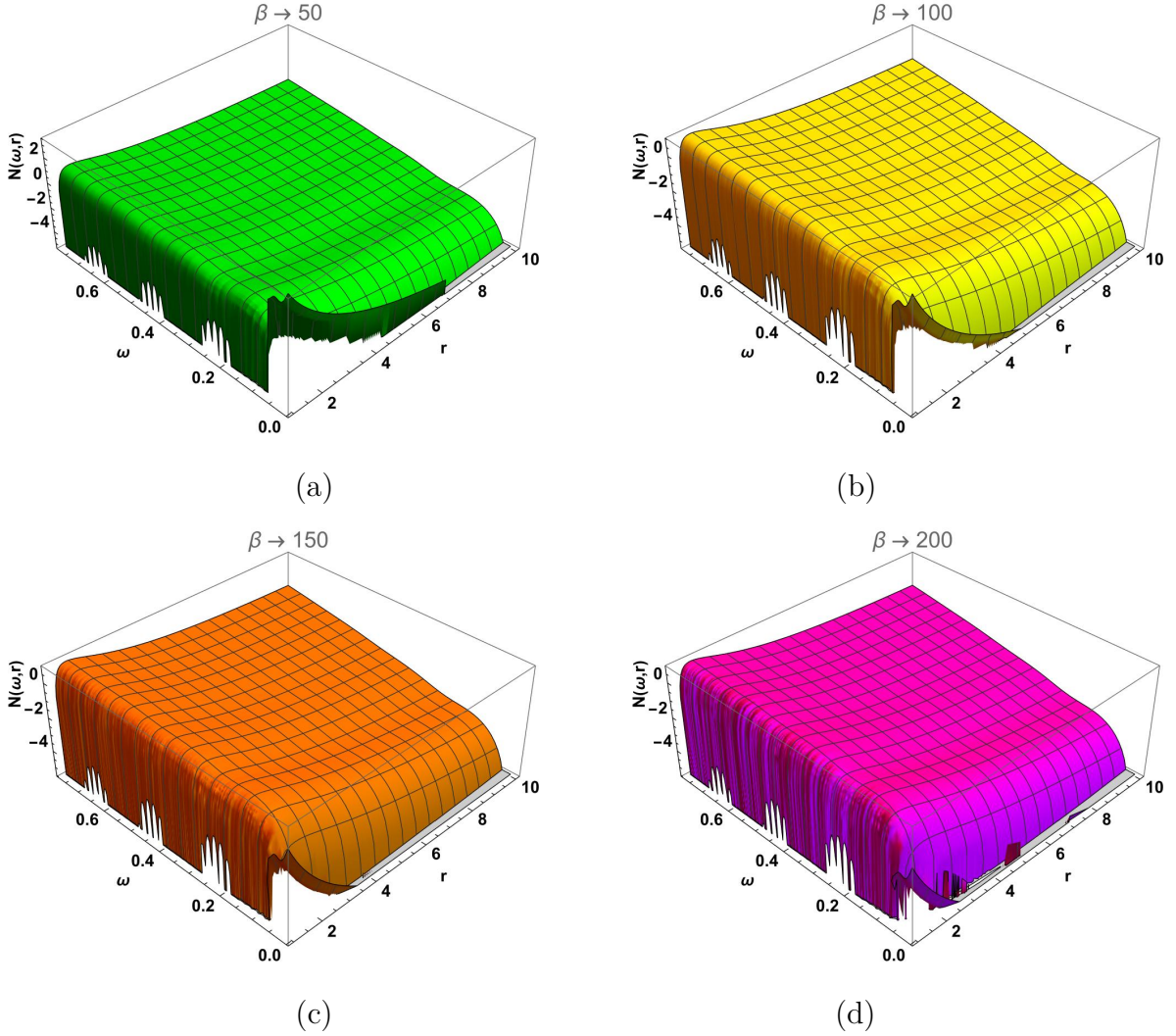
Figure 5.9: TLL DOS for **Hund metal** as a function of energy ω and the distance from the boundary r (tip of the carbon nanotube, unit of r is $1/V_F$); when (a) $\beta = 50$, (b) $\beta = 100$, (c) $\beta = 150$, (d) $\beta = 200$. The $\beta = 1/T$ is inverse temperature with a unit set by the fact that the unit of energy was set by $v_F = 1$.

function. Here, it is shown that the presence of boundary and the second TLL mode generalizes that expression into a combination of incomplete Beta functions, allowing for a connection between the two situations. The advantage of writing the expression in a less compact form, with $a = \omega + K$ in the denominator is that it manifestly has a form of a Lehman representation for a free boson propagator.

The local propagator, a quantity that is integrated over all momenta, was computed to obtain the above-mentioned denominator ($\pm\pi$) which implies that original LDOS has a plasmon pole form with bosons moving along the light rays defined as Dirac deltas $\delta(k - K_\nu/\beta)$. In our procedure, to obtain correlation functions, the fields have been re-scaled by K_ν to arrive at noninteracting theory, without Bogoliubov angle that would need to be nonlocal when left- and right-going fermions are coupled. In this case, as recently proven, the K_ν are becoming related to Thomas-Fermi screening length. Thus the shift of the plasmon pole can be interpreted as a characteristic screening length in the material.

Finally, we decided to keep the formula in its most general form as it will later enable

us to generalize to complex TLL parameters, that will encode non-Hermiticity in the presence of strong external field.

The most remarkable feature of Hund metal is the presence of a sharp peak in close vicinity of $\omega = 0$, which decays relatively quickly with r. This can be interpreted as an interference phenomenon. In the Coulomb metal case, not only is there no interference, but also any feature close to zero energy is suppressed by boundary conditions affecting phase shifts. Curiously, the peak seems to disappear as we move towards the lowest temperature. Perhaps this is a numerical artefact that is due to peak narrowing, although we have thoroughly checked various adaptive meshes and the feature seems to persist. An alternative interpretation is given below.

An even more remarkable interpretation is possible for the spin sector in the Hund metal case, where a strong, sharp peak close to zero energy is observed. In our range of parameters $K_s \ll 1$ we are deep inside the antiferromagnet (AFM) Ising phase, however gapless in the absence of a bulk gapping term. We thus expect to work in TLL but strongly anisotropic $J_z \gg J_\perp$ limit. This represents type-II Toulouse point, the decoupled boundary [189]. On the other hand, the radiative boundary condition represents strong
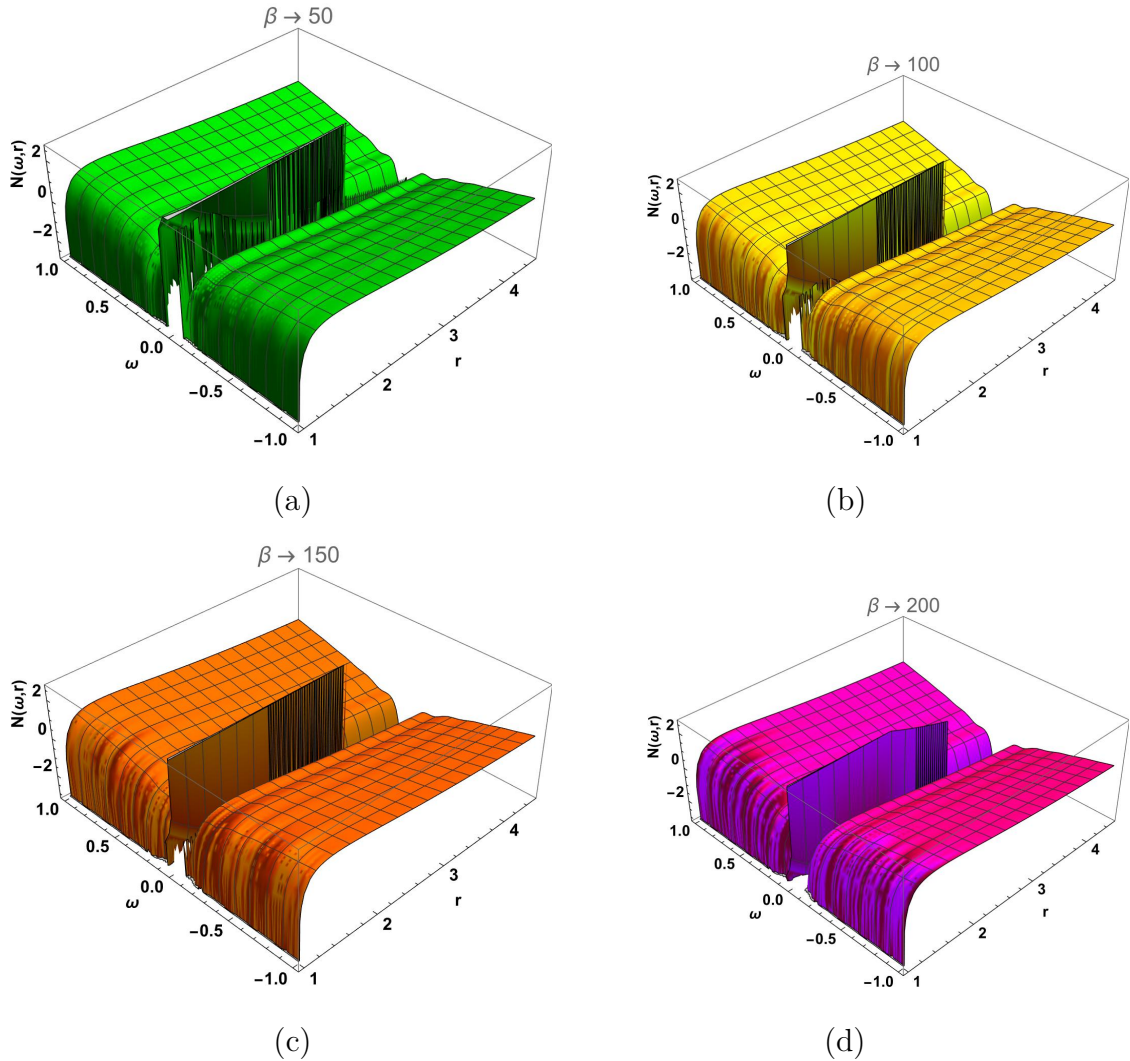
Figure 5.10: TLL DOS for **Hund metal** as a function of energy ω and the distance from the boundary r (tip of the carbon nanotube, the unit of r is $1/V_F$); when (a) $\beta = 50$, (b) $\beta = 100$, (c) $\beta = 150$, (d) $\beta = 200$. The $\beta = 1/T$ is inverse temperature with a unit set by the fact that the unit of energy was set by $v_F = 1$.
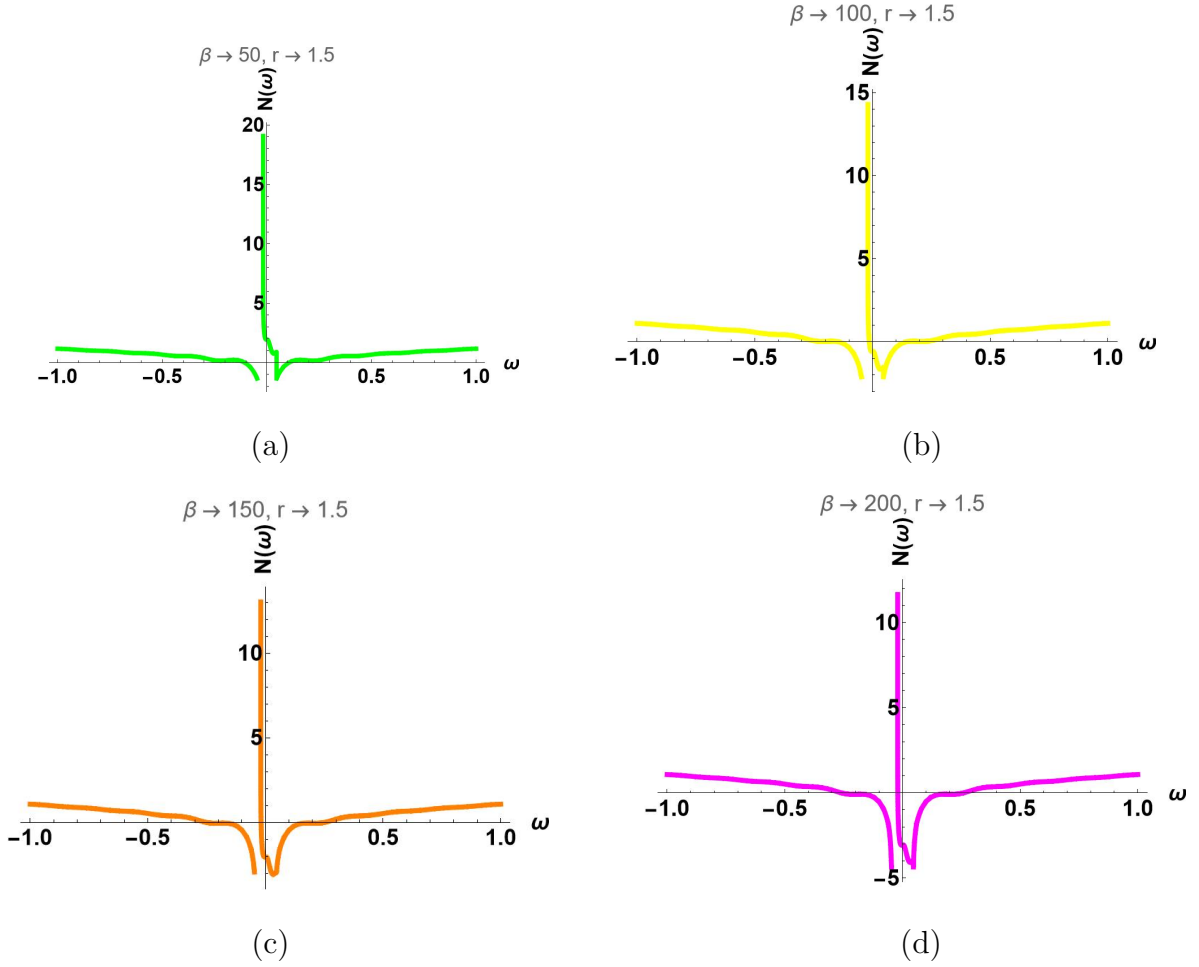
Figure 5.11: TLL DOS for **Hund metal** as a function of energy ω. The distance from the boundary r (tip of the carbon nanotube) is a constant, and $r = 1.50\frac{1}{V_F}$, (a) $\beta = 50$, (b) $\beta = 100$, (c) $\beta = 150$, (d) $\beta = 200$.
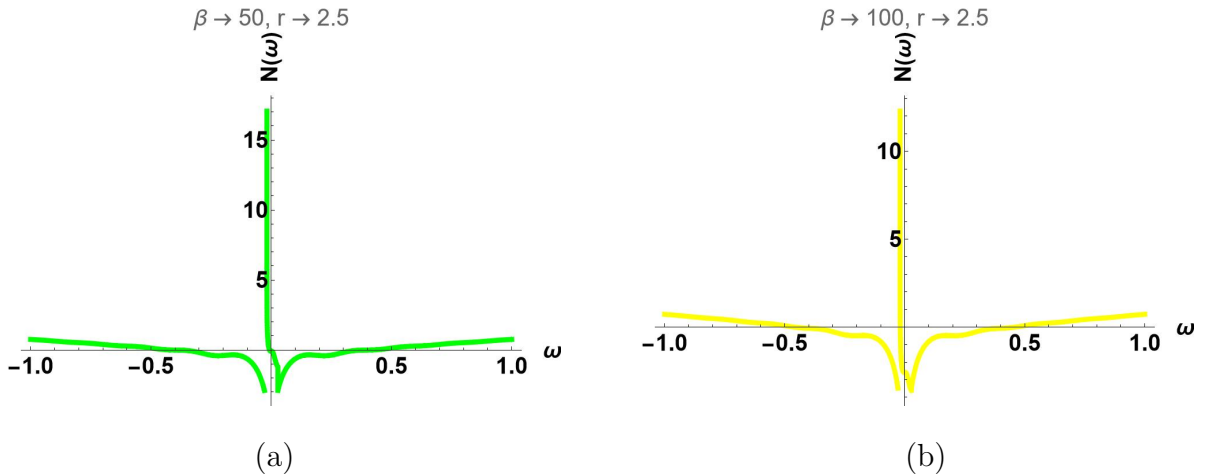
Figure 5.12: TLL DOS for **Hund metal** as a function of energy ω. The distance from the boundary r (tip of the carbon nanotube) is a constant, and $r = 2.50\frac{1}{V_F}$, (a) $\beta = 50$, (b) $\beta = 100$.
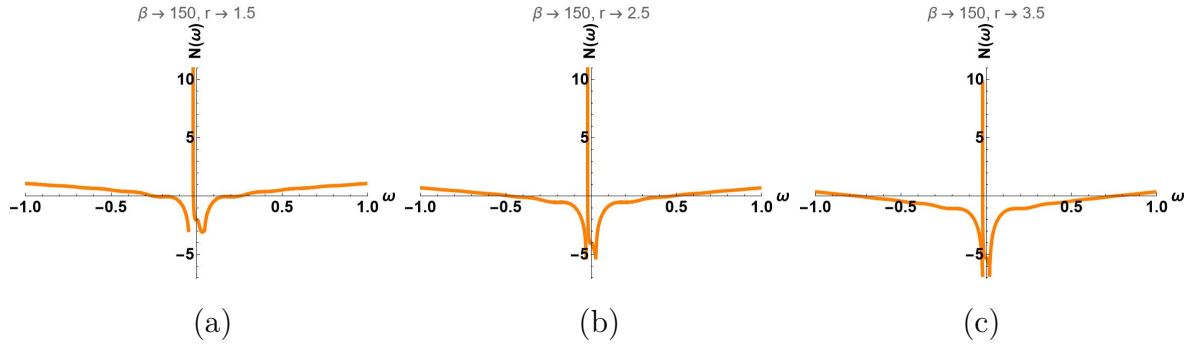
Figure 5.13: TLL DOS for **Hund metal** as a function of energy ω. r is the distance from the boundary (tip of the carbon nanotube) when $\beta = 150$, (a) $r = 1.51/V_F$, (b) $r = 2.51/V_F$, (c) $r = 3.51/V_F$.

Kondo-type coupling with an outside entity, and this is a spin-flip type coupling $\sim \theta_s$. At the lowest temperatures, the bulk and boundary are incompatible in the sense that an easy axis bulk cannot provide so much radiation coupling with an in-plane oscillating outside object. The bath and the boundary are orthogonal at $T = 0$. The situation changes at finite temperatures when TLL bosons start to be excited, and they can couple on the boundary. Consequently, a peak is observed that increases as the temperature is reduced; a behavior that is counter-intuitive for usual Kondo setting with constant J_K and isotropic bath. It should be emphasized that all the temperatures considered here are much below the Kondo coherence temperature T_K. In the close vicinity of the peak, we observe the negative LDOS, a phenomenon known to exist in low-dimensional systems [190], possibly due to *overscreening* by the massive zero-energy state. This is yet another phenomenon that occurs exclusively when the radiative boundary condition is imposed. Fig. 5.11 and Fig. 5.12 present the LDOS for Hund metal as a function of energy ω at various temperatures, corresponding to the profiles captured in Fig. 5.10 for a fixed distance from the boundary $r = 1.5\frac{1}{V_F}$ and $r = 2.5\frac{1}{V_F}$, respectively, while Fig. 5.13 shows the same temperature, but at different distances. The zero energy peak is a reproducible feature observed in all these cases.

The system has particle-hole symmetry, although it is not observed in the figures for Hund metal, specifically in regions close to zero energy. Further research is needed to address this, particularly in developing an adaptive mesh capable of accurately capturing the problem at energies close to zero.

5.4.4   Hund versus Coulomb metal

Here, the results of integral transforms for Coulomb and Hund metals are compared. It is observed that as we move away from the edge, in all cases, there is a sudden drop close to the boundary, then a broad maximum (in Hund metal very shallow) followed by a gradual decrease towards bulk behaviour.

The appearance of the broad peak is somewhat expected. From Ref. [173], it is known that LDOS should be a function of a variable $x\omega$. For the ω dependence of LDOS, it is evident that it scales as $\alpha_{bulk} - 1$ (in the bulk) or $\alpha_{edge} - 1$ (on the boundary). While α_{bulk} is always greater than one, upon choosing radiative boundary condition with $K_\sigma < 1/2$, $\alpha_{edge} < 1$ was taken, which gives an inverse scaling of LDOS close to the boundary.

The fact that in Hund metal both spin and charge modes, with different velocities, contribute to the spatial dependence, also manifests as weak oscillations, the beating phenomena which are visible the best for the smallest r.

An interesting dichotomy can be observed at the lowest energies. In the case of Coulomb metal, the LDOS has a simple zero bias anomaly, an interaction-induced pseudo-gap, as the Fermi level is approached. On the contrary, the most remarkable feature of Hund metal is the presence of a sharp peak in close vicinity of $\omega = 0$, which relatively quickly decays with r. This can be interpreted as an interference phenomenon. In the Coulomb metal case not only is there no interference, but also any feature close to zero energy is suppressed by boundary condition affecting phase shifts (that mathematically enter through partial integration explained in Sec. 5.4.1). Curiously, the peak seems to disappear as we move towards the lowest temperature. Initially, the numerical accuracy was blamed for that (as the standard Kondo peak is expected to narrow), but extensive trials of different meshes were not able to change this picture. It is thus necessary to understand better the specific regime of the spin system being tackled here.

Interpretation of the $\omega \to 0$ features

It is observed that the same LDOS can be produced for both K_ν and $1/K_\nu$ provided that boundary conditions are reversed. For a more intuitive $\phi_\nu(x = 0)$ boundary condition, strongly attractive interactions are observed within a charge sector $K_c \gg 1$. In the Coulomb metal case, this results in a broad maximum in the vicinity of the boundary, suggesting that electrons accumulate close to the boundary because it is energetically favorable for them to stay together in a constrained area. Similarly, the $K_s \gg 1$ for the spin sector implies that the system is in an Ising ferromagnet regime, where it has a tendency to develop easy-axis large local magnetization that decouples from the boundary at the lowest temperatures.

The situation for strong repulsive interactions $K \ll 1$, which is frequently more physically relevant, is even more interesting. It is clear that the radiative boundary condition $\theta_c(x = 0)$ for the charge sector induces an enlarged LDOS close to the end of 1D system. This suggests that charge accumulates there to facilitate in-out charge fluctuations.

The situation is even more remarkable for the spin sector in the Hund metal case, where a strong, sharp peak close to zero energy is observed. In our range of parameters $K_s \ll 1$, we are deep inside AFM Ising phase, however gapless in the absence of bulk gapping term. We thus expect to work in TLL but strongly anisotropic $J_z \gg J_\perp$ limit. On the other hand, the radiative boundary condition represents strong Kondo-type coupling with an outside entity, and this is a spin-flip type coupling $\sim \theta_s$. At the lowest temperatures, bulk and boundary are incompatible, in the sense that an easy axis bulk cannot provide such a large radiation coupling with an in-plane oscillating outside object. The situation changes at finite temperatures when TLL bosons start to excite and they can couple on the boundary. Therefore, with a reducing temperature an increasing peak is observed. This a behavior that is counter-intuitive to the usual Kondo setting with constant J_K and isotropic bath. It should be emphasized that all the temperatures considered here are well below the Kondo coherence temperature T_K.

5.5 $4k_F$ **charge susceptibility**

A similar approach, as for the spectral function, can be applied to two-body correlations, such as the susceptibilities. Of special interest is the charge susceptibility as it determines screening, and thus local dielectric constant. In our range of TLL parameters, when $K_\rho < 1/3$, the slowest decaying correlation is the $4k_F$ susceptibility. It represents a combination of two $2k_F$ susceptibilities; while in the bulk it is $\propto \chi_{2kF}(x,t) \otimes \chi_{2kF}(x,t)$, on the boundary there is also a term $\propto \chi_{2kF}(r,x,t) \otimes \chi_{-2kF}(-r,x,t)$ which will contribute to the uniform component. The χ_{4kF} depends on $\cos(4\phi_\rho)$ operator, without a component from the spin sector. Since the difference between Coulomb and Hund metals is in the spin sector, this dominant contribution to charge susceptibility is going to be the same for both Coulomb and Hund metals.

$$\chi^{TLL}(\omega,r) = \int dt \cos(\omega(t) \left(\frac{1}{\sinh^2\left(\frac{\pi t}{\beta}\right)} \right)^{2K_c} \left(\frac{1}{\sinh\left(\frac{\pi}{v_c\beta}\left(2r+v_ct\right)\right)\sinh\left(\frac{\pi}{v_c\beta}\left(2r-v_ct\right)\right)} \right)^{2K_c}$$
(5.36)

The above integral can be evaluated analytically for the case $\omega = 0$ and $2K_c = 1$, which is of our particular interest when calculating static interactions determining K_ρ. The result reads:

$$\chi^{TLL} = \frac{1}{4\pi}\beta\,\mathrm{csch}\left(\frac{2\pi r}{\beta v_c}\right)^3 \mathrm{sech}\left(\frac{2\pi r}{\beta v_c}\right)\left(-2\log\left(\sinh\left(\frac{\pi(-2r+tv_c)}{\beta v_c}\right)\right)\right.$$
$$+2\log\left(\sinh\left(\frac{\pi(2r+tv_c)}{\beta v_c}\right)\right) + \mathrm{csch}\left(\frac{\pi t}{\beta}\right)\left(\sinh\left(\frac{\pi(-4r+tv_c)}{\beta v_c}\right) - \sinh\left(\frac{\pi(4r+tv_c)}{\beta v_c}\right)\right)\right)$$
(5.37)

This result can be regularized in a similar manner as the LDOS. The resulting susceptibility is plotted in Fig. 5.14. Like before, a cross-over between two power laws is observed - boundary and bulk, with the boundary increase much steeper and the bulk decay much slower. This is in agreement with the result for longitudinal spin susceptibility reported in [191], if one recalls that we work in the limit of small K_ρ. Remarkably, the boundary peak of a two-body charge susceptibility is much more prominent than the single-particle boundary feature in the Coulomb metal, suggesting that probes measuring local susceptibilities like nuclear magnetic resonance (NMR) relaxation-time $1/T_1$ or Raman spectroscopy may be better suited to study these many-body changes of profile than the more frequently used STM.

Based on the random-phase approximation (RPA), which is known to hold in TLL, the dielectric function can now be estimated as $\epsilon(r) = 1 + c_{back}N_{em}\chi_\rho(r)$, where N_{em} is the density of emitted carriers and c_{back} is a geometry-dependent constant that describes the strength of back-reaction onto the TLL. At this point, it should be emphasized that, according to Dzyaloshinskii-Larkin theorem ([192], see also Fig. 1.10 in the textbook of T. Giamarchi [96]), vertex correction is prohibited in pure TLL. Thus, the correction to the dielectric function, and hence interaction, is possible due to the presence of emitted carriers. In the zeroth-order approximation, only those carriers are going to be affected by the spatially dependent screening.

On the bulk side (large r values), it can be observed that the dielectric function from TLL carriers initially increases as one approaches the end of the 1D system. This has important consequences, for instance, in the case of field emission. From electrostatics,
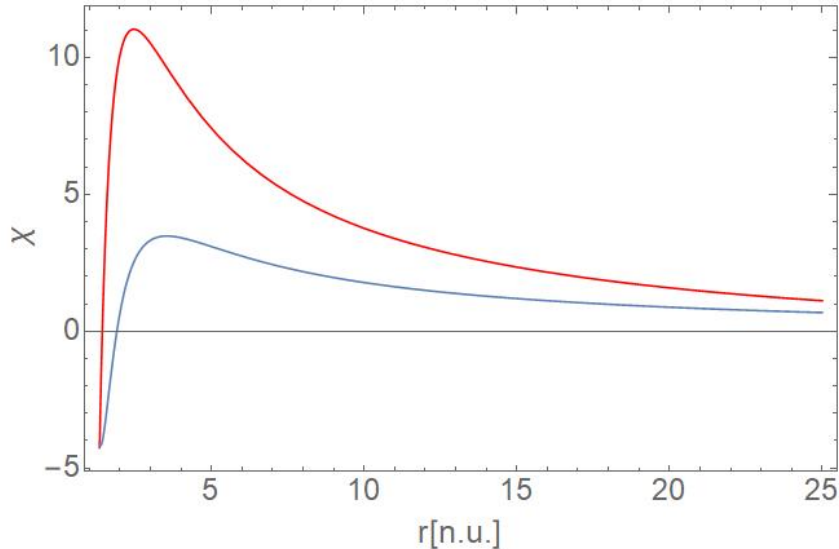
Figure 5.14: Illustration of the static ($\omega = 0$) $q = 4k_F$ charge susceptibility as a function of a distance from the boundary for two temperatures $\beta = 50$ (red) and $\beta = 100$ (blue).

it is expected that inter-tube screening should decrease and the external electric field should increase as the emitted carrier approaches the tip of the 1D system. However, the increase $\epsilon(r)$ when $r \to 0$ as observed here for $r > 1[n.u.]$, implies that this electrostatic effect is at least partially compensated by correlations, thus, for instance, an assumption of constant screening along the 1D system, which is used in field emission studies, is justified.

On the boundary side, a rapid increase in charge susceptibility is observed. This implies that somewhere close to the boundary, the relative dielectric constant will be smaller than one, and this will be a manifestation of strong radiation set on our boundary. In principle, this should be the point where the boundary condition is set, as a further decrease towards a negative relative dielectric constant indicates that our formalism would be breaking down therein. Here, employing the strong coupling approach becomes necessary.

5.6 Partial conclusions and perspectives

In this chapter, results for two types of TLLs are obtained: one is the Coulomb metal case, which has already been frequently recognised in the past, particularly in the context of carbon-nanotube types of materials (but also for p-orbital-based sparse quasi-1D materials). Another class was the Hund metal, the possible realization of which was identified as 1D wires made of heavy atoms, such as Au at stepped silicon surfaces. It should be noted that other realizations of Hund metal are also possible, especially based on $K \leftrightarrow 1/K$ duality upon $\theta \leftrightarrow \phi$ change of boundary condition. In this context, it is noted that nanotubes based on heavy p-elements, such as rolled sheets of stanene, will have a strong local in-plane spin-orbit interaction. Consequently, $K_\sigma \gg 1$, while the boundary conditions are set by $\cos \phi_\sigma$. Thus we are in the Hund metal regime. In this way, our framework covers all possible nanotubes based on p-elements hexagonal sheets, spanning from Coulomb to Hund metal.

While the focus of this study is mainly on the linear regime of low energy, there have been significant advances in the field that tackle the nonlinear regime in carbon nanotubes. No-

tably, recent works in Ref. [193] and Ref. [194] have explored nonlinear Luttinger liquids in carbon nanotubes, providing deeper insights into these systems. Such advancements provide exciting prospects for future study. These studies were done for SWCNT where a simple tight-binding description of the entire band structure works reasonably well: it is quite clear when the conducting p_z orbitals start to overlap with $\sigma^* - p_{x,y}$ orbitals and acquire a curvature, while for MWCNT, such microscopic modelling is prohibitively complicated, and some effective model for $V_F(q)$ needs to be developed. In principle, if such a model is found, it is possible to include curvature as a momentum/frequency-dependent velocity $V_F(q)$ (which holds for the neutral modes part of LDOS). However, what remains to be established is how the holon velocity v_ρ and TLL parameters K_ν would be affected by this change of the model and what momentum dependence they would acquire. Thus extending our model to incorporate these nonlinear effects is highly non-trivial and has to be left as an intriguing direction for future research. Curvature is equivalent to a mass term in the Hamiltonian, and there were experimental efforts to measure how this mass changes upon 1D to 2D cross-over [185]. In the context of arrays of nanotubes, this would be a case where electrons start to hybridize in between the tubes, i.e., the inter-tube distance of an Angstrom scale. However, this is beyond the scope of this work and actually beyond arrays that have been synthesized so far.

The UV cut-off within the Tomonaga-Luttinger liquid theory in our approach is purely phenomenological i.e., it is assumed that at some energy scale, the linear approximation of the spectrum will not be applicable any longer. For SWCNT, this can be related to the inverse lattice spacing, but for MWCNT the characteristic length scale may be much longer. Recent theoretical and experimental advances have provided a more detailed understanding of it. Works such as [195], [196] have provided a deeper theoretical understanding, while experimental studies [197] have substantiated these observations.

Chapter 6

Field emission from Carbon Nanotubes

6.1 Introduction

The method to calculate the field emission current is much less clear when interactions and correlations play a substantial role. The questions of how the electron-electron interactions affect the field emission, and how they conspire with thermal effect to produce the total current in a real device, remained largely unanswered. Here, we identify one class of materials—the arrays of nanotubes—where a fully analytic answer can be given to these questions.

Nanotubes and nanorods have been recently established as very good materials to work as electron sources in a field emission (FE) process. These are one-dimensional materials, and electron-electron interactions are expected to play a crucial role in their physics. The influence of electron-electron interactions on the field emission is studied here. The problem in the low energy regime is studied, thus it is necessary to abandon the anti-adiabatic approximation and derive tunneling amplitude for a finite duration of the tunneling process. The parameters for which an exact analytic expression for tunneling current can be provided were identified in this work. A formalism was obtained that enables to capture *at the same time* the collective effects due to electron-electron interactions and thermionic emission. Our results reveal that different types of nanotubes and their minigaps, Δ_ν and compressibility parameters K_ν can be easily distinguished, based on FE measurements on these materials.

The Chapter is organized as follows: Sec. 6.2 introduces the generalization of TLL to four modes in nanotubes, beginning with the real-space tight-binding Hamiltonian for graphene and its diagonalization in reciprocal space. Sec. 6.3 describes the quantum tunneling process in a dense array of nanotubes, focusing on the dynamics of electrons confined by quantum wells created by Coulomb interactions between nanotubes and modified by TLL parameters. Sec. 6.4 represents the tunneling current dependence on the power low parameter α, including the TLL parameters. In Sec. 6.5, the tunneling current calculations are presented from the entirely metallic nanotubes, zig-zag-like and armchair-like nanotubes. In Sec. 6.6, the variation of chemical potential along 1D metal under external electric field is introduced. Sec. 6.7 presents the modification of the work function in our formalism to adjust the electronic behavior in different materials. Sec. 6.8 concludes the chapter.

6.2 TLL in nanotubes: generalization to four modes TLL

The real-space tight-binding Hamiltonian for graphene reads:

$$H_{graph} = t(a_i^\dagger b_i + a_{i-1}^\dagger b_i + h.c) \tag{6.1}$$

where a_i, b_i are anihillation operators on bi-partite lattice. This can be diagonalized by moving to reciprocal space, where $\mathscr{H}$ is the Hamiltonian and $\mathscr{J}$ is the overlap matrix, associated with the two non-equivalent carbon atoms in the lattice [198]

$$\mathscr{H} = \begin{pmatrix} \epsilon_{2p} & -\gamma_0 f(k) \\ -\gamma_0 f(k)^* & \epsilon_{2p} \end{pmatrix} \quad \text{and} \quad \mathscr{J} = \begin{pmatrix} 1 & sf(k) \\ sf(k)^* & 1 \end{pmatrix} \tag{6.2}$$

to find the following expression for energies of lowest lying valence and conduction bands

$$E_\pm(k_x, k_y) = \pm\gamma_0 \left\{ 1 + 4\cos\frac{\sqrt{3}k_x a}{2}\cos\frac{k_y a}{2} + 4\cos^2\frac{k_y a}{2} \right\} \tag{6.3}$$

which in the vicinity of $K'K'$ point of Brillouin zone can be approximated as

$$E(k) = \pm\frac{\sqrt{3}}{2}\gamma_0 ka = \pm\frac{3}{2}\gamma_0 ka_{C-C} \tag{6.4}$$

where a_{C-C} is the nearest neighbor carbon-carbon distance, $a = 1.421 \times \sqrt{3}\text{Å}$ is the lattice constant for a 2D graphene layer, γ_0 is the nearest-neighbor $C-C$ energy overlap integral, ϵ_{2p} is the site energy of the $2p$ orbital, s is an overlap integral between the nearest A and B atoms and

$$f(k) = e^{ik_x a/\sqrt{3}} + 2e^{-ik_x a/2\sqrt{3}}\cos\frac{k_y a}{2}.$$

It is noted that the dispersion is indeed linear which is a required condition to realize the TLL. The implications of perpendicular quantization imposed, when graphene is rolled into SWCNT, have been thoroughly discussed in Chapter 3.

Additionally, electron-electron interactions are introduced:

$$H_{int} = \sum_{k,k'} V(k, k')(a_k^\dagger a_{k'} + b_k^\dagger b_{k'})(a_{k'}^\dagger a_k + b_{k'}^\dagger b_k) \tag{6.5}$$

which manifestly conserves the momentum. Because the interaction $V(k, k')$ in low dimensional system is weakly screened, it follows that:

$$V(k, k') \propto 1/|k - k'|$$

which implies that the Hartree processes with $k \approx k'$ dominate. Consequently, the interaction term simplifies to density-density form:

$$H_{int} = \sum_{i,j} V(i, j)\rho_i \rho_j \tag{6.6}$$

where it is noted that the sum of all reciprocal space density components $n_k = a_k^\dagger a_k$ gives the real space density ρ_i. With this, the description of collective modes can be set up.

TLL represents a unique solution for strongly correlated 1D systems, transitioning from interacting fermionic systems to a solvable bosonic model. In this model, fermionic fields $\psi^\dagger(x) \equiv \sum_{k \in ocupp} A_k(a_k^\dagger(x) + b_k^\dagger(x))$ (where we moved to continuum limit and the A_k are coefficients whose determination in TLL solves the problem) are expressed through bosonic fields $\phi(x)$ (density) and $\theta(x)$ (momentum):

$$\psi(x) = \exp\left(\imath k_F x\right) \exp \imath \left(\sum_\nu^N \phi_\nu(x) + \theta_\nu(x)\right)/\sqrt{N} \tag{6.7}$$

Here, N denotes the number of bosonic fields. The bosonized Hamiltonian, describing fluctuations of these collective bosonic modes, is given by:

$$H^{1D} = \sum_\nu^N \int \frac{\mathrm{d}x}{2\pi} \left[(v_\nu K_\nu)(\pi \Pi_\nu)^2 + \left(\frac{v_\nu}{K_\nu}\right)(\partial_x \phi_\nu)^2 \right] \tag{6.8}$$

The LDOS for the model $N = 4$, appropriate for CNT, was found in the previous chapter. Here, the solution of tunneling problem will be explored.

6.2.1 Tunneling barrier

The physics that we aim to capture is that of an electron tunneling through a barrier described by a potential $V(x)$. The lowest-order approach to this problem is through the WKB approximation. In past studies [118], when any attempt for exact analytical expression was made, the $V(x)$ was given by the following expression:

$$V_0(x) = h - eF_0\bar{\bar{x}} - \frac{e^2}{16\pi\epsilon_0 \bar{\bar{x}}} \tag{6.9}$$

where $h = \omega_0 - \omega$ (ω_0 is the work function characteristic of the given material and ω is the energy), and $\bar{\bar{x}}$ was defined in Chapter 3. The second term corresponds to an unscreened external electric field $F_0 = cste$, while the last term represents an interaction with an "image" hole left behind in a metal. This has led [127] to an expression for the tunneling probability in terms of elliptic integrals, which was later rewritten [128] as a solution to a hypergeometric equation, suggesting a possibility for further generalizations.

Looking for a description of a tunneling process from a correlated electron liquid, we turn to the generalization of this formalism presented in Chapter 4 where the potential is taken in the following form

$$V(x) = h - e\tilde{t}_{tun}F_{eff}\mathbf{d}_0 x^\alpha - \frac{e^2\mathcal{G}_{eh}}{16\pi\epsilon_0 \mathbf{d}_0 x^\alpha} \tag{6.10}$$

where the previous formula was generalized by admitting that the *driving* term is an arbitrary power law with a prefactor proportional to some effective tunneling amplitude $\tilde{t}_{tun}$ times some effective (screened) electric field F_{eff}, while the *interaction* term with nanotubes is proportional to some electron-hole propagator $\mathcal{G}_{eh}$. The $\tilde{t}_{tun} = t_{tun}/\Lambda$ is a relative probability that the carrier moving along the tube will tunnel out of it, while $\mathcal{G}_{eh} = G_{eh}(x = d_0) \cdot \Lambda$ gives a probability of co-moving electron and a hole; it is a two-body exciton-type propagator times the band-width. In Eq. 3.71, we have extracted spatial dependence of all these quantities to absorb them in the respective power law of a dimensionless x multiplied by dimension-carrying parameter $\mathbf{d}_0$. The assumption is that the functional dependence, namely the power-law remains, which as demonstrated below,

is indeed highly probable within the TLL environment. When $\alpha \equiv 1$, Eq. 6.10 simplifies to the previously considered Eq. 6.9. In Chapter 4, it was found that for the special case when the absolute value of powers in the last two terms are equal, the expression for the tunneling probability can be expressed in a close analytic form i.e., in terms of a hypergeometric function, see Eq. 6.13 below. $\alpha(K)$ will be obtained in Sec. 6.3.1.

The transmission probability is generally equal to the element of the density matrix corresponding to the system with an emitted carrier. This is equal to $\mathcal{T} = \rho_{tun}/Z$, where Z is a partition function of the system, given by $Z = \rho_0 + \rho_{tun} \approx 1 + \rho_{tun}$. Here, it is assumed that the tunneling process is so negligible that it does not affect the density matrix of the rest of the system. Since $\rho_{tun} = \exp(-S_{tun})$, and anticipating the result from Eq. 6.14, it is obtained that $\mathcal{T}$ is expressed by Kemble's improved Jeffreys–Wentzel–Kramers–Brillouin (JWKB) formula:

$$\mathcal{T}(F, \omega) = \frac{1}{1 + D(F, h = \omega - \omega_0)} \tag{6.11}$$

where, explicitly including the elementary constants e, m_e and $\hbar_P$ (which are set to $= 1$ from now on):

$$D(F, h) = exp\left[\left(\frac{m_e^{1/2}}{e\hbar}\right)\left(\frac{h^{3/2}}{F}\right)\left(\frac{h}{2eF\mathbf{d}_0}\right)^{\frac{1-\alpha}{\alpha}}\left(\frac{2^{1-\frac{1-\alpha}{\alpha}}}{\alpha}\right)I(F, h)\right] \tag{6.12}$$

and the WKB integral $I(F, h, x) = \int_{xin}^{xout} \sqrt{V(x)}dx$ reads:

$$I(F, h, x) = \frac{\pi\alpha x^{\frac{1}{\alpha}-\frac{3}{2}}\left(2\zeta x^2((\alpha-1)\zeta+1)\,_2F_1\left(\frac{1}{2}, \frac{3}{2}-\frac{1}{\alpha}; 1; 1-\zeta\right) - \alpha(\zeta+1)x^2\,_2F_1\left(-\frac{1}{2}, \frac{3}{2}-\frac{1}{\alpha}; 1; 1-\zeta\right)\right)}{(\alpha^2-4)} \tag{6.13}$$

where $\zeta = m/n$, $m = \left(\frac{h}{2eF\mathbf{d}_0}\right)^{\alpha-1}\left(\sqrt{1-\frac{F}{(\omega_0-\omega)^2}}+1\right)$, $n = \left(\frac{h}{2eF\mathbf{d}_0}\right)^{\alpha-1}\left(1-\sqrt{1-\frac{F}{(\omega_0-\omega)^2}}\right)$, see Eq. 4.11 applied to Eq. 6.10.

It was confirmed [105] that the expression above for $\alpha = 1$ simplifies the previously obtained result in terms of elliptic integrals [118], [119] for the single-particle case (Eq. 6.9). Our aim in the following section will be to build the connection between the exponent α in the formula above and the correlation effects in the nanotube.

6.3   Tunneling process

In the presence of an array of nanotubes, the escaping mode of the electron is confined, and it takes place in the quantum well created by neighbouring nanotubes (Fig. 6.1).

A dense array of nanotubes is considered, wherein "dense array" is an array that supports a quantum well and thus the confinement. The nanotubes interact with each other through Coulomb interactions creating narrow wells of potential between them and can also affect the physics of the tubes. Fortunately, this last phenomenon can be captured by an appropriate modification of the TLL parameters. To be precise, for Coulomb interactions, this affects only the effective $K_{\rho+}$ parameter [165]. Thus there remains a problem of motion within deep wells of potential between the tubes. Each tube is described by TLL with some effective $K_{\rho+}$, and emitted electrons are expected to propagate within these potential minima. The issue that is to be addressed here concerns the dynamics of an electron as it propagates *along* the nanotube and in the process can still interact with the TLL electrons inside the tube. The usual approximation is to compute a saddle
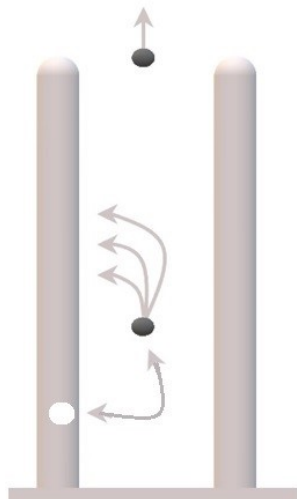
Figure 6.1: A schematic illustration of the problem considered here: an array of nanotubes vertically grown on the substrate. The electron (black dot) is emitted from the nanotube and still interacts with the hole inside of the nanotube (white spot) during the propagation.

point (quasi-classical) configuration of the fields for a tunneling event taking place in a negligibly short time – the instanton gas approximation. However, the situation in the nanotube array is different, as the tunneling electron has to travel all the way up towards the top of the nanotube, experiencing the influence of TLL in the meantime. To solve this complicated case, a decision was made to separate quasi-classical and quantum degrees of freedom [123]:

$$S = S_{clas}(q) + S_{quant}(\psi),$$

were the former describes the time-extended tunneling process $S_{clas}(q) \equiv S_{tun}(q)$, with $q(\tau)$ representing a trajectory of escaping single electron taking place in an effective, averaged potential determined by quantum fluctuations

$$S_{quant} \equiv \sum_i S_{1D}^{(i)},$$

where $\psi(x, t)$ indicate wavefunctions inside the nanotubes and i indicates the tube number. In other words, the classical trajectory includes the averaged TLL effect (encoded in known TLL's correlation functions), in the potential experienced by the escaping carrier. This may be considered as a vertex correction to the tunneling matrix (operator) elements, a significant quantity of which was emphasized previously [199], where it was accessed using alternative diagrammatic methods.

Following the seminal result by Coleman [125], the Euler-Lagrange equation for instanton gives a classical equation of motion

$$\ddot{q} = V_{saddle}(q(\tau))$$

which allows a tunneling type solution. This was presented in Chapter 3, Sec. 3.4.2. Upon inserting it into tunneling action one finds:

$$S_{tun} = \int d\tau \sqrt{V_{saddle}(q(\tau))} \tag{6.14}$$

where V_{saddle} (see Sec. 3.4.2) is expected to have the form of Eq. 6.10. Remarkably, for the simplest case of straightforward motion perpendicular to the barrier, this becomes equivalent to quasi-classical WKB result. However, in more complicated cases, such as ours, the trajectory of a particle will follow in a spirit similar to the path-integral formulation. Now the $q(\tau)$ is the saddle point trajectory and it is assumed that due to the geometry of the problem (the quantum well between nanotubes), a significant portion of the trajectory is such that $q(\tau)||x$. For a considerable time, the emitted electron continues to interact with surrounding TLLs. Our task is then to average out the quantum fluctuations, which can be made for TLL, in order to obtain effective parameters inside $V_{saddle}(x)$.

In realistic systems, neighbouring nanotubes may have different chirality and parameters, but the tube that is the most metallic, i.e., has the smallest gap, will provide the largest amount of screening. This justifies our approximation of a single-tube dominated process.

6.3.1 The dependence $\alpha(K_\nu)$

In Eq. 3.71, it is observed that there are two terms in the potential that need to be overcome by the tunneling electron. The last one is due to an interaction between the electron and the hole that has been left behind in the nanodevice, and the second one is due to the screened external potential. The question is what the form of these terms is in an environment defined by surrounding 1D nanotubes - TLLs.

The second term in Eq. 6.10 arises from an interaction with external potential that pulls an electron away from the nanodevice. By itself, the external electric field in the vicinity of the 1D conductor has a very weak spatial dependence, due to the under-screening property of 1D metal, known to follow logarithmic dependence $V_0(x) \sim ln(x)$. The spatial dependence arises then due to extended quantum fluctuations in TLL. Since seminal works by Furusaki [200], it is known that in the limit of the strong potential (in our language work-function equal or greater than bandwidth), the tunneling process can be described by instanton events which add the following cosine perturbation term to the TLL Hamiltonian:

$$H_{tun} = F_{ext} \int dx dt \hat{O}_{tun}(x,t)$$

where

$$\hat{O}_{tun}(x,t) = \cos(\theta_{\rho+}(x,t)) \cos(\theta_{\rho-}(x,t)) \cos(\theta_{\sigma+}(x,t)) \cos(\theta_{\sigma-}(x,t))$$

Here, a full fermion tunneling was taken, including all bosonic fields in $\hat{O}_{tun}$. In Chapter 3, Sec. 3.4, we arrived (for a single-mode TLL) at the result that the external field is renormalized by fluctuations of θ_ν fields around its minimum $\tilde{V} \to V(1 - (\theta - \langle\theta\rangle)/2)$ where we changed the notation, here $F \equiv V$. The correlation function

$$t_{eff}(x) = \langle \hat{O}_{tun}(x,t) \hat{O}_{tun}(0,0) \rangle$$

will indeed capture this effect of fluctuation between cosines' minima. The spatial spread of the tunneling amplitude $t_{tun}(x)$, the probability of these instanton events, is proportional to correlation functions of the canonically conjugate momentum θ_ν fields. As the electron moves along the nanotube, it will endeavour a series of such tunneling events which can be re-summed into the final effective tunneling rate as a geometric series [123], the accuracy of such approximation has been confirmed by bench-marking with the numerics in our previous work [105]. Thus, an overall effect of the quantum fluctuations

leads to the following spatial dependence: $\tilde{t}_{tun} = F/(1 - t_{tun})$, which, for sufficiently large tunneling probability, results in the following scaling relation:

$$\tilde{t}_{tun} \sim x^{2(\sum_\nu^N 1/K_\nu)/N} \tag{6.15}$$

Here, the exponent of the power law depends only on $1/K_\nu$ because we computed it specifically for the θ_ν fields (following the prescription given at the beginning of Chapter 5) and for equal times.

In the presence of an entire array of nanotubes, the electric field that pulls the carrier, is screened – a process described by a dielectric constant:

$$F_{ext} = F_{eff} = F_0/\epsilon(x).$$

These are density fluctuations $\propto \phi(x)$ terms, introduced as mass renormalization

$$\tilde{M} \to M(1 - (\phi - \langle\phi\rangle)/2)$$

at the end of Chapter 3. According to Dzyaloshinskii-Larkin reasoning [192], the RPA holds inside each TLL, and it can also be assumed that inter-tube interactions are long-range (the dilute limit for emitted electrons). Thus, the dielectric function of the array reads

$$\epsilon(q) = 1 + W(q)\chi^{irr}(q).$$

For long-range electron-electron interactions $W(q)$, the second term dominates in the long-wavelength limit. The TLL susceptibility is taken to be an irreducible part of susceptibility χ^{irr}, and therefore upon Fourier transform, $\epsilon(x) \approx \chi^{TLL}(x)$. The static charge susceptibility is proportional to the equal-time correlation function:

$$\chi^{TLL}(x) = \langle \hat{O}_{CDW}(x, t = 0)\hat{O}_{CDW}(0, 0)\rangle \tag{6.16}$$

with

$$\hat{O}_{CDW}(x, t = 0) = \cos(\phi_{\rho+}(x))\cos(\phi_{\rho-}(x))\cos(\phi_{\sigma+}(x))\cos(\phi_{\sigma-}(x)) \tag{6.17}$$

Thus, its correlation function scales like $\chi^{TLL}(x) \sim x^{\sum_\nu 2K_\nu 2K}$, because only ϕ_ν fields are involved. The only assumption used here is that the action of the external electric field on the TLL is independent of spin and valley degrees of freedom. Otherwise, a different form of $\hat{O}_{CDW}$ would need to be chosen to account for, e.g., magnetostriction.

Overall, the tunneling is due to an external electric field in the vicinity of TLL and scales like:

$$V_{ext}(x) = t_{eff}(x) \cdot \frac{F_0}{\epsilon(x)} \sim \left(x^{\sum_\nu 2/K_\nu} x^{\sum_\nu 2K_\nu}\right)^{1/N_\nu} \tag{6.18}$$

We now move to the interaction between the propagating electron and its "image"-hole inside the nanotube. This is an interaction with the solitonic wave which tunneling electron is pushing through the CNT as it moves along the $q(t)$ trajectory along the CNT. In Chapter 5, Sec. 5.2.3, we calculated, the Green's function for a single particle as an example; the characteristic exponent $\eta = A^2 \sum_\nu (K_\nu + 1/K_\nu)$ (where $A^2 = (1/\sqrt{2N})^2$) was obtained. The probability of electron-hole recombination at (x, t) (after both particles were created at the same point $(0, 0)$) in the simplest approximation will be given by a correlation function of two *distinguishable* co-propagating particles (one inside and one on the surface of the nanotube). The entire reasoning follows as before. However, in Eq.

5.15 we need to take two copies of each bosonic field, ultimately producing $A^2 = 2/N$. Therefore, the electron-hole recombination, which is an analogue of an image potential (i.e., the last term in Eq. 6.10) is predicted to have the following scaling:

$$V_{img}(x) \sim x^{-2^2 \eta} \tag{6.19}$$

with the single particle exponent known to be

$$\eta = (\sum_\nu K_\nu + 1/K_\nu)/2N.$$

In the language of Fukuyama's tunneling theory presented in Chapter 3, Sec. 3.4.1, this term needs to be added because tunneling out of TLL requires re-fermionization to get back a single electron, while the motion inside TLL is given by collective modes. This is a correction proportional to $\left(\frac{u(q)}{K(q)} - 1\right)$, and since the TLL parameter has strong q dependence in our case, this is like extracting the first moment in terms of bosonic fields, hence the second cumulant – in terms of fermionic fields. This confirms our physically motivated idea of the exciton's propagator, a square of a single fermion propagator.

It is observed that both exponents of power laws in Eq. 6.19 and Eq. 6.18 have the same absolute value, only with the opposite sign. Hence, our gFN formalism is applied, provided that the following conjecture is made:

$$\alpha \to 2(\sum_\nu K_\nu + 1/K_\nu)/N_\nu \tag{6.20}$$

The influence of electron-electron interactions on the tunneling current can thus be explored. To this end, the recently obtained generalization of Fowler-Nordheim theory will be applied.

6.4 Results, general case

6.4.1 The current's α dependence

The total tunneling current, the quantity of interest, is equal to:

$$J(\omega, F) = T(\omega, F)n_{tube}(\omega, F) \tag{6.21}$$

where the first term comes from our generalized Fowler-Nordheim (gFN) theory derived in Chapter 4, Eq. 4.11, and the second one is a density of states that is material specific and for MWCNT has been obtained in the previous chapter. While $T(\omega)$ determines the tunneling probability, the $n_{tube}(\omega)$ determines how many carriers there are, actually available to tunnel e.g. when one goes far above the Fermi energy, the tunneling probability will approach one (because emitted electrons are above the top of the barrier), but at the same time, the number of available carriers will go down to zero. This is obvious for single-particle Fermi-Dirac distribution when $\omega \gg T$ (where there are nearly no carriers for energy much higher than thermal effects), but as we saw in the previous chapter for interacting systems: interactions can broaden the distribution but not that substantially. Before the effects of $n_{tube}(\omega, F, r)$ are studied, we present the effect of gFN on $T(\omega)$ specifically including the implications of electron-electron interactions. In Fig. 6.2 the transmission probability is presented without the effect of the density of states.

We now wish to investigate the effect of varying TLL parameter on the current. For simplicity, we take two mode TLL and vary the charge parameter K_ρ. It is assumed that due to spin-rotational invariance $K_\sigma = 1$, and a step function is simply considered for DOS $n_{tube}(\omega)$, i.e., Fermi-Dirac distribution at zero temperature in a metal with constant dispersion. The result is shown in Fig. 6.3. Indeed, it can be seen that the tunneling probability is an increasing function of frequency ω (energy), but the effects of interactions are also important. The growth is fastest for noninteracting carriers $K_\rho = 1$, while the presence of interactions (both repulsive $K_\rho < 1$ and attractive $K_\rho > 1$) smooths the curve. This is a manifestation of the fact that for any $K_\rho \neq 1$, single-particle states fractionalize into collective bosonic states which need to be combined to emit the electron from the TLL.

Above, a constant density of states along the wire was assumed. If this does not hold, as we showed in Chapter 5 for MWCNT, the formula for the current needs to be generalized:

$$J(\omega, F) = \int dr T(\omega, F, r) n_{tube}(\omega, F, r) \tag{6.22}$$

where we included the possibility that the tunneling probability may also depend on the position, through x_{in}, x_{out}. In Fig. 6.4, we present this dependence on r. We see that for the lowest energies, $\omega \to 0$ and fields $F \to 0$, the probability of emission is strongly suppressed as we move deeper in between the tubes, i.e., when r is increasing. This is an intuitive behaviour that we are able to capture. We wish to point out that such spatial dependence $T(\omega, F; r)$ is an active field of research in CNT, e.g., see Ref. [201].

Finally, at finite temperature:

$$J(\omega, F; \beta) = \int dr T(\omega, F, r) n_{tube}(\omega, F, r; \beta) \tag{6.23}$$

where $n_{tube}(\omega, F, r; \beta) \equiv N(\omega + \mu(F, r), \beta, r)$, the quantity evaluated in Chapter 5. The $\mu(F, r)$ dependence is discussed in Sec. 6.6.
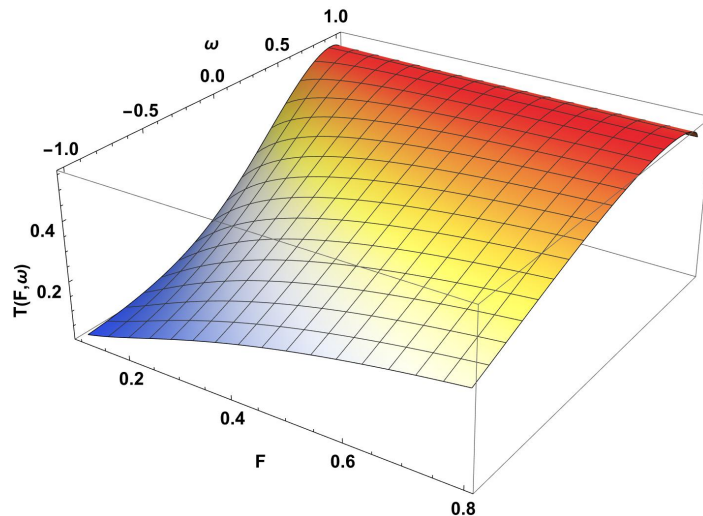
Figure 6.2: The transmission probability $T(F, \omega)$, shown like in Chapter 4 as a function of external field F and electrons energy ω. Here, power law parameter α includes the TLL parameters (Eq. 6.20): $K_{\sigma-} = 1$, $K_{\sigma+} = 1.51515$, $K_{\rho-} = 0.66$, $K_{\rho+} = 0.25$.
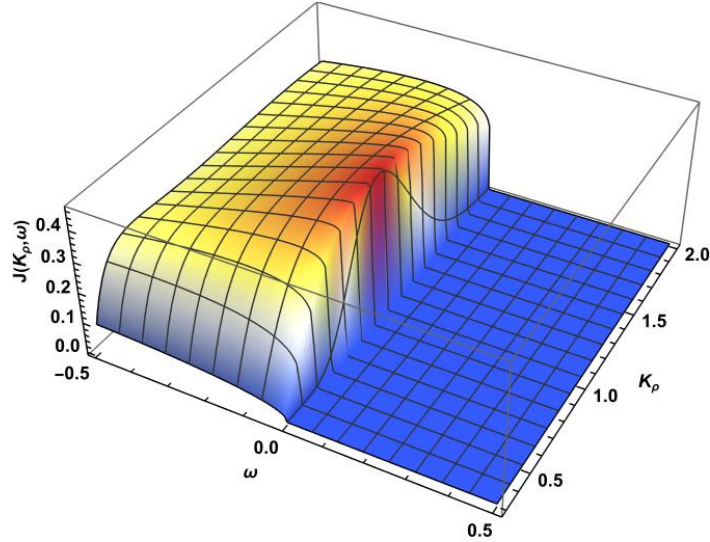
Figure 6.3: 3D plots of field emission current $J(K_\rho, \omega)$ as a function of energy ω and TLL charge interaction parameter K_ρ. $J(K_\rho, \omega)$ is plotted for a given constant value of external field $F = 0.8 V/\mu m$ keeping $K_\sigma = 1$. We took the Fermi-Dirac distribution for the density of states.

6.5   Results for nanotubes

The results for LDOS of the previous chapter (Sec. 5.4), can be used to obtain electron emission spectra for arrays of nanotubes. It is known that rolled hexagonal lattice, upon perpendicular quantization, may become either a metal or a semiconductor. The first case, realized in approximately one-third of all cases, is described as two-leg-ladder model. This model can develop mini-gaps in some of its four bosonic modes. The two legs model description is necessary due to an additional degree of freedom i.e., due to two valleys K, K', that are already present in 2D dispersion of graphene. This is valid and well established for carbon nanotubes, but not limited to them, since any rolled 2D analogue
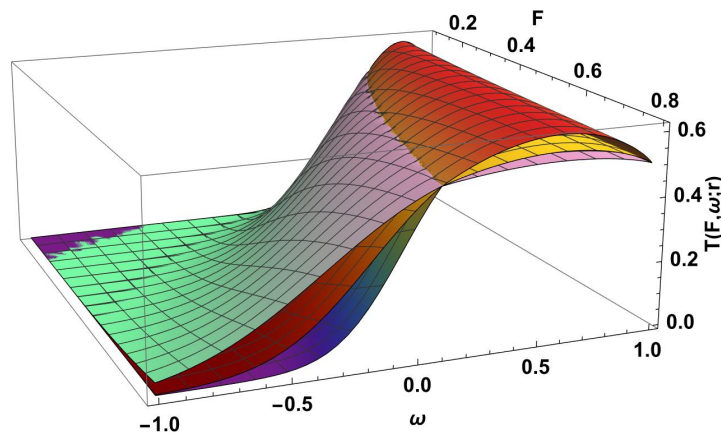
Figure 6.4: The transmission probability $T(F, \omega; r)$ as a function of electric field F and energy ω. We show the transmission probabilities for three distances r along the tube: $r = 2$, green surface (on the left side), $r = 4$, red, and $r = 8$, purple respectively. For the smallest energies ($\omega \to 0$), the transmission probability decreases significantly with increasing distance r along the tube.

based on p-orbitals (silicene, stanene, etc.) will share the same general properties, albeit with different values of parameters. Usually, nanotubes are grown using CVD on a pre-arranged catalyst array, and MWNTs are obtained. Although a multi-wall system is obtained, it can always be assumed that among several ($N > 3$) layers there will be at least one metallic.

The two-leg ladder description is obviously much more complicated than the spin-full chain considered so far, as there are four $\rho\pm, \sigma\pm$ instead of two bosonic modes. However, an extremely useful aspect of nanotubes dominated by the long-range interaction is that only the velocity of the charge-full $\rho+$ mode denoted as the $v_{\rho+}$, is strongly modified, while for the remaining three modes, the respective velocities stay close to V_F. Thanks to that, our original formulas for space-dependent spectral functions $N(\omega, r)$ can still be applied. However, it is necessary to take into account that now three modes K_ν will contribute to the previous a_s:

$$\tilde{a}_s = \frac{K_{\sigma+}^2 + K_{\sigma+}^{-2} + K_{\sigma-}^2 + K_{\sigma-}^{-2} + K_{\rho-}^2 + K_{\rho-}^{-2}}{8} \tag{6.24}$$

The advantage of this situation is that previously setting $b_s = 0$ determined the value $K_s = 1$, while what is now expected is that, for the case with long-range interactions, three neutral modes with nearly equal velocities $V_{\sigma+} \approx V_{\rho-} \approx V_{\sigma-} = V_F$ contribute to b_s. It is noted now that even if we take our specific analytical solution for LDOS, the choice of TLL parameters for the neutral modes is largely arbitrary, thus also the value of α in the tunneling function becomes a free parameter. The most likely situation is that of slow marginal flow towards ultra-low temperature ordering of $\cos \phi_{\sigma+}$ and $\cos \phi_{\rho-}$ terms, and then $K_{\rho-}^{-1} > 1$ will compensate the effect of $K_{\sigma+} < 1$ and the two, together with $K_{\sigma-} \approx 1$, will give at the same time $b_s = 0$ and a non-trivial value for the exponent of correlation function a_s as well as the exponent α inside the tunneling barrier expression.

6.5.1 Entirely metallic tube

We begin with the simpler case, when the nanotube is entirely metallic, which can happen when an achiral, armchair or zig-zag tube is present among MWNT layers. In this case, all the bosonic modes are massless because high symmetry prevents the emergence of any symmetry-breaking cosine term (e.g., dimerization), and one can immediately apply the results of the previous section with the substitutions described above.

The list of all values of K_ν parameters used for the calculations is presented in Table 6.1.

$K_{\sigma-}$	$K_{\sigma+}$	$K_{\rho-}$	$K_{\rho+}$
1	1.51	0.66	0.25
1	1.17	0.85	0.25

Table 6.1: Parameters used for the tunneling current's calculations

Fig. 6.5 shows the tunneling current for entirely metallic nanotubes when F changes from 0.01 to 0.2 V/m. Here, we focus on the small values of F to emphasize the significance of the K_ν parameter values. Indeed, the difference between the various values of $K_{\rho-}$ is clearly observable, which means that the values of $K_{\rho-}$ are meaningful and measurable quantities. As shown in the beginning of the previous chapter, $K_{\rho-}$ basically measures the distortion of the charge distribution along the circumference of the nanotube.

At higher temperature ($\beta = 50$, panel (a)), a double peak structure is observed, both below and above $\omega = 0$, the second one contains both thermal and interaction effects that are entangled. The case $K_{\rho-} = 1$ would correspond to a noninteracting system with charge evenly distributed on the circumference of the nanotube, the further one is from this value the stronger are electron-electron interactions. Thus the difference between red ($K_{\rho-} = 0.85$, weaker interactions) and green ($K_{\rho-} = 0.66$, stronger interactions) allows one to investigate their effect. Therefore, the more $K_{\rho-}$ parameter is different from one, the larger the current is (the green surface is higher than the red one), at least in the regime of the smallest F. It is thus seen that interactions do increase the amplitude of field emission. Sub-figure (b) shows that for this temperature ($\beta = 200$), there are no thermionic effects and the entire emission is driven by the interactions. For the smaller values of interactions, there is a very tiny emission, and for larger interactions, the two emission peaks clearly appear.

Fig. 6.6 and Fig. 6.8 illustrate the characteristics of the tunneling current for entirely metallic nanotubes, each described by specific parameters. The metallic nanotubes exhibit massless bosonic modes due to their high symmetry that protects against backscattering, resulting in unique electron emission properties. Both figures comprise two subfigures, (a) and (b), corresponding to different values of *temperature*. Sub-figure (a) shows the tunneling current as a function of energy and electric field when the temperature is higher $\beta = 50$, while sub-figure (b) displays the same for lower temperature $\beta = 200$.

In these figures, it is observed that tunneling current increases for negative ω (when ω changes from -1 to close to 0), the same behaviour is visible in Fig. 6.3 (for the transmission amplitude) and in TLL's LDOS for larger values of x. Hence, the peak-like structure for the negative ω appears as a product of both. Next, there is a deep at $\omega = 0$ point corresponding to the same feature of the deep visible in TLL's LDOS in Fig. 5.6. Similar to Fig. 5.6, the deep is sharper for lower temperatures. When $\omega > 0$, there is a double peak structure, a massive peak and a smaller shoulder. The shoulder structure
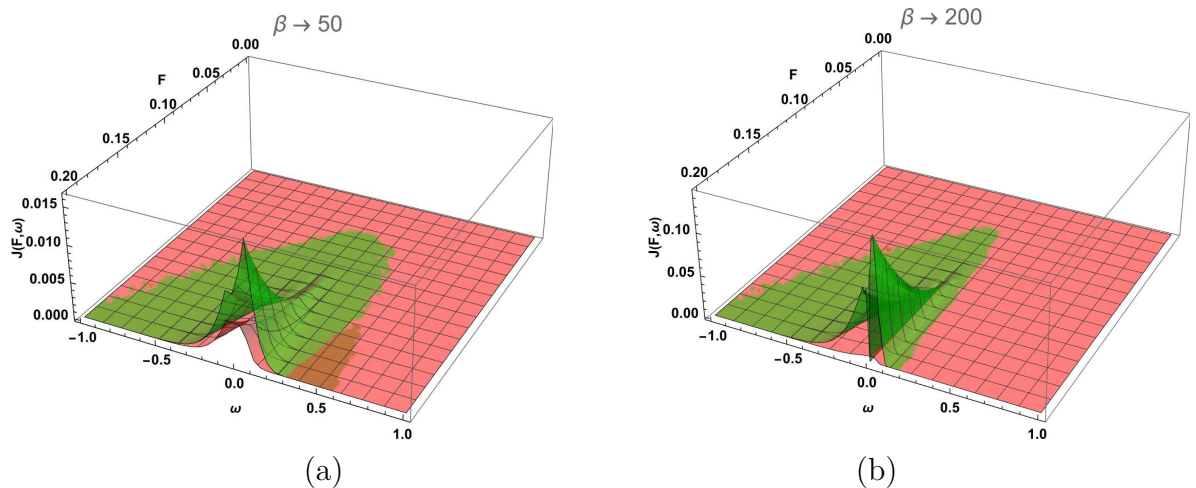
Figure 6.5: The tunneling current $J(\omega, F)$, plotted as a function of external electric field F and energy ω, measured with respect to Fermi level. The plots are for entirely metallic nanotubes described by the following parameters: (a)$\beta = 50$, (b) $\beta = 200$; Green: $K_{\sigma-} = 1$, $K_{\sigma+} = 1.51$, $K_{\rho-} = 0.66$, $K_{\rho+} = K^*$; Red: $K_{\sigma-} = 1$, $K_{\sigma+} = 1.17$, $K_{\rho-} = 0.85$, $K_{\rho+} = 0.25$. Here, the focus is on the lowest values of external electric fields. $\beta = 1/T$ is inverse temperature with a unit set by the fact that the unit of energy was given by $v_F = 1$.

(a)   (b)
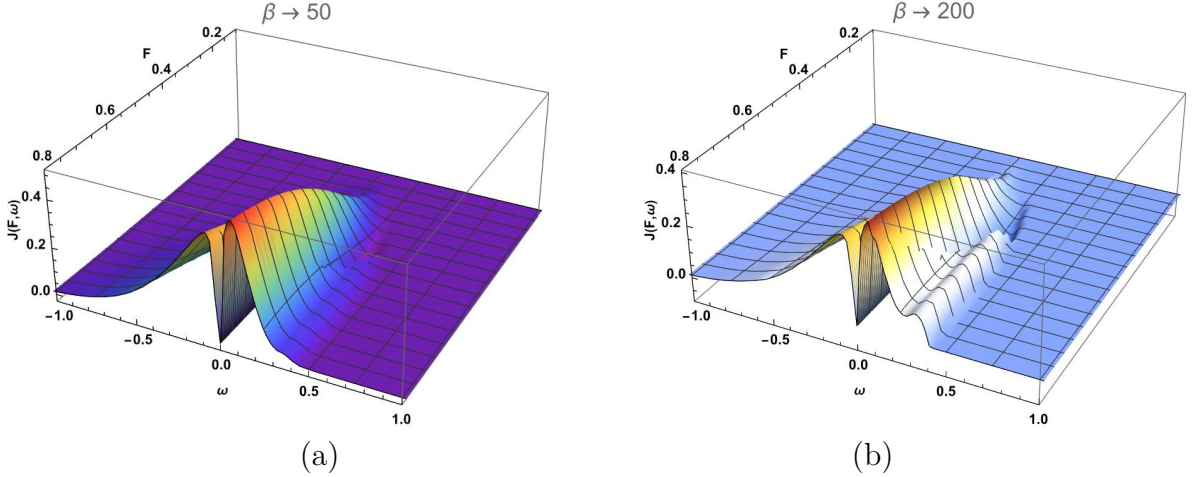
Figure 6.6: The tunneling current $J(\omega, F)$, plotted as a function of external electric field F and energy ω, measured with respect to the Fermi level. The plots are for entirely metallic nanotubes, described by the following parameters: $K_{\sigma-} = 1$, $K_{\sigma+} = 1.51$, $K_{\rho-} = 0.66$, $K_{\rho+} = K^*$; when (a) $\beta = 50$, (b) $\beta = 200$. Here and in all plots below, $v_s = 1$ [in V_F units] and $v_c = 4$ (with one exception of Fig. 6.7). The colour coding follows the J value on the vertical axis.

(a)   (b)
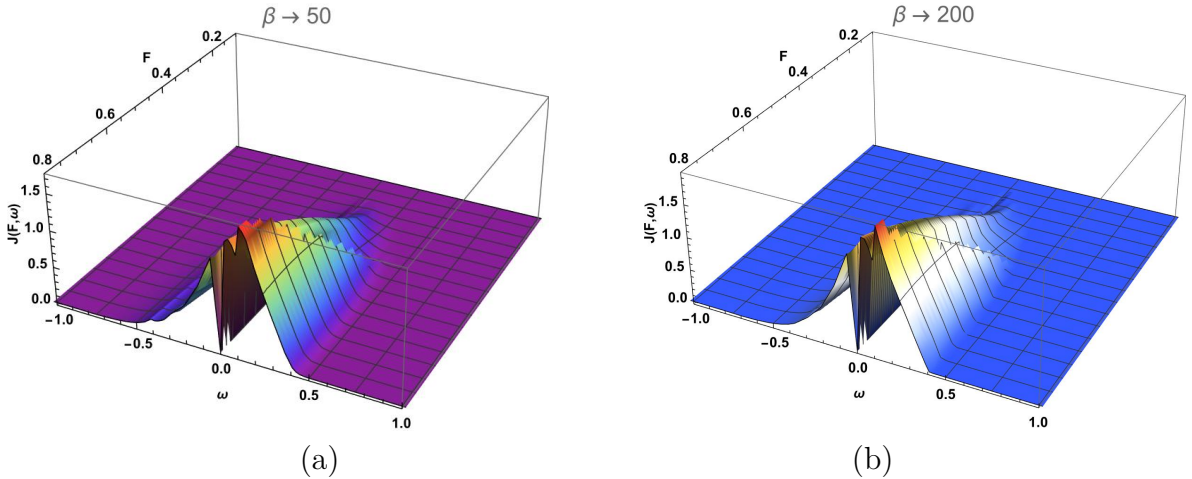
Figure 6.7: The tunneling current $J(\omega, F)$, plotted as a function of external electric field F and energy ω, measured with respect to the Fermi level. The plots are for entirely metallic nanotubes, described by the following parameters: $K_{\sigma-} = 1$, $K_{\sigma+} = 1.51$, $K_{\rho-} = 0.66$, $K_{\rho+} = K^*$ and $\boldsymbol{v_c}$**=1.5**; when (a) $\beta = 50$, (b) $\beta = 200$. This is the only plot in this chapter when $v_c \neq 4$.

is more visible when interactions are stronger ($K_{\rho-} = 0.66$) and it is smoother when interactions are weaker ($K_{\rho-} = 0.85$).

Galilean invariance implies that $v_\nu K_\nu = V_F = cste$. Thus, in all of the plots in this chapter, we use $v_c = 4$, so that Galilean invariance will be obeyed by the charge-carrying particles for which we always set $K_{\rho+} = K^* \approx 0.25$. The only plot with a different value of charge velocity is Fig. 6.7. We can investigate the effects of modified velocity by comparing Fig. 6.7 and Fig. 6.6 (all other parameters are kept the same for clarity). We observe that in comparison with Fig. 6.6, in Fig. 6.7, we see a much closer peak with approximately equal amplitude to the first, rather than a separate small peak. The fact that the secondary peak (sometimes visible only as the "shoulder") is much bigger
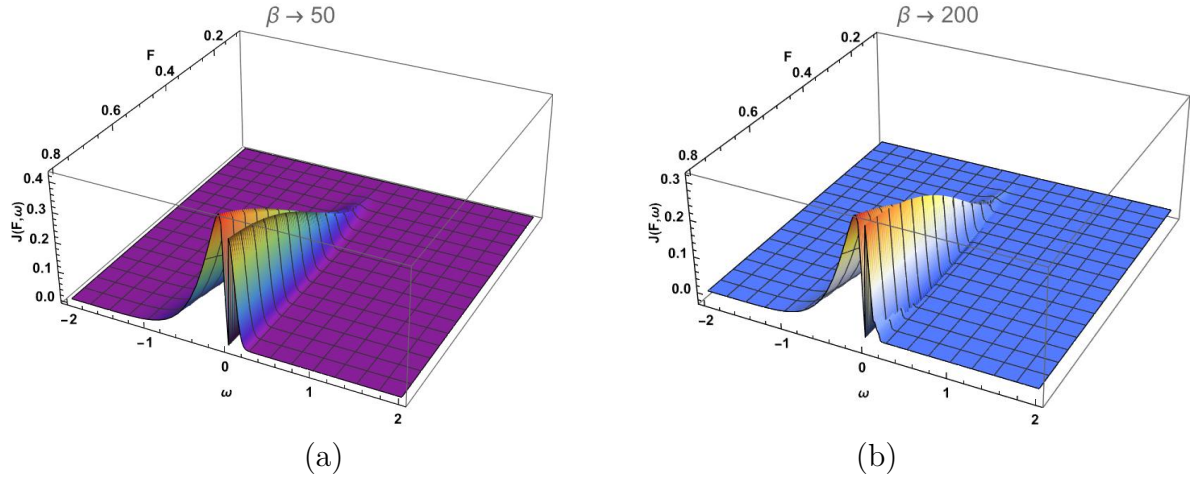
Figure 6.8: The tunneling current $J(\omega, F)$ for entirely metallic nanotubes described by the following parameters: $K_{\sigma-} = 1$, $K_{\sigma+} = 1.17$, $K_{\rho-} = 0.85$, $K_{\rho+} = K^* = 0.25$; when (a) $\beta = 50$, (b) $\beta = 200$.

when the velocities of all modes are closer can be interpreted in the following way: from energy-momentum conservation, we deduce that in the standard case, when $v_c = 4v_s$, we need four neutral particles combined to reach the energy shell of holons. These are very rare events. On the other hand, when v_c is close to v_s, such events are more frequent, and various bosons can easily transfer energy-momentum among themselves. Their probabilities should then be nearly equal. Finally, we notice that the overall current is noticeably larger when velocities are closer to each other. This is due to the fact that the full fermion is much easier to reconstruct back from a system of bosons moving with similar velocities.

When the temperature is higher, the $\omega > 0$ structure has a larger amplitude, which is in agreement with an expectation for thermionic emission. Furthermore, all figures show that as the external electric field F increases, the overall peaks' height and area grow larger. Initially, for lower fields, the height grows fast, but later saturation is observed, especially for the thermionic peak ($\omega > 0$). For larger fields, an increased range of contributing ω and the shoulder feature are also observed indicating that we are beyond the single particle regime.

6.5.2   The case of gapped neutral modes

More complicated, but more likely is the situation when the nanotube has lower symmetry, specifically when it is chiral, as therefore mini-gaps can open in certain bosonic modes. These classes of nanotubes were introduced in Chapter 1. Indeed, while the achiral tubes are very special, the chiral metallic tubes are rather common: 1/3 of all nanotubes belong to this class. Their characteristic feature is that they are not protected by symmetry, thus curvature effects will perturb them. While applying the TLL ideas in large gap semiconductors is problematic, in narrow gap semiconductors, it is possible. Moreover, large-gap semiconductors, contrary to narrow-gap superconductors, will give negligible contribution to the low energy field emission, a subject of this thesis.

There have been several works dedicated to the problem how to incorporate curvature terms within the TLL theory. The general consensus [202], [203], [204], [205] is that they
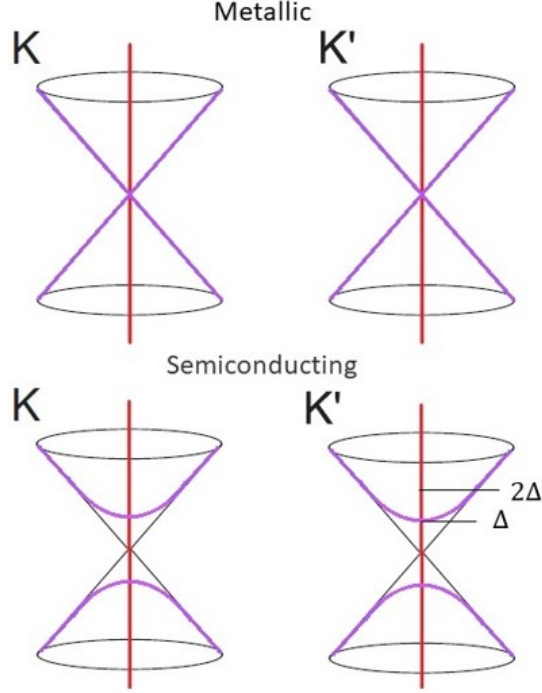
Figure 6.9: The illustration of band structures in metallic and semiconducting regimes at K and K' points: the diagrams above demonstrate the metallic behaviour where the conduction and valence bands meet at the Fermi level without a gap, the diagrams below depict the semiconducting behaviour with an existing gap Δ between the conduction and valence bands.

will give rise to so-called dimerization terms. These can be further re-written [56] as a sum of double products of cosines:

$$H_{curv} = \Delta \left(\sum_{\nu,\nu'} \int dx \cos 2\phi_\nu(x,t) \cos 2\phi_{\nu'}(x,t) \right) \tag{6.25}$$

where the summation ν, ν' runs only along neutral modes because the charged $\rho+$ mode has a much larger velocity and has been averaged out in anti-adiabatic limit. The amplitude Δ is a sum of spin-orbit and curvature effects (Fig. 6.9):

$$\Delta = \Delta_{curv} + \Delta_{so} \tag{6.26}$$

and it is assumed that the Δ is uniform along the tube (generalization to non-uniform $\Delta(x)$ can be accommodated in our formalism where analytic expression for the space-dependent LDOS has been found).

This curvature-induced perturbation has to be taken into account with local correlations on-site g_U, which are of the same order of magnitude [151] although less relevant. Past research on the so-called two-leg ladder models [96] indicates that equal size gaps in $\phi_{\sigma+}$ and $\phi_{\rho-}$ modes are the most likely outcome. Overall, this suggests that in the minimal model at least the following perturbation to the TLL Hamiltonian needs to be added:

$$H_{cos} = \Delta_{tot} \int dx \cos(2\phi_{\rho-}) \cos(2\phi_{\sigma+}) \tag{6.27}$$

where $\Delta_{tot} = \Delta + g_U$. This results, in the lowest energies, in two bosonic fields locking at the minimum of the cosine. The gaps of the two modes are equal and entangled by
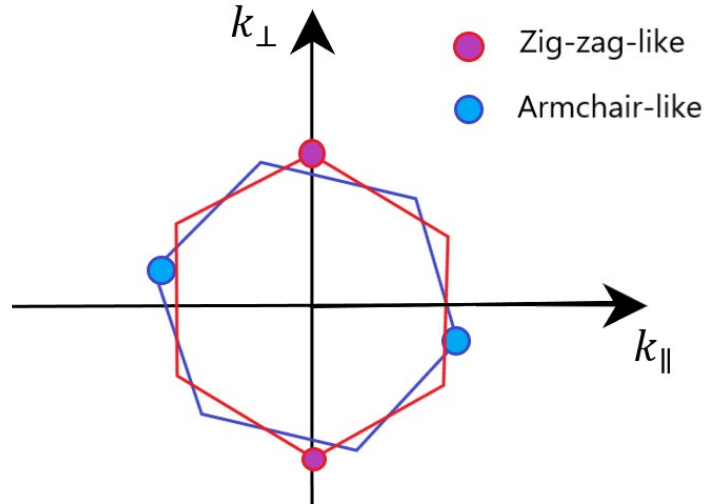
Figure 6.10: Zigzag-like nanotubes: Dirac points collapse to the origin of the longitudinal Brillouin zone, resulting in metallic behaviour and armchair-like nanotubes: Dirac points are well separated in longitudinal momentum space, giving rise to metallic behaviour.

construction. There are also other cosine terms in a two-leg ladder description, but they contain an equal number of canonically conjugated $\cos\phi_{\sigma-}$ and $\cos\theta_{\sigma-}$ terms, which implies that an ultra small gap is present only through re-fermionization of this field. It is also assumed that the tube is not commensurate; hence umklapp terms, involving a $\cos(\phi_{\rho+})$ term, are not present.

The remarkable point is that for the many-body problem, when the single-particle electron emission gap is $\Delta = \Delta_{\sigma+} + \Delta_{\rho-}$, the two-particle probes such as charge susceptibility or electron-hole spectral function, detect a gap of two times larger size $\Delta_{2p} = 2\Delta$. This implies that for energies $\Delta < \omega < 2\Delta$, we shall have an intermediate regime where the modes $\sigma+$ and $\rho-$ do not contribute to characteristic exponents, and certainly, do not contribute to characteristic exponent α.

In the mini-gap situation $\rho-$ and $\sigma+$ modes become gapped and one ought to skip $K_{\rho-}$ and $K_{\sigma+}$, parameters resulting in a condition $K_s = K_{\sigma-}$.

More information about this regime can be gathered from several studies, for instance, by Essler and Tsvelik [206], [207], where they have computed spectral function for the sine-Gordon model. They showed that indeed while the spectral function has a gap Δ below which any tunneling is impossible, the characteristic double dispersion (spinon and holon) of TLL is recovered only for energies above 2Δ. In the intermediate regime, the dispersion characteristic of the gapped state is observed [1]. From this, the following *ansatz* is deduced: in the intermediate regime, we shall also take the a_s exponent inside $N_{TLL}(\omega, r)$ independent of bosonic modes $\sigma+$ and $\rho-$. Additionally, we assume that dielectric properties along the tube are modulated with periodicity q_0 which means that a simple integral for the current $J(\omega)$ is now becoming a Fourier transform:

$$J(\omega, F; T) = \int dr \, \cos(q_0 r) N_{TLL}(\omega, r) T(\omega, F) \tag{6.28}$$

where q_0 is the distance between Fermi points, i.e., the distance between the two K, K'

---

[1]Mathematically, this is related to the fact that the energy and momentum are given by *cosh* and *sinh* functions of rapidity q, and we recover simple linear relation of TLL only when $q > 2$, specifically when $\tanh q \to 1$.

valleys, measured along nanotube axis. In the following, two cases will be considered: $q_0 = 0$ for zigzag, and $q_0 \neq 0$ for armchair.

The intermediate regime postulated here can be noticed in a two-stage activation behaviour of $J(\omega, F; T)$, as revealed in the plots below. Depending on the details of the perpendicular quantization condition, two types of chiral tubes can be distinguished [208]: zig-zag-like and armchair-like, see Fig. 6.10.

6.5.3 Zig-zag-like nanotubes

In this case, $q_0 = 0$ and Eq. 6.28 reduces to the previously used formula, but with a different $N(\omega)$: $N(|\omega| < \omega_0) = 0$ and $N(\omega_0 < |\omega| < 2\omega_0) = N_{2TLL}(\omega)$, where $N_{2TLL}(\omega)$ is the LDOS for TLL with only two free modes (and the α exponent in $T(\omega)$ modified accordingly). Fig. 6.11 and Fig. 6.12 present the tunneling current behaviour in zig-zag-like nanotubes with different interaction parameters. The left and right panels in both figures show the tunneling current at different temperatures (a) $\beta = 50$, and (b) $\beta = 200$. Here, $\omega_0 = 0.1$ is chosen. As shown in the figures, when $|\omega| < 0.1$, the tunneling current is equal to 0, and there is no emission due to the presence of mini-gaps in some bosonic modes. And when $0.2 > |\omega| > 0.1$, there is anomalous tunneling. When $|\omega| > 0.2$, the behaviour of tunneling current is similar to the previous case (Fig. 6.6 and Fig. 6.8).
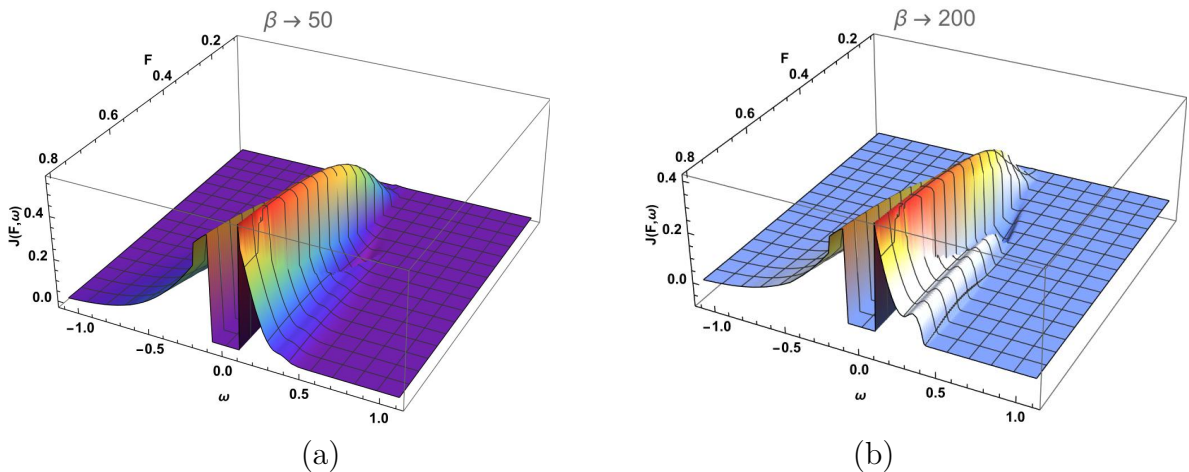
Figure 6.11: The tunneling current for Zig-zag-like nanotubes, described by the following parameters: $K_{\sigma-} = 1$, $K_{\sigma+} = 1.51515$, $K_{\rho-} = 0.66$, $K_{\rho+} = K^* = 0.25$, $\omega_0 = 0.1$; when (a) $\beta = 50$, (b) $\beta = 200$.

In comparison with Fig. 6.6 and Fig. 6.11, differences are obvious in the new intermediate regime. The emission peak for $\omega < 0$ now has a larger amplitude; a discontinuity is actually observed at $\omega = -2\omega_0$, which is due to the fact that $N(\omega)$ has been defined in an unphysical, piecewise manner.

In reality, some crossover between two- and four- modes TLLs is expected (the study of the right crossover function is postponed to later research). The larger amplitude of emission is probably due to the fact that two bosonic modes are not mobile, hence they do not need to be captured when a single fermion is re-constituted. The emission peak for $\omega > 0$ grows faster as a function of F and reaches saturation at smaller values of F. For the largest ω, the shoulder peak is even better expressed, especially at lower temperatures and stronger interactions, shown in Fig. 6.6 (b).
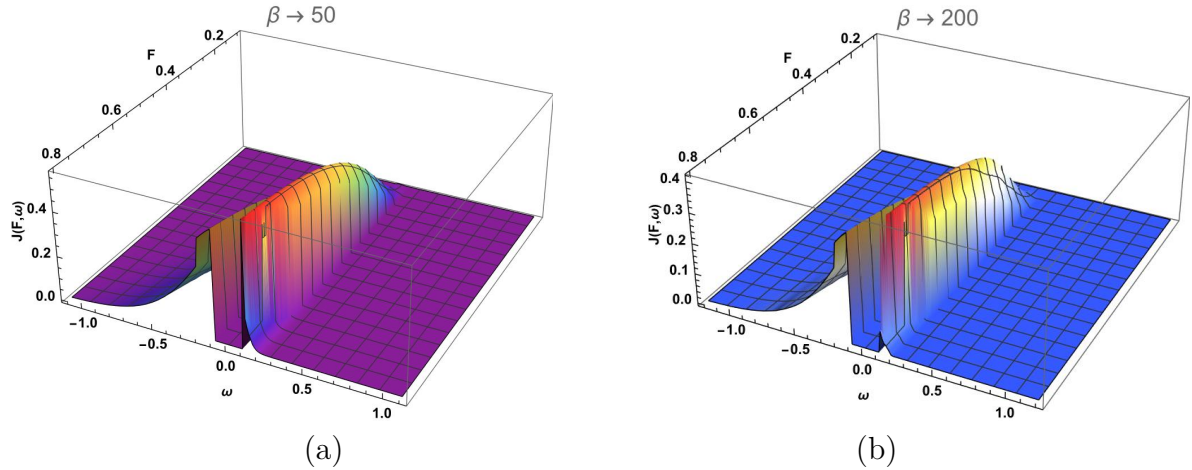
Figure 6.12: The tunneling current for Zig-zag-like nanotubes, described by the following parameters: $K_{\sigma-} = 1$, $K_{\sigma+} = 1.17$, $K_{\rho-} = 0.85$, $K_{\rho+} = K^* = 0.25$, $\omega_0 = 0.1$; when (a) $\beta = 50$, (b) $\beta = 200$.

6.5.4   Armchair-like nanotubes

In this case, $q_0 \neq 0$ (actually q_0 can be as large as a third of BZ), and Eq. 6.28 takes a more complicated form of Fourier-transform. Hence, the fact that we know the LDOS distribution along the tube $N_{TLL}(\omega, r)$, plays a vital role.
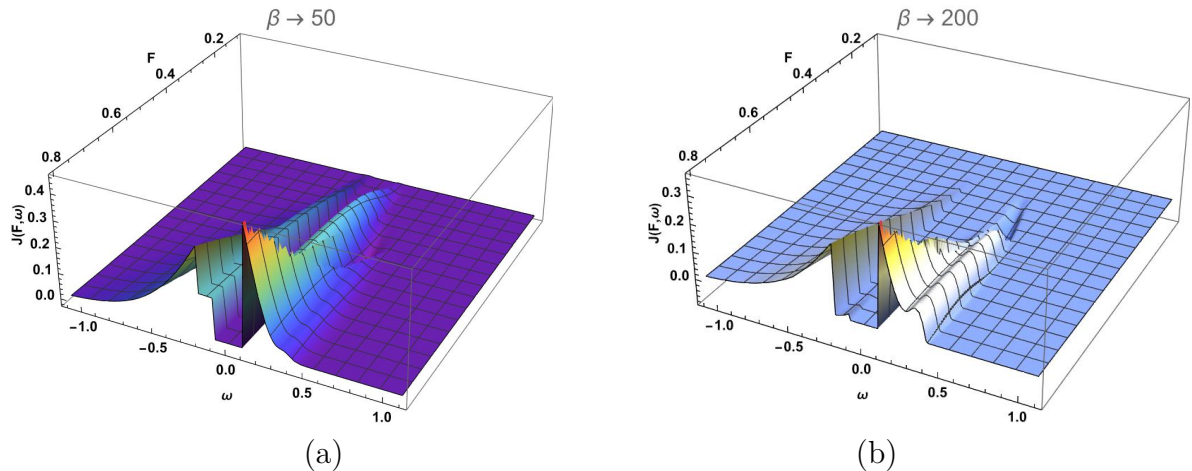
Figure 6.13: The tunneling current for armchair-like nanotubes, described by the following parameters: $K_{\sigma-} = 1$, $K_{\sigma+} = 1.51$, $K_{\rho-} = 0.66$, $K_{\rho+} = K^* = 0.25$, $\omega_0 = 0.1$; when (a) $\beta = 50$, (b) $\beta = 200$.

Fig. 6.13 and Fig. 6.14 present the behaviour of the tunneling current in armchair-like nanotubes, exhibiting mini-gaps in bosonic modes, each described by specific parameters. The system is described within the framework of a TLL model. For illustration purposes, q_0 is set to $1/(3a)$. As seen in the figures, when ω changes from -1 to -0.2, the current gradually increases; then at $\omega = -0.2$, there is a sharp decrease (a discontinuity, like before), and the current stays the same, constant up to the point when $\omega = -0.1$. In the region of ω changing from -0.1 to 0.1, the current is forced to be zero. At $\omega = 0.1$, there is a sharp increase and in the region of 0.1 to 0.2, the current decreases. When $\omega > 0.2$, the current behaves as in the previous case (Fig. 6.11 and Fig. 6.12). Comparing these
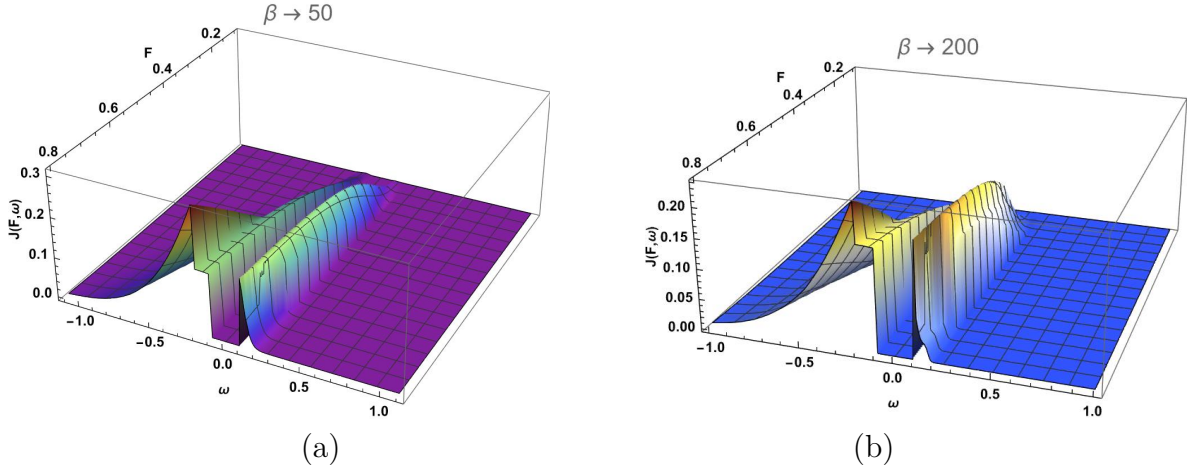
Figure 6.14: The tunneling current for armchair-like nanotubes, described by the following parameters: $K_{\sigma-} = 1$, $K_{\sigma+} = 1.17$, $K_{\rho-} = 0.85$, $K_{\rho+} = K^* = 0.25$, $\omega_0 = 0.1$; when (a) $\beta = 50$, (b) $\beta = 200$.

results with those for zig-zag-like tubes, namely Fig. 6.11, Fig. 6.12 and Fig. 6.13, Fig. 6.14, it can now be observed that in the periodically modulated case, the increase of $J(F)$ is actually delayed. For stronger interactions, intense growth occurs only for the largest electric fields F without any observed saturation. The amplitudes of all current peaks are smaller, as clearly revealed by the discontinuity at $\omega = -0.2$. The presence of spatial modulation of the nanotube properties should be thus visible in this non-trivial way in the (ω, F) characteristics of the material.

6.6 Chemical potential variation

The case of a 3D metal is relatively simple: external electric field cannot penetrate it, screening is perfect, and chemical potential inside the material is constant. On the contrary, 1D metals can screen the external electric field only partially; hence, a finite slope of chemical potential can be expected when the nanotube is subjected to a strong external electric field, the $\mu(r, F)$ dependence. The problem of a chemical potential μ in a TLL under external bias has been solved in [177] and we shall use this solution here. Given that $K_{\rho+} \approx 1/4$ in our case, the TLL in the vicinity of Mott transition is being dealt with. This means that the term in Eq. 5.8 is close to being relevant. In fact, some past works [209] indicated that at the lowest energies, MWCNT can undergo partial localization, leading to the fragmentation of conducting liquid. We then extend the single impurity treatment used in Ref. [177] by considering the continuous distribution of unitary scattering centers $\lambda_B \approx 1$, where λ_B is the amplitude of local back-scattering in the notation of that paper. We aim to know the voltage drop U_x in such an effective medium that mimics MWCNT.

The exact analytical solution, that connects the externally applied field F with the gradual voltage drop inside 1D system U_x has been obtained therein[177]. More precisely we use a derivative of their solution since we work in the continuous scatters limit. The self-consistent relation reads:

$$U_x = Im\left[\psi\left[0.5 + \frac{0.5 + \imath(2U_x - 1.5F)}{2\pi T}\right]\right] \tag{6.29}$$

where $\psi(...)$ is the digamma function. We solve this equation numerically to obtain the relation $U_x(F)$. The four-voltage potential derivative U_x was associated with chemical potential gradient and an external bias with external electric field F to which the nanotube is subjected. A solution of this equation U_x is the desired slope of electro-chemical potential, a quantity that is included inside our formulas. Namely we take $\mu(r) = rU_x$ with a boundary condition that $\mu(r = L) = E_F$ i.e. deep at the bottom of the nanotube chemical potential is equal to MWCNT Fermi energy.

6.7 Dependence on work-function

Our formalism also enables us to directly modify the work function of the material under consideration. The work function is a key component in the analysis of the electronic properties of materials [210]. It characterizes the material which is observable in the effects it has. In composite materials, such as those presented in Chapter 4, Sec. 4.4.3, the work function can be tuned in a certain range of parameters. It is a characteristic property of the material, and if a different material is taken, our formalism entirely captures all that by adjusting the unit of energy, indicated as ω_0. Basically, our formalism is applicable to different values of work function. The ability to adjust the work function allows for enhanced control over the electronic behavior of the material. This additional feature is inspected here. Physically, this corresponds to changing the material.
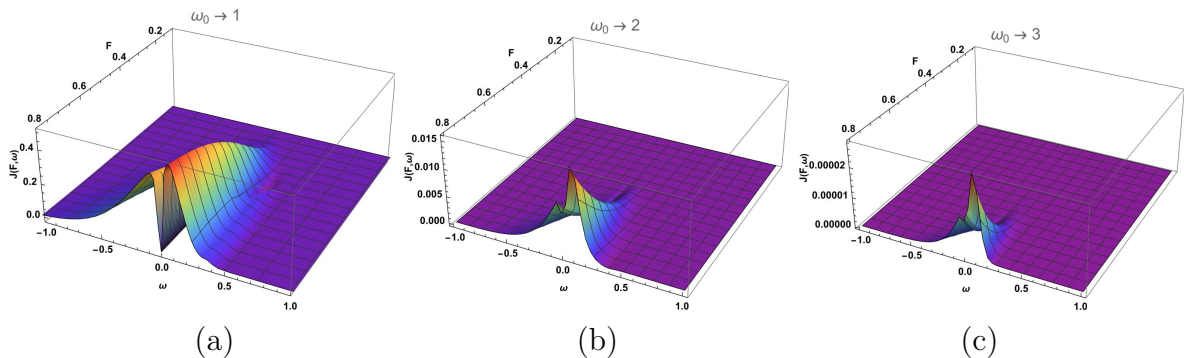

Figure 6.15: The tunneling current for nanotubes, described by the following parameters: $K_{\sigma-} = 1$, $K_{\sigma+} = 1.51$, $K_{\rho-} = 0.66$, $K_{\rho+} = K^* = 0.25$, $\beta = 50$, when (a) $\omega_0 = 1$, (b) $\omega_0 = 2$, and (c) $\omega_0 = 3$.

Fig. 6.15 and Fig. 6.16 present the tunneling current for different work functions, when $\beta = 50$ and $\beta = 200$ accordingly. As shown in the figures, in the case of higher work function, the tunneling current is smaller, as the barrier that the election has to overcome to exit, is becoming much larger. It should be noted that panel (a) in both figures (Fig. 6.15 and Fig. 6.16) is the same as (a) and (b) in Fig. 6.6.

One can also imagine the situation when we dope additives on the surface of MWCNT. Such chemical modification of the surface is a frequently used method of nano-engineering. Since we have computed the space-dependent n_{tube}, it should be rather straightforward for us to incorporate also the space-dependent $\omega_0(x)$ inside $T(\omega, F, x)$ in Eq.6.22 if a specific experimental device requires that. The study of a surface with different $\omega_0(x)$ has been performed in the second half of Chapter 4, thus we are able to predict the effects that are expected to be seen for such a composite system.
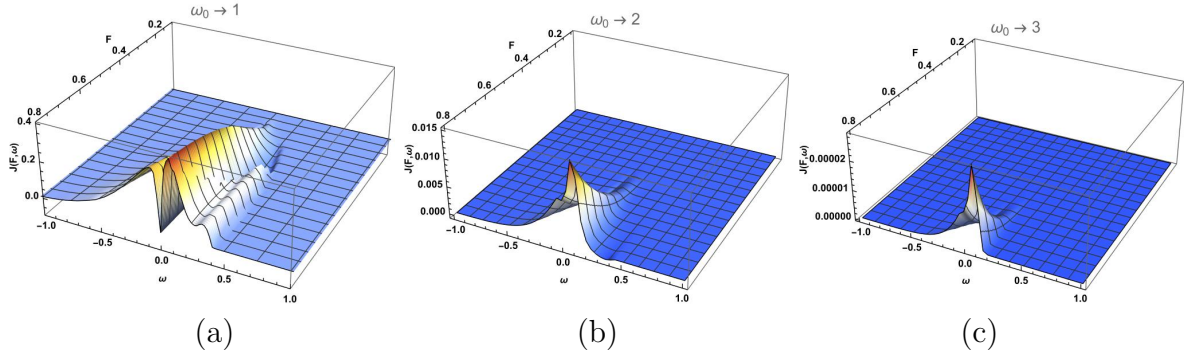
Figure 6.16: The tunneling current for nanotubes, described by the following parameters: $K_{\sigma-} = 1$, $K_{\sigma+} = 1.51$, $K_{\rho-} = 0.66$, $K_{\rho+} = K^* = 0.25$, $\beta = 200$, when (a) $\omega_0 = 1$, (b) $\omega_0 = 2$, and (c) $\omega_0 = 3$.

6.8 Discussion and Conclusions

The main outcome of this work is to show that the effects of emission due to temperature and electron-electron interactions can be simultaneously and non-perturbatively accounted for in a closed analytic formula. It is observed that both lead to potentially observable effects. In our work, setting the bandwidth as a unit of energy, the results are easily transferable from one material to another, for instance, from carbon to silicon-based nanotubes. An open issue is the role of many-body interactions when the emission takes place from the tip of the nanotube. There were studies showing an emergence of additional purely many-body peaks on the tip [211], showing that the standard single-particle approach may be insufficient here as well. This will obviously depend on the microscopic structure of the tip in a given system, and an in-depth study of this effect is left for the future. Our considerations of exact quantum mechanical solutions at the end of Chapter 4 showed that these effects can be potentially linked with our formalism. One further example of such a many-body resonant peak is what was discovered in Hund metal case. Therefore, to compute the emission current in Hund's case, it would be necessary to capture this effect.

Taking into account the geometrical smallness of the tip, Coulomb-blockade effects should be always present. This will generally decrease the current from the tip, thus increasing the importance of the side-surface (background) current studied here.

Another open issue is the experimental relevance of the observed phenomena. Naturally, the temperature and the external field are parameters that can be varied in an experiment; our formula offers a possibility to fit these characteristics. Importantly, the TLL parameters can also be modified experimentally. For instance, the ways in which $K_{\sigma+}$ can be affected by an external magnetic field have been studied in detail in the work of Egger et al [212]. This parameter will also be modified for nanotubes made from heavier elements with stronger spin-orbit coupling. On the other hand, the $K_{\rho-}$ parameter is usually linked to the strength of the effective on-site Hubbard parameter and on the strength of inter-valley hybridization. Both of them are largely unknown and can also lead to a mini-gap in the spectrum, the effects of which have been investigated in the later part of this study. However, our connection of the $K_{\rho-}$ parameter value with the charge inhomogeneities on the circumference indicates that this quantity should be susceptible to tension and chemical modifications of MWCNTs. Hence, this may also allow for a control of this parameter.

This last remark, regarding unknown parameters in effective low-energy physics of multi-wall nanotubes, brings up another relevant aspect of our work. In our plots, qualitative differences between various types of nanotubes are clearly evident. These differences can even be quantified if the TLL parameters are sought after. This implies that our results could serve as a tool to *diagnose* arrays of MWNT, in order to determine, through low energy field emission, the fraction of nanotubes representing certain properties, and also to specify whether the fabrication method has any influence on that. Although more crude, this may be a fast and efficient alternative for Raman spectroscopy methods [213] that are used now for this daunting task of distinguishing the chirality of nanotubes. It is worth emphasizing that the field mission can also be used with microscopically small electrodes. Therefore, it should be possible to obtain valuable space-resolved information about the many-body effects in arrays of nanotubes.

Moreover, while discussing experimental techniques, it is essential to differentiate between ARPES [214] and the FE method (which is the focus of our study). In FE, the focus is on varying the amplitude of the external electric field, adjusting frequency through photon-assisted FE, or regulating back-gate potential. In ARPES, which has also been done in CNTs [73], it is necessary to resolve problems of light wave interference and light polarization (that determine dipole moments of the transition), i.e., everything under the assumption that the amplitude of the dynamic external field is weak (within a linear response regime). Though the two techniques differ in their foundational principles, they complement each other, as seen in the emergent research on photon-assisted FE [215].

Our study will also have implications for the modelling of nanotube arrays. Although our focus is on one specific range of parameters, where our analytic formula works, the advantage of our result is that it is an exact method, with no approximation involved. Thus, it can serve as a benchmark for numerical calculations. The fact that it is analytic means that the formula may be easily transferred from one material to the other simply by modifying parameters. It can also be applied for processes other than FE, where electron tunneling in a large side-surface of nanotube arrays plays a vital role, for instance, in chemical and materials engineering processes geared towards catalysis or hydrogen storage.

Chapter 7

Nanotubes' Array: role of geometry

7.1 Introduction

The focus of the previous chapter was the regime of small external electric fields. It is there where the correlation phenomena are most pronounced. However, one can also inquire what the role of the geometry of the nanotube array is. The parameters that can be varied are the distances between the nanotubes, the radii of the nanotubes and the height of the nanotubes. They will have the biggest influence in the regime of the high external electric field. In that case, the bottleneck determining the transport, the field emission, is set by the solution of the electrostatic Poisson equation. The geometry defines the boundary condition for Poisson equation, playing a crucial role [137]. This chapter is dedicated to studying these geometrical effects.

7.2 Electron Emission Theory for Nanotube Array

So far detailed analytical and numerical solutions have been given for the case of the tip of a single nanotube only [10], [216]. Here we fill this gap in our knowledge of real enginnering devices and give a detailed analysis of how the geometrical arrangement of an entire array of nanorods influences the resulting emission current. Our formalism is general, however, for specificity, triangular and square arrangements of the tubes are considered below.

7.2.1 Formalism

In this part of the work, a relatively simple modelling of electrostatic potential around an *array* of nanorods is employed. We would like to fit the electrostatic potential as a power law with an arbitrary exponent. Then, one would be able to straightforwardly consider electron-electron correlations as well, and this formalism can be incorporated into the recently developed generalization of Fowler-Nordheim formalism (Chapter 4). As a result, a closed analytic formula is obtained, allowing for a rather straightforward inspection of how the geometry of an array influences the field emission current.

To compute the field emission current density $j(E)$ we use the recently developed (Chapter 4) generalization of Fowler-Nordheim formalism, which accounts for a tunneling bar-

rier described by an arbitrary power law. In this case, the formula for $J(E)$ is the Eq. 3.21.

To implement it, an expression for the electric field potential outside the emitting rod is required, which is assumed to be in the same form as before, i.e. given by the following expression:

$$V(x) = h - eF\mathbf{d}_0 x^\alpha - \frac{e^2}{16\pi\epsilon_0\mathbf{d}_0 x^\alpha} \tag{7.1}$$

where, once again, we introduced a characteristic length $\mathbf{d}_0$ that scales the distance. Here, it is a free parameter that one aims to fix from the electrostatic solutions. On the other hand, for a *single* nanotube, one can use a known formula (from the textbook [217]), which is a formula for elongated spheroid and provides the electric potential around the spheroids. This will be used as a starting point, and then a combination of these formulas will be implemented for various distributions for spheroids [218]. The single spheroid potential reads:

$$f_{\phi U}(x, y, z) = \frac{1}{2\ln(2H/R)} \cdot \ln\frac{\sqrt{\xi + H^2} + \sqrt{H^2 - R^2}}{\sqrt{\xi + H^2} - \sqrt{H^2 - R^2}} \tag{7.2}$$

where

$$\xi = -p + \sqrt{p^2 - q}; \tag{7.3}$$

$$p = \frac{H^2 + R^2 - (x^2 + y^2 + z^2)}{2} \tag{7.4}$$

$$q = H^2 R^2 - H^2\left(x^2 + z^2\right) - R^2 y^2; \tag{7.5}$$

Eq. 7.5 presents the potential for a single spheroid, and now the potential for a few spheroids is being calculated, it is necessary to take the superposition of this potential with appropriately shifted reference points where the x_i, y_i, and z_i are the centres of the spheroids we have.

$$V = \left[\sum_{i=1}^{N} V(x - x_i, y - y_i, z - z_i)\right] \tag{7.6}$$

where N is the number of rods taken to evaluate the potential. First, a point in the $x - z$ plane is chosen where the potential should be calculated. For example, in the case of an equilateral triangle, the point is at the center of the triangle O. The potential is then calculated along the height of the rod for various y_i, e.g., at half-height and full height. It is assumed that the rods form a potential well, from which the electron can escape. Then the axial value of the potential is plotted in *log* scale as a function of the *log* of the perpendicular distance. For a given value of an external potential, it is observed that the electron will leave the well at a certain y_{exit} point. Assuming that the external potential is given in the form of a power law, as shown in Eq. 7.7, the log of the potential will give us the slope or the alpha power coefficient for each value of y (Eq. 7.8):

$$V = y^\alpha \tag{7.7}$$

$$\log V = \alpha \log y \tag{7.8}$$

The average value of the power law coefficient is then calculated, as the electron crosses the barrier, up to the exit point. As the barrier becomes longer, and the exit point further away, the effective exponent will differ as the shape of the barrier will changes.

7.2.2 Results

Nanotubes are placed in the corners of the equilateral triangle and in the corners of the square (the side of the triangle and the side of the square are equal to d_0, see Fig. 7.1).

(a)   (b)
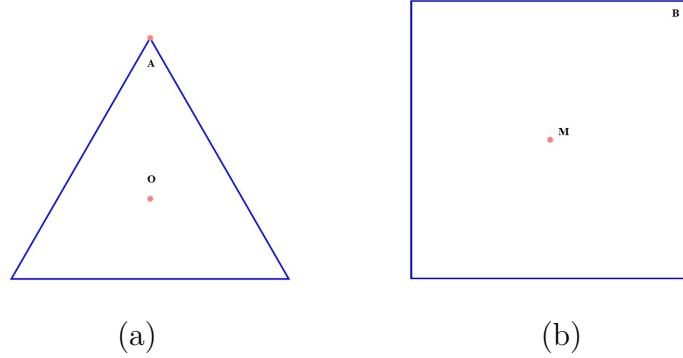
Figure 7.1: Equilateral triangular array and square array (the rods are in the angles of the triangle and square respectively), the calculations are done at the points $A(d_0/2, d_0\sqrt{3}/2)$ and $O(d_0/2, d_0\sqrt{3}/6)$ for triangle and at the points $B(d_0, d_0)$, $M(d_0/2, d_0/2)$ for square. The side of the triangle and the side of the square are equal to d_0.

The calculations have been made for various geometrical arrangements (Table 7.1). Next, the dependence on the geometry has been discussed, as well as the distinctive effects when the rods are made thicker or thinner, longer or shorter.

Distances between the rods d_0 (μm)	Radius R (nm)	Height H (μm)
100	25	1
200	25	1
1	25	1
100	25	2
100	12.5	1

Table 7.1: Geometrical parameters of nanotube arrays, detailing the distances between the rods, their radii, and heights

We begin by showing values of the potential on the (x, z) surface to show that it correctly mimics the chosen positions of the rods (Fig. 7.2). These plots serve as a cross-check to verify the consistency of the calculated electric potential with the physical arrangement of the charged rods. They confirm that the potential is well-defined and accurately reflects the expected influence of the rods' positions and geometries.

Emission currents at various characteristic points can now be studied. In the first step, the result of Eq. 7.1 is calculated along the axis of nanotubes; hence, the axis is perpendicular to the surface, and approximated by a power law with a varying exponent.

(a)   (b)
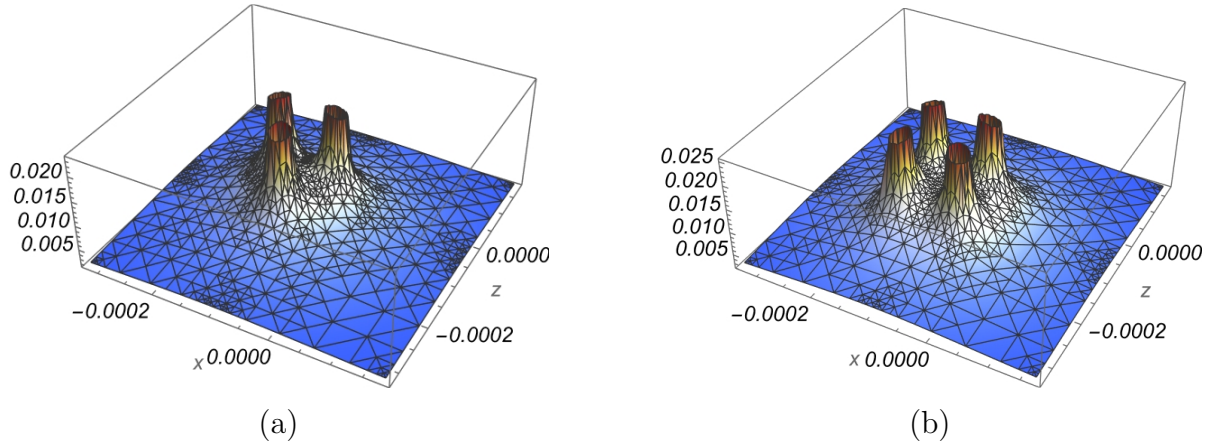
Figure 7.2: The electric potential (a) at the centre of the triangle O in $H/2$ height of rod, (b) at the centre of the square M in H height of the rod.

In the following figures (Fig. 7.3 - 7.8), the transmission, as calculated above, has been multiplied by the Lorentzian peak for the high-energy single-particle density of states. This approximation should hold for the strongest electric fields when electrons are instan-

(a)   (b)

(c)   (d)
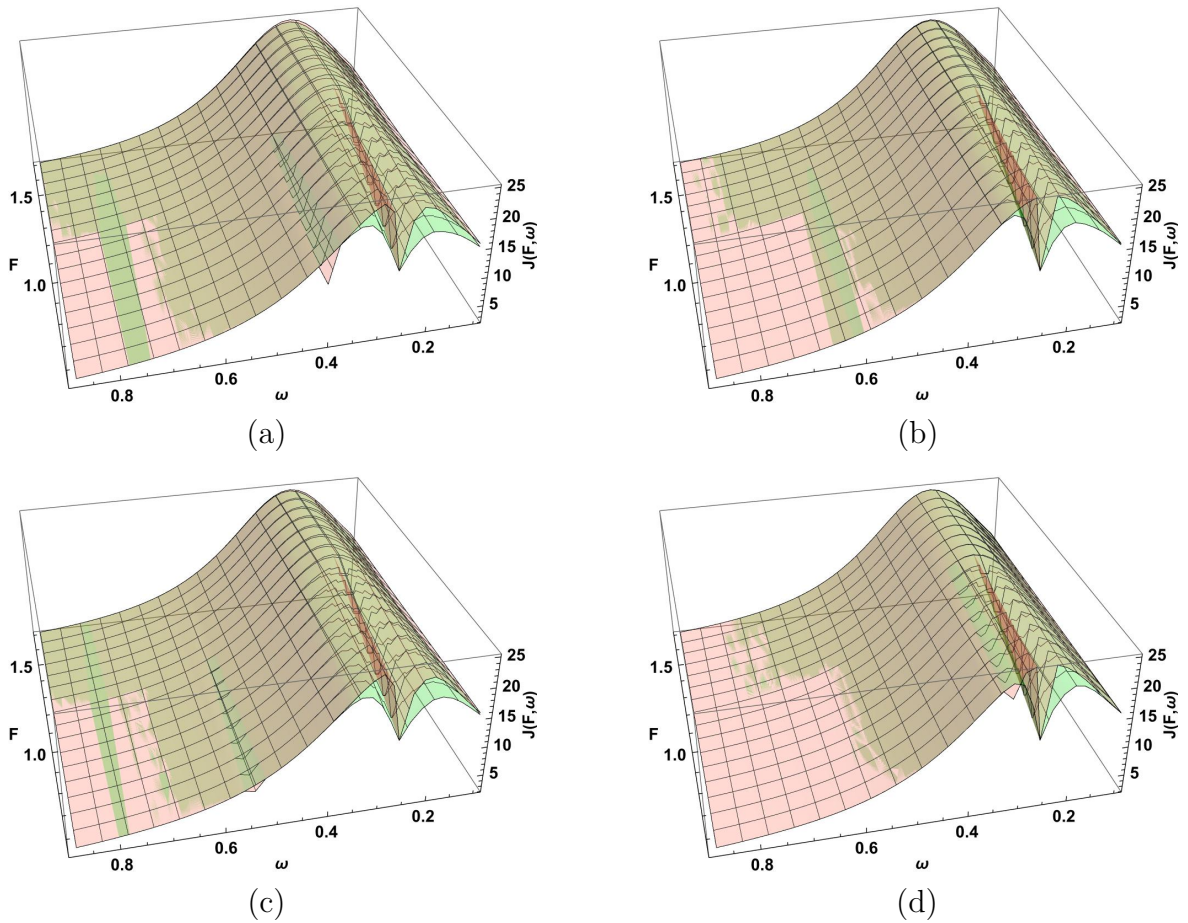
Figure 7.3: The electric current comparison depending on the distances between the rods in the (a) centre of the triangle O; (b) angle of the triangle A; (c) centre of the square M (d) angle of the square B; accordingly Green: $H = 1\mu m$, $R = 25nm$, $\boldsymbol{d_0}\boldsymbol{=}\boldsymbol{100\mu m}$, Pink: $H = 1\mu m$, $R = 25nm$, $\boldsymbol{d_0}\boldsymbol{=}\boldsymbol{200\mu m}$.
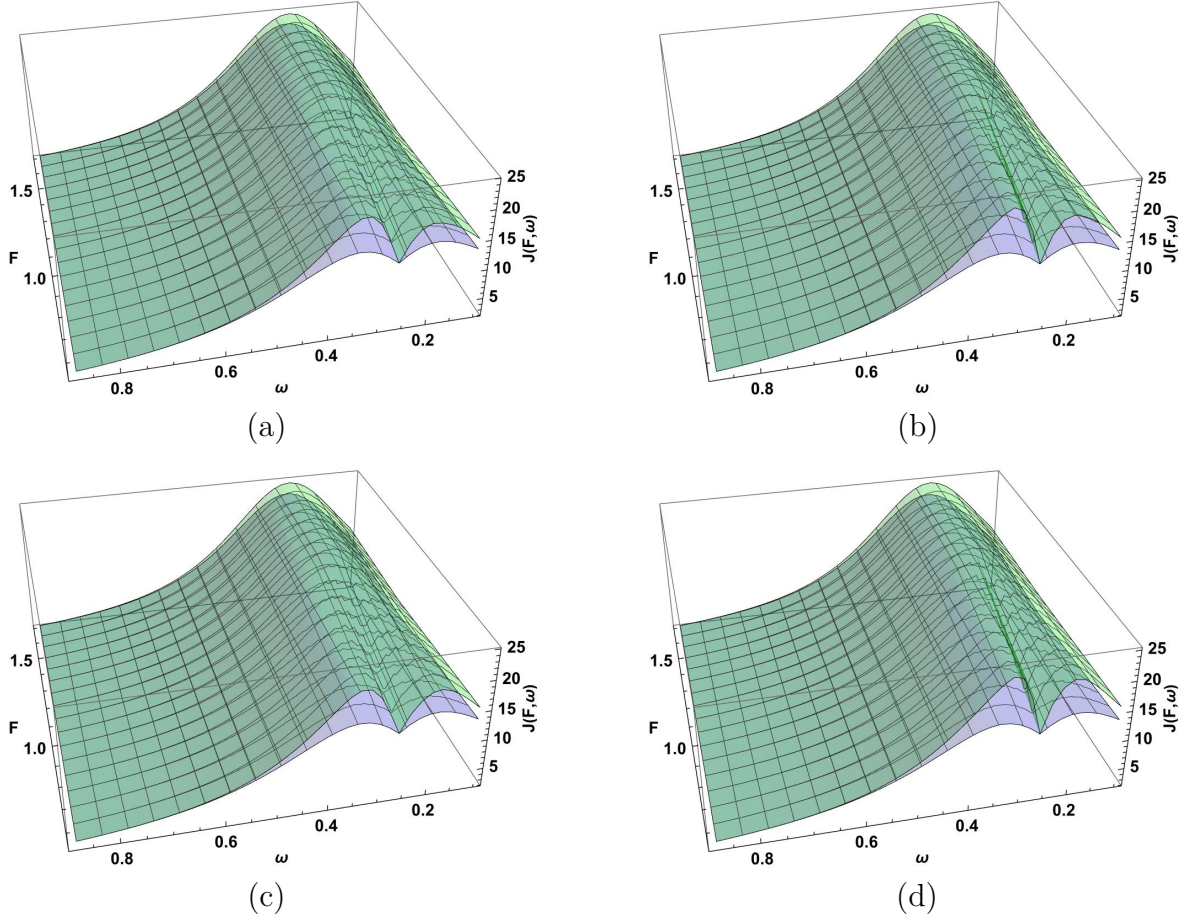
Figure 7.4: The comparison of the electric current in terms of long (d_0=100μm, green) and short (d_0=1μm, blue) distances between the rods in the (a) centre of triangle O, (b) angle of triangle A, (c) centre of square M, (d) angle of square B; when $R = 25nm$ and $H = 1\mu m$.

taneously pulled away from the nanotube. What is observed is the dip in the Lorentzian, corresponding to the ZBA detected in the previous chapter. Here it is noted how the ZBA gradually disappears for the largest applied fields F.

Fig. 7.3 and Fig. 7.4 present the electric current comparison depending on the distances between the rods. All comparisons are made with the case when the height of rods is $H = 1\mu m$, the radius of rods is $R = 25nm$, and the distance between the rods is $d_0 = 100\mu m$.

Fig. 7.5 presents the electric current comparison depending on the height of rods in the (a) centre of the triangle O; (b) angle of the triangle A; (c) centre of the square M; (d) angle of the square B. Fig. 7.7 presents the electric current comparison depending on the radius of rods in the (a) centre of the triangle O; (b) angle of the triangle A; (c) centre of the square M; (d) angle of the square B.

As shown in the figures, variations in the radius size and the height of the rods appear to have a negligible impact on the results. This is evident from the similarity of the response surfaces across different values of rod radius and height. However, the distance between the rods significantly affects the outcomes. The response surfaces vary when the inter-rod distance changes, indicating that this parameter is a critical factor in the electric current comparison.
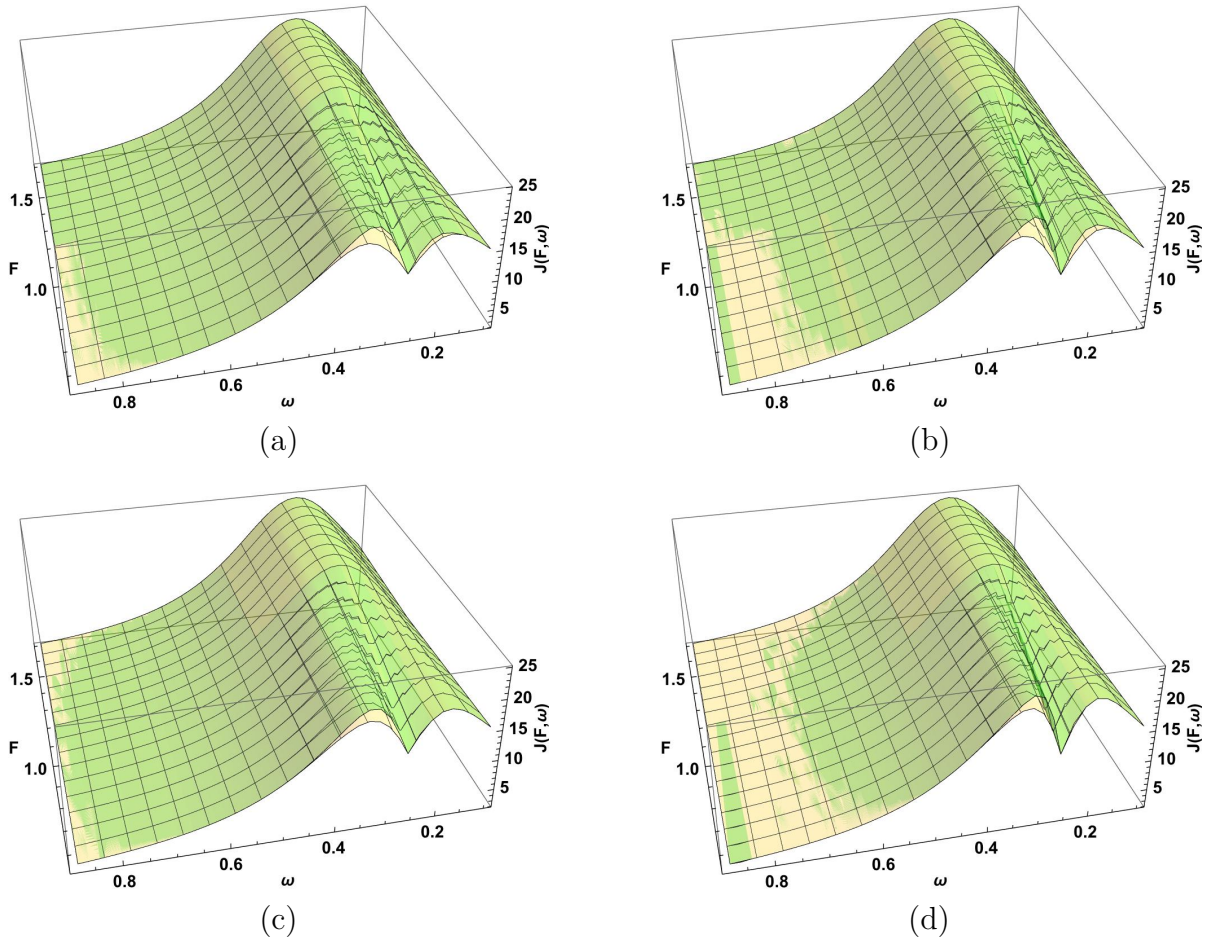
Figure 7.5: The electric current comparison depending on the height of rods in the (a) centre of triangle O; (b) angle of triangle A; (c) centre of square M; (d) angle of square B; accordingly Green: $\boldsymbol{H=1\mu m}$, $R = 25nm$, $d_0 = 100\mu m$, Yellow: $\boldsymbol{H=2\mu m}$, $R = 25nm$, $d_0 = 100\mu m$.
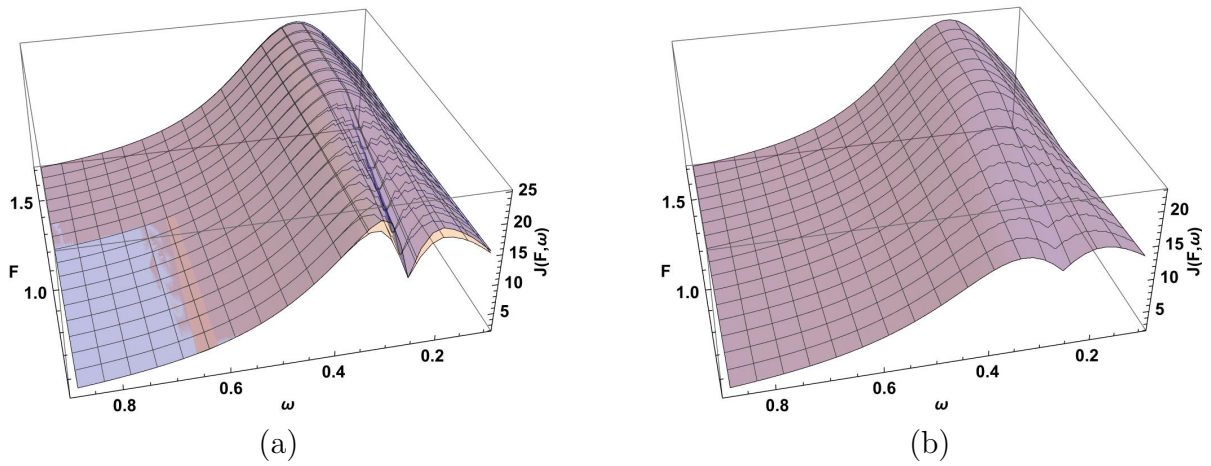
Figure 7.6: The electric current comparison in the centre of triangle O (Orange) and in the angle of triangle A (Blue), when (a) $H = 1\mu m$, $R = 25nm$, $\boldsymbol{d_0=100\mu m}$, (b) $H = 1\mu m$, $R = 25nm$, $\boldsymbol{d_0} = 1\mu m$.
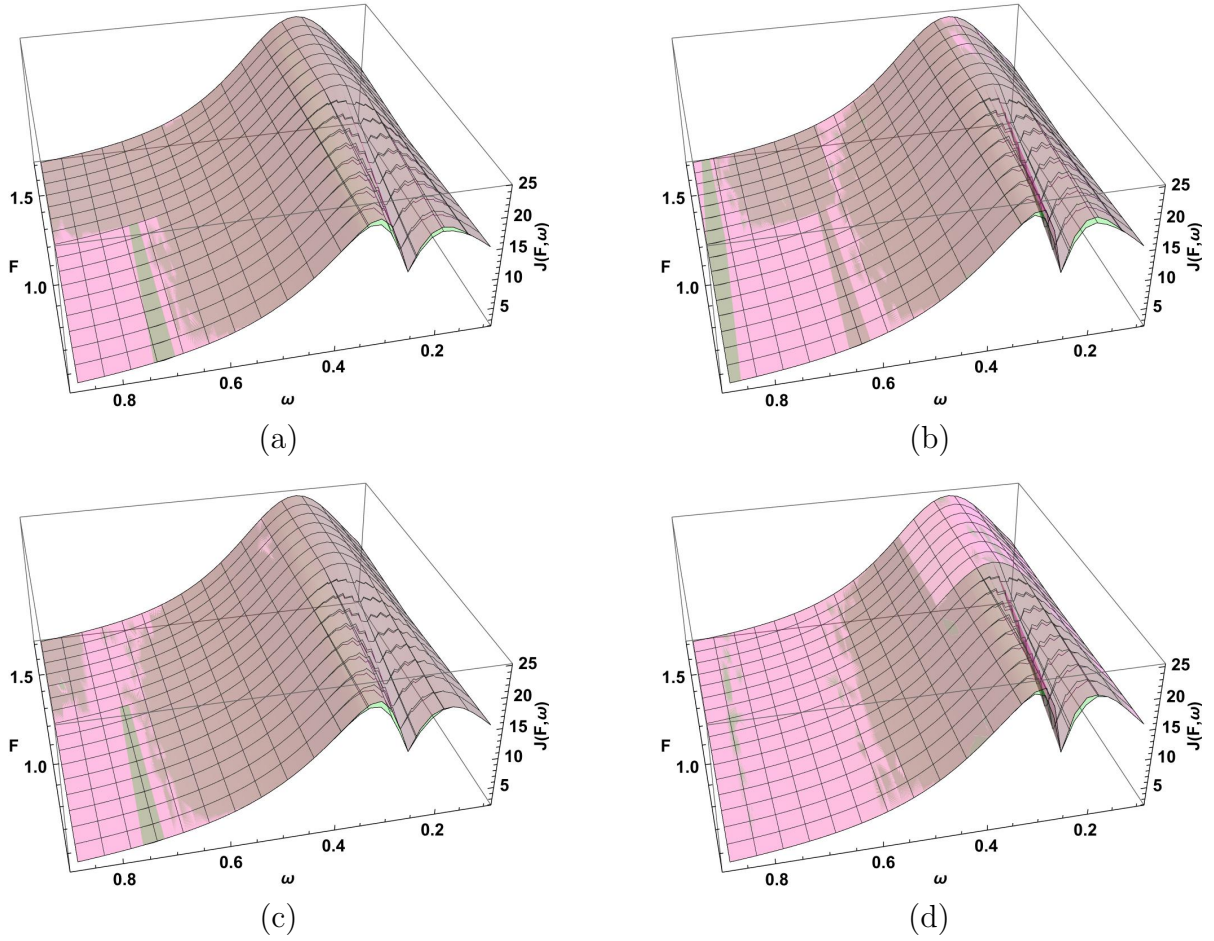
Figure 7.7: The electric current comparison depending on the radius of rods in the (a) centre of triangle O; (b) angle of triangle A; (c) centre of square M; (d) angle of square B; accordingly Green: $H = 1\mu m$, **$R=25nm$**, $d_0 = 100\mu m$, Magenta: $H = 1\mu m$, **$R=12.5nm$**, $d_0 = 100\mu m$.
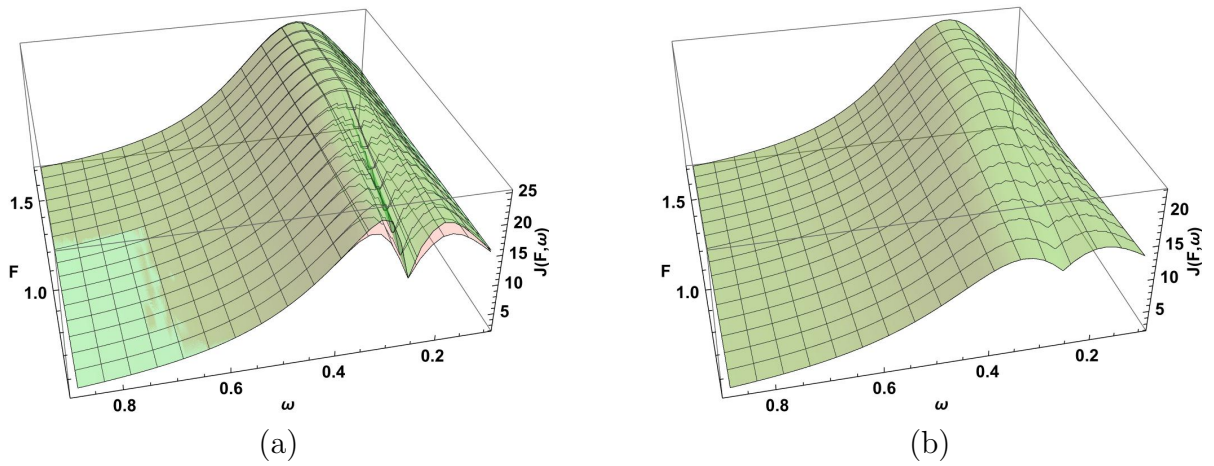
Figure 7.8: The electric current comparison in the centre of square M (Pink) and in angle of square B (Green); when (a) $H = 1\mu m$, $R = 25nm$, **$d_0=100\mu m$**, (b) $H = 1\mu m$, $R = 25nm$, **$d_0=1\mu m$**.

In Fig. 7.6, the electric current measurement point is set in the centre of triangle O and in the angle of triangle A, and in Fig. 7.8, it is in the centre of square M and in the angle of square B, at different rod parameter configurations on different points. As observed from the figures, the geometrical point of calculation is essential when the distances between the rods are large, while in the case of small distances, it becomes negligible.

7.3   Partial Conclusion

This chapter provides an analysis of the influence of nanowire geometry on electric field emission. It is established that the distance between nanorods is a main factor affecting the emission current, with significant changes observed in response to changes in this parameter. Conversely, changes in the height and radius of the nanorods have little effect on the emission current. Based on gFN formalism, it serves as a fundamental tool to forecast and adjust the electron emission properties of nanomaterials according to their geometrical configurations.

Future perspectives: Based on the findings discussed in this chapter, future research should focus on direct experimental validation and comparison of these calculations. Experimental setups could be designed to specifically manipulate the geometrical parameters of nanorod arrays, such as distances between rods, their heights, and radii, to directly observe their influence on electron emission. These parameters can be adjusted by the CVD method: varying the geometry of the catalyst mask, the time of growth, and the size of the catalyst, respectively. This approach would not only validate the theoretical models but also provide practical insights into optimizing nanodevice designs for specific applications in field emission technologies. Additionally, exploring the interaction of these geometric factors with different materials and surface coatings can enhance the efficiency and stability of electron emission, allowing for new applications in electronic devices.

Chapter 8

Conclusion and Outlook

> There are two possible outcomes: if the result confirms the hypothesis, then you've made a measurement. If the result is contrary to the hypothesis, then you've made a discovery.
>
> *Enrico Fermi*

This thesis has been presented in the research field of quantum tunneling and electron interactions in nanostructures, particularly focusing on the analytic modelling of tunneling phenomena and the effects of temperature and electron-electron interactions in nanotubes.

The original research outputs obtained in the thesis are:

1. in Chapter 4, formula for field emission with arbitrary exponent of tunneling potential [105], in particular

   a) The canonical Fowler–Nordheim theory is extended by computing the zero-temperature transmission probability for the more general case of a barrier described by a fractional power law. The theory captures the screening of external field interaction with the image potential.

   b) An exact analytical formula is derived, expressed in terms of Gauss hypergeometric functions. The new formulation is compared with the most advanced existing formulation of Fowler-Nordheim theory by then, expressed in terms of elliptic integrals.

   c) The transmission probability from the composite surfaces is presented, and its dependence on the power law exponent is analyzed.

   d) The formalism is also bench-marked against a numerical scattering matrix method. Our analytical formula provides the same accuracy with negligible computational cost.

2. in Chapter 5, we study space-dependent properties of 1D collective liquid (known as Tomonaga-Luttinger liquid, TLL) that exists inside carbon nanotube, in particular

   a) The analytic expression for Fourier transform of LDOS was obtained and analysed for both Coulomb metal and Hund metal.

   b) The spectral function analysis approach was extended to explore two-body correlations, focusing on charge susceptibility. $4k_F$ susceptibility is shown to

be a combination of two susceptibilities $2k_F$, with distinct behaviors in bulk and at boundaries (the $4k_F$ susceptibility, dependent on the $\cos(4\phi_\rho)$ operator and not influenced by the spin sector, is found to be the same both for Coulomb and Hund metal).

3. in Chapter 6, the current is computed by connecting TLL framework (where material dependence comes from the parameters K_ν) with the above-mentioned results of Chap.4, namely:

   a) The analytical results from Chapters 4 and 5 are used to calculate the field emission current for various nanotubes.

   b) The importance of electron-electron interaction and temperature effects on the tunneling current is demonstrated. It is shown that electron-electron interactions have a significant impact on the emission and can be used to distinguish types of nanotubes.

   c) A widely applicable model has been developed incorporating tunable material-specific parameters that can be applied to various nanostructures by changing parameters such as electron velocity and UV cut-off.

4. in Chapter 7 we study effects of an electrostatic potential derived from a geometry of the nanotubes' array

   a) An in-depth analysis is provided on how the geometry of nanowires affects electric field emission.

   b) It establishes that the distance between nanorods is a critical factor that significantly influences the emission current.

Achieving these outputs allows for the feasibility of such formalism, in terms of analytic solution, for the field emission from MWCNT. The formalism incorporates both the effects of arbitrary temperature and of strong correlations within 1D system. Thus, the initial **hypothesis**, suggesting that such formalism is possible, ***has been assessed positively***. The significant impact of electron interactions across both small and large external fields has been captured. Specifically, conditions for the monochromaticity of the outgoing electron beam, a crucial aspect for applications, were determined: improving electrons' beam monochromaticity will expand the accuracy of future SEM and TEM devices where beam coherence and uniformity are of primary importance.

The results derived here are applicable to a wide range of materials: it is sufficient to change the value of material-specific parameters – velocity and UV-cut-off – to move from carbon nanotubes to nanotubes based on different elements, or potentially to columnar materials, as well. In this latter case, for a denser system, the emitted current may need to be convoluted with some characteristic penetration depth.

Limits of validity of the approach

Like any theoretical formalism, our approach also has its limits of validity. The most important one is that we rely on TLL description of 1D carriers. On the lowest energy side, it was demonstrated how to go beyond that and accommodate the effects of minigaps in the spectrum. On the higher energy side, the problem is more profound due to the entry of band curvature effects. It is known that in this case, some spectral weights will be shifted into the area between holon and spinon dispersions. However, the majority of LDOS remains in the holon and spinon poles, implying that our approach serves as a good first-order approximation.

Actually, the most pertinent problem is not necessarily the one with spinon dispersion curvature, as this can be taken into account in the lowest-order approximation through substitution $v_\sigma \to v_\sigma(q)$. In fact, we studied the effect of changing boson velocity, as shown in Fig. 6.7, so we can even make predictions how such effect will manifest. The issue is with other higher-energy bands that may be activated at very large values of ω and F. The fact that TLL is valid only within a finite frequency window is accounted by UV cut-off (or by introducing incomplete Beta functions like in Ref. [219]). There is, however, an issue of LDOS from these other bands. To be precise, the TLL states will extend to these higher energies, but will be convoluted with the response of other carriers. The most sensible approach would be to take some form of a polaronic picture, where single particle LDOS of the other carriers will be dressed through the Land-Frisov transformation, with 1D bosons – both spinons and holons. Thus, the formalism derived here will nevertheless play a role. Obviously, this is a material-specific problem, since in each material, even in each device realization, the other band carriers will enter at different energies.

Future perspectives of this work

At the end of each chapter, we have indicated possible extensions of our formalism, namely how to incorporate resonant states, chemical modification of the surface, or varying velocities of the collective modes, to name the most important ones. This is to indicate that our formalism is not a closed analytical formula that will not lead to any further description of more complex realistic systems, but instead is open for further developments. Naturally, applicability to various other quasi-1D platforms can be achieved by simply changing the parameters. This versatility opens up possibilities for exploring new classes of materials and functionalities. Here we showed the way to quantify it. Further, device-specific studies are possible.

The TLL LDOS is also known for pumped systems, developing these was an active field of research in the last decade. Therefore, together with the fact that in Eq. 6.22 we can straightforwardly incorporate diffraction phenomena through spatially dependent field amplitude $F(x)$ our formalism can be also extended to address problems involving interaction with light. This includes time-resolved and femtosecond field emission, paving the way for advances in ultrafast electronic and photonic devices.

Another issue is that a relatively weak external electric field was assumed. Strong fields can affect the parameters of the TLL, making them spatially dependent, and increase the density of emitted carriers in between the tubes. This leads to the problem of the plasmon-polariton coupling regime. The problems of the TLL with spatially varying

$K_\rho(r)$ and non-hermitian TLL are currently being intensely studied in the literature. It has been recently shown [220] that extension to complex-valued TLL parameters can capture these phenomena. This gives hope that this regime can be incorporated in the formalism developed in this thesis. This also implies that curvature-induced holon lifetimes could be described by imaginary velocities in certain energy ranges, potentially overcoming the key limitation of this formalism, making it a universal description of the MWCNT platform.

Our results also hold significant implications for chemical reactivity on surfaces. In particular, our approach can be extended to study light-induced or plasmon-induced chemical reactions. This could improve our understanding of surface-mediated reactions and open new ways for research in material science and surface chemistry.

The assumption is that the chemical reactivity on the surface will depend on the amount of electrons available to perform the chemical reaction. This partially relates to the recent idea of plasmonic catalysis. Thus basically, by taking nanorods of some material and shining a light on them, plasmons with a certain density along the nanorod are induced. These plasmons, therefore, are observed inside the nanorod, allowing for some previously difficult chemical reactions to perform more easily now. So this is one possible pathway in which our calculations can be useful considering the density of electrons along the rod and the probability of an electron going out from the nanorod.

By acknowledging these potential extensions, we emphasize the broader impact and future potential of our work in both electronic and chemical applications.

Appendix A

Bosonization details

The derivations in this Appendix are based on the textbook of T. Giamarchi [96].

A.1 Derivation of fields

We consider the model of 1D fermions with linear dispersion:

$$H = V_F \sum_k k c_k^\dagger c_k \tag{A.1}$$

where $c_k^\dagger, c_k$ are their creation/annihilation operators in reciprocal space. The corresponding chiral fermionic field is $\psi_{r=R,L}$.

The basic quantity, that will also determine electron-electron interactions, is real space density $\rho(x)$. The Fourier component $\rho_r^\dagger(p)$ of the density is defined by

$$: \rho_r(x) := \frac{1}{\Omega} \sum_p : \rho_r(p) : e^{ipx} \tag{A.2}$$

where we identified normal ordering : ... : to avoid an infinite number of occupied states. It is defined as:

$$: \rho_r^\dagger(p) := \begin{cases} \sum_k c_{r,k+p}^\dagger c_{r,k} \ if \ (p \neq 0) \\ \sum_k [c_{r,k}^\dagger c_{r,k} - \langle 0| c_{r,k}^\dagger c_{r,k}|0\rangle], \ if \ (p = 0) \end{cases} \tag{A.3}$$

Let us call $\psi_R(x)$ (resp. $\psi_L(x)$) the operator destroying a right (resp. left) going fermion at point x. It satisfies the following commutation relation:

$$[\rho_r^\dagger(p), \psi_r(x)] = \frac{1}{\sqrt{\Sigma}} \sum_{k,k_1} e^{ik_1 x}[c_{r,k+p}^\dagger c_{r,k}, c_{r,k_1}] = -e^{ipx}\psi_r(x) \tag{A.4}$$

From that, we can postulate the bosonization formula, i.e, give an operator written directly in terms of boson operators, and that would produce the same commutation relations:

$$\psi_r(x) \simeq e^{\sum_p e^{ipx}\rho_r^\dagger(-p)(\frac{2\pi r}{pL})} \tag{A.5}$$

Rather than to work directly in terms of the density operators, it is convenient to introduce the two fields $\phi(x)$ and $\theta(x)$, which are defined by

$$\phi(x), \theta(x) = \mp(N_R \pm N_L)\frac{\pi x}{L} \mp \frac{i\pi}{L}\sum_{p\neq 0}\frac{1}{p}e^{-\alpha|p|/2-ipx}(\rho_R^\dagger(p) \pm \rho_L^\dagger(p)) \quad \text{(A.6)}$$

where the upper signs are for ϕ. Using these canonically conjugated bosonic fields, the single-particle operator and the *exact* expressions for the fermionic field are

$$\psi_r(x) = U_r \lim_{\alpha\to 0}\frac{1}{\sqrt{2\pi\alpha}}e^{ir(k_F-\pi/L)x}e^{-i(r\phi(x)-\theta(x))} \quad \text{(A.7)}$$

where we have added the so-called Klein factor operator U_r, which ensures proper anti-commutation relation obeyed by the fermionic field $\psi_r(x)$. From this we see that e.g. the kinetic energy term (Eq.A.1) which is proportional to $\sum_r(\nabla\psi_r)^\dagger(\nabla\psi_r)$ (upon applying chain rule and bringing derivative into exponential) will contribute $(\nabla\theta)^2$ to the Hamiltonian, a term that is present in Eq.3.48.

A.2   Correlation function

We now wish to obtain correlation function of fermionic field in Eq. A.7. Formally, the expression for time-ordered correlation reads:

$$G_R(r) = \langle\psi_R(r)\psi_R^\dagger(0)\rangle = -\frac{e^{ik_F x}}{2\pi\alpha}\langle e^{i(\phi(r)-\theta(r))}e^{-i(\phi(0)-\theta(0))}\rangle \quad \text{(A.8)}$$

where the relation $\exp A \exp B = \exp(A+B)\exp[A,B]/2$ to bring it to the same expression as Eq. 5.15 in the main text. We then split the terms in the exponential into the $G_{\phi\phi}$, i.e., averages of $\phi(x,\tau)\phi(0,0)$, the $G_{\theta\theta}$ plus the term $G_{\phi\theta}$ that arises from a finite commutator $[\phi,\theta]\neq 0$, which we will call $F_2(r)$ and evaluate it later on. In order to evaluate those first terms, we use a quite general relation (Debye-Waller):

$$\langle T_\tau e^{\sum_j i(A_j\phi(r_j)+B_j\theta(r_j))}\rangle = e^{-\frac{1}{2}\langle T_\tau[\sum_j(A_j\phi(r_j)+B_j\theta(r_j))]^2\rangle}$$
$$= e^{-\frac{1}{2}\sum_{i<j}[-A_iA_jK^2-B_iB_jK^{-2}]F_1(r_1-r_j)+[A_iB_j+B_iA_j]F_2(r_1-r_j)} \quad \text{(A.9)}$$

which allows to move the average into the exponential, i.e. move from the first to second line in Eq. 5.16 in Chapter 5. I have put back the time ordering to emphasize that this relation is valid for operators (here $r = (x, v_\nu\tau)$ is a coordinate on the space-imaginary time plane). We now look specifically into the correlation $G_{\phi\phi}$ of the bosonic fields. The average $\langle\rangle$ means time-ordered product so just for the next few lines I put back explicitly the time-ordered product and denote $\langle\rangle_0$ the averages without the time-ordered product, that is, simply $Tr[e^{-\beta(H-\mu N)}\ldots]/Z$

$$G_{\phi\phi}(x,\tau) = K^2\langle T_\tau[\tilde\phi(x,\tau) - \tilde\phi(0,0)]^2\rangle_0$$
$$= 2K^2[\langle\tilde\phi(0,0)\tilde\phi(0,0)\rangle_0 - Y(\tau)\langle\tilde\phi(x,\tau)\tilde\phi(0,0)\rangle_0 - Y(-\tau)\langle\tilde\phi(0,0)\tilde\phi(x,\tau)\rangle_0)] \quad \text{(A.10)}$$

We can now use the fact that averages, functional integrals of fields $\tilde\phi$, in TLL theory, are that of Gaussian matrix form, with a determinant equal to $\omega^2 + u^2k^2$ (in reciprocal space), see Eq. A.24, where the action matrix is given explicitly for chiral modes. In real space and zero temperature, this evaluates to:

$$G_{\phi\phi}(x,\tau) \;=\; K^2 \int_0^\infty \frac{dp}{p} e^{-\alpha p}[1 - e^{-v|\tau|p}\cos{(px)}] \;=\; \frac{K^2}{2}\log\left[\frac{(x^2 + v|\tau|+\alpha)^2}{\alpha^2}\right] \quad \text{(A.11)}$$

where a term under integral will be called $F_1(r)$. The α is a UV cut-off needed to regularize the integral. We have thus arrived at the same result as presented in the main text without details, the Eq. 5.16.

By collecting back all terms (a similar derivation for $G_{\theta\theta}$ will give a term proportional to $1/K^2$), we obtain:

$$G_R(r) = \langle \psi_R(r)\psi_R^\dagger(0)\rangle = -\frac{e^{ik_F x}}{2\pi\alpha}\langle e^{i(\phi(r)-\theta(r))}e^{-i(\phi(0)-\theta(0))}\rangle = -\frac{e^{ik_F x}}{2\pi\alpha}e^{-\left[\frac{K^2+K^{-2}}{2}F_1(r)+F_2(r)\right]}$$
$$\text{(A.12)}$$

Finally, let us derive the expression for $F_2(r)$. If we had to compute the single-particle Green's function

$$\langle T_\tau^F \tilde{\psi}_R(r)\tilde{\psi}_R^\dagger(0)\rangle$$

we would have to use the *fermionic* time-ordered product T_τ^F. Instead, all calculations we have done for the correlations of ϕ and θ, assume a *bosonic* time-ordered product (see Eq. A.10). Thus, instead of

$$Y(\tau)\langle\tilde{\psi}_R(x,\tau)\tilde{\psi}_R^\dagger(0)\rangle - Y(-\tau)\langle\tilde{\psi}_R^\dagger(0)\tilde{\psi}_R(x,\tau)\rangle \quad \text{(A.13)}$$

the corresponding correlation function in bosons

$$\langle T_\tau^B e^{-i(\phi(r)-\theta(r))}e^{i(\phi(0)-\theta(0))}\rangle = e^{-\left[\frac{K^2+K^{-2}}{2}F_1(r)+F_2(r)\right]} \quad \text{(A.14)}$$

corresponds to Eq. A.13 but with a plus sign for the second term. To correct it, we have to put a minus sign if $\tau < 0$. This can be achieved by multiplying the result by

$$e^{\pm i\pi Y(-\tau)} \quad \text{(A.15)}$$

If we take the convenient choice

$$e^{i\pi Y(-\tau)\text{Sign}(x)} \quad \text{(A.16)}$$

this amounts into replacing in F_2 the arctangent by

$$\text{Sign}(\tau)\arctan\left[\frac{x}{v|\tau|+\alpha}\right] + \pi Y(-\tau)\text{Sign}(x) \quad \text{(A.17)}$$

which is nothing but the argument of the complex number $y_\alpha + ix$ ($y_\alpha = v\tau + \alpha\,\text{Sign}(\tau)$). We can thus absorb the phase factor simply by changing the definition of F_2 the arctangent by the argument. The argument is defined with a cut on the negative real axis. It is easy to see that this modification takes care of *all* phase factors even in more complicated objects. Indeed, in an operator that contains a number n of fermionic operators either θ disappears (as in the density operator) or occurs with a coefficient n. In the formula Eq. A.9, the extra phase of π only appears if n is odd, which indeed corresponds to a fermion-like operator for which the time-ordered product should be taken with a minus sign. For n, even a term $e^{in\pi}$ appears, which leaves the results unchanged.

A.2.1 Retarded correlation function

The retarded correlation function can thus be written as

$$\chi_{BA}^R(t) = iY(t)[\chi_{BA}^T(t) - (\chi_{A^\dagger B^\dagger}^T(-t))^*] \tag{A.18}$$

where $\chi_{BA}^T(t)$ is the susceptibility of A, B operators, thus for $A \equiv c^\dagger, B \equiv c$, it is the time ordered Green's function as evaluated just above, but here defined on the real time axis (we shall also use the fact that for Green's function, the two terms in the parenthesis in Eq. A.18 are equal). It is thus enough to obtain the time-ordered correlation functions in real time to get the retarded correlation function. Green's function upon Wick rotation will read as follows:

$$e^{-[\frac{K_\rho^2+K_\rho^{-2}}{4}F_1(x,v_\rho\tau)+\frac{1}{2}F_2(x,v_\rho\tau)]} \rightarrow \left(\frac{\epsilon^2}{x^2+(it+\epsilon)^2}\right)^{\frac{K_\rho^2+K_\rho^{-2}}{8}-\frac{1}{4}}e^{-\frac{1}{2}\log[(y_\epsilon-ix)/\epsilon]}$$

$$= \left(\frac{\epsilon^2}{x^2+(it+\epsilon)^2}\right)^{\frac{K_\rho^2+K_\rho^{-2}}{8}-\frac{1}{4}}\frac{\sqrt{\epsilon}}{\sqrt{i(v_\rho t-x)}+\epsilon} \tag{A.19}$$

where we have used the following real-time integrals, as defined by Voit [170]:

$$F_1(x,t) + F_2(x,t) = -\frac{1}{2}[2V^\nu(x,t) - 2rV_0^\nu(xt)] \tag{A.20}$$

$$V^\nu(xt) = \frac{1}{2}\int_0^\infty \frac{dp}{p}e^{-\epsilon p}[1 - \cos(px)e^{-iv_\nu(p)pt}] \tag{A.21}$$

$$V_0^\nu(xt) = \frac{i}{2}\int_0^\infty \frac{dp}{p}e^{-\epsilon p}\sin(px)e^{-iv_\nu(p)pt} \tag{A.22}$$

and for the moment, for clarity, we dropped the "$cut-off$" subscript. To be very precise, it is commonly assumed that holon's velocity is a function of momentum $v_\rho(p)$ equal to v_ρ, when $p < \alpha$, and to V_F for larger momenta. The α is thus the UV cut-off of the theory above which other bands intervene and curve the metallic conduction band. The above given integrals thus need to be split $\int_0^\alpha ... + \int_\alpha^\infty$. It is upon this split that we get the pre-factor in the final Eq. 5.19, the final Eq. 5.19 is then recovered from Eq. A.19 and the two terms in Eq. A.18.

A.2.2 Chiral fields

When computing correlations for the boundary, we use chiral bosonic fields. We can rewrite the Gaussian action using these fields:

$$\begin{aligned}\phi_R &= K^2\theta - \phi\\\phi_L &= K^2\theta + \phi\end{aligned} \tag{A.23}$$

which are the fields only containing right (resp. left) movers (see Section 3.2). In the functional integral, the chiral fields decouple and have the action

$$S = \frac{1}{4\pi K^2}\frac{1}{\beta\Omega}\sum_{k,\omega_n}(\phi_*^{R,q}, \phi_*^{L,q})\begin{pmatrix}k(uk-i\omega_n) & 0\\0 & k(uk+i\omega_n)\end{pmatrix}\begin{pmatrix}\phi_{R,q}\\\phi_{L,q}\end{pmatrix} \tag{A.24}$$

The correlation functions of these fields are easily obtained and given

$$\langle \phi^*_{R,q} \phi_{R,q} \rangle = \frac{2\pi K^2}{k(uk - i\omega_n)}$$
$$\langle \phi^*_{L,q} \phi_{L,q} \rangle = \frac{2\pi K^2}{k(uk + i\omega_n)}$$
(A.25)

Of course, one can also recover the correlation functions between the fields ϕ and θ, using Eq. A.23 and Eq. A.25.

Appendix B

Field emission results: validation and applications

B.1   Scrutiny of past experimental results

A pivotal aspect of materials engineering stems from an ability to change the functional properties of a material by changing its structure on a mesoscopic scale. This shows that not only the atomistic, physical properties of constituting elements do determine the properties, but one can improve material by modifying its structure on intermediate scales. One remarkable example of such a situation is a phenomenon of field emission from carbon-based materials. The task is to pull electrons out of a material as efficiently as possible; thus, the escape route out of the sample matters significantly. In particular, one may expect that a vertically ordered array, with an easy escape route, will be much superior to a random sponge where outgoing electrons will suffer multiple collisions/reabsorption on their way out. The aim of this short appendix is to make the case that this indeed happens and then postulate devices that could profit from such a specific structure. This also justifies why in the main text, we have focused *on this and only this* specific structure.

In 1995, field emission (FE) from an isolated single multi-walled nanotube (MWNT) was first reported by Rinzler et al. [221], and FE from a MWNT film was reported by de Heer et al. [89]. In the early days, 20-30 years ago, the nanotubes were usually manufactured in a form of a dense paste printed on the substrate, at best on a micron scale. The field emission from such devices has been explored [87], but in this case only a tiny fraction of tubes, randomly sticking out of an amorphous composite of tubes and metal particles, can contribute to FE signal. Such material is not a subject of the PhD thesis.

The breakthrough came in 1998 when Ren and his team studied a large-scale method for fabricating well-aligned carbon nanotube (CNT) arrays on glass substrates using plasma-enhanced hot filament chemical vapor deposition [59], [222]. Thus, the idea of an array of vertically aligned tubes has been transferred from the realm of idealized model into physical reality of concrete devices and experimental benchmarks. Later, they explored potential applications of CNT arrays, such as cold-cathode flat panel displays, vacuum microelectronics, and hydrogen storage. Later, experiments on vertically aligned multi-walled carbon nanotube (MWCNT) arrays were again conducted by Ren's group [223], [224], [225] from MIT. Nanotubes made of different materials were also manufactured and they gave similar FE results. In Ref. [226], Fowler–Nordheim (FN) plots of ZnO nanowires are demonstrated (Fig. 5 in Ref. [226]), showing non-linear behaviour with
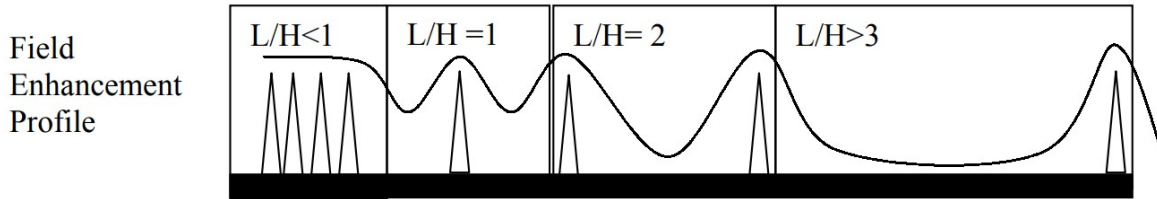
Figure B.1: Equipotential line for different densities of vertically aligned tubes. H is the height of the nanotubes, and L is the distance between the nanotubes. The L/H is a dimensionless parameter that describes the spacing of the array. For a dense array of nanotubes, the field cannot enter the areas in between the tubes, while for the sparse array, the line is directly above the substrate. The best arrays are those with intermediate L/H (Figure from [227]).

straight segments separated by slope changes – straight, then deviating, then straight again – suggesting multiple emission regimes.

The density of CNTs plays an essential role in determining their field emission properties (see Fig. B.2). As shown in Fig. B.2, the best field emission exists with sample F, when the nanotube is the longest with the intermediate density. When the density of nanotubes is smaller, the electric field can penetrate between the nanotubes [227], [228] (see Fig. B.1), enhancing the local electric field by each nanotube and improving electron emission. In contrast, when the nanotubes are dense, their electric fields overlap, reducing the effective field on each individual CNT [229]. The situation would be even worse in the amorphous cases - the electric field cannot enter between the nanotubes. In terms of length dependence, longer CNTs enhance field emission due to their higher aspect ratio, but this effect decreases at very high densities due to electric field screening. The field enhancement factor depends on the electric field, which proves that it is not only a factor but a function of F.

In Ref. [230], CNTs were grown by plasma-enhanced chemical vapor deposition on Ni nanoparticles made by electrochemical deposition, and then CNT arrays were half-embedded in the polymer. Next, fibre-free cloth was used to polish the surface that mechanically breaks the top part of the CNTs and exposes the tip of the CNTs, blocking the emission from the sides of CNTs.

Nanotubes can be coated for better control of the photonic crystal parameters. In order to create nonmetallic photonic arrays, such as nonmetallic 2D bandgap crystals, nanotubes can also be utilized as structural templates [231].

Upon these works, CNTs have been extensively studied for their FE properties due to their high aspect ratio, excellent electrical conductivity [232], and mechanical stability. The FE characteristics of CNTs have shown encouraging results for applications in vacuum microelectronics, flat panel displays [87], and electron sources. Ongoing research focuses on material engineering, surface modification, and advanced deposition techniques.

B.1.1 Dependence of $j(F)$ on the specific device

Naturally, since the current $j(F)$ depends on the local electric field in the area of the cathode (not simply on the external electric field F_{ext}), the outcome will depend on the specific arrangement of electrodes in the device under consideration. This is a problem
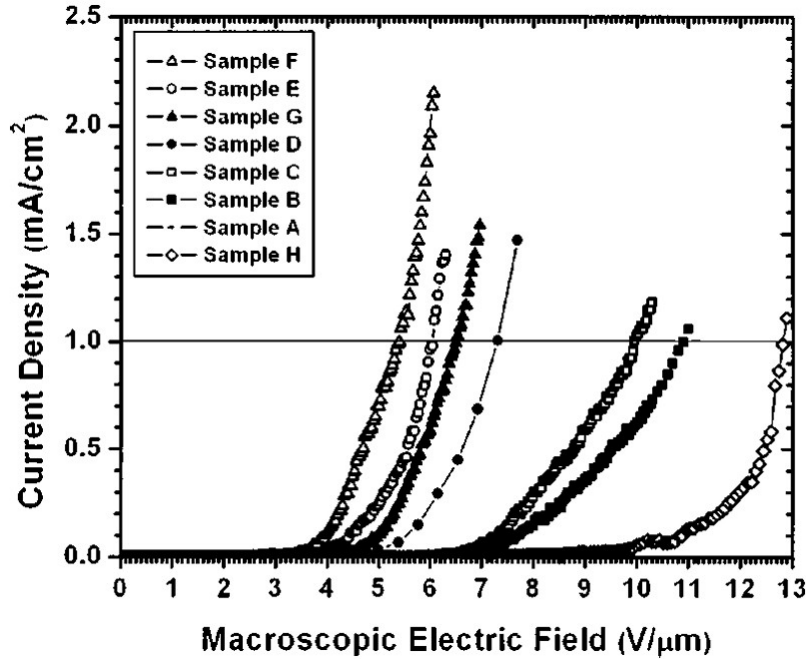
Sample	Length (μm)	Density (/cm^2)
A	4.0	6×10^6
B	5.5	5×10^6
C	7.0	2×10^6
D	8.5	1×10^6
E	10.5	1×10^6
F	12.5	3×10^6
G	12.5	6×10^6
H	8.5	4×10^7

Figure B.2: The measured current densities as a function of the macroscopic electric field for eight samples of vertically aligned MWCNT arrays. As expected from Fig. B.1, the intermediate densities support the strongest currents. The length dependence supports the conjecture of side-surface emission (Figure and table from Ref. [229]).

of electrical engineering; hence; not the subject of the thesis. There are, however, also material-specific factors that we shall briefly review below.

Field electron emission depends on microstructure

Field electron emission (FEE) from CNT arrays shows strong dependence on the microstructure of the emitter. Specifically, the arrangement, alignment, and density of the CNTs affect both the emission intensity and stability. Many studies [233], [234] show that variations in the structural parameters can lead to notable differences in emission characteristics. The structural parameters, such as grain size, surface morphology, crystallographic orientation, defect density, and overall structural uniformity, play essential roles in determining the efficiency and stability of electron emission [216].

Control and optimization of these parameters might be essential for developing efficient and reliable CNT-based electron emitters.

j(F) **depends on vacuum**

The effect of different vacuum levels on the field emission characteristics of CNT arrays was investigated [235], introducing electron-molecule collision ionization as a significant factor affecting field emission under non-vacuum conditions. The presence of gas molecules significantly affects the field emission behaviour, as different pressures influence the collision probability between electrons and gas molecules, resulting in changes in the emission current density. Higher vacuums result in more stable and stronger field emission.

B.1.2   The nanotube structure is fragile; device stability

Field emission from vertically aligned carbon nanotubes was tested experimentally, and the phenomenon was strong, particularly at the lowest values of the electric field [236]. Experiments show that at high voltages, the structures are fragile, and they can be easily damaged.
CNT structures are fragile due to their nanoscopic dimensions and sensitivity to mechanical and thermal stresses [237]. The nanotubes can easily deform or degrade when exposed to high voltages or strong forces, making it crucial to maintain structural stability and preserve their performance as field emission cathodes.
Field electron emission at low voltages is significant because it allows efficient electron release without applying excessive voltage. Scanning electron microscope (SEM) analysis shows that the nanotube structures experience structural changes after current extraction at high voltages, ensuring improved but less controllable emission properties [238].
Low voltage operation improves the stability and the long life of the CNT field emission cathodes. Studies confirm that low-field emission requires fewer high-energy interactions that could damage the nanotube array. Therefore, achieving efficient electron emission at lower voltages enhances performance and extends the lifespan of the CNT cathode.

B.1.3   Comparison with experiment

Until now, all experimental works have nearly always been compared with the traditional Fowler-Nordheim expression for field emission. This is despite the fact that more advanced theoretical expressions have been known for a few decades, for instance, Murphy and Good (MG) written in terms of elliptic integrals [127]. Instead, experimentalists have added an extra free parameter (β) to their expression to generalize it phenomenologically. This is a rather frustrating situation, which motivated some theorists to inquire what the connection is between phenomenological β and those more advanced, e.g. MG, expressions. We should note here that based on extensive research of Richard Forbes [239], [240], we can see that generalizing the Fowler-Nordheim theory in this way is equivalent to introducing the hypergeometric function into the exponential. In fact, Forbes criticized the simplistic use of the β enhancement coefficient [241], [242], and he developed phenomenological models that connect β to the local electric field F, considering the emitter's electrostatic properties [243]. This approach was an effort to connect the theory and experiment. From that, we deduce that also for our formalism, one expects to observe on the FN plot a straight line but with the non-linear corrections. This is because

MG expression, just like ours can be written in terms of a hypergeometric function, thus a polynomial, which can indeed be rescaled by a given β.

As already mentioned in the main text (Sec. 1.2.6), the current understanding of emission from carbon nanotubes is insufficient as underlined in experimental evidence emphasizing the need for additional research. The standard Fowler-Nordheim theory for single particle emitters does not apply, particularly at low voltages (Fig. 1.12, originally from Ref. *[93]*). In this figure, we observed a behaviour similar to the one observed in Ren's group [226]: instead of one single FN curve, we see different behaviour at the lowest voltages, an additional signal that should not be there. The field enhancement factor is not any longer a constant, but it depends on the applied field. In Ref. *[94], [95]*, the extra factor β was defined in terms of two parameters (one for thermionic and one for field emission), and it turns out that both ought to be taken as functions. Thus, it has been detected from the experiments that the β factor actually strongly depends on both the electric field and the temperature. Therefore, it is not a factor but a function of F and T, precisely as it has been computed in Chapter 6. In all these cases, the β needs to be taken as large as of the order of 10^4.

To conclude, computing an exact value of an absolute field emitted current is quite a difficult task. This is because the final result will depend on the finest details of a specific device. However, if one knows the amplitude of current at one specific field F, and light frequency ω for photon-assisted process, it is possible to predict the signal for all other (F, ω) points.

B.2 Bringing back dimensionality

Dimensionality of energy: TLL is characterized by a linear dispersion of the conduction band close to the Fermi energy and is assumed to have no other bands around it. This implies that there is an ultraviolet cutoff Λ in the theory, at energy where these conditions are not fulfilled any longer. Then, in principle, if we know this Λ, which equals half of the characteristic spectral gap $\Delta/2$ of other bands, it will determine the energy scale of the problem. Thus, everything on the energy scale ω will be essentially multiplied by this characteristic gap $\Delta[eV]$ resulting in a real value of energy that can be compared with the experiment. Each material has a given spectral gap of other, non-conduction bands which determines its energy scale Δ, thus redefining the energy dimensionality.

Dimensionality of the electric field F: The electric field axis also requires a definition of a characteristic length-scale $d_0[m]$. In Chapter 4, this is determined by *geometry* and can be set to be $\approx 1\mu m$. If we set our characteristic length $\overline{d}_0^{(geom)}[m]$ to be $1\mu m$ (usual size of microstructures), then the unit of F should be $V/\mu m$ (see e.g. caption of Fig. 6.3). In Chapter 5, we fix the velocity V_F, and so the characteristic length is set to $\overline{d}_0^{(V_F)} = V_F/\Delta$, where V_F is a *material*-dependent quantity. It is equal to the velocity of electrons in the conduction band. The unit of the electric field is then $[\Delta[eV]/d_0[m]]$. Our formalism is thus general and by choosing appropriate V_F one can capture MWNT made from arbitrary 2D sheets.

To give a specific example, for a SWCNT, we can take $\Delta = 1eV = 10^{14}Hz$ and the Fermi velocity of graphene $V_F = 3.6 \cdot 10^6 m/s$ which leads to $\overline{d}_0^{(V_F)} \approx 10nm$. If we take the value of the velocity for the carbon (graphene sheet) that corresponds to the metallic SWCNT,

the value of the characteristic length will thus be $10nm$. If we choose a different material than carbon (graphene sheet), with a different cutoff and different velocity, then it will be of a similar order of magnitude but not exactly the same value of the $\overline{d}_0^{(V_F)}$. This is, in fact, the smallest possible value of $\overline{d}_0$ determined for a given material of the electrode. If we arbitrarily assume that we are working with some geometrical features on the surface, such as corrugations or similar structures that are orders of μm, we will arrive at different characteristic d_0.

Dimensionality of current (vertical axis):   The low value on the vertical axis of the current is due to the fact that the calculation has been done for a single emitter and this is going to be modified by the fact that we have quite a lot of nanotubes on each surface. In reality, the arrays of carbon nanotubes contain millions of them per cm^2, therefore the field will be multiplied by the density of carbon nanotubes in the arrays.

B.3   Applications

B.3.1   Applications of field electron emission from Carbon nanotubes arrays

FEE from carbon nanotubes (CNTs) has transformed various technologies due to their excellent electrical conductivity, nanoscale size, and mechanical strength. The main applications of CNTs in FEE span industries and technologies.
In **electron holography**, CNTs act as ultra-bright, coherent electron sources, enabling high-resolution imaging of electric and magnetic fields for advanced material research.
The high level of ordering and uniformity in CNT arrays is useful for applications in **data storage, field emission displays and sensors** [244], and offers the prospect of deriving computational functions from the collective behavior of symmetrically coupled nanotubes.
In electronics, due to their conductivity, CNT-based **field emission displays (FEDs)** provide energy-efficient, high-contrast, slim panels that replace bulky cathode-ray tubes. In the medical and industrial sectors, CNTs serve as very effective field emitters, allowing them to serve as electron sources for **X-ray sources**, with specific advantages over traditional thermionic tubes. **CNT-derived X-ray sources** can create X-ray pulses of any duration and frequency, gate the X-ray pulse to any source, and allow the placement of many sources in close proximity [245].
CNT array electron emission properties also power **electron microscopy and lithography** [246], where arrays provide stable, high-current beams for nanoscale patterning and atomic-resolution imaging.

B.3.2   Specific devices supported by our results

Facing the above-described difficulties with a direct one-to-one comparison with experimental results, one can try to answer another question: among the multitude of current applications of field electron emissions, which ones are particularly well-suited for our candidate material? In particular, to be specific, we consider the below devices working in the regime of low-energy electron emission. This last assumption is not really necessary: if one is able to create a finite-time impulse of current $J(t_0 < t < t_1)$ at a given

energy, then by applying a system of electrodes (with impulses of voltages), one can in principle accelerate an electron beam to any desired energy. However, here we wish to investigate the situation where the electric setting of the device is kept simple.

In order to answer this question, one must first identify the key advantages of working with collective field emission from an array of nano-tubes. These are:

1. the emitting surface, the side of MWNT is now large: one expects a reasonably strong current even if the probability of emission per surface unit is small;

2. the emitted electrons, coming from in-between the tubes are naturally collimated: those with tilted trajectories ought to be reabsorbed into MWNT;

3. the sharpness of peaks, as obtained in Chapter 6 of this thesis (Fig. 6.11 - 6.14), suggests that for a given value of electric field, there is a well-defined monochromatic frequency of the beam;

4. the velocity of emitted carriers v_{emit} is determined by Coulomb interactions, and the emitting array is built out of Coulomb-coupled MWNT; thus, the velocities of different emitted carriers must be very close to each other;

5. the primary emission of electrons is into quantum well states in between the tubes; thus, they are all confined to wave functions with quite similar spatial distribution.

The advantage of working at weak currents is that even in a very long run, the emitter should not be affected or even damaged as was reported for single wire devices. At low voltages, conditions ionizing of atoms and molecules is less of a problem. It also means less energy consumption (relevant for green economy) and greater safety of the device. With the beam being naturally collimated, there is no need for additional grated gates, which are also prone to damage in the long run. While point 1 above has implications for stability and durability, the other points (p.2-5) are very favorable for the quality of the beam itself. The general desire is to obtain large area monochromatic plane wave that will move coherently to be used in any further application. Below, based on the results of the thesis, we propose two modes in which the array of MWNTs can be employed to achieve novel functionalities; i.e., as a material, platform of which novel devices can be designed. In principle, these novel devices can be patented. One of the devices will be able to explore *spatial* dimension that has been so far inaccessible, the other device will be able to explore the *temporal* dimension.

Spatial resolution

Firstly, we note that although low energy field emitted electrons offer lower lateral resolution (due to a diffraction limit) that can be partially improved through phase-sensitive probes, they offer electrons with much higher penetration depths. Thus, they offer the possibility to investigate the in-depth dimension of the sample. This naturally suggests a potential application in a field of electron holography (or low-energy-electron diffraction). Electron holography is nowadays an intensely developed experimental probe that allows researchers to understand the 3D structure of proteins or 3D patterns of (e.g. magnetic) ordering on the surface of nanoparticles. Electron holography provides a unique perspective into electromagnetic fields, charge distributions, and electrostatic potentials at the nanoscale by capturing the phase change of an electron wave as it passes through or interacts with a sample [247], [248], [249]. Electron holography in transmission electron

microscopy (TEM) offers a solution. A hologram is recorded by superposition with a coherent reference wave, from which the image wave can be completely reconstructed by amplitude and phase [250].

Here, we postulate to use MWNT array both as an emitter and a receptor of the electron wave. The wave is reflected and half of it moves through the sample, while the other half serves as a reference.

Plane waves are particularly well-suited here. Afterwards, both reach the MWNT array, where they interfere, which now works in the *receptors'* mode. Integration of MWNT arrays in electron holography has been already explored experimentally, and it has been shown that these setups offer several advantages, such as enhanced spatial resolution [251], [252], signal stability [234], [253], and compact device architecture [86], [254], [255]. This setup enhances phase stability and enables a more efficient electron holography system with potential applications.

The central idea of holography is to gain access to the 3D structure of an object by studying the interference pattern between two beams of electrons: one that has gone through the sample and another that has not. The fact that nanotubes are aligned vertically paves the way to determine the interference pattern also in this third direction. To this end, we propose a device that is built on the top of standard CCD camera concept. The operation of 2D CCD camera is based on the fact that the system detects the transistor status at each pixel. In our concept, at each pixel we propose to inject an impulse of charge current. Then a time-of-flight type of measurement could be used where an electron wave packet is injected at a given time into a given MWNT and then backscattered by the electron wave maximum. By measuring the time of flight
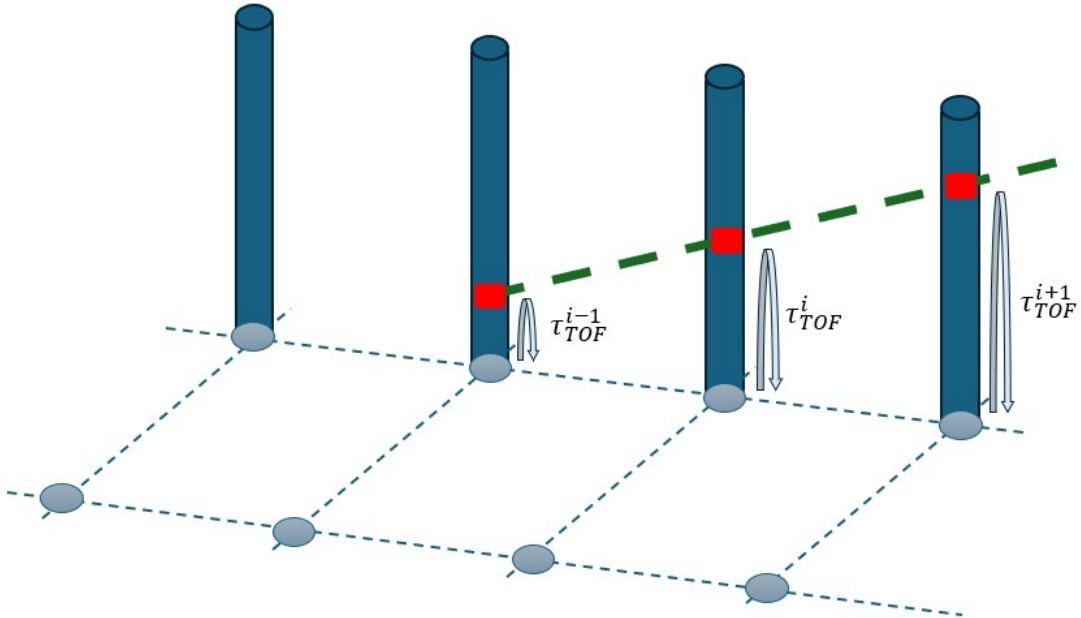
Figure B.3: Receiving mode: the blue rods show schematically MWNT which form the array of vertically aligned nanotubes, a front of an electron wave interacting with MWNTs is indicated as green dashed line, red points are the zones of plasmon-polariton interaction. These points are specified not only in 2D plane but in 3D space. It is thanks to the time-of-flight method applied inside each MWNT, the measurement of τ_{TOF}^i. This information can be used in electron wave holography devices.

<center>(a)   (b)</center>
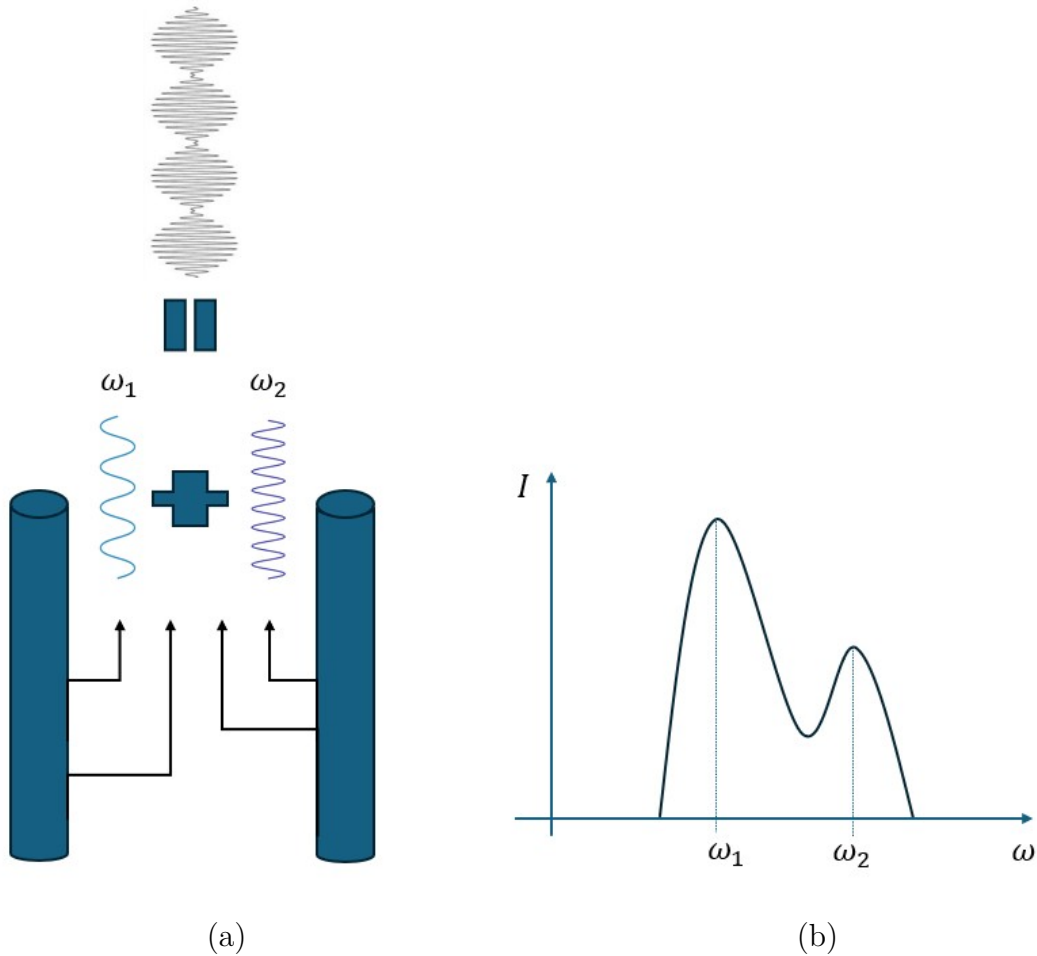
Figure B.4: Emitting mode **(a)** vertical nanotubes emitting electrons into a potential well in between them. When the emitted electrons have two close frequencies ω_1 and ω_2 the resulting electron wave will exhibit the beating phenomenon as shown on the top of this panel; **(b)** the schematic illustration of results in Chapter 6, low temperature, strong interactions, large enough $F = cste$, e.g. in panels (b) in Fig. 6.11 or Fig. 6.13, where in the spectrum for positive ω there are indeed two close peaks at ω_1 and ω_2.

(back-and-forth) τ^i at a given i-th pixel, one can deduce where the maximum of electron wave is located in 3D. The idea is illustrated in Fig. B.3. The theory of conductivity in nanotubes is a well-developed field, the only unknowns here are material structure-specific properties, namely the exact electron distribution along the tube (in particular local susceptibility), and the way the local symmetry breaking affects the local TLL parameters. Both problems were solved in this thesis, in Chapter 5 (in particular, Sec. 5.5) and Chapter 6 (Sec. 6.2), respectively. Those results make the case that such a phenomenon is feasible to observe and quantify the expected backscattering strength.

Temporal resolution

The results of our calculations in Chapter 6 show a new interesting phenomenon: in the case of lower temperature and stronger interactions, as reported in Fig. 6.11 (b) and 6.13 (b), one can observe two neighbouring peaks of current. This means that the beating of two waves can be induced in the outgoing electron beam. This is technologically quite

interesting because it can allow probing the sample stroboscopically, thus accessing the dynamics of the measured system. The distance between the two peaks determines the beating frequency, thus the time intervals at which we shine the electron beam on the sample. From Fig. 6.11 (b), we see that the distance between peaks can be as small as 0.2 of the conduction band bandwidth, which for MWNT (with reduced electron dispersion), can be as small as $0.1eV$, which is the energy scale of magnetic soliton-type excitation in nanoparticles, and also corresponds to picoseconds time scales. The picosecond time scales are those of rotational correlation times of molecules or a lifetime of ionized hydronium. Thus, they are relevant for applications in nano-biochemistry. In Fig. 6.11 (b) and 6.13 (b), we clearly see that the relative amplitude of the two waves varies as a function of the applied electric field F; this operation of the proposed device is fully controllable and can be even done in a lock-in mode.

Bibliography

[1] K. L. Jensen, *Introduction to the physics of electron emission.* John Wiley & Sons, 2017.

[2] R. H. Fowler and L. Nordheim, "Electron emission in intense electric fields," *Proc. Roy. Soc. Lond. A*, vol. 119, pp. 173–181, 1928.

[3] L. A. DuBridge and W. Roehr, "The thermionic and photoelectric work functions of molybdenum," *Physical Review*, vol. 42, no. 1, p. 52, 1932.

[4] S. Dushman, "Thermionic emission," *Reviews of Modern Physics*, vol. 2, no. 4, p. 381, 1930.

[5] E. Baroody, "A theory of secondary electron emission from metals," *Physical Review*, vol. 78, no. 6, p. 780, 1950.

[6] I. Langmuir, "The effect of space charge and residual gases on thermionic currents in high vacuum," *Physical Review*, vol. 2, no. 6, p. 450, 1913.

[7] D. M. Trucchi and N. A. Melosh, "Electron-emission materials: Advances, applications, and models," *Mrs Bulletin*, vol. 42, no. 7, pp. 488–492, 2017.

[8] E. L. Chaffee et al., "Theory of thermionic vacuum tubes," *Fundamentals. Amplifiers. Detectors. New York & London, mcGraw Hill*, vol. 8, 1933.

[9] Y. Saito et al., "Field emission from carbon nanotubes and its application to cathode ray tube lighting elements," *Applied Surface Science*, vol. 146, no. 1-4, pp. 305–311, 1999.

[10] Y. Saito and S. Uemura, "Field emission from carbon nanotubes and its application to electron sources," *Carbon*, vol. 38, no. 2, pp. 169–182, 2000.

[11] S. S. Baturin, T. Nikhar, and S. V. Baryshev, "Field electron emission induced glow discharge in a nanodiamond vacuum diode," *Journal of Physics D: Applied Physics*, vol. 52, no. 32, p. 325 301, 2019.

[12] W. Kang et al., "Diamond vacuum field emission devices," *Diamond and Related Materials*, vol. 13, no. 11-12, pp. 1944–1948, 2004.

[13] C. Li et al., "Highly electron transparent graphene for field emission triode gates," *Advanced Functional Materials*, vol. 24, no. 9, pp. 1218–1227, 2014.

[14] D. Garner and G. Amaratunga, "Analytic modelling of the thin-film field-emission triode," *Solid-State Electronics*, vol. 45, no. 6, pp. 879–886, 2001.

[15] F. Jin, Y. Liu, C. M. Day, and S. A. Little, "Enhanced electron emission from functionalized carbon nanotubes with a barium strontium oxide coating produced by magnetron sputtering," *Carbon*, vol. 45, no. 3, pp. 587–593, 2007.

[16] A. Talin, K. Dean, and J. Jaskie, "Field emission displays: A critical review," *Solid-state electronics*, vol. 45, no. 6, pp. 963–976, 2001.

[17] I. Shah, "Field-emission displays," *Physics World*, vol. 10, no. 6, p. 45, 1997.

[18] A. A. Kuznetzov, S. B. Lee, M. Zhang, R. H. Baughman, and A. A. Zakhidov, "Electron field emission from transparent multiwalled carbon nanotube sheets for inverted field emission displays," *Carbon*, vol. 48, no. 1, pp. 41–46, 2010.

[19] H. Seiler, "Secondary electron emission in the scanning electron microscope," *Journal of Applied Physics*, vol. 54, no. 11, R1–R18, 1983.

[20] J. Pawley, "The development of field-emission scanning electron microscopy for imaging biological surfaces," *SCANNING-NEW YORK AND BADEN BADEN THEN MAHWAH-*, vol. 19, pp. 324–336, 1997.

[21] M. Krysztof, "Field-emission electron gun for a MEMS electron microscope," *Microsystems & Nanoengineering*, vol. 7, no. 1, p. 43, 2021.

[22] V. Filip, L. D. Filip, and H. Wong, "Review on peculiar issues of field emission in vacuum nanoelectronic devices," *Solid-State Electronics*, vol. 138, pp. 3–15, 2017, Selected papers from INEC 2016 and ISNE 2016, ISSN: 0038-1101.

[23] D. K. Schroder and D. L. Meier, "Solar cell contact resistance — A review," *IEEE Transactions on electron devices*, vol. 31, no. 5, pp. 637–647, 1984.

[24] T. Zhai et al., "One-dimensional inorganic nanostructures: Synthesis, field-emission and photodetection," *Chemical Society Reviews*, vol. 40, no. 5, pp. 2986–3004, 2011.

[25] S. X. Tao, H. W. Chan, and H. Van der Graaf, "Secondary electron emission materials for transmission dynodes in novel photomultipliers: A review," *Materials*, vol. 9, no. 12, p. 1017, 2016.

[26] R. R. Meyer and A. Kirkland, "The effects of electron and photon scattering on signal and noise transfer properties of scintillators in CCD cameras used for electron detection," *Ultramicroscopy*, vol. 75, no. 1, pp. 23–33, 1998.

[27] M. R. Bruce and V. J. Bruce, "ABCs of photon emission microscopy," *Electronic Device Failure Analysis*, vol. 5, pp. 13–22, 2003.

[28] C. Roques-Carmes et al., "A framework for scintillation in nanophotonics," *Science*, vol. 375, no. 6583, eabm9293, 2022.

[29] S.-D. Liang, *Quantum tunneling and field electron emission theories*. World Scientific, 2013.

[30] L. Lambert and T. Mulvey, "Ernst ruska (1906–1988), designer extraordinaire of the electron microscope: A memoir," in *Advances in imaging and electron physics*, vol. 95, Elsevier, 1996, pp. 2–62.

[31] J. H. Winkler, *Thoughts on the properties, effects and causes of electricity: together with a description of two new electrical machines*. Breitkopf, 1744.

[32] J. J. Thomson, *Cathode rays*. Academic Reprints, 1897.

[33] O. W. Richardson, *The Emission of Electricity From Hot Bodies*. Longmans, Green and Co, 1916.

[34] A. Einstein, "On a heuristic point of view about the creation and conversion of light," *Annalen der Physik*, vol. 17, no. 6, pp. 132–148, 1905.

[35] R. A. Millikan and C. F. Eyring, "Laws governing the pulling of electrons out of metals by intense electrical fields," *Physical Review*, vol. 27, no. 1, p. 51, 1926.

[36] B. Gossling et al., "The emission of electrons under the influence of intense electric fields," *Philosophical Magazine*, vol. 1, no. 3, pp. 609–635, 1926.

[37] R. Millikan and C. C. Lauritsen, "Relations of field-currents to thermionic-currents," *Proceedings of the National Academy of Sciences*, vol. 14, no. 1, pp. 45–49, 1928.

[38] J. R. Oppenheimer, "Three notes on the quantum theory of aperiodic effects," *Physical Review*, vol. 31, pp. 66–81, Jan. 1928.

[39] E. W. Müller, "Elektronenmikroskopische beobachtungen von feldkathoden," *Zeitschrift für Physik*, vol. 106, no. 9-10, pp. 541–550, 1937.

[40] C. Davisson and L. H. Germer, "Diffraction of electrons by a crystal of nickel," *Physical Review*, vol. 30, no. 6, p. 705, 1927.

[41] C. Davisson and L. H. Germer, "The scattering of electrons by a single crystal of nickel," *Nature*, vol. 119, no. 2998, pp. 558–560, 1927.

[42] G. P. Thomson and A. Reid, "Diffraction of cathode rays by a thin film," *Nature*, vol. 119, no. 3007, pp. 890–890, 1927.

[43] T. I. Awan, A. Bashir, A. Tehseen, and S. Bibi, "Chapter 7 - electrons in nanostructures," in *Chemistry of Nanomaterials*, T. I. Awan, A. Bashir, and A. Tehseen, Eds., Elsevier, 2020, pp. 179–206, ISBN: 978-0-12-818908-5.

[44] L. D. Landau, "The theory of a Fermi liquid," *Soviet Physics JETP*, vol. 3, no. 6, pp. 920–925, 1957.

[45] S. Iijima, "Helical microtubules of graphitic carbon," *nature*, vol. 354, no. 6348, pp. 56–58, 1991.

[46] L.-M. Peng, Z. Zhang, and S. Wang, "Carbon nanotube electronics: Recent advances," *Materials today*, vol. 17, no. 9, pp. 433–442, 2014.

[47] H. Dai, "Materials science of carbon nanotubes: Fabrication, integration and properties of macroscopic structures of carbon nanotubes," *Acc Chem Res*, vol. 35, pp. 1045–53, 2002.

[48] H. He, L. A. Pham-Huy, P. Dramou, D. Xiao, P. Zuo, C. Pham-Huy, et al., "Carbon nanotubes: Applications in pharmacy and medicine," *BioMed research international*, vol. 2013, 2013.

[49] X. Wang and Z. Liu, "Carbon nanotubes in biology and medicine: An overview," *Chinese Science Bulletin*, vol. 57, pp. 167–180, 2012.

[50] P. A. Tran, L. Zhang, and T. J. Webster, "Carbon nanofibers and carbon nanotubes in regenerative medicine," *Advanced drug delivery reviews*, vol. 61, no. 12, pp. 1097–1114, 2009.

[51] K. Shi, M. Ren, and I. Zhitomirsky, "Activated carbon-coated carbon nanotubes for energy storage in supercapacitors and capacitive water purification," *ACS Sustainable Chemistry & Engineering*, vol. 2, no. 5, pp. 1289–1298, 2014.

[52] R. Amin, P. R. Kumar, and I. Belharouak, "Carbon nanotubes: Applications to energy storage devices," *Carbon Nanotubes-Redefining the World of Electronics*, vol. 10, pp. 5772–94 155, 2020.

[53] L. Boumia, M. Zidour, A. Benzair, and A. Tounsi, "A Timoshenko beam model for vibration analysis of chiral single-walled carbon nanotubes," *Physica E: Low-dimensional Systems and Nanostructures*, vol. 59, pp. 186–191, 2014.

[54] L.-C. Qin, "Determination of the chiral indices (n, m) of carbon nanotubes by electron diffraction," *Physical Chemistry Chemical Physics*, vol. 9, no. 1, pp. 31–48, 2007.

[55] M. Meo and M. Rossi, "Prediction of Young's modulus of single wall carbon nanotubes by molecular-mechanics based finite element modelling," *Composites Science and Technology*, vol. 66, no. 11-12, pp. 1597–1605, 2006.

[56] P. Chudzinski, "Spin-orbit coupling and proximity effects in metallic carbon nanotubes," *Physical Review B*, vol. 92, p. 115 147, Sep. 2015.

[57] M. Del Valle, M. Margańska, and M. Grifoni, "Signatures of spin-orbit interaction in transport properties of finite carbon nanotubes in a parallel magnetic field," *Physical Review B*, vol. 84, no. 16, p. 165 427, 2011.

[58] F. Kuemmeth, S. Ilani, D. Ralph, and P. McEuen, "Coupling of spin and orbital motion of electrons in carbon nanotubes," *Nature*, vol. 452, no. 7186, pp. 448–452, 2008.

[59] Z. Huang, J. Xu, Z. Ren, J. Wang, M. Siegal, and P. Provencio, "Growth of highly oriented carbon nanotubes by plasma-enhanced hot filament chemical vapor deposition," *Applied Physics Letters*, vol. 73, no. 26, pp. 3845–3847, 1998.

[60] L. Ping, P.-X. Hou, C. Liu, and H.-M. Cheng, "Vertically aligned carbon nanotube arrays as a thermal interface material," *APL Materials*, vol. 7, no. 2, 2019.

[61] S. Xie, W. Li, Z. Pan, B. Chang, and L. Sun, "Carbon nanotube arrays," *Materials Science and Engineering: A*, vol. 286, no. 1, pp. 11–15, 2000.

[62] S. Fan et al., "Carbon nanotube arrays on silicon substrates and their possible application," *Physica E: Low-dimensional Systems and Nanostructures*, vol. 8, no. 2, pp. 179–183, 2000.

[63] W. Hu et al., "Growth of well-aligned carbon nanotube arrays on silicon substrates using porous alumina film as a nanotemplate," *Applied Physics Letters*, vol. 79, no. 19, pp. 3083–3085, 2001.

[64] C. Kocabas, S.-H. Hur, A. Gaur, M. A. Meitl, M. Shim, and J. A. Rogers, "Guided growth of large-scale, horizontally aligned arrays of single-walled carbon nanotubes and their use in thin-film transistors," *small*, vol. 1, no. 11, pp. 1110–1116, 2005.

[65] C. Kocabas, M. Shim, and J. A. Rogers, "Spatially selective guided growth of high-coverage arrays and random networks of single-walled carbon nanotubes and their integration into electronic devices," *Journal of the American Chemical Society*, vol. 128, no. 14, pp. 4540–4541, 2006.

[66] J. Xiao et al., "Alignment controlled growth of single-walled carbon nanotubes on quartz substrates," *Nano letters*, vol. 9, no. 12, pp. 4311–4319, 2009.

[67] O. Guellati et al., "CNTs' array growth using the floating catalyst-CVD method over different substrates and varying hydrogen supply," *Materials Science and Engineering: B*, vol. 231, pp. 11–17, 2018.

[68] H. Ago, K. Nakamura, K.-i. Ikeda, N. Uehara, N. Ishigami, and M. Tsuji, "Aligned growth of isolated single-walled carbon nanotubes programmed by atomic arrangement of substrate surface," *Chemical Physics Letters*, vol. 408, no. 4-6, pp. 433–438, 2005.

[69] D. Li, Y. Cheng, Y. Wang, H. Zhang, C. Dong, and D. Li, "Improved field emission properties of carbon nanotubes grown on stainless steel substrate and its application in ionization gauge," *Applied Surface Science*, vol. 365, pp. 10–18, 2016.

[70] Y. Yun et al., "Carbon nanotubes grown on stainless steel to form plate and probe electrodes for chemical/biological sensing," *Journal of nanoscience and nanotechnology*, vol. 7, no. 3, pp. 891–897, 2007.

[71] S. Neupane, M. Lastres, M. Chiarella, W. Li, Q. Su, and G. Du, "Synthesis and field emission properties of vertically aligned carbon nanotube arrays on copper," *Carbon*, vol. 50, no. 7, pp. 2641–2650, 2012.

[72] X. Chen et al., "Synthesis and characterization of superhydrophobic functionalized $Cu(OH)_2$ nanotube arrays on copper foil," *Applied Surface Science*, vol. 255, no. 7, pp. 4015–4019, 2009.

[73] M. Dresselhaus, R. Smalley, G. Dresselhaus, and P. Avouris, "Electron spectroscopy studies of carbon nanotubes," in *Carbon Nanotubes: Synthesis, Structure, Properties, and Applications* (Topics in Applied Physics), Topics in Applied Physics. Springer Berlin Heidelberg, 2001, pp. 247–272, ISBN: 9783540410867.

[74] N. Grobert, "Carbon nanotubes–becoming clean," *Materials today*, vol. 10, no. 1-2, pp. 28–35, 2007.

[75] S. Mikhailov, *Physics and applications of graphene: Experiments*. BoD–Books on Demand, 2011.

[76] P. Haris, A. Hirsch, and C. Backes, *Carbon nanotubes science: Synthesis, properties and applications. vol. 102*, 2009.

[77] Y. M. Manawi, Ihsanullah, A. Samara, T. Al-Ansari, and M. A. Atieh, "A review of carbon nanomaterials' synthesis via the chemical vapor deposition (CVD) method," *Materials*, vol. 11, no. 5, p. 822, 2018.

[78] M. Kumar and Y. Ando, "Chemical vapor deposition of carbon nanotubes: A review on growth mechanism and mass production," *Journal of nanoscience and nanotechnology*, vol. 10, no. 6, pp. 3739–3758, 2010.

[79] I. R. Shapiro, S. D. Solares, M. J. Esplandiu, L. A. Wade, W. A. Goddard, and C. P. Collier, "Influence of elastic deformation on single-wall carbon nanotube atomic force microscopy probe resolution," *The Journal of Physical Chemistry B*, vol. 108, no. 36, pp. 13 613–13 618, 2004.

[80] R. Garcia and A. San Paulo, "Attractive and repulsive tip-sample interaction regimes in tapping-mode atomic force microscopy," *Physical Review B*, vol. 60, no. 7, p. 4961, 1999.

[81] A. San Paulo and R. García, "High-resolution imaging of antibodies by tapping-mode atomic force microscopy: Attractive and repulsive tip-sample interaction regimes," *Biophysical Journal*, vol. 78, no. 3, pp. 1599–1605, 2000.

[82] R. Garcia and A. San Paulo, "Dynamics of a vibrating tip near or in intermittent contact with a surface," *Physical Review B*, vol. 61, no. 20, R13381, 2000.

[83] J.-L. Kwo, M. Yokoyama, W.-C. Wang, F.-Y. Chuang, and I.-N. Lin, "Characteristics of flat panel display using carbon nanotubes as electron emitters," *Diamond and Related Materials*, vol. 9, no. 3-6, pp. 1270–1274, 2000.

[84] Q. Wang, A. Setlur, J. Lauerhaas, J. Dai, E. Seelig, and R. Chang, "A nanotube-based field-emission flat panel display," *Applied Physics Letters*, vol. 72, no. 22, pp. 2912–2913, 1998.

[85] Y. Li, Y. Sun, and J. Yeow, "Nanotube field electron emission: Principles, development, and applications," *Nanotechnology*, vol. 26, no. 24, p. 242 001, 2015.

[86] N. De Jonge and J.-.-M. Bonard, "Carbon nanotube electron sources and applications," *Philosophical Transactions of the Royal Society of London. Series A: Mathematical, Physical and Engineering Sciences*, vol. 362, no. 1823, pp. 2239–2266, 2004.

[87] N. Lee et al., "Application of carbon nanotubes to field emission displays," *Diamond and related materials*, vol. 10, no. 2, pp. 265–270, 2001.

[88] J. Chen, X. Zhou, S. Deng, and N. Xu, "The application of carbon nanotubes in high-efficiency low power consumption field-emission luminescent tube," *Ultramicroscopy*, vol. 95, pp. 153–156, 2003.

[89] W. A. De Heer, A. Chatelain, and D. Ugarte, "A carbon nanotube field-emission electron source," *science*, vol. 270, no. 5239, pp. 1179–1180, 1995.

[90] P. G. Collins and A. Zettl, "A simple and robust electron beam source from carbon nanotubes," *Applied Physics Letters*, vol. 69, no. 13, pp. 1969–1971, 1996.

[91] Q. Wang, T. Corrigan, J. Dai, R. Chang, and A. Krauss, "Field emission from nanotube bundle emitters at low fields," *Applied Physics Letters*, vol. 70, no. 24, pp. 3308–3310, 1997.

[92] J.-M. Bonard, J.-P. Salvetat, T. Stöckli, W. A. De Heer, L. Forró, and A. Châtelain, "Field emission from single-wall carbon nanotube films," *Applied Physics Letters*, vol. 73, no. 7, pp. 918–920, 1998.

[93] J.-M. Bonard, C. Klinke, K. A. Dean, and B. F. Coll, "Degradation and failure of carbon nanotube field emitters," *Physical Review B*, vol. 67, no. 11, p. 115 406, 2003.

[94] S. C. Lim, H. J. Jeong, K. S. Kim, D. J. Bae, Y. H. Lee, et al., "Extracting independently the work function and field enhancement factor from thermal-field emission of multi-walled carbon nanotube tips," *Carbon*, vol. 43, no. 13, pp. 2801–2807, 2005.

[95] S. Kolekar, S. P. Patole, S. Patil, J. Yoo, and C. Dharmadhikari, "Study of thermal-field emission properties and investigation of temperature dependent noise in the emission current form vertical carbon nanotube emitters," 2017.

[96] T. Giamarchi, *Quantum Physics in One Dimension*. Oxford University Press, 2003, ISBN: 9780198525004.

[97] Y.-H. Su and H.-T. Lu, "Breakdown of Landau Fermi liquid theory: Restrictions on the degrees of freedom of quantum electrons," *Frontiers of Physics*, vol. 13, pp. 1–19, 2018.

[98] S.-i. Tomonaga, "Remarks on Bloch's method of sound waves applied to many-fermion problems," *Progress of Theoretical Physics*, vol. 5, no. 4, pp. 544–569, 1950.

[99] D. Bohm and D. Pines, "A collective description of electron interactions: III. Coulomb interactions in a degenerate electron gas," *Physical Review*, vol. 92, no. 3, p. 609, 1953.

BIBLIOGRAPHY

[100] J. Luttinger, "An exactly soluble model of a many-fermion system," *Journal of mathematical physics*, vol. 4, no. 9, pp. 1154–1162, 1963.

[101] D. C. Mattis and E. H. Lieb, "Exact solution of a many-fermion system and its associated boson field," *Condensed Matter Physics and Exactly Soluble Models: Selecta of Elliott H. Lieb*, pp. 645–653, 2004 (republished from 1965).

[102] F. Haldane, "'Luttinger liquid theory' of one-dimensional quantum fluids. I. Properties of the Luttinger model and their extension to the general 1D interacting spinless Fermi gas," *Journal of Physics C: Solid State Physics*, vol. 14, no. 19, p. 2585, 1981.

[103] L. Landau, "On the theory of the Fermi liquid," *Sov. Phys. JETP*, vol. 8, no. 1, p. 70, 1959.

[104] S. Eggert, "One-dimensional quantum wires: A pedestrian approach to bosonization," *arXiv preprint arXiv:0708.0003*, 2007.

[105] N. Grigoryan, A. Roszkiewicz, and P. Chudzinski, "Generalizing Fowler–Nordheim tunneling theory for an arbitrary power law barrier," *physica status solidi (b)*, vol. 260, no. 6, p. 2 200 599, 2023.

[106] N. Grigoryan and P. Chudzinski, "Role of electron-electron interactions in electron emission from nanotube materials," *Phys. Rev. Mater.*, vol. 8, p. 016 003, Jan. 2024.

[107] E. Schrödinger, "An undulatory theory of the mechanics of atoms and molecules," *Physical Review*, vol. 28, no. 6, p. 1049, 1926.

[108] F. Horst, "Compact dc modeling of tunnel-fets," Ph.D. dissertation, Universitat Rovira i Virgili, 2019.

[109] G. Wentzel, "A generalization of the quantization conditions for the purpose of wave mechanics," *Zeits. F. Phys*, vol. 38, pp. 518–529, 1926.

[110] H. A. Kramers, "Wellenmechanik und halbzahlige quantisierung," *Zeits. F. Phys*, vol. 39, no. 10-11, pp. 828–840, 1926.

[111] L. Brillouin, "La mécanique ondulatoire de Schrödinger; une méthode générale de résolution par approximations successives," *CR Acad. Sci*, vol. 183, no. 11, pp. 24–26, 1926.

[112] H. Jeffreys, "On certain approximate solutions of lineae differential equations of the second order," *Proceedings of the London Mathematical Society*, vol. 2, no. 1, pp. 428–436, 1925.

[113] A. Modinos, "Secondary electron emission spectroscopy," in *Field, Thermionic, and Secondary Electron Emission Spectroscopy*, Springer, 1984, pp. 327–345.

[114] J. J. Quinn and K.-S. Yi, *Solid state physics: principles and modern applications.* Springer Science & Business Media, 2009.

[115] D. Bohm, *Quantum theory.* Courier Corporation, 2012.

[116] A. Toubiana, L. Canto, and M. S. Hussein, "Improved WKB approximation for quantum tunneling: Application to heavy-ion fusion," *The European Physical Journal A*, vol. 53, pp. 1–8, 2017.

[117] E. C. Kemble, "A contribution to the theory of the BWK method," *Physical Review*, vol. 48, no. 6, p. 549, 1935.

[118] R. G. Forbes, "Use of a spreadsheet for Fowler–Nordheim equation calculations," *Journal of Vacuum Science & Technology B: Microelectronics and Nanometer Structures Processing, Measurement, and Phenomena*, vol. 17, no. 2, pp. 534–541, 1999.

[119] R. G. Forbes and J. H. Deane, "Reformulation of the standard theory of Fowler–Nordheim tunnelling and cold field electron emission," *Proceedings of the Royal Society A: Mathematical, Physical and Engineering Sciences*, vol. 463, no. 2087, pp. 2907–2927, 2007.

[120] A. Ghosh and S. Chakrabarty, "Fowler-Nordheim electron cold emission formalism in presence of strong magnetic field," *arXiv preprint arXiv:1206.3024*, 2012.

[121] Y. Suzumura and H. Fukuyama, "Localization-delocalization transition by interactions in one-dimensional fermion systems," *Journal of the Physical Society of Japan*, vol. 52, no. 8, pp. 2870–2874, 1983.

[122] Y. Suzumura and H. Fukuyama, "Anderson localization in one-dimensional interacting electron systems," *Journal of the Physical Society of Japan*, vol. 53, no. 11, pp. 3918–3928, 1984.

[123] T. Saso, Y. Suzumura, and H. Fukuyama, "Localization and Interaction in One-Dimensional Electron Systems," *Progress of Theoretical Physics Supplement*, vol. 84, pp. 269–295, Apr. 1985, ISSN: 0375-9687.

[124] J. Von Delft and H. Schoeller, "Bosonization for beginners—refermionization for experts," *Annalen der Physik*, vol. 510, no. 4, pp. 225–305, 1998.

[125] S. Coleman, "Fate of the false vacuum: Semiclassical theory," *Physical Review D*, vol. 15, pp. 2929–2936, May 1977.

[126] M. Zubair, Y. S. Ang, and L. K. Ang, "Fractional Fowler–Nordheim law for field emission from rough surface with nonparabolic energy dispersion," *IEEE Transactions on Electron Devices*, vol. 65, no. 6, pp. 2089–2095, 2018.

[127] E. L. Murphy and R. Good Jr, "Thermionic emission, field emission, and the transition region," *Physical Review*, vol. 102, pp. 1464–1473, Jun. 1956.

[128] J. H. Deane and R. G. Forbes, "The formal derivation of an exact series expansion for the principal Schottky–Nordheim barrier function v, using the Gauss hypergeometric differential equation," *Journal of Physics A: Mathematical and Theoretical*, vol. 41, no. 39, p. 395 301, Aug. 2008.

[129] B. Dwork, "On Kummer's twenty-four solutions of the hypergeometric differential equation," *Transactions of the American Mathematical Society*, vol. 285, no. 2, pp. 497–521, 1984.

[130] S. Mubeen, M. Naz, A. Rehman, and G. Rahman, "Solutions of-hypergeometric differential equations," *Journal of Applied Mathematics*, vol. 2014, 2014.

[131] N. Fröman and P. O. Fröman, *JWKB approximation*. North-Holland Publishing Company Amsterdam, 1965.

[132] D. L. Hill and J. A. Wheeler, "Nuclear constitution and the interpretation of fission phenomena," *Physical Review*, vol. 89, no. 5, p. 1102, 1953.

[133] F. Albiol, S. Navas, and M. V. Andres, "Microwave experiments on electromagnetic evanescent waves and tunneling effect," *American Journal of Physics*, vol. 61, no. 2, pp. 165–169, 1993.

[134] A. Roszkiewicz and W. Nasalski, "Transmission and reflection properties of two-dimensional finite metal crystals," *The European Physical Journal D*, vol. 71, pp. 1–12, 2017.

[135] C. Huang, S. Chao, D. Hang, and Y. Lee, "On the transfer matrix method and the WKB approximation for the Schrödinger equation with position-dependent effective mass," *Chinese Journal of Physics*, vol. 46, no. 3, 2008.

[136] Z. C. Zhao and D. R. McKenzie, "Antireflection coating of barriers to enhance electron tunnelling: Exploring the matter wave analogy of superluminal optical phase velocity," *Scientific Reports*, vol. 7, no. 1, p. 12 772, 2017.

[137] D. L. Jaeger, J. J. Hren, and V. V. Zhirnov, "Local electrostatic effects of surface structure on field emission," *Journal of applied physics*, vol. 93, no. 1, pp. 691–697, 2003.

[138] A. Kyritsakis, G. Kokkorakis, J. Xanthakis, T. Kirk, and D. Pescia, "Self focusing of field emitted electrons at an ellipsoidal tip," *Applied Physics Letters*, vol. 97, no. 2, p. 023 104, 2010.

[139] K. L. Jensen, "Field emission—Fundamental theory to usage," *Wiley encyclopedia of electrical and electronics engineering*, pp. 1–29, 2014.

[140] J. D. Jackson, *Classical electrodynamics.* John Wiley & Sons, 2021.

[141] A. M. Essin and D. J. Griffiths, "Quantum mechanics of the $1/x^2$ potential," *American Journal of Physics*, vol. 74, no. 2, pp. 109–117, 2006.

[142] A. Cuyt and W.-s. Lee, "Multivariate exponential analysis from the minimal number of samples," *Advances in Computational Mathematics*, vol. 44, pp. 987–1002, 2018.

[143] B. El-Kareh and L. N. Hutter, *Fundamentals of semiconductor processing technology.* Springer Science & Business Media, 2012.

[144] H. Cruz, A. Hernández-Cabrera, and A. Munoz, "Resonant tunnelling of electrons through parabolic quantum wells: An analytical calculation of the transmission coefficient," *Semiconductor science and technology*, vol. 6, no. 3, p. 218, 1991.

[145] I. Affleck, "Boundary condition changing operations in conformal field theory and condensed matter physics," *Nuclear Physics B-Proceedings Supplements*, vol. 58, pp. 35–41, 1997.

[146] I. Affleck and A. W. Ludwig, "The Kondo effect, conformal field theory and fusion rules," *Nuclear Physics B*, vol. 352, no. 3, pp. 849–862, 1991.

[147] I. Affleck and A. W. Ludwig, "Exact critical theory of the two-impurity Kondo model," *Physical review letters*, vol. 68, no. 7, p. 1046, 1992.

[148] I. Affleck and A. W. Ludwig, "Exact conformal-field-theory results on the multi-channel Kondo effect: Single-fermion Green's function, self-energy, and resistivity," *Physical Review B*, vol. 48, no. 10, p. 7297, 1993.

[149] A. O. Gogolin and A. Komnik, "Field emission from Luttinger liquids and single-wall carbon nanotubes," *Physical Review Letters*, vol. 87, no. 25, p. 256 806, 2001.

[150] A. Komnik and A. O. Gogolin, "Multiparticle effects in nonequilibrium electron tunneling and field emission," *Physical Review B*, vol. 66, p. 035 407, Jul. 2002.

[151] R. Egger and A. O. Gogolin, "Correlated transport and non-Fermi-liquid behavior in single-wall carbon nanotubes," *The European Physical Journal B-Condensed Matter and Complex Systems*, vol. 3, no. 3, pp. 281–300, 1998.

[152] C. Schoenenberger, A. Bachtold, Strunk, C, J.-P. Salvetat, and L. Forro, "Interference and interaction in multi-wall carbon nanotubes," *Applied Physics A*, vol. 69, pp. 283–295, 1999.

[153] B. Stojetz, C. Hagen, C. Hendlmeier, E. Ljubović, L. Forro, and C. Strunk, "Ensemble averaging of conductance fluctuations in multiwall carbon nanotubes," *New Journal of Physics*, vol. 6, no. 1, p. 27, 2004.

[154] B. Stojetz, C. Miko, L. Forró, and C. Strunk, "Effect of band structure on quantum interference in multiwall carbon nanotubes," *Physical review letters*, vol. 94, no. 18, p. 186 802, 2005.

[155] H. Li, W. Lu, J. Li, X. Bai, and C. Gu, "Multichannel ballistic transport in multiwall carbon nanotubes," *Physical review letters*, vol. 95, no. 8, p. 086 601, 2005.

[156] J.-M. Bonard, H. Kind, T. Stöckli, and L.-O. Nilsson, "Field emission from carbon nanotubes: The first five years," *Solid-State Electronics*, vol. 45, no. 6, pp. 893–914, 2001, ISSN: 0038-1101.

[157] S. Bellucci, J. Gonzalez, and P. Onorato, "Crossover from the Luttinger-liquid to Coulomb-blockade regime in carbon nanotubes," *Physical review letters*, vol. 95, no. 18, p. 186 403, 2005.

[158] R. Egger and A. Gogolin, "Bulk and boundary zero-bias anomaly in multiwall carbon nanotubes," *Physical Review Letters*, vol. 87, no. 6, p. 066 401, 2001.

[159] A. Abrikosov Jr, D. Livanov, and A. Varlamov, "Electronic spectrum and tunneling properties of multiwall carbon nanotubes," *Physical Review B—Condensed Matter and Materials Physics*, vol. 71, no. 16, p. 165 423, 2005.

[160] M. Shuba, G. Y. Slepyan, S. Maksimenko, C. Thomsen, and A. Lakhtakia, "Theory of multiwall carbon nanotubes as waveguides and antennas in the infrared and the visible regimes," *Physical Review B—Condensed Matter and Materials Physics*, vol. 79, no. 15, p. 155 403, 2009.

[161] A. Di Carli et al., "Commensurate and incommensurate 1D interacting quantum systems," *Nature Communications*, vol. 15, no. 1, p. 474, 2024.

[162] Y. Ashida, *Quantum many-body physics in open systems: Measurement and strong correlations*. Springer Nature, 2020.

[163] V. Berezinskii, "Destruction of long-range order in one-dimensional and two-dimensional systems having a continuous symmetry group I. Classical systems," *Sov. Phys. JETP*, vol. 32, no. 3, pp. 493–500, 1971.

[164] J. M. Kosterlitz and D. J. Thouless, "Ordering, metastability and phase transitions in two-dimensional systems," *Journal of Physics C: Solid State Physics*, vol. 6, no. 7, p. 1181, 1973.

[165] H. J. Schulz, "Long-range Coulomb interactions in quasi-one-dimensional conductors," *Journal of Physics C: Solid State Physics*, vol. 16, no. 35, p. 6769, Dec. 1983.

BIBLIOGRAPHY

[166]   T. Dumitrică, C. M. Landis, and B. I. Yakobson, "Curvature-induced polarization in carbon nanoshells," *Chemical Physics Letters*, vol. 360, no. 1-2, pp. 182–188, 2002.

[167]   J. Sólyom, "The Fermi gas model of one-dimensional conductors," *Advances in Physics*, vol. 28, no. 2, pp. 201–303, 1979.

[168]   Y. Suzumura, "The Density of States of the Tomonaga-Luttinger Model," *Progress of Theoretical Physics*, vol. 63, no. 1, pp. 51–61, Jan. 1980, ISSN: 0033-068X.

[169]   J. Voit, "Charge-spin separation and the spectral properties of Luttinger liquids," *Journal of Physics: Condensed Matter*, vol. 5, no. 44, p. 8305, 1993.

[170]   J. Voit, "One-dimensional Fermi liquids," *Reports on Progress in Physics*, vol. 58, no. 9, p. 977, 1995.

[171]   F. H. Essler, H. Frahm, F. Göhmann, A. Klümper, and V. E. Korepin, *The one-dimensional Hubbard model.* Cambridge University Press, 2005.

[172]   B. Lake et al., "Multispinon continua at zero and finite temperature in a near-ideal Heisenberg chain," *Physical Review Letters*, vol. 111, no. 13, p. 137 205, 2013.

[173]   A. E. Mattsson, S. Eggert, and H. Johannesson, "Properties of a Luttinger liquid with boundaries at finite temperature and size," *Physical Review B*, vol. 56, pp. 15 615–15 628, Dec. 1997.

[174]   S. Eggert and I. Affleck, "Magnetic impurities in half-integer-spin Heisenberg antiferromagnetic chains," *Physical Review B*, vol. 46, no. 17, p. 10 866, 1992.

[175]   S. Eggert and I. Affleck, "Impurities in s= 1/2 Heisenberg antiferromagnetic chains: Consequences for neutron scattering and knight shift," *Physical Review Letters*, vol. 75, no. 5, p. 934, 1995.

[176]   J. Cardy, *Scaling and renormalization in statistical physics.* Cambridge university press, 1996, vol. 5.

[177]   R. Egger and H. Grabert, "Applying voltage sources to a Luttinger liquid with arbitrary transmission," *Physical Review B*, vol. 58, pp. 10 761–10 768, Oct. 1998.

[178]   C. Wu, W. V. Liu, and E. Fradkin, "Competing orders in coupled Luttinger liquids," *Physical Review B*, vol. 68, no. 11, p. 115 104, 2003.

[179]   P. Chudzinski, M. Gabay, and T. Giamarchi, "Orbital current patterns in doped two-leg Cu-O Hubbard ladders," *Physical Review B—Condensed Matter and Materials Physics*, vol. 78, no. 7, p. 075 124, 2008.

[180]   A. Iucci, G. A. Fiete, and T. Giamarchi, "Fourier transform of the $2k_F$ Luttinger liquid density correlation function with different spin and charge velocities," *Physical Review B—Condensed Matter and Materials Physics*, vol. 75, no. 20, p. 205 116, 2007.

[181]   M. Bockrath et al., "Luttinger-liquid behaviour in carbon nanotubes," *Nature*, vol. 397, no. 6720, pp. 598–601, 1999, ISSN: 1476-4687.

[182]   V. V. Deshpande, B. Chandra, R. Caldwell, D. S. Novikov, J. Hone, and M. Bockrath, "Mott insulating state in ultraclean carbon nanotubes," *Science*, vol. 323, no. 5910, pp. 106–110, 2009.

[183]   O. Auslaender et al., "Spin-charge separation and localization in one dimension," *Science*, vol. 308, no. 5718, pp. 88–92, 2005.

[184] Y. Jompol et al., "Probing spin-charge separation in a Tomonaga-Luttinger liquid," *Science*, vol. 325, no. 5940, pp. 597–601, 2009.

[185] P. Vianez et al., "Decoupling of the many-body effects from the electron mass in GaAs by means of reduced dimensionality," *Physical Review B*, vol. 107, no. 11, p. 115 128, 2023.

[186] B. Kim et al., "Distinct spinon and holon dispersions in photoemission spectral functions from one-dimensional $SrCuO_2$," *Nature Physics*, vol. 2, no. 6, pp. 397–401, 2006.

[187] R. Claessen, M. Sing, U. Schwingenschlögl, P. Blaha, M. Dressel, and C. S. Jacobsen, "Spectroscopic signatures of spin-charge separation in the quasi-one-dimensional organic conductor TTF-TCNQ," *Physical Review Letters*, vol. 88, no. 9, p. 096 402, 2002.

[188] J. Vijayan et al., "Time-resolved observation of spin-charge deconfinement in fermionic Hubbard chains," *Science*, vol. 367, no. 6474, pp. 186–189, 2020.

[189] G. Kotliar and Q. Si, "Toulouse points and non-Fermi-liquid states in the mixed-valence regime of the generalized Anderson model," *Physical Review B*, vol. 53, no. 18, p. 12 373, 1996.

[190] A. Efros, "Negative density of states: Screening, einstein relation, and negative diffusion," *Physical Review B—Condensed Matter and Materials Physics*, vol. 78, no. 15, p. 155 130, 2008.

[191] I. Schneider, I. Mandal, P. Matveeva, D. Strassel, and S. Eggert, "Boundary logarithmic corrections to the dynamical correlation functions of one-dimensional spin-1/2 chains," *Physical Review B*, vol. 106, no. 15, p. 155 104, 2022.

[192] I. Dzyaloshinskii and A. Larkin, "Correlation functions for a one-dimensional Fermi system with long-range interaction (Tomonaga model)," *Sov. Phys. JETP*, vol. 38, p. 202, 1974.

[193] S. Wang et al., "Nonlinear Luttinger liquid plasmons in semiconducting single-walled carbon nanotubes," *Nature Materials*, vol. 19, no. 9, pp. 986–991, 2020.

[194] P. M. Vianez et al., "Observing separate spin and charge Fermi seas in a strongly correlated one-dimensional conductor," *Science Advances*, vol. 8, no. 24, eabm2781, 2022.

[195] A. Imambekov, T. L. Schmidt, and L. I. Glazman, "One-dimensional quantum liquids: Beyond the Luttinger liquid paradigm," *Reviews of Modern Physics*, vol. 84, no. 3, p. 1253, 2012.

[196] O. Tsyplyatyev et al., "Hierarchy of modes in an interacting one-dimensional system," *Physical Review Letters*, vol. 114, no. 19, p. 196 401, 2015.

[197] Y. Jin et al., "Momentum-dependent power law measured in an interacting quantum wire beyond the Luttinger limit," *Nature Communications*, vol. 10, no. 1, p. 2821, 2019.

[198] M. S. Dresselhaus, "Solid state physics optical properties of solids," 2022.

[199] T. Schmidt and A. Komnik, "On the visibility of electron–electron interaction effects in field emission spectra," *Solid State Communications*, vol. 135, no. 7, pp. 455–460, 2005, ISSN: 0038-1098.

BIBLIOGRAPHY

[200] A. Furusaki and N. Nagaosa, "Single-barrier problem and Anderson localization in a one-dimensional interacting electron system," *Physical Review B*, vol. 47, no. 8, p. 4631, 1993.

[201] N. Shimoi, "Conductive effect of increased crystallinity of single-walled carbon nanotubes as field emitter," in *Perspective of Carbon Nanotubes*, IntechOpen, 2019.

[202] A. Kleiner and S. Eggert, "Band gaps of primary metallic carbon nanotubes," *Physical Review B*, vol. 63, no. 7, p. 073 408, 2001.

[203] S. T. Carr, A. O. Gogolin, and A. A. Nersesyan, "Interaction induced dimerization in zigzag single wall carbon nanotubes," *Physical Review B*, vol. 76, p. 245 121, Dec. 2007.

[204] A. Nersesyan and A. Tsvelik, "Coulomb blockade regime of a single-wall carbon nanotube," *Physical Review B*, vol. 68, no. 23, p. 235 419, 2003.

[205] L. Levitov and A. Tsvelik, "Narrow-gap Luttinger liquid in carbon nanotubes," *Physical Review Letters*, vol. 90, no. 1, p. 016 401, 2003.

[206] F. H. L. Essler and A. M. Tsvelik, "Weakly coupled one-dimensional Mott insulators," *Physical Review B*, vol. 65, p. 115 117, Mar. 2002.

[207] F. H. Essler, A. M. Tsvelik, and G. Delfino, "Quasi-one-dimensional spin-1/2 Heisenberg magnets in their ordered phase: Correlation functions," *Physical Review B*, vol. 56, no. 17, p. 11 001, 1997.

[208] M. Marganska, P. Chudzinski, and M. Grifoni, "The two classes of low-energy spectra in finite carbon nanotubes," *Physical Review B*, vol. 92, p. 075 433, Aug. 2015.

[209] R. Egger and A. Gogolin, "Intrinsic coulomb blockade in multi-wall carbon nanotubes," *Chemical Physics*, vol. 281, no. 2, pp. 447–454, 2002, ISSN: 0301-0104.

[210] A. V. Kesavan, A. C. Khot, T. D. Dongale, K. R. Son, P. C. Ramamurthy, and T. G. Kim, "Graphite–metal composite electrodes with a tunable work function for use in optoelectronic devices," *Journal of Materials Chemistry C*, vol. 10, no. 41, pp. 15 358–15 366, 2022.

[211] D. F. Urban and A. Komnik, "Interaction-induced beats of Friedel oscillations in quantum wires," *Physical Review Letters*, vol. 100, p. 146 602, Apr. 2008.

[212] A. Schulz, A. De Martino, and R. Egger, "Spin-orbit coupling and spectral function of interacting electrons in carbon nanotubes," *Physical Review B*, vol. 82, p. 033 407, Jul. 2010.

[213] J. Maultzsch, S. Reich, and C. Thomsen, "Chirality-selective Raman scattering of the D mode in carbon nanotubes," *Physical Review B*, vol. 64, p. 121 407, Sep. 2001.

[214] S. Borisenko, "99 years of ARPES," *Nature Reviews Physics*, vol. 3, no. 8, pp. 539–539, 2021.

[215] R. Haindl, K. Köster, J. H. Gaida, M. Franz, A. Feist, and C. Ropers, "Femtosecond tunable-wavelength photoassisted cold field emission," *Applied Physics B*, vol. 129, no. 3, p. 40, 2023.

[216] W. Milne et al., "Carbon nanotubes as field emission sources," *Journal of Materials Chemistry*, vol. 14, no. 6, pp. 933–943, 2004.

[217] J. A. Stratton, *Electromagnetic theory*. John Wiley & Sons, 2007, vol. 33.

[218] M. Rezinkina, "Modelling of electric field strength amplification at the tips of thin conductive rods arrays," *Progress In Electromagnetics Research M*, vol. 88, pp. 111–119, 2020.

[219] P. Chudzinski, "Contribution of 1D topological states to the extraordinary thermoelectric properties of Bi_2Te_3," *Proceedings of the Royal Society A*, vol. 476, no. 2239, p. 20 200 088, 2020.

[220] K. Yamamoto, M. Nakagawa, M. Tezuka, M. Ueda, and N. Kawakami, "Universal properties of dissipative Tomonaga-Luttinger liquids: Case study of a non-hermitian XXZ spin chain," *Physical Review B*, vol. 105, no. 20, p. 205 125, 2022.

[221] A. Rinzler et al., "Unraveling nanotubes: Field emission from an atomic wire," *Science*, vol. 269, no. 5230, pp. 1550–1553, 1995.

[222] Z. Ren et al., "Synthesis of large arrays of well-aligned carbon nanotubes on glass," *Science*, vol. 282, no. 5391, pp. 1105–1107, 1998.

[223] W.-Z. Wang et al., "Aligned ultralong ZnO nanobelts and their enhanced field emission," *Advanced Materials*, vol. 18, no. 24, pp. 3275–3278, 2006.

[224] S. Jo, D. Wang, J. Huang, W. Li, K. Kempa, and Z. Ren, "Field emission of carbon nanotubes grown on carbon cloth," *Applied physics letters*, vol. 85, no. 5, pp. 810–812, 2004.

[225] G. Liu, Y. Lin, Y. Tu, and Z. Ren, "Ultrasensitive voltammetric detection of trace heavy metal ions using carbon nanotube nanoelectrode array," *Analyst*, vol. 130, no. 7, pp. 1098–1101, 2005.

[226] D. Banerjee, S. H. Jo, and Z. F. Ren, "Enhanced field emission of ZnO nanowires," *Advanced Materials*, vol. 16, no. 22, pp. 2028–2032, 2004.

[227] D. Carnahan, M. Reed, Z. Ren, and K. Kempa, "Field emission from arrays of carbon nanotubes," *www. nano-lab. com*, 1998.

[228] L. Dong, A. Subramanian, D. Hugentobler, B. J. Nelson, and Y. Sun, "Nano encoders based on vertical arrays of individual carbon nanotubes," *Advanced Robotics*, vol. 20, no. 11, pp. 1281–1301, 2006.

[229] S. Jo, Y. Tu, Z. Huang, D. Carnahan, D. Wang, and Z. Ren, "Effect of length and spacing of vertically aligned carbon nanotubes on field emission properties," *Applied Physics Letters*, vol. 82, no. 20, pp. 3520–3522, 2003.

[230] Y. Tu, Y. Lin, and Z. Ren, "Nanoelectrode arrays based on low site density aligned carbon nanotubes," *Nano Letters*, vol. 3, no. 1, pp. 107–109, 2003.

[231] K. Kempa et al., "Photonic crystals based on periodic arrays of aligned carbon nanotubes," *Nano Letters*, vol. 3, no. 1, pp. 13–18, 2003.

[232] S. H. Lee, J. S. Han, H. Go, and C. J. Lee, "Enhanced field electron emission properties of graphite nanoplatelet paste emitters using graphite binder and graphite nanoparticle filler," *AIP Advances*, vol. 11, no. 3, p. 035 307, 2021.

[233] K. Wu, E. Wang, Z. Cao, Z. L. Wang, and X. Jiang, "Microstructure and its effect on field electron emission of grain-size-controlled nanocrystalline diamond films," *Journal of applied physics*, vol. 88, no. 5, pp. 2967–2974, 2000.

[234] Y. Cheng and O. Zhou, "Electron field emission from carbon nanotubes," *Comptes rendus. Physique*, vol. 4, no. 9, pp. 1021–1033, 2003.

[235] J. Hu, B. Bai, and D. Chen, "Effect of different vacuum on field emission of carbon nanotube arrays," *International Journal of Applied Electromagnetics and Mechanics*, vol. 64, no. 1-4, pp. 675–683, 2020.

[236] M. Li, Q. Wang, J. Xu, J. Zhang, Z. Qi, and X. Zhang, "Optically induced field-emission source based on aligned vertical carbon nanotube arrays," *Nanomaterials*, vol. 11, no. 7, p. 1810, 2021.

[237] M. Khodke, U. Chavan, S. Joshi, and S. Shinde, "Experimental studies on carbon nanotube strain sensors," *Materials Today: Proceedings*, 2023.

[238] T. A. Yu et al., "Comparison and analysis of field emission characteristics of carbon cathodes based on PAN fiber and CNT filaments," *Advanced Materials & Technologies*, vol. 7, no. 1, pp. 46–57, 2022.

[239] S. V. Filippov, A. G. Kolosko, E. O. Popov, and R. G. Forbes, "Field emission: Calculations supporting a new methodology of comparing theory with experiment," *Royal Society Open Science*, vol. 9, no. 11, p. 220 748, 2022.

[240] R. G. Forbes, "5.4: Analysis of experimental field emission current-voltage characteristics (especially those from carbon nanotubes)," in *International Vacuum Nanoelectronics Conference*, IEEE, 2010, pp. 92–93.

[241] R. G. Forbes, "Simple good approximations for the special elliptic functions in standard Fowler-Nordheim tunneling theory for a Schottky-Nordheim barrier," *Applied Physics Letters*, vol. 89, no. 11, p. 113 122, 2006.

[242] R. G. Forbes, "On the need for a tunneling pre-factor in Fowler–Nordheim tunneling theory," *Journal of Applied Physics*, vol. 103, no. 11, 2008.

[243] R. G. Forbes and J. H. Deane, "Transmission coefficients for the exact triangular barrier: An exact general analytical theory that can replace Fowler & Nordheim's 1928 theory," *Proceedings of the Royal Society A: Mathematical, Physical and Engineering Sciences*, vol. 467, no. 2134, pp. 2927–2947, 2011.

[244] J. Li, C. Papadopoulos, J. Xu, and M. Moskovits, "Highly-ordered carbon nanotube arrays for electronics applications," *Applied physics letters*, vol. 75, no. 3, pp. 367–369, 1999.

[245] Y. Z. Lee, L. Burk, K.-h. Wang, G. Cao, J. Lu, and O. Zhou, "Carbon nanotube based X-ray sources: Applications in pre-clinical and medical imaging," *Nuclear instruments and methods in physics research section A: Accelerators, spectrometers, detectors and associated equipment*, vol. 648, S281–S283, 2011.

[246] A. Corletto and J. G. Shapter, "Nanoscale patterning of carbon nanotubes: Techniques, applications, and future," *Advanced Science*, vol. 8, no. 1, p. 2 001 778, 2021.

[247] M. R. McCartney, R. E. Dunin-Borkowski, and D. J. Smith, "Quantitative measurement of nanoscale electrostatic potentials and charges using off-axis electron holography: Developments and opportunities," *Ultramicroscopy*, vol. 203, pp. 105–118, 2019.

[248] H. Ochner, S. Szilagyi, M. Edte, L. Malavolti, S. Rauschenbach, and K. Kern, "Phase reconstruction of low-energy electron holograms of individual proteins," *ACS Nano*, vol. 16, no. 11, pp. 18 568–18 578, 2022, PMID: 36367752.

[249] F. Zheng, V. Migunov, J. Caron, H. Du, G. Pozzi, and R. E. Dunin-Borkowski, "Nanoscale three-dimensional charge density and electric field mapping by electron holographic tomography," *Nano letters*, vol. 23, no. 3, pp. 843–849, 2023.

[250] H. Lichte and M. Lehmann, "Electron holography—basics and applications," *Reports on Progress in Physics*, vol. 71, no. 1, p. 016 102, 2007.

[251] M. Beleggia, T. Kasama, R. E. Dunin-Borkowski, S. Hofmann, and G. Pozzi, "Direct measurement of the charge distribution along a biased carbon nanotube bundle using electron holography," *Applied physics letters*, vol. 98, no. 24, 2011.

[252] J. Cumings, A. Zettl, M. McCartney, and J. Spence, "Electron holography of field-emitting carbon nanotubes," *Physical review letters*, vol. 88, no. 5, p. 056 804, 2002.

[253] J. M. Thomas, E. T. Simpson, T. Kasama, and R. E. Dunin-Borkowski, "Electron holography for the study of magnetic nanomaterials," *Accounts of chemical research*, vol. 41, no. 5, pp. 665–674, 2008.

[254] P. Ajayan, J.-C. Charlier, and A. Rinzler, "Carbon nanotubes: From macromolecules to nanotechnology," *Proceedings of the National Academy of Sciences*, vol. 96, no. 25, pp. 14 199–14 200, 1999.

[255] Y. Wang, G. Sun, X. Zhang, X. Zhang, and Z. Cui, "Advancement in carbon nanotubes optoelectronic devices for terahertz and infrared applications," *Advanced Electronic Materials*, vol. 10, no. 10, p. 2 400 124, 2024.